Technische Universität Dresden

# Wide tuning of electronic properties in strained III-V core/shell nanowires

**Leila Balaghi, M. Sc.**

der Fakultät Elektrotechnik und Informationstechnik der Technischen Universität Dresden

zur Erlangung des akademischen Grades

**Doktoringenieur**

(Dr.-Ing.)

genehmigte Dissertation

Vorsitzender: Prof. Dr. rer. nat. Stefan Mannsfeld
1. Gutachter: Prof. Dr.-Ing. Thomas Mikolajick
2. Gutachter: Prof. Dr. Marius Grundmann
3. Gutachter: Prof. Dr. Manfred Helm

Tag der Einreichung: 07.09.2020
Tag der Verteidigung: 12.01.2021

*To my husband Martin,*

*my sister Sima,*

*my little son Lukas,*

*and my dear parents*

**Abstract**

The monolithic integration of III-V semiconductors on Si substrates is a part of a long-term technological roadmap for the semiconductor industry towards More-than-Moore technologies. Despite of the different lattice constants and thermal expansion coefficients, research efforts over the last two decades have shown that III-V crystals with a high structural quality can be grown epitaxially in the form of nanowires directly on Si using CMOS-compatible (Au-free) methods. Among other III-V compounds, $In_xGa_{1-x}As$ is of the special interest for the use in infrared photonics and high-speed electronics due to its tunable direct bandgap and low electron effective mass, respectively. For comparison, $In_xGa_{1-x}As$ thin films are typically grown on lattice-matched InP substrates with a limited range of compositions at around x=0.52. The realization of $In_xGa_{1-x}As$ nanowires on Si, though, has been proved challenging owing to the limited In-content when the nanowires are grown Ga-catalyzed or the high density of stacking faults when the nanowires are grown catalyst-free.

In this work, the use of highly lattice-mismatched GaAs/$In_xGa_{1-x}As$ and GaAs/$In_xAl_{1-x}As$ core/shell nanowires on Si(111) substrates have been studied as an alternative to $In_xGa_{1-x}As$ nanowires. The core/shell mismatch strain and its accommodation within the nanowires plays an important role in the growth, the structural, and the electronic properties of the nanowires. A key parameter in this work was the unusually small diameter of 20 – 25 nm of the GaAs core.

First, the strain-induced bending of the nanowires during the growth of the shell by molecular beam epitaxy was investigated. It was apparent that the nanowires bend as a result of a preferential incorporation of In adatoms on one side of the nanowires. To obtain straight nanowires with symmetric shell composition and thickness around the core, it was necessary to choose relatively low growth temperatures and high growth rates that limited the surface diffusivity of In adatoms.

Second, the strain accommodation in straight nanowires was investigated as a function of the shell thickness and composition using a combination of Raman scattering spectroscopy and X-ray diffraction. For a fixed shell composition of x=0.20 and small enough shell thicknesses, the strain in the shell is compressive and decreases progressively as the shell grows thicker. On the other hand, the strain in the core is tensile with hydrostatic character and increases with shell thickness. Finally, for shell thicknesses larger than 40 nm, the shell becomes strain-free, whereas the strain in the core saturates at 3.2% without any dislocations. For a fixed shell thickness of 80 nm, the strain in the core was further increased by increasing the In-content in the shell,

reaching values as high as 7% for x=0.54. A plastic relaxation via misfit dislocations was observed only for the next highest In-content of x=0.70.

In agreement to theoretical predictions, the tensile strain in the core resulted in a large reduction of the GaAs bandgap (as measured by photoluminescence spectroscopy), up to approximately 40% of the strain-free value. A similar reduction in electron effective mass is also expected. The transport properties of electrons inside the strained GaAs core were assessed by optical-pump terahertz-probe spectroscopy. Quite high mobility values of approximately 6100 $cm^2/Vs$ at 300 K for a carrier concentration of $9\times10^{17}$ $cm^{-3}$ were measured, which are the highest reported in the literature for GaAs nanowires, but also higher than the values for unstrained bulk GaAs.

The importance of the results in this work is two-fold. On the one hand, strain-free $In_xGa_{1-x}As$ nanowire shells were grown on Si substrates with x up to 0.54 and thicknesses well beyond the critical thickness of their thin film counterparts. Such shells could potentially be employed as conduction channels in high electron mobility transistors (HEMTs) integrated in Si platforms. On the other hand, highly tensile-strained GaAs cores with electronic properties like those of $In_xGa_{1-x}As$ thin films were obtained. In this case, the results demonstrate, that GaAs nanowires can be suitable for photonic devices across the near-infrared range, including telecom photonics at 1.3 and potentially 1.55 μm, as well as for high-speed electronics. GaAs as a binary material is expected to be advantageous compared to $In_xGa_{1-x}As$ due to the absence of structural imperfections typically present in ternary alloys.

Finally, to explore the potential of the core/shell nanowires as HEMTs, self-consistent Schrödinger-Poisson calculations of two different modulation-doped heterostructures were performed. In the case of a strained GaAs core overgrown by an unstrained $In_xGa_{1-x}As$ shell and an additional unstrained Si-doped $In_xAl_{1-x}As$ shell, the possibility to form a cylindrical-like two-dimensional electron gas inside the $In_xGa_{1-x}As$ shell was found. In the alternative case of a strained GaAs core overgrown by an unstrained Si-doped $In_xAl_{1-x}As$ shell, it was found that it is possible to form a quasi-one-dimensional electron gas at the center of the core. Both structures are the subject of ongoing research.

**Kurzzusammenfassung**

Die monolithische Integration von III-V-Halbleitern auf Si-Substraten ist Teil eines langfristigen technologischen Plans der Halbleiterindustrie hin zu More-than-Moore-Technologien. Trotz der unterschiedlichen Gitterkonstanten und Wärmeausdehnungskoeffizienten haben Forschungsanstrengungen in den letzten zwei Jahrzehnten gezeigt, dass III-V-Kristalle mit hoher struktureller Qualität unter Verwendung von CMOS-kompatiblen (Au-frei) Methoden epitaktisch in Form von Nanodrähten direkt auf Si gezüchtet werden können. Innerhalb der III-V-Verbindungshalbleitern ist $In_xGa_{1-x}As$ aufgrund seiner einstellbaren direkten Bandlücke bzw. der geringen effektive Masse der Elektronen für Anwendungen in der Infrarotphotonik und Hochgeschwindigkeitselektronik von besonderem Interesse. Dem Gegenüber werden $In_xGa_{1-x}As$ -Dünnschichten typischerweise auf gitterangepassten InP-Substraten gezüchtet, wobei deren Zusammensetzung mit etwa x = 0,52 begrenzt ist. Allerdings hat sich auch die Umsetzung von $In_xGa_{1-x}As$-Nanodrähten auf Si durch den begrenzten In-Gehalt während deren Ga-katalysierten Wachstums oder der hohen Dichte von Stapelfehlern bei deren katalysatorfreien Wachstum als schwierig erwiesen.

In dieser Arbeit wurde die Verwendung von hochgradig gitterfehlangepassten GaAs/$In_xGa_{1-x}As$- und GaAs/$In_xAl_{1-x}As$ -Kern/Schalen-Nanodrähten auf Si (111)-Substraten als Alternative zu InxGa1-xAs-Nanodrähten untersucht. Die durch die Gitterfehlanpassung hervorgerufene Spannung zwischen Kern und Schale und deren Ausgleich innerhalb der Nanodrähte spielen eine wichtige Rolle für das Wachstum, die Struktur und die elektronischen Eigenschaften der Nanodrähte. Ein ausschlaggebender Faktor in dieser Arbeit war der ungewöhnlich geringe Durchmesser des GaAs-Kerns, von nur 20 - 25 nm.

Zunächst wurden die spannungsinduzierte Biegung der Nanodrähte während des Wachstums der Hülle durch Molekularstrahlepitaxie untersucht. Es wurde ersichtlich, dass sich die Nanodrähte aufgrund eines bevorzugten Einbaus von In-Adatomen auf einer Seite der Nanodrähte verbiegen. Um gerade Nanodrähte mit symmetrischer Hüllenzusammensetzung und Dicke um den Kern zu erhalten, mussten relativ niedrige Wachstumstemperaturen und hohe Wachstumsraten gewählt werden, welche die Oberflächendiffusionsfähigkeit von In-Adatomen begrenzten.

Zweitens wurde die Spannungsanpassung in geraden Nanodrähten als Funktion der Schalendicke und deren Zusammensetzung mittels Raman-Spektroskopie und Röntgenbeugung untersucht. Bei einer festen Zusammensetzung von x = 0,20 und ausreichend kleinen Schalendicke ist die Dehnung in der Schale kompressiv und nimmt mit zunehmender Dicke der

Schale schrittweise ab. Dem Gegenüber befindet sich der Kern unter Zugspannung mit hydrostatischem Charakter, welche mit der Schalendicke zunimmt. Wird die Schalendicken schließlich größer als 40 nm, so wird die Schale spannungsfrei, während die Dehnung im Kern bei 3,2% gesättigt ist, ohne das Versetzungen auftreten. Bei einer festen Schalendicke von 80 nm wurde die Dehnung im Kern durch einen gesteigerten In-Gehalt weiter erhöht, und Werte von bis zu 7% konnten für x = 0,54 erreicht werden. Eine plastische Relaxation durch Fehlversetzungen wurde nur für den nächsthöheren In-Gehalt von x = 0,70 beobachtet.

In Übereinstimmung mit theoretischen Vorhersagen führte die Zugspannung im Kern zu einer starken Verringerung der GaAs-Bandlücke (welche mittels Photolumineszenz-Spektroskopie untersucht wurde) bis zu ungefähr 40% der spannungsfreien Werte. Eine ähnliche Verringerung der effektiven Elektronenmasse wird ebenfalls erwartet. Die Transporteigenschaften von Elektronen innerhalb des verspannten GaAs-Kerns wurden durch „Optical Pump–Terahertz Probe“-Spektroskopie beurteilt. Bei 300 K konnten relativ hohe Mobilitätswerte von ungefähr 6100 $cm^2/Vs$ bei eine Ladungsträgerdichte von $9 \times 10^{17}$ $cm^{-3}$ gemessen werden, welche die höchsten in der Literatur angegebenen Werte für GaAs-Nanodrähte sind, aber auch höher als die Werte für spannugsfreie GaAs-Volumenkristalle.

Die Ergebnisse dieser Arbeit sind von zweifacher Bedeutung. Einerseits wurden spannungsfreie $In_xGa_{1-x}As$-Nanodrahtschalen auf Si-Substraten mit x bis zu 0,54 und mit Dicken gewachsen, welche weit über der kritischen Schichtdicken ihrer Dünnschicht-Pendants liegen. Solche Schalen könnten möglicherweise als Leitungskanäle in Transistoren mit hoher Elektronenmobilität (HEMTs) verwendet werden, die in Si-Plattformen integriert sind. Andererseits wurden hochgradig zugbelastete GaAs-Kerne mit elektronischen Eigenschaften vergleichbar mit denen von $In_xGa_{1-x}As$ -Dünnfilmen erreicht. In diesem Fall zeigen die Ergebnisse, dass GaAs-Nanodrähte für photonische Bauelemente im nahen Infrarotbereich, einschließlich Telekommunikationsphotonik bei 1,3 und möglicherweise 1,55 µm, sowie für Hochgeschwindigkeitselektronik geeignet sein könnten. Es wird erwartet, dass GaAs als binäres Material im Vergleich zu $In_xGa_{1-x}As$ vorteilhaft ist, da keine strukturellen Mängel vorliegen, die typischerweise in ternären Legierungen vorhanden sind.

Um das Potenzial dieser Kern/Schalen-Nanodrähte als HEMTs zu untersuchen, wurden abschließend selbstkonsistente Schrödinger-Poisson-Berechnungen von zwei verschiedenen modulationsdotierten Heterostrukturen durchgeführt. Im Fall eines verspannten GaAs-Kerns, der von einer unverspannten $In_xGa_{1-x}As$-Hülle und einer zusätzlichen unverspannten Si-dotierten $In_xAl_{1-x}As$-Hülle überwachsen ist, wurde die Möglichkeit für die Bildung eines zylindrischen, zweidimensionalen Elektronengases innerhalb der $In_xGa_{1-x}As$ -Schale gefunden.

Im alternativen Fall eines gespannten GaAs-Kerns, der von einer ungespannten Si-dotierten $In_xAl_{1-x}As$-Hülle überwachsen ist, wurde festgestellt, dass es möglich ist ein quasi eindimensionales Elektronengas in der Mitte des Kerns zu bilden. Beide Strukturen sind Gegenstand laufender Forschung.

**Contents**

## 1 Introduction

As semiconductor industries increasingly move beyond traditional Si CMOS (complementary metal oxide semiconductor) technology toward hybrid material structures on Si, there is a rising research activity to integrate other semiconductors on Si substrates. III-V semiconductors are exquisite candidates owing to their high electron mobility and widely tunable bandgap, which allows their wide use in electronics and photonics by adding new applications via integrated direct bandgap materials. GaAs is one of the well-known III-V semiconductors as it has been utilized in several different electronic and optoelectronic applications due to its high mobility and direct bandgap properties. Therefore, GaAs has been used in high-speed applications such as high electron mobility transistors (HEMTs), laser diodes, and radio frequency devices for optical communication systems. For an example, GaAs has been applied in advanced mobile communication applications. Besides the performance, the advantages are a very low off-state power consumption and its high current amplifications [1], [2], [3], [4], [5]. $In_xGa_{1-x}As$ is another representative example of III-V semiconductors in the near-infrared range, where the In-content can be tuned to provide suitable bandgaps for multi-junction photovoltaics, light emitting diodes and photodiodes, or telecom photonics. Nevertheless, not all compositions and corresponding bandgaps between the two endpoint binaries of a ternary alloy (e.g. GaAs and InAs for $In_xGa_{1-x}As$) are feasible because of the unavailability of lattice-matched substrates as well as the spinodal decomposition. Furthermore, the alloy disorder is another factor that affects the performance of ternary alloys [6], [4], [7], [8], [9].

Co-integration of these types of semiconductors as GaAs with Si-CMOS logics can pave a new path to scalable CMOS nodes. To achieve a monolithic integration of GaAs on Si, a direct epitaxy on Si is demanded. Here, a major hurdle is the presence of a large lattice mismatch of $\sim 4\%$ between them, causing the formation of crystalline defects to accommodate the resulting strain. One solution to reduce these defects is to shorten the interface between GaAs and the lattice mismatched Si substrate [10], [11], [12] ,[13].

The great advantage of materials in a nano-scale regime like nanowires is to have a small footprint (meaning a smaller interface with the substrate) and higher aspect ratio allowing the large tolerance to the lattice mismatch strain. The accommodation of strain through nanowires enables us to grow very dissimilar materials on Si with a high crystal quality [14], and [15].

$In_xGa_{1-x}As$ alloy in particular is the material of our interest in this thesis. The Ga-assisted VLS growth of $In_xGa_{1-x}As$ nanowires on Si by molecular beam epitaxy (MBE) is challenging. The major issues were referred in a droplet-mediated and droplet-free growth, according to the report of

Heiss et al. and Treu et al, respectively [16], [17]. In the droplet-mediated VLS growth ([17]), due to the very low In incorporation through liquid Ga droplets, the In composition cannot reach beyond 3-5% and for the growth temperature < 575 °C a radial In-rich shell forms. Based on the report of Treu et al., using a droplet-free, vapor-solid (VS) growth mechanism via a selective area epitaxy, enabled them to tune the In composition over a broader range. Nonetheless, the obtained $In_xGa_{1-x}As$ nanowires contained a high density of stacking faults. Thus, the MBE growth of free-standing $In_xGa_{1-x}As$ nanowires with a high crystal quality on Si remains very difficult. For this reason, the approach in this work is to grow $In_xGa_{1-x}As$ shells round the GaAs nanowire core.

The progress in the crystal growth of nanowires has led to the formation of coherent crystalline nanowires with core-shell geometry. The shell growth for the use in nano-photonics or -electronics applications has been developed in different aspects such as surface passivation, strain engineering of the lattice mismatched core/shell heterostructures as well as charge carrier confinements in two-dimensional electron gas systems using modulation-doped techniques [18], [19], [20], and [21].

In photonics, bandgap/strain engineering of core/shell nanowires makes it possible to widely tune the bandgap for various device applications (e.g. UV- IR lasers, tunable photo diode lasers, LEDs, solar cells, and sensors) [18], [7], [22]. Strain-induced changes in the bandgap of the core in core/shell nanowires have been already reported for GaAs/GaP, $GaAs/Al_xGa_{1-x}As$, $InAs/InAs_xP_{1-x}$, and $GaN/Al_xGa_{1-x}N$. In all cases, the core was compressively strained, and its bandgap increased, in the most extreme case by 260 meV. Tensile strain and up to 150 meV smaller bandgap in the core have been reported only for $GaAs/Ga_xIn_{1-x}P$ nanowires. Nevertheless, extending the same concept to higher strain values is not straightforward owing to limiting factors like plastic relaxation and/or morphological instabilities [23], [24], [25], [26], [27], [20], [28] .

In electronics, nanowire-based field effect transistors (nanowire-FETs) open up new routes in enhanced transconductance, superior electrostatic gate while suffering from the scattering at the nanowire surface and ionized impurities, where the remote doping concept (modulation doped technique) is demanded. Modulation doped InAs/InP and GaAs/AlGaAs core/shell nanowires have exhibited room-temperature mobilities of 2000 $cm^2V^{-1}s^{-1}$ and 2200 $cm^2V^{-1}s^{-1}$ respectively; however the electron mobility is still lower than of equivalent planar systems [29], [30], and [31].

This thesis is categorized in five chapters. The first chapter gives the reader an introduction and motivation to the strain/bandgap engineering in III-V core/shell nanowire heterostructures.

The second chapter introduces the fundamentals such as the electronic and structural properties of compound III-Vs semiconductors and gives an overview of the growth of nanowires on Si substrates and of different types of core/shell structures. Additionally, the chapter highlights potential applications for nanowire heterostructures with a review on the state-of-the-art in the scientific field, presenting the distinct features of the core/shell nanowires. Strain engineering in core/shell nanowires is discussed, where nanowire properties are differentiated from epilayers. Particularly, the remarkable effect of strain on the band structure of III-V semiconductors, specifically GaAs, is outlined. Towards the end of the chapter, modulation-doped heterostructures based on III-V semiconductors, which is one of the intriguing outcomes of bandgap engineering, is mentioned. The third chapter is dedicated to the experimental setups and their working principles with regards to the application of nanowires, where the major focus is on optical spectroscopy such as Raman scattering spectroscopy and photoluminescence spectroscopy. The optical pump terahertz probe spectroscopy and the corresponding background are also described. Furthermore, the workflow employed in the software 'nextnano', which was used for the simulation of the electronic and optoelectronic properties of the semiconductors and the influence of strain on them, is also presented. Additionally, device processing tools and the related procedure for the contact fabrication on nanowires are mentioned. Other techniques which are utilized in this thesis such as optical and electron microscopies, X-ray diffraction spectroscopy, and molecular beam epitaxy are summarized. At the end of the chapter, the procedure for the growth of these core/shell nanowires is described. The fourth chapter focuses on the main results and findings of this work. In the first section of this chapter the structural and compositional analyses of straight lattice-mismatched core/shell nanowires, including the limits for their coherent growth are shown. The challenges in the growth of these highly lattice-mismatched core/shell nanowires, which results in their bending, are discussed and the strategy to suppress this deformation is shown. Following this discussion, the strain analyses in the core/shell nanowires are in the focus to gain a deeper understanding of the strain distribution as a function of nanowire dimensions and their chemical composition. The modification of the electronic properties of GaAs as the bandgap, electron effective mass and electron mobility under the tensile strain are demonstrated. At the end of the fourth chapter, the simulation results for modulation-doped heterostructures in coaxial core/multishell nanowires are shown, pointing towards future application possibilities. Finally, initial results on the deposition of metal contacts to the nanowires are presented, which allowed their IV characterization as a first step toward their future device integration. A final overview of the major findings of this work with an outlook concludes this thesis in chapter 5.

*Jerry Dunn*

*“Don’t limit your challenges, challenge your limits!”*

# 2 Fundamentals and state-of-the-art

This chapter introduces the required knowledge in solid state physics and material science related to the subject of this thesis. The electronic and structural properties of III-V semiconductors, growth of III-V semiconductor nanowires on Si, strain in core/shell heterostructure nanowires, strain engineering in core/shell nanowires and its effect on band parameters, and finally modulation-doped III-V semiconductor heterostructures are presented in this chapter.

## 2.1 Electronic and structural properties of III-V semiconductors

This chapter provides the basic structural and electronic properties of III-V semiconductors and III-V semiconductor nanowires. Semiconductors are materials with a bandgap of up to 6 eV and an electrical conductivity that can be adjusted via doping. Specifically, the direct bandgap of III-As semiconductors can be tailored in the mid-infrared range from 0.65 to 2 eV depending on the alloy composition.

III-V semiconductor-based devices have been revolutionized a wide range of technologies in the last four decades. They have been utilized in high-frequency electronics, high electron mobility transistors (HEMTs), fiber-optic communications, wireless communications, light-emitting diodes, laser diodes, photodetectors, photovoltaics, thermo-photovoltaics, magnetic sensors, THz emitters, etc. To highlight a few large-scale impacts of III-V compounds, one can mention fiber-optic communicational systems, satellite communications, infrared imaging, etc [32], [33], [34].

Conventional pseudomorphic high electron mobility transistors (pHEMTs) with lattice matched $In_{0.53}Ga_{0.47}As/In_{0.52}Al_{48}As$ on costly InP substrates exhibit high mobility and saturation velocity. Therefore, they are highly attractive for the fabrication of three-terminal low noise and high frequency devices, which operate at 300 K. This material system in spite of the high cost, has already been used in fabricating monolithic microwave integrated circuit devices including very low-noise amplifiers and receivers, mainly due to the outstanding combination of high frequency operations and low noise properties [33], [34], [35], [36].

Integration of III-V semiconductors with Si CMOS platform can improve device performances in particular due to their higher electron mobility values and direct-tunable bandgaps. However, their integration via epitaxial growth of III-V thin films on Si substrates is hampered by the lattice mismatch between the two. Here, nanowires offer advantages due to their high aspect ratio and small footprints, thereby offering high crystal quality of the III-V material directly on a Si platform.

The band structure of the exemplary III-As semiconductor GaAs, calculated using the tight-binding (TB) as a semi-empirical modeling at 300 K, is shown in Figure 2.1 (a). In solid state physics, the TB and k.p model are methods for computing the electronic band structure in k-space using the set of wave functions like atomic orbitals [37].

The corresponding Brillouin zone (BZ) of the face-centered cubic (fcc) unit cell of GaAs is shown as a truncated octahedron in the inset of Figure 2.1 (a). The conduction band (CB) minimum and the valence band (VB) maximum are at the Γ point (center of BZ) indicating its direct band gap nature. VB at Γ-point consists of three bands, i.e., the two degenerate bands of heavy holes (HH) and light holes (LH), and the split-off (SO) band due to spin-orbit coupling. The direct band gap energy of GaAs ($E_{gap}^{\Gamma}$) at 300 K is 1.424 eV with SO energy ($\Delta_{SO}$) of 0.31 eV as also shown in Figure 2.1 (a) [37], [38], [39].

In a broader view, the elements of group III and V share their three and five outer shell electrons, respectively, generating an average of four valence electrons per atom available for binding. 25 possible binary III-V compounds have been known so far. Among all binary III-V compounds, some are technologically recognized as GaAs, AlN, GaN, GaP, InP, and InSb. Each of these binary materials has a different bandgap [32].

Furthermore, mixing two group III elements and one group V element produces ternary crystals such as $In_xGa_{1-x}As$, $In_xAl_{1-x}As$, and $Al_xGa_{1-x}As$. Ternary crystals can be created with one group III element and two group V elements as well. Thus, ternary compounds are synthesized by the combination of three elements in total. Most of the properties of any ternary material are the weighted average of their composed binary compound properties. For an instance, $In_xGa_{1-x}As$ can be viewed as an alloy with a composition of x mol.% of InAs and (1-x) mol.% of GaAs and its bandgap lies between GaAs and InAs depending on x. The bandgap energy of any ternary material ($E_g(x)$) has a nonlinear trend between its two constituent binary compounds [32].

$$E_g(x) = xE_1 + (1-x)E_2 - cx(1-x) \quad (1).$$

In eq. (1), $E_1$ is bandgap energy of one of the binaries corresponding to x=1 and $E_2$ is the bandgap energy of the other binary corresponding to x=0. The constant $c$ (which is independent from composition x) stands for the empirical bowing parameter accounting for the nonlinearity [32]. In the literature, eq. (1) is modified as follows

$$E_g(x) = a + bx + cx^2 \quad (2).$$

In eq. (2), the corresponding constants of $a$, $b$, and $c$ are equal to $E_2$, $E_1 - E_2 - c$, and c, respectively. In Table 1, bandgap relationships for three III-As ternaries at 300 K for the range of direct energy gap are presented [32].

The bandgap energy curves of $In_xGa_{1-x}As$ and $In_xAl_{1-x}As$ as a function of composition x have been shown in Figure 2.1 (b). A quaternary compound is a mixture of binary or ternary compounds. The properties of a quaternary compound (e.g $.A_xB_{1-x}C_yD_{1-y}$) can be interpolated between two ternary compounds (such as ACD and BCD materials). A quaternary compound such as $In_xAl_{1-x}Ga_yAs_{1-y}$ can be described as a mixture of $In_xGa_{1-x}As$ and $Al_xGa_{1-x}As$ materials [32].

$$E_g\left(A_xB_{1-x}C_yD_{1-y}\right) = xE_{ACD} + (1-x)E_{BCD} - \Delta \quad (3).$$

In eq. (3), $\Delta = x(1-x)\{(1-y)c_{ABD} + yc_{ABC}\} + y(1-y)\{xc_{ACD} + (1-x)c_{BCD}\}$ and $c_{ABD}$ $c_{ABC}$, $c_{ACD}$, $c_{BCD}$ are the bowing parameters of the corresponding ternary compounds ($A_xB_{1-x}D, A_xB_{1-x}C, AC_yD_{1-y}, BC_yD_{1-y}$). The bowing parameter of the quaternary compound is linearly interpolated between the four mentioned ternary materials [32].

Table 1: Bandgap equations vs. x for III-As ternaries [32]

| Ternary compound | bandgap (eV) | |
|---|---|---|
| $In_xGa_{1-x}As$ | $1.424 - 1.503x + 0.43x^2$ | |
| $Al_xGa_{1-x}As$ | $1.424 + 1.247\text{x}$ | $0 < \text{x} < 0.45$ |
| $Al_xGa_{1-x}As$ | $1.424 + 1.087\text{x} + 0.438\text{x}^2$ | $\text{x} > 0.45$ |
| *$In_xAl_{1-x}As$ | $2.946 - 2.83\text{x} + 0.24\text{x}^2$ | $x > \sim 0.37$ |

* It should be noted that $In_xAl_{1-x}As$ is known as an indirect material for x < ~ 0.37 [40], [41].

Higher-order III-V compounds like pentanary and quintanary materials can be achieved using the mixture of five and six elements, respectively. The aim for adding more complexity to the chemical composition of III-V compounds is to approach desirable properties of the material e.g. bandgap for a certain application. To date, III-V compound-based devices have been designed mostly based on binary, ternary, and quaternary materials and the use of higher-order compounds are less common [32], [33], [42].

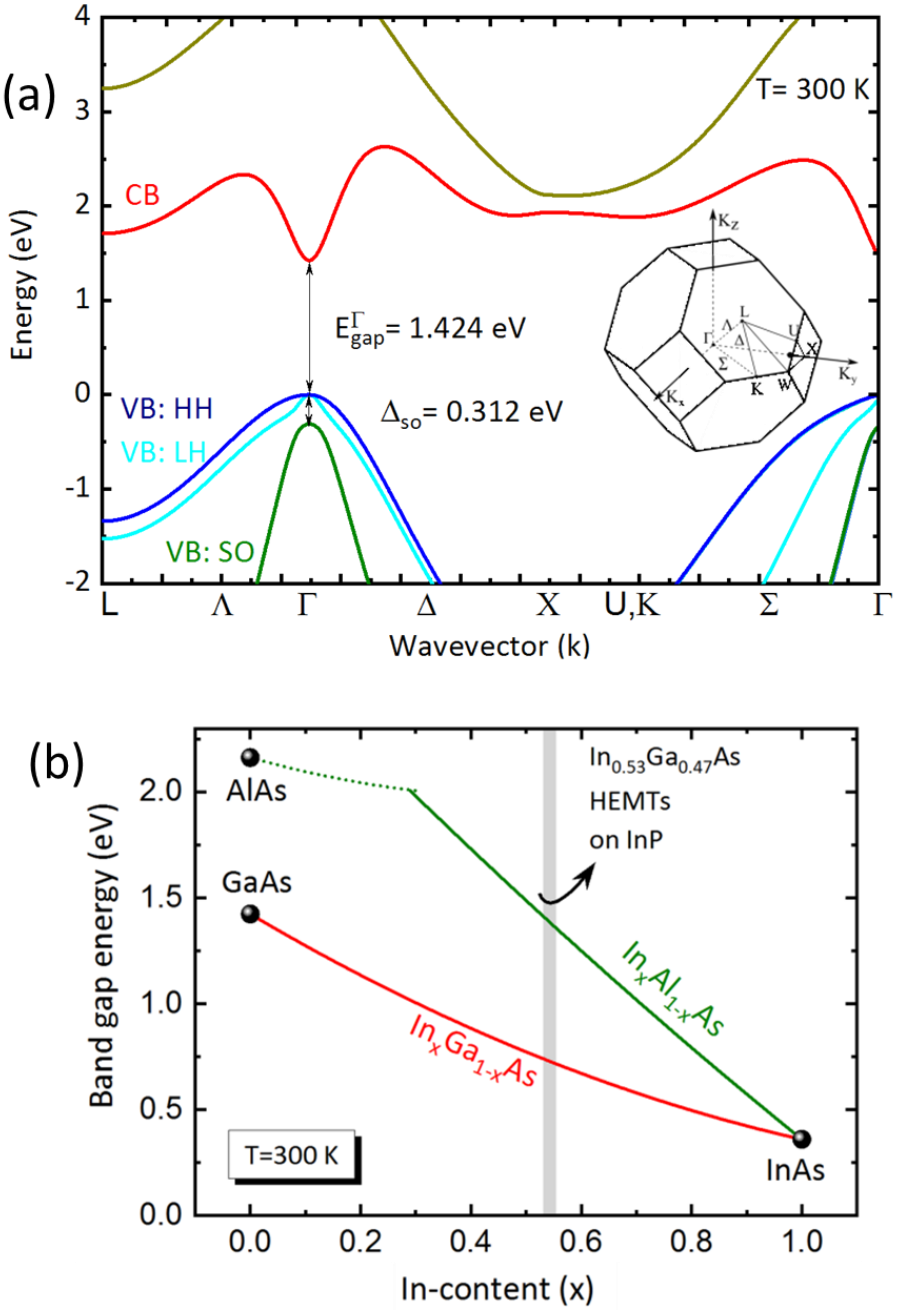


Figure 2.1 (a) TB band structure of GaAs including spin-orbit coupling in the Brillouin zone at 300 K. The inset shows the first BZ of fcc ZB crystal structure in a Cartesian coordinate system in k= ($k_x$,$k_y$,$k_z$) (b) Band gap energy of the basic III-As semiconductor alloys at 300 K as a function of their composition x. $Al_xGa_{1-x}As$ curve can be located between two binaries, GaAs and AlAs. $In_xAl_{1-x}Ga_yAs_{1-y}$ can be located in the area between two $In_xGa_{1-x}As$ and $Al_xGa_{1-x}As$ materials. The lattice-matched material system of $In_{0.53}Ga_{0.47}As/In_{0.52}Al_{48}As$ on costly InP substrate is well-known for HEMTs application as shown by the grey regime.

One important semiconductor parameter for HEMTs is the carrier effective mass, which is related to the carrier mobility [52].

The effective mass of electrons or holes is inversely proportional to the second derivative of the energy dispersion of CB or VB, respectively.

$$\frac{1}{m^*} = \frac{1}{\hbar^2}\frac{\partial^2 E}{\partial^2 K} \quad (4).$$

The resulting effective mass for CB ($m_e^*$), which have ellipsoidal constant energy surfaces, is given by:

$$m_e^* = \frac{3}{(1/m_l^*) + 2(1/m_t^*)} \quad (5).$$

In eq. (5), $m_l^*$, $m_t^*$ are the longitudinal and the transverse masses in minima of the bands [38], [43], [44].

The charge carrier mobility can be calculated with the following equation.

$$\mu_c = \frac{e}{m^* \gamma_c} \quad (6).$$

In eq. (6), $m^*$ is the effective mass of either electrons or holes. $\gamma_c$ is momentum of charge carrier scattering , $\mu_c$ is the mobility of either electrons or holes, and *e* is the electronic charge [45].

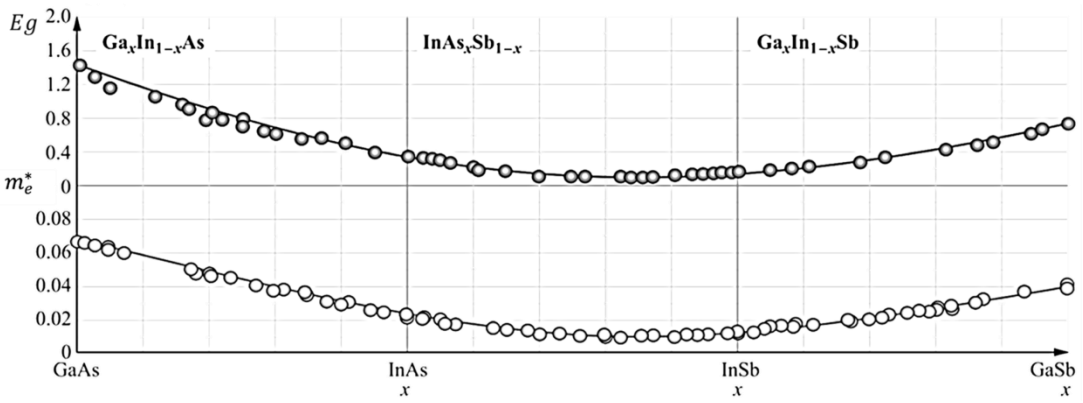


Figure 2.2 Variation of bandgap and electron effective mass at Γ in CBs of $Ga_xIn_{1-x}As$, $InAs_xSb_{1-x}$ and $Ga_xIn_{1-x}Sb$ III-V ternaries (at 300 K). The experimental data are collected from different sources. The solid lines are calculated from eq. (2) using the binary endpoint values and bowing parameters. Note: The composition x in this plot belongs to Ga mol. Fraction. Reproduced from [44] with permission of Springer.

Like eq. (1), the effective mass of any ternary material has also a nonlinear trend between its two constituent binary compounds.

$$m_{12}^*(x) = xm_1^* + (1-x)m_2^* - c_m x(1-x) \quad (7).$$

In eq. (7), $m_1^*$ is the effective mass of one of the binaries corresponding to x=1 and $m_2^*$ is the effective mass of the other binary corresponding to x=0. The constant $c_m$ (which is independent from composition x) stands for the bowing parameter for the effective mass [46].

The composition dependence of $E_g$ and $m_e^*$ for $Ga_xIn_{1-x}As$, $InAs_xSb_{1-x}$, and $Ga_xIn_{1-x}Sb$ III-V semiconductors at 300 K are shown in Figure 2.2. The reduction of the bandgap as a function of x is typically followed by the reduction of the electron effective mass as shown in Figure 2.2. It should be noted that in this plot x belongs to Ga mol. fraction. The solid lines are calculated based on the bowing parameters at two endpoints of the binaries using eq. (7). Bowing parameters of the effective masses are based on the values in [44]. The experimental values are collected from different sources (see Figure 2.2) [44].

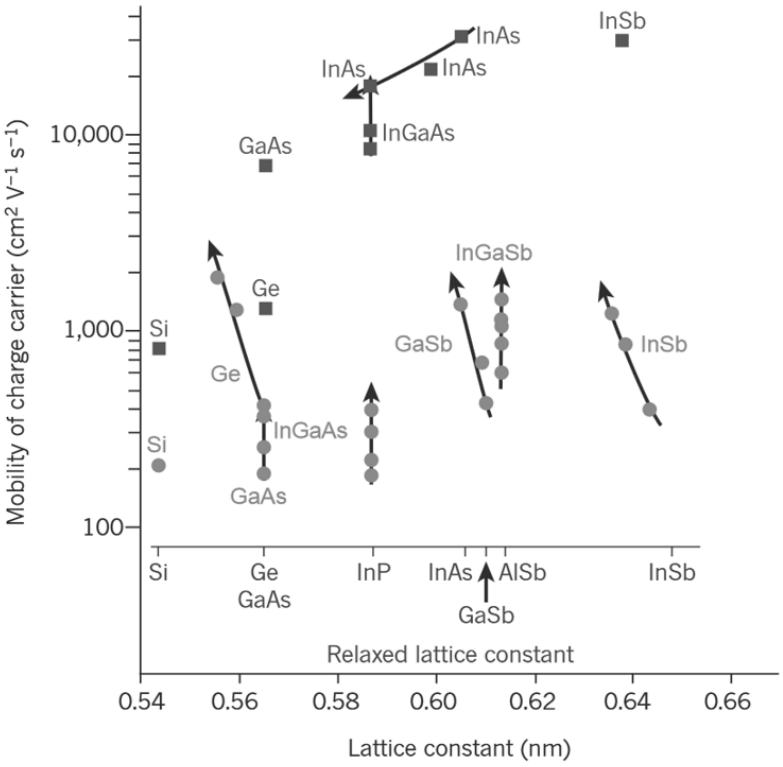


Figure 2.3 Electron and hole mobilities of various III-V semiconductors compared with Si. Data points in circles and squares belong to the mobility values of holes and electrons, respectively. Reprinted by permission from Macmillan Publishers Nature [47], copyright 2011.

The superior electron transport properties of III-V semiconductors (in Figure 2.3) as GaAs, InAs, InSb, and their corresponding ternary and quaternary compounds come by virtue of their $m_e^*$. The low effective masses translate into high low-field mobilities meaning high-mobility materials. In principle, III-V semiconductors have distinguishable higher electron mobilities as compared with Si [47], [48]. However, finding an alternative for Si CMOS as the very heart of the

intrinsic transistors is a daunting task. On the other hand, the excellent transport properties of III-V materials present an exciting opportunity for improved performance in advanced CMOS nodes [47], [48]. In this respect, one solution is to combine the mature Si technology with III-V semiconductor nanowires (such as GaAs or InGaAs). However, the misfit in lattice constants between III-Vs and Si typically results in performance-limiting defects at the interfaces, when fabricating them on large scale via thin film growth. Therefore, nanostructures, such as nanowires, are currently investigated, which offer a small interface and hence can be grown with a high crystal quality, directly on Si substrates [48].

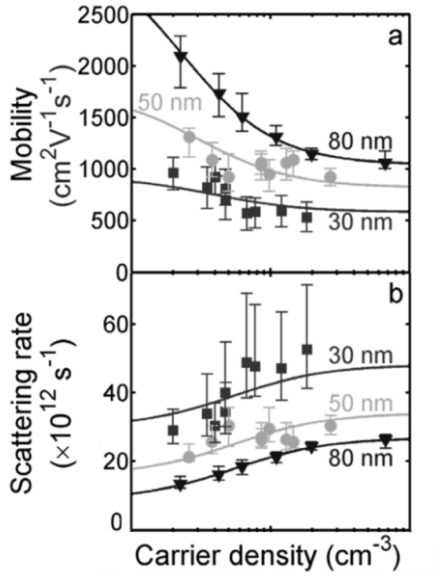


Figure 2.4 (a) Electron mobilities, and (b) electron scattering rates as a function of photoexcited electron density for GaAs nanowires with diameters of 30 nm (squares), 50 nm (circles) and 80 nm (triangles) have been presented. Reprinted from [49] with permission of *J. Phys. D. Appl. Phys.*

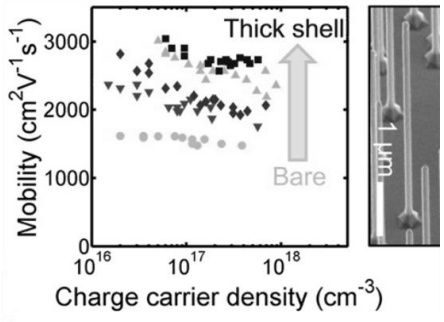


Figure 2.5 Carrier density-dependent electron mobilities measured for bare GaAs nanowires (circles) and GaAs/$Al_{0.40}Ga_{0.60}As$ core/shell nanowires (including a capping outer shell to avoid Al oxidation) with $Al_{0.40}Ga_{0.60}As$ shell thicknesses of 5 nm (triangles pointing down), 10 nm (diamonds),16 nm (triangles pointing up), and 34 nm (squares). A scanning electron microscopy (SEM) image of their GaAs/$Al_{0.40}Ga_{0.60}As$ core/shell nanowires with core diameter of 50 nm and shell thickness of 34 nm and 5 nm GaAs capping layer is presented in the left side. Adapted with permission from [50]. Copyright 2014 American Chemical Society.

However, despite their superior material quality, the diameter of nanowires and surface passivation of nanowires have an effective impact on the carrier mobility values. There is a major challenge to achieve bulk-like mobilities in nanowire-based devices. H J Joyce et al in 2017 have reported that the electron mobility and scattering rate have a strong systematic dependence on the nanowire diameter, as shown in Figure 2.4. Specifically, narrowing the diameter of the nanowires increases the scattering rate and lowers the electron mobility. This dependence designates that scattering at the nanowire surface, due to charged surface states and surface roughness, has a strong impact on the electron mobility in GaAs nanowires. Nanowires with the smaller diameter have a larger degradation of electron mobility because a larger fraction of free carriers interact with the surface of the nanowires [49]. Furthermore, the results in Figure 2.4 show that the mobility decreases with carrier density due to the increased rate of carrier-carrier scattering. The surface passivation of the nanowires (meaning covering the surface states with a higher bandgap material) can enhance the carrier mobility. A typical passivation layer of GaAs is AlGaAs due to its higher bandgap and lattice-match with GaAs. H J Joyce et al in 2014 have proved that the electron mobility can be enhanced noticeably by increasing $Al_{0.40}Ga_{0.60}As$ shell thickness as shown in Figure 2.5, [50]. Thus, such an optimized material system of GaAs/$Al_{0.40}Ga_{0.60}As$ core/shell nanowires resulted in electron mobilities up to 3000 $cm^2\ V^{-1}\ s^{-1}$, reaching 65% of the electron mobility of high quality undoped bulk GaAs at equivalent photoexcited carrier densities. H J Joyce et al also pointed out a high interface quality and very low levels of ionized impurities and lattice defects in their nanowires [50].

III-As semiconductors are typically crystallized in the zinc blende (ZB) structure, where every group-III atom forms covalent bonds ($sp^3$ hybrids) with four As atoms. These bonds are polar owing to the different electronegativity of group-III and As atoms. The corresponding unit cell is sketched in Figure 2.6. A ZB crystal structure of GaAs with its face-centered cubic (fcc) unit cell is shown (Ga atoms in blue color and As atoms in green color). GaAs as a ZB crystal structure is an isometric system with a lattice-constant or lattice parameter ($a_{ZB}$) of 5.65315 Å at 300K. A single GaAs bond (as shown in orange color of Figure 2.6) is highlighted with a yellow color in Figure 2.6, showing their different electronegativity. GaAs has a Ga atom and an As atom with a tetrahedral angle of 109.47˚ in a four nearest neighbor bonds with a length of 0.245 nm. GaAs family planes can be either non-polar, e.g. (110) or polar, e.g. (111). GaAs wafer can be cleaved easily along the family plane with equal number of Ga and As atoms e.g. non polar (110), but it cannot be cleaved easily along the (111) planes containing either only Ga atoms or As atoms (the latter and former are known as (111A) and (111B), respectively).

It is well-known that in non-nitride III-V nanowires, two crystal phases ZB or wurtzite (WZ) can be found. Indeed, in bulk III-V material systems, only ZB crystal structure has been reported, while III-V nanowires possess the ZB or WZ phase depending on their growth conditions. The WZ phase crystal needs a small energy to form in comparison with the ZB phase crystal [51], [52]. The WZ phase is often obtained for gold-catalyzed III–V nanowires; however the ZB phase is mostly obtained for the Ga-assisted growth (self-catalyzed growth), [52].

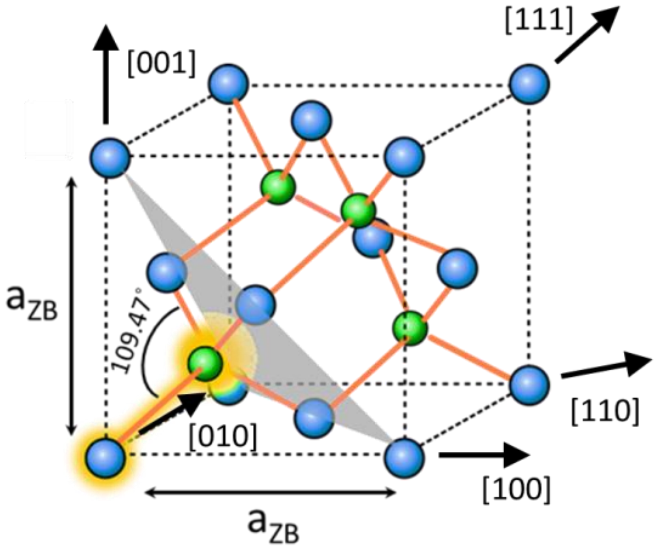


Figure 2.6 Conventional fcc unit cell of ZB GaAs (Ga and As atoms in blue and green color, respectively.) with a (111) plane (a grey triangular). Note: [111] is the crystallographic growth axis of the nanowires in this thesis.

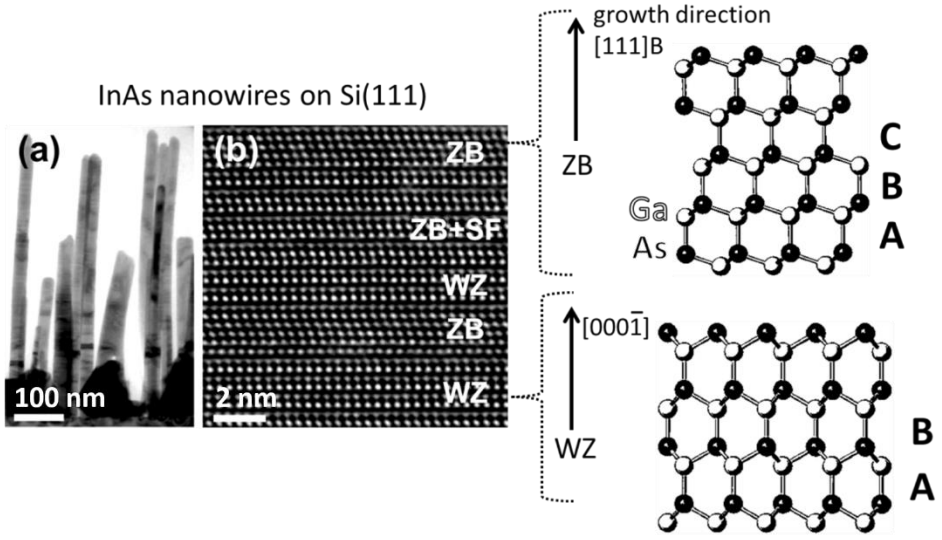


Figure 2.7 Si-doped InAs nanowire with WZ and ZB and SF segments grown on Si (111); (a) a low-resolution transmission electron microscopy image of free-standing InAs nanowires, (b) high resolution transmission electron microscopy (HR-TEM) shows the various crystal structures along the growth axis of nanowires. Reprinted from [53], with the permission of AIP Publishing.

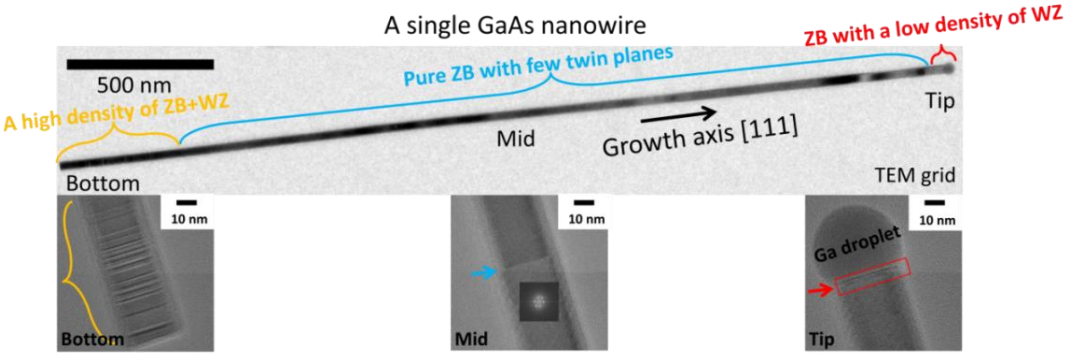


Figure 2.8 A single GaAs nanowire placed flat on TEM grid. The crystal growth axis of the nanowire is along [111]. The three areas related to different crystal structures approximately are pointed in the upper image of the whole nanowire. In the three lower images, an example of HR-TEM picture corresponding to those in upper image is presented. Such GaAs nanowires were grown by molecular beam epitaxy (MBE) at HZDR, Germany.

E Dimakis et al 2013 have reported the structural properties of Si-doped InAs nanowires grown on Si (111) as shown in Figure 2.7, [53]. Low- and high-resolution TEM images of these nanowires have shown in Figure 2.7 (a) and (b), respectively. Regardless of the doping level, these nanowires exhibited a strong polytypism [54] (meaning a variation of the crystal structure in the direction perpendicular to growth plan) within their whole length [51]. The fluctuation of the two polytypes (ZB and WZ) along the nanowire length was observed by the corresponding intensity contrast changes in the low-resolution TEM image of Figure 2.7 (a). The occurrence of very short ZB and WZ segments, along with planar stacking faults (SFs) presented in the high-resolution TEM image of Figure 2.7 (b). The ZB phase consists of a stacking of atomic layers in the sequence of …ABCABC… in <111> direction, while the WZ structure consists of a stacking of atomic layers in the sequence of …ABAB… in <0001> direction [51], [54], [55]. This report, [53], is an example for III-V nanowires showing a combination of ZB and WZ in the <111> direction, while their bulk counterparts commonly crystallize in ZB crystal structure. Figure 2.8 presents the structural analysis of a single GaAs nanowire (which is in focus of this thesis). The low-resolution TEM image in upper side displays the whole length of the nanowire, which was transferred on a TEM grid. This nanowire is divided in three major segments including the crystal structure for each. The HR-TEM image of one segment from each of these three parts is shown in the lower side of Figure 2.8. A high (very low) density of twins and stacking faults exist at the nanowire bottom (tip) of this nanowire, while the mid part shows a pure ZB phase (as proved by the diffraction pattern from TEM) with few twin planes. In the high-resolution images of Figure 2.8, the orange curved bracket, the blue arrow and the red rectangular with arrow point

toward the existence of SFs, twin boundary, and again to SFs, respectively. SFs and twin boundaries constitute defective segments inside the crystal lattice which affect the device performance, e.g. via a variation of charge carrier concentration or an increased phonon scattering, and thus a reduced carrier mobility [51],[55], [56]. On the one hand, the polytypism can be controlled by varying the growth parameters such as the V/III ratio or the temperature, but on the other hand it also depends on the nanowire geometry [51].

During thin film growth of III-Vs, it is desirable to choose lattice matched substrates for the epilayers, to suppress strain at the interface. However, where such a substrate is not available or where a lattice mismatched substrates is more desirable, one can employ graded buffer layers in which the lattice constants in the epilayer are adjusted by an altered composition of an alloyed layer stack from bottom to top during the growth. This allows adjusting the lattice constant to the substrate in the beginning of the growth, while altering it towards the desired composition toward the top of the buffer layer. This approach can substantially reduce strain but is also accompanied by a graded band gap. The plot in Figure 2.9 displays bandgaps vs. lattice parameters of III–V compounds with additional SiGe alloys. The blue dots and line segments indicate direct-gap materials. Indirect materials with six-fold CB symmetry are presented in red, and materials with eight-fold CB symmetry are displayed in green. The vertical-colored bars highlighted common commercial substrates. The width of each bar indicates the range of lattice parameters that strain up to 1%, showing the range of alloys that can be grown nearly lattice matched. The lack of available lattice matched substrates for some conventional pairings of substrates and epitaxial layers is a serious issue, strongly impeding the design and fabrication devices in certain bandgap ranges [42].

$$\alpha_{\mathrm{In_xGa_{1-x}As}} = (1-\mathrm{x})\alpha_{GaAs} + x\alpha_{InAs}\,, \quad \alpha_{\mathrm{In_xAl_{1-x}As}} = (1-\mathrm{x})\alpha_{GaAs} + x\alpha_{AlAs} \qquad (8), (9).$$

The lattice parameter or lattice constant ($\alpha$) of ternaries or quaternaries follows approximately Vegard's law ( e.g. eq. 8 or 9 for $In_xGa_{1-x}As$ or $In_xAl_{1-x}As$) to vary linearly with composition [44]. In Figure 2.10, the lattice parameters for $In_xGa_{1-x}As$ and $In_xAl_{1-x}As$ ($\alpha_{\mathrm{In_xGa_{1-x}As}}$ and $\alpha_{\mathrm{In_xAl_{1-x}As}}$ ) have been calculated using eq. 8 and 9. The bandgap of $In_xGa_{1-x}As$ is smaller than $In_xAl_{1-x}As$ (as shown in Figure 2.1 (b) and Figure 2.9), while their lattice constants are almost identical as shown in Figure 2.10. Thus, due to this property and low electron effective mass of $In_xGa_{1-x}As$ (at 300 K) , conventional pseudomorphic HEMTs are based on lattice-matched $In_xGa_{1-x}As/In_xAl_{1-x}As/InP$ [57], [58].

The limitation of nearly lattice-matched materials drove early device designers to develop quaternary alloys (e.g., GaInAsP, AlGaInAs), such that the bandgap could be changed over a

broader design region without switching the lattice parameter; quaternary alloys are crucial to the operation of telecommunication devices grown on costly InP substrates. Todays, state-of-the-art lasers show the applications of quaternary or quintenary alloy, which have up to five elements, to enable engineering of the lattice constant, bandgap, or the VB offset [59], [60]. Device designers are also highly attracted to further develop semiconductor band extrema by deliberately growing heavily strained layers that may have elastic strain approaching 3%. However, this is extremely difficult since layers including this high amount of strain are on the edge of stability. In order to remain dislocation free such layers can only be grown with few monolayers thicknesses [61], [62] . Considering the complexity involved in the higher numbers of alloy components or highly strained layers with such a thin critical thickness illustrates the demand to increase the degree of freedom that can be employed to produce high quality epitaxial materials [42], [63].

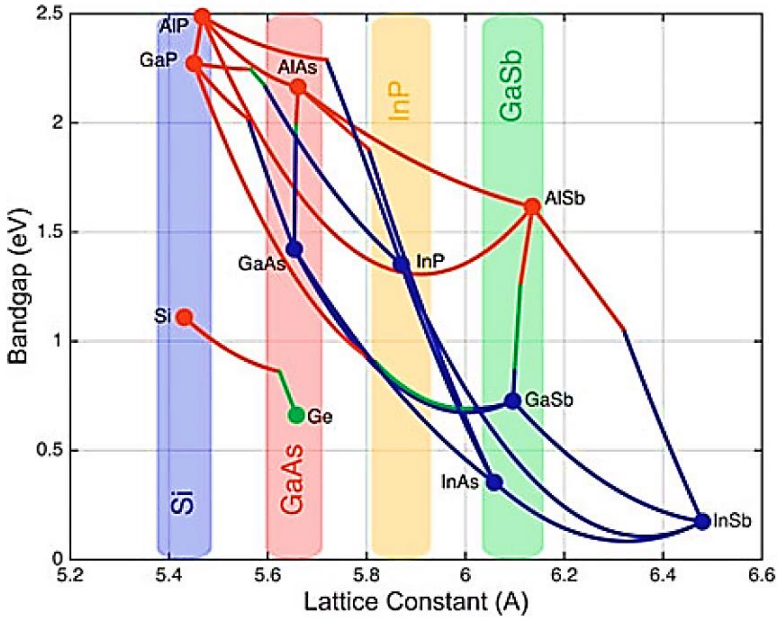


Figure 2.9 Bandgaps as a function of lattice parameters for III-V compounds and SiGe alloy at 300 K. Reproduced from [42] with permission of Springer.

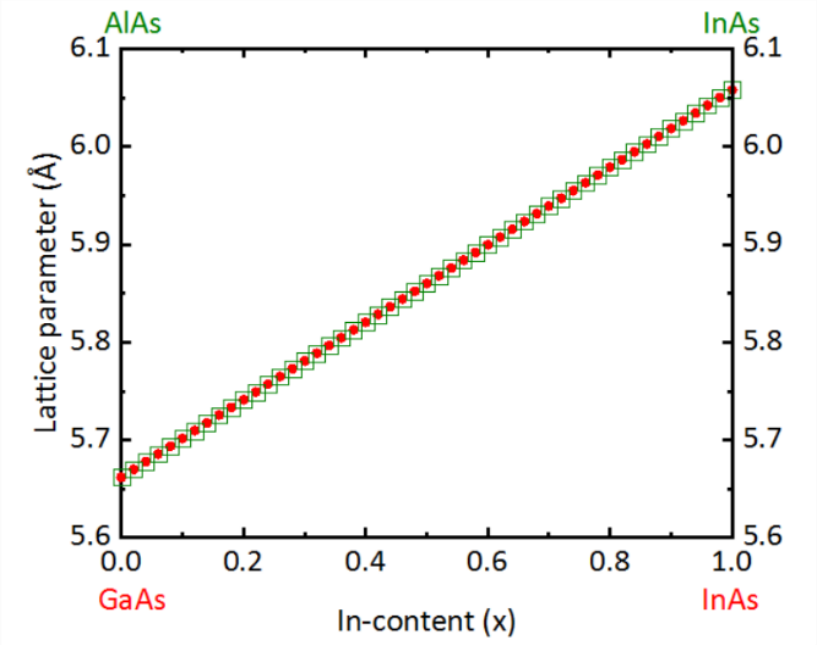


Figure 2.10 The lattice parameters of $In_xGa_{1-x}As$ ( in red) and $In_xAl_{1-x}As$ ( in green) at 300 K based on the Vegard's law are presented, where $\alpha_{GaAs} = 5.6533$ Å , $\alpha_{InAs} = 6.0583$ Å, and $\alpha_{AlAs} = 5.6620$ Å are used [46], [46], [44].

## 2.2 Growth of III-V nanowires on Si

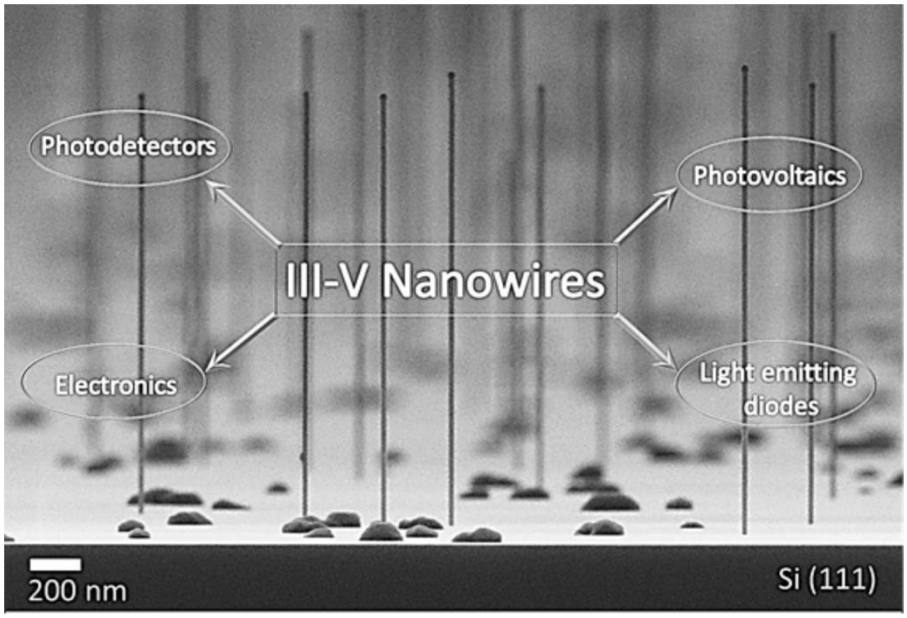


Figure 2.11 III-V semiconductor nanowires are multi-tasking. An example of the SEM image of the self-catalyzed growth of vertical free-standing very thin GaAs nanowires (~ 25 nm in diameter) on $SiO_x$/Si(111) substrate is shown. Such very thin GaAs nanowires were grown by MBE at HZDR.

This chapter provides a general overview of III-V semiconductor nanowires on Si as well as their various application possibilities and introduces several fabrication strategies including their potential compatibility with Si electronics.

A direct growth of defect-free planar layers from III-V semiconductor materials on Si substrates is not feasible; simply due to two reasons: the lattice misfit strain and the polarity. The lattice misfit strain causes dislocations at the interface between III-V materials and Si which is a serious barrier for epilayer growers to achieve a thin film with a high crystal quality. However, strain is not the only issue for the planar film growth of III-V on Si. The growth procedure on the Si substrate surface is typically with monoatomic steps while III-V semiconductors have bi-atomic steps. This causes a situation during the growth in which the atomic stacking of III–V nuclei formed on adjacent terraces are not matched together at the boundaries that they adjoin. This different nature of growth procedure between III-V material and Si is resulting in formations of defects which are known as antiphase domains and antiphase boundaries. These issues are eliminated while using III-V nanowires on Si [64]. The definition of lattice misfit (*f*) with a positive or negative sign is described in the following:

Materials with different chemical compositions have different lattice constants. The lattice misfit (*f*) between two materials is defined as

$$f = \frac{a_L - a_s}{a_s} \quad (10),$$

where $a_L$ and $a_s$ are the strain-free lattice parameters of the epilayer and the substrate, respectively. The epilayer is compressively strained ($f > 0$) when $a_L > a_s$ or tensile strained ($f < 0$) when $a_L < a_s$ [46].

One of the intriguing features of nanowires stems from their very small interface with the substrate (also known as footprint), and their high aspect ratio. It has been demonstrated that heterostructures with large differences in their lattice parameters can remain dislocation free due to the very efficient radial relaxation of the strain produced by the lattice mismatch at the interface between those dissimilar materials [14], [15], [65], [66]. The narrow interface and volume of nanowires substantially accommodate the strain by lateral expansion and due to that, most of the nanowires nucleate on those terraces and avoid coinciding with the steps on the Si surface [64].The growth of free-standing vertical nanowires with epitaxial orientation of the substrate is technologically impressive class of material structures that offers the highest degree of control over the growth mechanism. Growth III-V often terminates in {111} or {111}B directions [64]. An example of self-catalytically grown, very thin GaAs nanowires (~ 25 nm in diameter) on Si(111), is presented in Figure 2.11. The formation of misfit dislocations in equivalent planar heterostructures (e.g., GaAs epilayers on Si) substantially reduces the crystal quality. Thus, the small dimension of the nanowires open up ways for the coupling of the superior optoelectronic properties of III-V compound semiconductor with Si-based CMOS electronics [18], [66], [67].

By considering the different groups of nanowires, it concluded that semiconductor nanowires are multi-tasking (see Figure 2.11 and Figure 2.12 ) and have various potential applications [68], [69], [70], [71] such as electronic (logic devices, diodes, novel nanotransistor like reconfigurable transistors) [72], [73], photonic (laser, photodetector, LED) [18], [71], [74] ,[75], [76], biological (sensors, drug delivery) [71], [77], energy (batteries, solar cells, thermo-electric-generators) [22], [71], [78] and magnetic (spintronic, memory) devices [69], [79]. An example of the schematic representation of the future integrated nano-photonic chip based on nanowires is shown in Figure 2.12 [71].

III-V nanowire growth on Si is the most promising applications of nanowires to be able to integrate on Si. The vertical growth of nanowires on Si where the gate wrap around the

nanowires has been used which is one of the attractive device architecture showing a very good electrostatic control over the gate channel of a transistor [64]. In this regard, C Rehnstedt et al have fabricated wrap-gated FET transistors by vertically aligned epitaxial InAs nanowires grown on Si. The electrical properties of these transistors can be affected by charges accumulated in the multi-interfaces of such a structure as InAs/HfO2, Si/HfO2, InAs/Si, and the band offset between InAs and Si, as well [80].

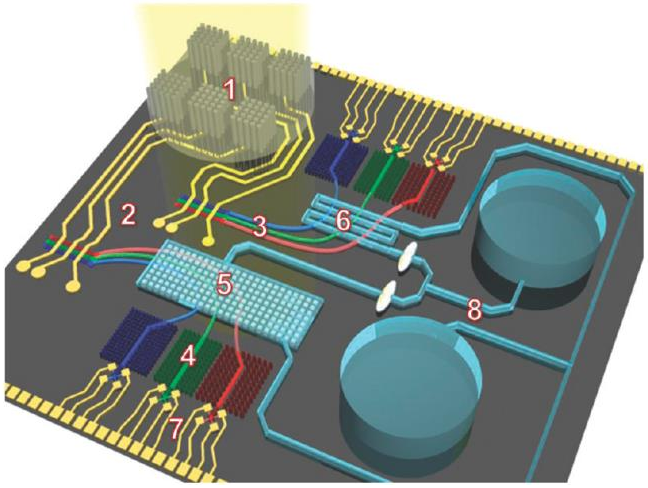


Figure 2.12 Schematic representation for future nano-photonic circuits to integrate different nanowire-based devices like nanowire solar cells as on-chip power supplies (1), laser diodes/LEDs as light sources (2), nano ribbons (3) and 2D photonic bandgap nanowire arrays (4) as filters and waveguides to select and route input and output signals; (6) sample analysis chambers, such as silver nano cube arrays for surface enhanced Raman spectroscopy ([81]) (5) or nano ribbon/sample intersection for absorption analysis; nanowire based photodectectors (7) and a microfluidic system for liquid sample transport (8). Reprinted (adapted) with permission from [71]. Copyright 2010 American Chemical Society.

The group of H Riel, M. T. Björk et al, from IBM Research-Zurich have demonstrated the fabrication of diodes that conduct through quantum mechanical tunneling (Esaki tunnel diodes) [82]. K Tomioka and T Fukui in the research center for integrated quantum electronics, Hokkaido University, reported the fabrication of tunnel FET with III-V nanowires on Si heterojunctions with the gate all-around. These devices based on nanowires were grown by selective area epitaxy (SAG) on p-type Si (111) showing switching behavior with an average sub-threshold slope of 104 mV/dec under reverse bias condition [83]. In 2016, H Kim et al from Department of Electrical Engineering, University of California Los Angeles, in US, have shown monolithically integrated InGaAs semiconductor nanowires on a silicon-on-insulator (SOI) grating for energy-efficient on-chip optical links with the potential of using in photonics and optoelectronic devices (see Figure 2.13). The nanowire arrays were grown by SAG on Si where a high number of SFs and no

threading dislocations have been observed in HR-TEM. It has also shown that the broad tunability of composition in InGaAs nanowires can cover the telecommunication wavelengths of both 1.31 and1.55 µm [2]. The lower power operation of the transistor devices based on nanowires namely on Si substrates compare to the conventional ones is one of the advantages of nanowire-based devices that could potentially pave the way for monolithic integration of III-V semiconductors on Si platform as well as the downscaling of microelectronics [2], [83], [84].

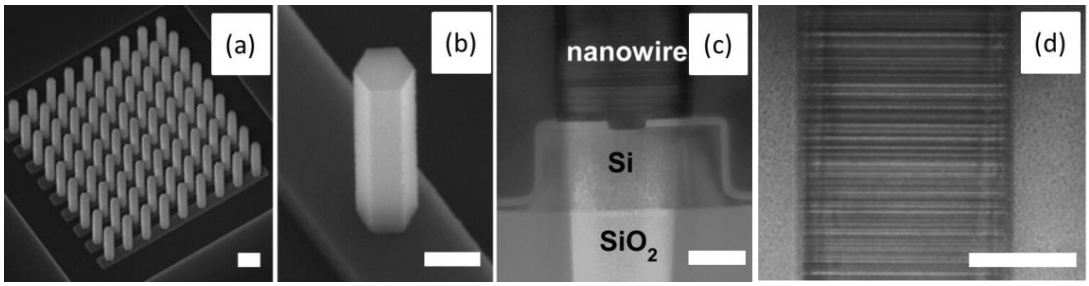


Figure 2.13 Monolithically integrated III−V nanowires on a SOI platform for energy-efficient on-chip optical links, (a) SEM image of InGaAs nanowire array on an SOI grating, (b) SEM image of a Single nanowire on an SOI waveguide structure, (c) SEM image (cross-section view) of an InGaAs nanowire, (d) HR-TEM image of segment from a InGaAs nanowire. Scale bars are 500 nm, 200 nm, 100 nm, and 100 nm for (a), (b), (c), and (d), respectively. Adapted with permission from [2]. Copyright 2016 American Chemical Society.

Having mentioned the interesting aspects of III-V nanowires applications namely on Si wafers, various ways for the fabrication of nanowires will be reviewed in the following section regarding the crystal quality of the nanowires which plays a key role for the device characteristics.

There are different ways for the fabrication of nanowires, each having advantages and disadvantages in terms of the integration with Si-CMOS technology. Nanowire syntheses can be categorized in two major strategies; top-down and bottom-up [66], [69]. The top-down approach relies on having a bulk starting material of high crystal quality, from which the final (quasi-)1D structure can be selectively etched, sculptured or carved [69]. The top-down approach is limited to the already available high-quality bulk materials or planar heterostructures that can be etched to shape and form the quasi-1D geometries like nanowires or nanorods. There are various reports in which this fabrication strategy for nanowires was successfully demonstrated and further developed to increase the device performances as compared to bulk material or introducing new functionalities. In 2016, a group, at the physics departments of both Eindhoven and Delft Universities of Technology under the leadership of E P A M Bakkers and J E M Haverkort, has demonstrated experimentally that an array of tapered InP nanorods can boost the radiative efficiency as compared to an equivalent planar solar cells by a factor of 14 [85]. The group of J E M Haverkort, D van Dam et al have shown a InP solar cell

with a power conversion efficiency value of 17.8% which is the world record in nanowire-based solar cell technologies [86]. In 2014, N Waldron et al, in a group at imec (Leuven) Belgium, reported the first InGaAs gate-all-around nanowire devices (with 6 nm nanowire diameters) fabricated on 300 mm Si substrates, compatible with very large scale integration (VLSI), demonstrating a noticeable improvement over similarly processed FinFETs in terms of the short channel effect as well as on the on-state performance [87]. In 2014, Ray LaPierre's group from Department of Engineering Physics, at McMaster University, Hamilton Canada has reported a strong absorption of GaAs arrays in the visible spectrum and the tunability of the absorption [88]. These are only few examples of many other reports based on the top-down approach showing the promising future for nanowire-based devices [89], [90], [91]. The need for precise addressability in microelectronics strongly relies on the strategy of fabrication, where top-down fabrication offers some advantageous. Nonetheless, the invasive nature of the top-down fabrication often results in lateral damages and the formation of defects during several etching processes, and a high amount of material consumption. Furthermore, the severe lattice restrictions to the previously grown bulk heterostructures are substantial drawbacks of this fabrication strategy [66], [69].

In contrast, the aforementioned drawbacks can be eliminated while employing the bottom-up fabrication strategy. The bottom-up approach relies on randomly distributed starting materials that are assembled (grown), of the nanostructures by supplying the appropriate precursors for the respective material combination at appropriate growth conditions, such as temperature, and pressure [69], [66] . This strategy of fabrication can be realized in gas-phase and solution-phase chemistry and has enabled a variety of new material systems and morphologies to be obtained with improved control of the crystalline and chemical properties. A large amount of research projects has been dedicated in understanding nanowire growth at the atomic level and to precisely control the nanowire dimensions, crystal structure, composition, growth pattern, and structural/compositional complexity [92]. Bottom-up nanowire growth allows accessing structures that may not be possible by the top-down approach, and furthermore may allow unusual materials that have not been obtainable in the bulk wafer form. The bottom-up semiconductor nanowire growth often results in faceted surfaces that may not be attainable by the top-down fabrication. Nanowires synthesized by this approach are particularly interesting because of their atomically smooth side walls and high crystal quality that can for example allow photons to propagate along the nanowires with low losses, making them highly attractive for photonic circuits [92]. Control over the crystal surface

facets formed while the nanowire growth may enable manipulate the density of interface states at nanowire surfaces, which is an important issue for Ge and III−V materials to further increase device performance [69].

In recent years, the significant progresses in the bottom-up strategy of fabrication have offered the possibility of a synergy between the bottom-up and top-down processes to possess the benefits of both [69], [93]. An example for this matter can be referred to the report of C G Núñez et al, in 2018, where they developed a contact-printing system to efficiently transfer the bottom-up and top-down semiconductor nanowires, preserving their as-grown features with a good control over their electronic properties [93]. The required fabrication strategy for future semiconductor nanowire-based integrated circuits (IC) is still unclear; even so, it is likely that both the top-down and bottom-up approaches will be employed in tandem to allow a scalable path to nanowire based-IC fabrication. In this thesis, the focus is on the bottom-up approach [69].

The bottom-up strategy of fabrication includes different growth methods such as Au-catalyzed, self-catalyzed, and SAG techniques. Each of this method differs regarding nanowire nucleation, doping, and possibilities for the formation of heterostructures that are critical for the electronic and optoelectronic devices.

The Au-catalyzed growth is often referred to as vapor-liquid-solid (VLS) [66]. The VLS crystal growth method is undoubtedly the most widely adopted approach to grow semiconductor nanowires because of its great flexibility [94]. In VLS growth, solid nanowires precipitate from liquid droplets, supersaturated with the vapor phase precursors [94], [95]. However, many fundamental aspects of VLS growth have remained unclear. VLS growth of nanowires incorporates three distinct stages as alloying, nucleation, and growth and since the kinetics are very rapid under conventional growth conditions, it is very complicated to distinguish the whole events at each stage of VLS growth [92]. The history of the bottom-up approach goes back to 1964, in which R S Wagner, and W C Ellis at Bell laboratories demonstrated the first (VLS) growth of Si whiskers using Au-Si liquid alloy [94], [96] . In 1974 (after one decade), R B Finkelman, R R Larson, and E J Dwornik have observed the first naturally occurring terrestrial example, GeS, of VLS growth where the TEM image of the rods showed the finest rod ~ 40 nm in diameter. Later, in 1975, E I Givargizov showed the various stages of the VLS process for the periodic instability in Si whiskers and for the first time, the GaAs whiskers growth on GaAs (111) substrate of various orientations in sub micrometer region. In 1991, a research team at Hitachi Central Research Lab outside Tokyo, under the leadership of K Hiruma, demonstrated for the first time, a p-n junction based on GaAs wire crystals of ~ 100 nm in diameter employing metal-organic-vapor-phase-

epitaxy (MOVPE) [97]. This was the first proof of nanowires's potential use as an optoelectronic device such as LEDs. In 1995, K Hiruma et al, reported the free-standing GaAs/InAs heterostructure wires as thin as 20 nm and as long as 1 μm via VLS growth using MOVPE. In 2000, (after the initiation of the III-V semiconductor nanowire technology in Japan), X Duan and C M Lieber showed laser-assisted catalytic growth of a broad range of compound semiconductor nanowires as III-V binary (GaAs, GaP, InAs, and InP), III-V ternary (GaAs/P, InAs/P), II-VI binary (ZnS, ZnSe, CdS, and CdSe), and binary SiGe alloy as well with a high purity of above 90% single crystals within three to tens of nanometer in diameter and tens of micrometer regime. Their report over the various compound semiconductors opened up the path toward nano-scale LEDs and laser devices using more complex material systems including single-wire homo- and heterojuctions [98]. Since then many research studies have been performed worldwide to investigate bottom-up grown 1D nano-scale material structures in the field of nanoscience and nanotechnology [66], [67].

Foreign-metal-catalyst nanowire growth using Au/Si VLS systems is nowadays very common in the bottom-up approach where both, MBE and MOVPE are utilized for the epitaxial growth. In a conventional VLS growth mode, the metal droplet in nano-scale size is quite stable during nanowire growth. Hence, the control over the diameter and length of the nanowires can be independent from the size of the metal droplet and the growth duration [92]. However, there are few serious concerns in using Au droplets for nanowire growth. For the case of Si nanowire on Si substrate, it has been found that the surface of substrate is covered by one monolayer of Au on the places without nanowires indicating the loss of Au atoms from the droplets. This issue can be suppressed by using low-level oxygen to oxidize partly nanowire surface. Still, in such a Au/Si VLS system, the Au atoms migration on nanowire surface is problematic since Au ruins the electronic properties of the Si nanowires in an uncontrolled way through creation of scattering centers or non-radiative recombination sources of electrons-holes [99]. The presence of Au atoms in Si crystal lattice reduces the lifetime of excess electrons and holes in p- and n-type material [100]. Furthermore, not only Au catalyst but also Al catalyst showed the same issue as well. Thus, it is very convincing that the loss of such a foreign metal catalyst may be common for any other foreign-metal-nanoparticle-mediated nanowire growth [101], [102], [103], [104]. In 2012, M Bar-Sadan et al has demonstrated the incorporation of Au atoms during GaAs nanowire growth resulting in the reduction of the electron mean free path and degradation of the electronic properties [105], [106]. Though, the most common catalyst for the VLS growth is

Au-assisted growth, unfortunately it is not compatible with Si-CMOS VLSI technology as a backbone of current electronic technology [95].

An alternative solution for the Au-free growth is the self-catalyzed growth, which has the promise to be fully compatible with Si CMOS platforms [14], [15], [107], [108]. The self-catalyzed growth relies on employing the low melting temperature of the group III elements as nano-droplets for the nanowire growth, providing crucial advantages over the Au nano-droplets, where no impurities are anticipated to be introduced in the nano-droplets. Furthermore these nano-droplets can be consumed in order to switch from an axial to a radial growth mode [66], [106]. For the self-catalyst growth, MBE seems to be the better suited technique as compared to MOVPE, though the latter has been also utilized to some extent. One established example of self-catalyzed VLS growth is Ga-assisted growth of GaAs nanowires by MBE where Ga nano-droplets are employed (instead of Au nano-droplets) to be supersaturated by As precursors for precipitating GaAs underneath [14], [66], [95], [109]. Ga-assisted growth using MBE can be used for precipitation of other binaries or ternaries III-V compounds such as GaP, GaAsP, GaAsSb, and InGaAs as well [66], [95]. Indium droplets can also be used for nucleation of other materials such as InAs or InP [110]. While there are other nano-droplets for the nucleation of the target material in the literatures [66] in this thesis, the focus is on the Ga-assisted growth of GaAs nanowires on Si by MBE.

For GaAs nanowire growth on Si substrates, pre-treatments of Ga droplets and $SiO_x$/Si turns out to be the key for a successful process [15]. The nucleation of GaAs nanowires via Ga nano-droplets includes the use of an oxide to promote nucleation both on GaAs and Si. This oxide layer can be either native or non-native oxide, e.g. thermally grown $SiO_2$. By using a native oxide or $SiO_x$, randomly distributed pin holes form by pre-treatment of the oxide layer. This pre-treatment is mainly annealing the $SiO_x$/Si to a certain temperature until already deposited Ga droplets evaporate while leaving behind those pin holes [15]. Later, supplying Ga adatoms results in formation of Ga nano-droplets inside those generated pinholes. These Ga nano-droplets are in contact with the crystalline substrate. By a continuous supply of Ga and As beams toward these re-generated Ga nano-droplets, the solid phase GaAs starts to nucleate and GaAs growth in the axial direction through a layer by layer growth mode at the droplet interface with the solid substrate [15],[65], [94].

By optimizing the oxide layer and formation of Ga nano-droplets inside the pinholes, it is very likely to obtain high yield (e.g. 95%) of vertical GaAs nanowires on Si [15], [107]. In Figure 2.11, an example of the SEM image of the self-catalyzed growth (Ga-assisted growth) of vertical free-standing very thin GaAs nanowires (25 nm in diameter) on $SiO_x$/Si(111) substrate is shown.

These thin nanowires have been studied and characterized in this thesis. In 2017 and 2018 Tauchnitz et al from HZDR in Germany [15], [111] have shown an MBE grown GaAs nanowire using Ga-assisted growth on $SiO_x$/Si substrate where the formation of pinholes inside the native oxide after pre-treatment of $SiO_x$/Si substrate has been explained in details, where their methodology results in a high yield (80%) of vertical grown nanowires (vs islands) with a superior uniform length distribution of the nanowires. The distinct feature of the self-catalyzed way of growth is the resulting remarkably high crystal of the GaAs nanowires on Si (111) with the predominant ZB crystal structure [14], [15], [99]. The absence of misfit dislocation between the small interface of a vertical GaAs nanowire and $SiO_x$/Si substrate has been shown in the cross-sectional TEM images [15]. No misfit dislocation were observed between GaAs and Si, in spite of having a large lattice misfit (*f*) of 4%, allowing their high quality growth independent of the target substrates lattice constant [65].

Though, the high crystal quality of nanowires as the outcome of the self-catalyzed growth is highly desirable, still there are hurdles in the growth of different compound III-V semiconductors on Si as the high goal for the coupling of III-V nanowires with Si CMOS. One example is the direct growth of vertical $In_xGa_{1-x}As$ nanowires on Si by MBE. $In_xGa_{1-x}As$ alloy in particular is the material of our interest in this thesis. The self-catalyzed (Ga-assisted) VLS growth of pure $In_xGa_{1-x}As$ nanowires grown on Si by MBE is quite challenging. The major problems can be referred in droplet-mediated and droplet-free growth, according to the report of Heiss et al. and Treu et al, respectively [16], [17]. In droplet-mediated VLS growth (Heiss et al, [17]), due to very low In incorporation through Ga droplet, In composition cannot exceed 3-5% and for growth temperature < 575 °C a radial In-rich shell forms. Base on the report of Treu et al., using a droplet-free, vapor-solid (VS) growth mechanism via SAG, enabled them to tune the In composition over a broader range. However, they only obtained $In_xGa_{1-x}As$ nanowires with a high density of SFs. Thus, the MBE growth of free-standing $In_xGa_{1-x}As$ nanowires with a high crystal quality on Si appears challenging.

So far, the Au-assisted and Ga-assisted growth mode as two approaches for the bottom-up formation of nanowires have been described. In the following, the SAG will be briefly introduced. MOVPE is a technique that is very common for the SAG of nanowires. Employing a template mask in SAG helps to define the positions that epitaxial growth of nanowires will take place, which is in contrast to the self-assembled Au- or self-catalyst growth [66]. SAG can also be called template-mediated growth which is a droplet-free method. The first SAG was reported in 1960 and afterwards this approach was further developed for the growth of nanowires, where

novel laser and transistor structures were demonstrated [112], [113], [114]. In 1990, GaAs nanorods with a size of 53 nm were produced using SAG [115]. The significant advances in SAG have been occurred in T Fukui group (this noticeable group from Japan) in 2000, where materials such as GaAs, InAs, InP and InGaAs were grown by MOVPE [116], [117], [118], [119]. Later several groups started to employ SAG using either MBE or MOVPE to grow different materials [66].

Even though by SAG, one could control the positioning of nanowire growth but often result in formation of a high density of randomly distributed planar defects or so-called polytypism [2], [29], [120], [121]. One example of the SAG of InGaAs nanowires on Si has shown already by HR-TEM image in Figure 2.13 (d). Based on the report of G Koblmüller and G Abstreiter from Walter Schottky Institute in Germany, for SAG of InGaAs nanowires on Si, even though SFs are undesirable and degrade electrical and optical characteristics, removal of SFs might be possible by precisely controlling the growth temperature and the V/III ratio [122].

In this thesis, GaAs nanowires are grown by the bottom-up approach using self-catalyzed MBE growth (with the VLS growth) for very thin GaAs nanowires on $SiO_x$/Si(111) substrates. After the core growth, the $In_xGa_{1-x}As$ or $In_xAl_{1-x}As$ shell growth (with the VS growth) has been employed to take advantageous of various possibilities in engineering the optical and electrical properties of the material to be used as a potential opto-electronic device. Generally, the shell growth around the core enriches the wealth of applications and device possibility for various core/shell nanowires and adds more freedom in engineering the material properties.

### 2.3 Core/shell heterostructure nanowires

This chapter gives a brief overview of various types of core/shell heterostructure nanowires including their specific applications. And few reports on the state-of-the-art among various types of core/shell nanowires related to the investigation for this thesis are mentioned.

The intriguing possibility of heterostructure growth (combination of different materials) constitutes one of the most appealing features of the nanowires grown via the bottom-up approach. In recent years radial heterostructure nanowires have attracted increased attention because of their geometry, which can enhance the performance and/or add novel properties in the devices [123]. The advantages of radial core/shell heterostructure nanowires in view of certain applications can be summarized as follows: i) The enhancement of the operation of nanowire devices, where the shell is used for removing the surface states and to confine the

carriers inside the core, resulting into the reduction of surface scattering and the fundamental understanding of the quantum confinement. ii) Their potential use for high efficiency optoelectronic devices such as lasers [19], solar cells [22], LEDs [18], surrounding-gate architecture for transistors [124], [67]. iii) Importantly the high freedom in bandgap/strain engineering of the material through the shell growth [65], [125]. iv) Their applications for high electron mobility transistors on Si [67]. v) Monolithic integration of III-V devices on Si [65], [94], [126], [125]. vi) Adding novel concepts like Majorana fermions [127], [128], spin-related coherent quantum transport, spintronic devices, topological quantum computation [129], [130], emission of entangled photon pairs [131], and thermoelectric properties [132]. The points iii) and iv) will be covered in the later chapters (2.5 and 2.6, respectively) and more information about the point vi) can be found in the corresponding references.

The radial heterostructure nanowires are core/shell nanowires, where the nanowire at the core is wrapped by one single or multiple shells [67]. Historically, there has been a vast amount of studies in radial heterostructures with the self-catalyzed growth strategy. One possible reason for promoting core/shell nanowires by the self-catalyzed growth can be that in contrast to the Au-assisted growth, in the self-catalyzed growth, the liquid droplet can be consumed or solidified *in-situ*, which is not the case for Au-assisted way of growth. The combination of the self-catalyzed growth strategy with the MBE growth technique has introduced various core/shell or core/multi-shell nanowire heterostructures which are limited to be grown as epilayers with such a high crystal quality and thicknesses [66], [67].

In 2002, L J Lauhon et al (in the group of C M Lieber) reported the first epitaxial Si/Ge core/shell and core/multi-shell nanowire heterostructures with B doped Si shell, which were employed as coaxially gated nanowire transistors [133]. Later, M Ben-Ishai and F Patolsky showed the smooth and single crystal Ge(core)/Si–Ge–Si(multi-shell) and Si(core)/Ge–Si (multi-shell) nanowires [134]. In 2004 and 2005, the first report for III-V group was by F Qian et al (in the group of C M Lieber) based on n-GaN/InGaN/p-GaN and $In_xGa_{1-x}N$/GaN/p-AlGaN/p-GaN core/multi-shell nanowires as LED devices [135], [136]. Mohan et al fabricated SAG of InP/InAs/InP core/multi-shell nanowires. Instead of changing the shell composition, they tuned the electronic structure of the InAs shell by the using quantum confinement effect as well as strain where InAs and InP have a 3.2% lattice mismatch. 4K PL measurements proved the presence of strained InAs quantum well on InP (110) sidewalls [137]. Later, in 2007, P K Mohseni et al (in the group of R R LaPierre) demonstrated the interplay between axial (VLS) and radial

growth for GaP/GaAsP/GaP core/multi-shell nanowires on Si(111). TEM and XRD spectroscopy showed the WZ phase in these nanowires [138].

Back into 1973, it is interesting to see 3D light guides in a single crystal GaAs/AlGaAs using photolithography have been developed, where AlGaAs is used as cladding layer to encapsulate GaAs [139]. In 2008, the development of core/shell nanowires via MBE growth based on group-III-arsenides was initiated by A Fontcuberta i Morral et al (in the group of G Abstreiter). They could grow a prismatic quantum radial heterostructure by the self-catalyzed MBE growth based on GaAs/$Al_{0.40}Ga_{0.60}As$ core/shell nanowires as well as a thin layer of GaAs sandwiched between two $Al_{0.40}Ga_{0.60}As$ barriers [140]. In the same year, M Heigoldt et al (in the group of A Fontcuberta i Morral) studied the optimal growth condition for such AlGaAs quantum coaxial structures and found the growth temperature of 465 °C results into the best quality and highly uniform shell growth [141]. Sooner afterwards, the lattice matched GaAs/AlGaAs core/shell nanowires in the literatures became the most favorable heterostructure nanowires for studying of the outstanding optical and electrical properties of low dimensional materials as compare to the bulk [67]. The Ga-assisted core/shell nanowires such as GaAs/$Al_xGa_{1-x}As$ core/shell nanowires by MBE can be grown as following steps: after the GaAs core growth which typically happens at a high growth temperature around of 640 °C, V/III flux ratio of 60 and the growth rate equivalent of the planar growth rate of 0.03 $nms^{-1}$, and a certain growth time (depending on the desired length or diameter of nanowire), the shell growth begins. The shell growth which is a radial growth requires the solidification of the Ga droplet meaning switching to the VS growth mode. This happens by increasing the As pressure to a certain value such as $2x10^{-5}$ mbar. Then substrate temperature switches to a lower temperature like 460 °C while Ga shutter stays shutdown in order to stop unintentional GaAs shell growth. Then after reaching to the target shell growth temperature, the Ga and Al sources are introduced together with a certain Ga flux and an Al flux to obtain the desired composition inside the shell meaning Al/(Ga+Al)= x (for a certain growth time depending on the $Al_xGa_{1-x}As$ shell thickness). Finally, it is very common to encapsulate $Al_xGa_{1-x}As$ shell with a very thin GaAs in order to prevent Al oxidation [142], [143]. SEM pictures presented in E Dimakis et al for the shell growth in VS mode around GaAs core show the solidification of Ga droplet at the tip of the GaAs nanowires [106].

Radial heterostructures formed by the overgrown layer around the initial nanowire passivate surface states, which can act as scattering centers for charge carriers or recombination sources for electron-hole pairs [64], [66]. The surface states, [144], strongly affect the electron transport properties in semiconductors like GaAs, resulting in a degradation of device characteristics e.g. a dramatic decrease of the carrier lifetime. Narrowing the size of the material in the form of

nanowires enlarges the impact of the nanowire surfaces and deteriorates the opto-electronic properties of nanowires and thus, making the nanowires 'properties different from the known properties of bulk GaAs. The high density of surface states cause Fermi level pining depending on the doping level and the size of the nanowires [145], [146]. Typically, a surface passivation layer forms a thin film of an inert material which lowers the density of surface states via removing the native oxide from the complex surface of GaAs [147].

Among different materials, overgrowth of the almost lattice-matched AlGaAs layer around GaAs has been found to nearly perfectly passivate the GaAs surface states [147]. Similar epitaxial growth materials for the passivation of GaAs surface states are GaAsP, AlInP, and GaN. The Ga-N bonds are highly stable and best candidate for passivation of GaAs, but the large lattice misfit of 20% between GaAs and GaN causes the limitation for the coherence growth and thus the limited GaN thickness of up to 2 monolayers [146]. The passivation of the GaAs surface states drastically improves the brightness of the photoluminescence and solar cell efficiency [146]. Another novel example of surface passivation of GaAs is presented in this thesis where the overgrowth of lattice mismatched $In_{0.54}Al_{0.46}As$ layer around GaAs passivates the GaAs surfaces as shown in the cross-sectional scanning TEM image in Figure 2.14.

N Jiang et al (in the group of C Jagadish) investigated on the impact of AlGaAs shell thickness and growth time on the minority charge carrier lifetime inside the GaAs core of GaAs/AlGaAs core/shell nanowires. An increase of carrier lifetime up to a certain value with increasing the shell thickness has been reported which is the result of suppressing the tunneling probability of carriers through the AlGaAs shell [148].

D Rudolph et al demonstrated a detailed material compositional analyses of GaAs/$Al_{0.30}Ga_{0.70}As$ core/shell nanowire grown by MBE on silicon. The cross-section TEM image reveals Al-rich line, like Figure 2.14, inside the $Al_{0.30}Ga_{0.70}As$ alloy due to interface segregation, nanofaceting, and local alloy fluctuations. A 6-fold Al-rich substructure along the corners of the hexagonal $Al_{0.30}Ga_{0.70}As$ shell has been observed where the Al composition is up to $x \sim 0.60$, a factor of 2 larger than the body of the shell. This is attributed to facet-dependent capillarity diffusion due to the nonplanarity of shell growth [149]. A similar scenario as GaAs/$Al_{0.30}Ga_{0.70}As$ core/shell nanowire has been for the phase segregation in GaAs/AlInP core/Shell nanowires by N Sköld et al (in the group of L Samuelson). This is associated with the formation of nanofaceted corner profiles which results in elemental enrichment that can be applied universally to the synthesis of multi-component nanowire shells regardless of the exact material system or growth technique [149]. Later, Y Zhang et al reported for the first time a quasi-3-fold composition

symmetry with a polarity difference in III−V−V core/shell nanowires where the P-rich lines show the polarity along both ⟨112⟩A and B directions [150]. In 2020, S Assali et al showed the cross-sectional morphology of Ge/GeSn core/shell nanowire changes from hexagonal to dodecagonal shape through increasing the Sn composition. This drastic shape shift compared to other reports is due to Sn phase segregation and faceting at {112} surfaces, where Ge bonds are under tensile strain. Furthermore, the tunability of PL with varying composition and morphology of the GeSn shell as their findings indicates the feasible use of core/shell nanowires for optoelectronic devices operating at mid-infrared wavelengths [151]. Another detailed growth study over phase segregation in strain-free core/shell nanowires reported by R Bergamaschini et al. They simulated the sunburst pattern by kinetic compositional segregation which is dominantly triggered by the enhanced growth rate at the facet edges, whereas surface anisotropy keeps the stripes thin [152].

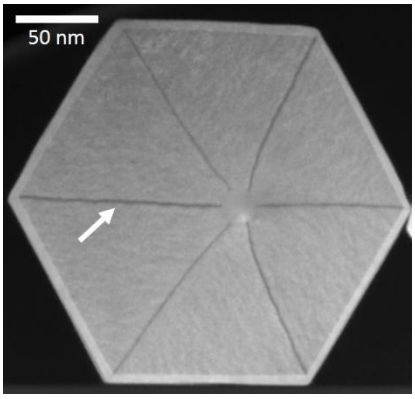


Figure 2.14 An example of scanning TEM image of GaAs/$In_{0.54}Al_{0.46}As$ core/shell nanowires with a thin lattice matched $In_{0.55}Ga_{0.45}As$ capping layer. This is an example for showing the typical phase segregation occurs in core/shell nanowire. The white arrow points toward the Al rich line along [112]. The detailed explanations of the nanowires are described in the result chapter 4.1. The TEM measurement has been performed at HZDR.

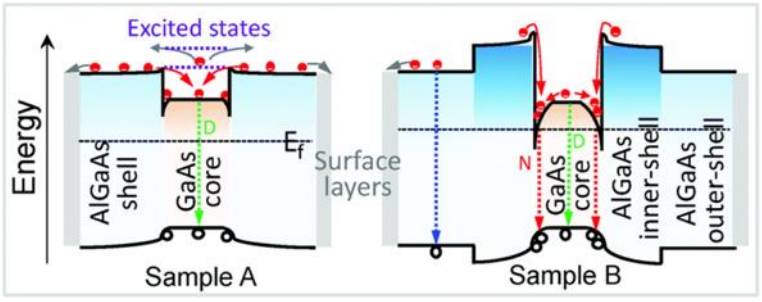


Figure 2.15 The assumed band alignment and possible recombination transitions marked D and N in two samples, in which band bending at GaAs/AlGaAs core/shell interface was mainly considered. The observed prolonged carrier lifetime was associated with the increased electron confinement at the core–inner-shell interface and the delayed recombination of photoexcited electron–hole pairs. Reproduced from [143] with permission from the Royal Society of Chemistry.

In 2013, M Heiss et al (in the group of A Fontcuberta i Morral) have found self-assembled quantum dots located at the apex of GaAs/$Al_{0.30}Ga_{0.70}As$ core/shell nanowires. The emission of these quantum dots embedded within the shell has blue shift emission relative to the lowest energy continuum states of the GaAs core [153]. Later, in 2015, N Jeon et al demonstrated alloy fluctuations that can act as quantum dot-like emitters with sharp PL lines in GaAs/AlGaAs core/shell nanowires [154]. In 2019, H Aruni Fonseka et al demonstrated the presence of novel self-assembled triplet quantum wires exchanging along ⟨112⟩A and B radial directions at the interface of $GaAs_xP_{1-x}$/$GaAs_yP_{1-y}$ core/shell nanowires grown by MBE on Si(111) with ZB phase, where they showed the origin of three quantum wires is due to 3-fold symmetry of ZB phase on (111) plane and further more forming quantum dots at the twin boundaries of these quantum wires. Their performed optical spectroscopy verified the quantum emitters in the twinned individual nanowires [155].

The shell can be designed in such that the carriers are confined in the core or interface between core/shell, to keep them away from the surface state scattering, which leads into the enhancement of the conductivity (see Figure 2.15) [156], [143]. In 2019, C Zhou et al reported carrier dynamics for two different samples of GaAs/AlGaAs core/shell nanowires. In sample A, both Ga and Al beams were supplied with the Al flux/(Ga flux + Al flux) of ∼23% (for 30 min growth time of the AlGaAs shell). In sample B, an additional AlGaAs shell with a higher Al composition of ∼38% was grown for 5 min between the nanowire core and shell. Based on time-resolved PL experiments and accordingly the decays of the carrier lifetime of the GaAs core with a mono-exponential decay for both samples , it has been extracted that the carrier lifetime of sample B is ∼34% longer than A. In both A and B, electrons diffuse from AlGaAs into GaAs, causing a band bending at the interface as shown in Figure 2.15. Also, the excited electrons in the AlGaAs shells may have the poosibility to diffuse to the low-energy and small-band-gap GaAs core. For sample A with a lower Al composition, and thereby with a less band bending, the direct recombination of the electrons-holes inside the GaAs core is dominant (as marked by the green dotted arrow D). The excited electrons in the CB of the core may transfer to the AlGaAs shell due to a relatively low energy barrier for electron escape, which may be confined at the nanowire surface layers and cause a non-radiative recombination and a relatively short carrier lifetime. For sample B, the AlGaAs inner-shell with a high Al concentration has a wider bandgap, causing a relatively large difference in the Fermi level ($E_f$) between GaAs and AlGaAs, and thus the more significant band bending. The red dotted arrow marked with N indicates an additional

transition path inside this triangular well for the sample B which might be the reason for the slight longer carrier lifetime as shown in Figure 2.15 [143].

Moreover, low refraction index shells improve the confinement of photons, promoting waveguiding or lasing inside the shell [67]. B Mayer et al (in the group of J J Finley) demonstrated the infrared lasing up to 300 K for individual GaAs/AlGaAs core/shell nanowires inside the active GaAs region. They believed by precisely designing the shell composition, high performance infrared lasers based on nanowires might be feasible using such III/V semiconductor heterostructures. P Krogstrup et al (in the group of A Fontcuberta i Morral) demonstrated a solar cell device based on a single GaAs nanowire (with a p–i–n junction) which can boost the solar cell efficiency beyond the Shockley–Queisser limit [22]. In 2020, E M Fadaly et al demonstrated direct-bandgap emission from hexagonal Ge and SiGe alloys and showed the development of Si–Ge alloys that have superior optoelectronic properties with the high potential of the improvement of photonics technologies that are compatible with current Si electronic platform [125], [157]. With regards to the photonic device technology such as LEDs or solar cells, the reports of P Krogstrup et al [22] and E M Fadaly et al [125] can be considered as the state-of-the-art in the nanowire society.

Another aspect of core/shell nanowire property as surrounding-gate architecture can be mentioned. Generally, small band gap with small effective mass III-V semiconductors boost the tunneling probability and consequently the tunneling current to be used as TFETs with an excellent ON and OFF ratio. In nanowire-based devices, enhancing the drive current at a certain supply voltage or keeping a drive current constant for a weakened supply voltage might be obtainable via increasing the cross-sectional area of a device, while, in return electrostatic characteristics degrade. Gate-all-around nanowire devices are the most favorable electrostatic configuration to decrease short channel effects; but addressing the drive current in the arrays of vertical nanowires is still an issue that requires an additional chip area. Using a III-V core/shell nanowire as a transistor provides an impressive means to address the drive current issue without compromising neither chip area nor device electrostatics [124]. In 2019, T Vasen et al reported vertical gate-all-around nanowire GaSb/InAs core/shell for n-Type TFETs with the possible realization of CMOS footprint requirements [158] .

Monolithic integration of III-V nanowires or even core/shell nanowires on Si is still in a premature phase to be entered the VLSI industry [26], [99]. Typically, in order to study the fundamental opto-electronic properties of nanowires, they are removed from the original substrate onto another substrate depending on the type of experiment. From technological perspective, nanowires should not be removed from their grown substrate and all device

processing and experiments should be performed on the original substrate (same substrate) to fulfill monolithic integration of III-V nanowires on Si. To achieve this idea, there has been significant engineering efforts commenced. Thus, accordingly few promising reports in the following can be outlined [159]. In 2012, K Tomioka et al demonstrated high performance vertical transistors, HEMTs, based on InGaAs/InP/InAlAs/InGaAs core/multi-shell nanowires grown by SAG on Si substrate [29]. G Koblmüller et al have offered different schemes for monolithic integration of GaAs based nanowires as lasers. They reported how such vertical cavities (e.g. GaAs/AlGaAs core/shell nanowires) can be a good candidate for low-threshold lasing, high spontaneous emission coupling and ultra-fast emission characteristics [163]. In 2020, Y Ra and C Lee have demonstrated the monolithic integration of multiple-color emission on the same substrate (not Si) by using the multiple-stacked tunnel junction shell nanowire heterostructure [133]. For lasing or LED applications in the UV spectral range, GaN or AlGaN nanowire-based devices are premiers due to their high refractive index contrast with Si, providing strong modal reflectivity and waveguiding modes inside these type of nanowires as compared to GaAs based nanowires [113], [163].

In this thesis, the focus will be on two types of core/shell nanowires as GaAs/ $In_xGa_{1-x}As$ and GaAs/ $In_xAl_{1-x}As$ grown directly on Si(111) by MBE with a predominant ZB crystal structure. To enable more freedom in In composition, x, while maintaining a high crystal quality; $In_xGa_{1-x}As$ or $In_xAl_{1-x}As$ as a shell layer around GaAs nanowires, constituting the core on Si(111) has been grown resulting in lattice mismatched core/shell nanowires where the strain between core and shell in these novel low-dimensional heterostructures is one of the main challenges to be investigated. Strain engineering of GaAs through the shell growth has been employed which can open up potential applications of these material structures for the future devices based on nanowires structure such as widely tunable laser, HEMTS (remote doping technique), and nanowire-based FET.

### 2.4 Strain in epilayers and core/shell nanowires

This chapter provides the fundamentals as the strain(stress), strain in heterostructure epilayer compared to core/shell nanowires. By incorporating coherent strain in a proper design of the material structure, it has been shown that the device performance can be substantially increased. Therefore, strain engineering is an intriguing strategy for improving device performance [160] which is even in a wide use for Si-CMOS technology [161], [162]. While planar

layers suffer from a high density of dislocations due to the lattice-mismatched substrates, core/shell nanowires can efficiently pass the strain into the core and are thus promising for a coherent system [94].

A system is called “elastic” when it can return to its initial state after being deformed by an external force. For a small deformation, the elastic behavior of most materials (e.g. spring) shows a linear elasticity which stands for the linear relation between stress and strain.

$$F = Kx \quad (11).$$

$$\sigma = E\varepsilon \quad (12).$$

The relation of stress ($\sigma$) and strain ($\varepsilon$) is also originated from Hooke’s law. This law can be described by a tensile force ($F$) and its corresponding displacement $x$. In eq. (11), $K$ is a constant known as a spring constant and in eq. (12), $E$ is known as the elastic modulus or Young’s modulus [163], [164], [165], [166], [167].

$$\sigma_{ij} = C_{ij}\varepsilon_{kl} \quad (13).$$

$$\begin{bmatrix}\sigma_{xx}\\ \sigma_{yy}\\ \sigma_{zz}\\ \sigma_{yz}\\ \sigma_{xz}\\ \sigma_{xy}\end{bmatrix} = \begin{bmatrix}C_{11} & C_{12} & C_{12} & 0 & 0 & 0\\ C_{12} & C_{11} & C_{12} & 0 & 0 & 0\\ C_{12} & C_{12} & C_{11} & 0 & 0 & 0\\ 0 & 0 & 0 & C_{44} & 0 & 0\\ 0 & 0 & 0 & 0 & C_{44} & 0\\ 0 & 0 & 0 & 0 & 0 & C_{44}\end{bmatrix} \cdot \begin{bmatrix}\varepsilon_{xx}\\ \varepsilon_{yy}\\ \varepsilon_{zz}\\ 2\varepsilon_{yz}\\ 2\varepsilon_{xz}\\ 2\varepsilon_{xy}\end{bmatrix} \quad (14).$$

As mentioned, the Hooke’s law has a limitation for its linearity. Within this limit, it can be generalized for 3 dimensional elastic objects in ZB crystals, e.g. GaAs. In eq. (13), $C_{ij}$ is the elastic stiffness tensor. The whole matrix component of $\sigma_{ij}$ is written as eq. (14). For crystals with cubic symmetry, the tensor elements can be simplified as $C_{1111}$=$C_{11}$, $C_{1122}$= $C_{12}$, $C_{1212}$= $C_{44}$, etc. Thus due to the cubic symmetry, the $C_{ij}$ tensor is based on only three constants, $C_{11}$, $C_{12}$, and $C_{44}$ [163], [164], [165], [166], [167]. For GaAs material, the elastic stiffness constants are reported as following:

$$C_{11} = 118 \text{ GPa}, C_{12} = 53.8 \text{ GPa}, \text{ and } C_{44} = 59.4 \text{ GPa} \quad (15).$$

Also, the stress tensor can be defined by the elastic compliance tensor ($S_{ij}$) which is the inversion of matrix in eq. (14) [163], [164], [165], [166], [167].

$$\begin{bmatrix}\varepsilon_{xx}\\ \varepsilon_{yy}\\ \varepsilon_{zz}\\ 2\varepsilon_{yz}\\ 2\varepsilon_{xz}\\ 2\varepsilon_{xy}\end{bmatrix} = \begin{bmatrix}S_{11} & S_{12} & S_{12} & 0 & 0 & 0\\ S_{12} & S_{11} & S_{12} & 0 & 0 & 0\\ S_{12} & S_{12} & S_{11} & 0 & 0 & 0\\ 0 & 0 & 0 & S_{44} & 0 & 0\\ 0 & 0 & 0 & 0 & S_{44} & 0\\ 0 & 0 & 0 & 0 & 0 & S_{44}\end{bmatrix} \cdot \begin{bmatrix}\sigma_{xx}\\ \sigma_{yy}\\ \sigma_{zz}\\ \sigma_{yz}\\ \sigma_{xz}\\ \sigma_{xy}\end{bmatrix} \quad (16).$$

Basically, the relation of the elastic compliance constants $S_{ij}$ to the elastic stiffness constants can be obtained via eq. (17-19) [163], [164], [165], [166], [167].

$$S_{11} = \frac{C_{11} + C_{12}}{{C_{11}}^2 + C_{11}C_{12} - 2{C_{12}}^2} \quad (17).$$

$$S_{11} = \frac{-C_{12}}{{C_{11}}^2 + C_{11}C_{12} - 2{C_{12}}^2} \quad (18).$$

$$S_{44} = \frac{1}{C_{44}} \quad (19).$$

A fractional change of crystal volume under a 3-dimensional strain or hydrostatic strain ($\varepsilon_h$) can be introduced as,

$$\frac{\Delta V}{V} = \varepsilon_{xx} + \varepsilon_{yy} + \varepsilon_{zz} \quad (20),$$

where, $\frac{\Delta V}{V}$ is the relative change in a crystal volume (a fractional change in the volume) [168], [169].

Any stress may be categorized in three types: uniaxial stress, shear stress, and hydrostatic stress (see Figure 2.16). Uniaxial tensile or compressive stresses, $\sigma_{xx}$, $\sigma_{yy}$, and $\sigma_{zz}$, are originated by force pairs acting perpendicular to the surfaces (see Figure 2.16). If the forces are applied tangentially, they cause shear stresses as $\sigma_{xy}$, $\sigma_{yz}$, and $\sigma_{xz}$ [163], [164], [165], [166], [167]. If a crystal is deformed in 3 dimensions, it can be named “hydrostatic strain”. However, the hydrostatic strain does not necessarily mean the equal strain in all 3 dimensions. In case of the equal strain deformation in all 3 dimensions, it can be named “isotropic hydrostatic strain” and in case of non-equal, it can be named “an-isotropic hydrostatic strain” [163], [164], [165], [166], [167].

For isotropic solids (meaning solid materials that their physical properties are independent of the orientation of the material system) only 2 independent stiffness constants exist, describing the response on axial and shear stress. For such materials in ZB phase, the elastic constants as $C_{44}$ = 1/2($C_{11}$ − $C_{12}$) can be related. The two independent elastic constants are known as Lamé constants μ and G, in which, μ = G = $C_{44}$ and λ = $C_{12}$. G is known as the shear modulus. There are a few relations exist to show their dependences. If the elastic properties of isotropic solids are expressed in terms of components of the compliance matrix $S$, the two independent components are $S_{11}$ = 1/E and $S_{12}$ =−ν/E; $S_{44}$ = $S_{55}$ = $S_{66}$ =(2+2ν)/E. In these

relations, E is known as Young's modulus and expresses the ratio stress/strain, and ν is called Poisson's ratio. These two quantities are related to the Lamé constants as follows,

$$E = \frac{\mu\,(2\mu + 3\lambda)}{\mu + \lambda} \qquad (21),$$

$$\nu = \frac{\lambda}{2(\mu + \lambda)} \qquad (22).$$

When a solid material is under a transverse tensile strain in one direction, simultaneously it deforms longitudinally compressed in the other direction. Such deformations in material property is termed Poisson's ratio, ν = − (transverse strain/longitudinal strain), for a uniaxial tensile stress applied in longitudinal direction. For cubic materials and stress along an axis of the unit cell, the ratio is ν = $C_{12}/(C_{11}+C_{12})$. Values for Poisson's ratios range between 0.5 (incompressible medium) and −1 (perfect compressibility).

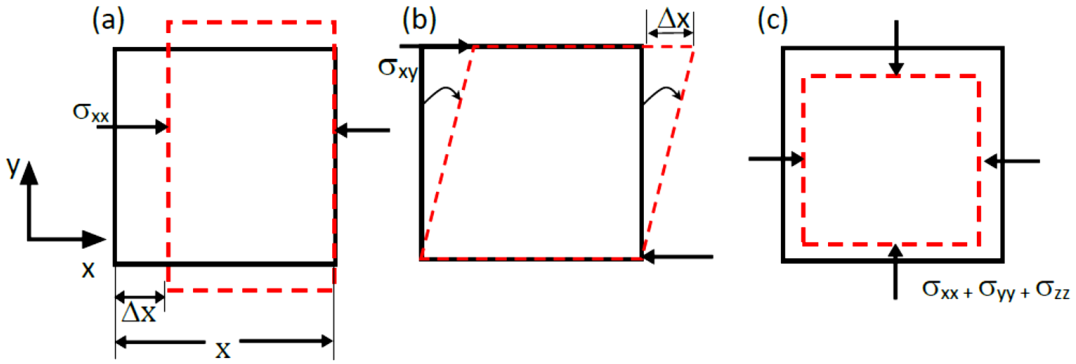


Figure 2.16 Different types of a solid lattice deformation by (a) uniaxial stress, (b) shear stress, and (c) hydrostatic stress.

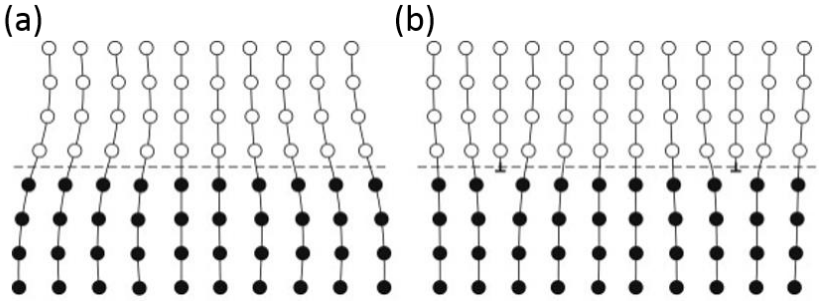


Figure 2.17 Two types of interfaces (a) strained coherent interface, (b) semi-coherent interface with dislocations which one of them is shown as ⊥. Reprinted with permission from from [170]. Copyright 2014 Elsevier.

In the pseudomorphic growth, the epitaxial layer laterally strained (either in a tensile or compressive regime) in order to be lattice-matched with the crystalline substrate or layer underneath, e.g. InGaAs on GaAs substrate. Beyond a critical thickness of the film, defects or misfit dislocations through a plastic relaxation are produced. A coherent interface is constructed

when the two crystal lattices or part of the them has a good 'match' and the two crystal lattices are continuous across the interface and this occurs when both of their interfacial plane has the same atomic configuration. Still, the SF interface (discussed in chapter 2.2) is counted as a typical coherent interface. When the 'lattice match' at the interface is not good, it is still possible to sustain coherent interface by straining one or both lattices, as shown in Figure 2.17 (a). These coherent interfaces through the strain rise the elastic energy density ($w$) in the volume (V), and for higher misfits it becomes energetically more favorable to shape a semi-coherent interface (see Figure 2.17 (b)) where the lattice mismatch is periodically taken up by misfit dislocations. Then such a strained coherent interface can be relieved by a cross-grid of dislocations ($\perp$) in the interface plane, the spacing of which depends on Burgers vectors of dislocations and misfits. The Burgers vector is a vector, that shows the magnitude and direction of the lattice distortion as a result of a dislocation in a crystal lattice. The atoms in a crystal accommodating a dislocation are displaced from their perfect lattice sites, and the resulting distortion generates a stress field in the crystal around the dislocation. Thus, the dislocation is a source of internal stress in the crystal. The interfacial energy for semi-coherent interfaces appears from any chemical contribution as for fully coherent interfaces, and the energy of the dislocations. The energy of a semi-coherent interface goes higher with reducing dislocation spacing as far as the dislocation strain fields overlap. When this happens and continues beyond a certain limit, the discrete nature of the dislocations will be ruined, and therefore, the interface becomes incoherent [170].

Eventually, the growth of a single crystal in a lattice-mismatched structure is crucial, since strain can produce easily different types of defects in an improper geometrical design and growth conditions, which cause severely a device performance degradation like a charge carrier mobility reduction. Such defects are one of the major sources in a degradation of charge carrier mobilities [65], [171]. Hence, defects are a serious discussion in crystalline solids and epitaxy. Generally, crystals can consist of imperfections such as point, line, surface or volume defects which disturb locally the regular atomic arrangement of the crystals. The line defects can also be called dislocations which are an important class of defect in solid crystals. There is a critical shear stress field which causes a plastic deformation, where the dislocations appear inside a single crystal system such as threading dislocations and misfit dislocations [172]. Threading dislocations originate from lattice mismatching and extend from the surface of a strained layer, passes through the entire layer and penetrate the substrate while bend at the interface into misfit dislocations [172]. The examples for the presence of threading dislocations related to

planar heterostructures on Si (001) inside GaAs, InAlAs in Figure 2.18 (a), and inside GaAs, InP, InGaAs are brought in Figure 2.18 (b) [173].

A free-standing cubic crystalline heterostructure with two layers having individual strain-free lattice constants of $a_1$ and $a_2$ as shown in Figure 2.19 (a) can be assumed with a coherent strained interface, where the $f$ is not too high (e.g. below 1%). The layer with larger lattice constant ($a_1$) strains compressively while the one with smaller lattice constant ($a_2$) strains tensilely. In such a heterostructure owing the nature of the biaxial strain, the lattice constant parallel to the interface, $a_{\|}$ (the in-plane lattice constant), reaches values between $a_1$ and $a_2$ (the individual lattice constant of respective layer) and the out-of-plane ($\perp$) strain forms as a result of already-generated strain in in-plane ($\|$) directions. The out-of-plane strain values of layer 1 and layer 2, $a_{1\perp}$ and $a_{2\perp}$, approach to the values higher than $a_1$ and lower than $a_2$ for the respective layer. Assuming a cubic structure, in-plane strain components are equal ($\varepsilon_{xx} = \varepsilon_{yy} = \varepsilon_{\|}$). In such a free-standing layered structure, the sign of out-of-plane strain ($\varepsilon_{\perp}$) is opposite from $\varepsilon_{\|}$. Thus, there is a relation between $\varepsilon_{\perp}$ and $\varepsilon_{\|}$. Theoretical calculations (for such a biaxial deformation in the cubic phase) by assuming zero in-plane shear strain and (001) orientation of the interface plane result in the following eq.(31) and (32) [174].

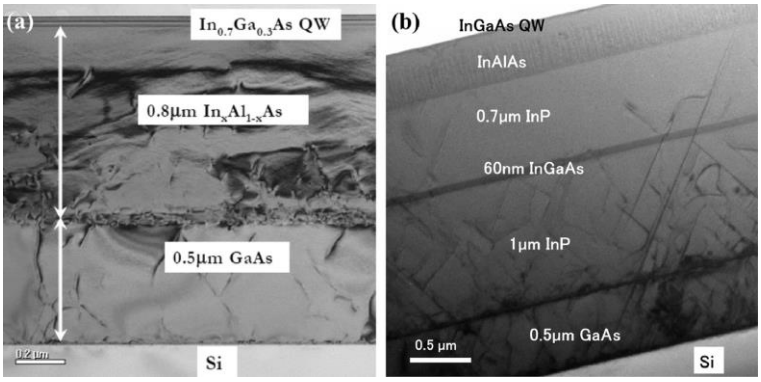


Figure 2.18 Some examples for presence of threading dislocations observed in cross-sectional TEM image of InGaAs quantum well field-effect transistor structures on Si using compositionally graded InAlAs/GaAs buffer (a) by MBE and (b) InP/GaAs buffer by MOCVD. Reprinted with permission from [173]. Copyright 2017 Elsevier.

$$\varepsilon_{i\perp} = \frac{a_{\|}}{a_i} - 1 \qquad (23).$$

$$\varepsilon_{i\|} = \frac{a_{i\perp}}{a_i} - 1 \qquad (24).$$

After the description of the free-standing layers, the focus is on the case when one layer (substrate) is far thicker than the other layer (thin film) as shown in Figure 2.19 (b) and (c). Due to the thick substrate, it is unstrained, and the deformation occurs inside the epitaxial layer (thin

film). Assuming an elastic relaxation of strain meaning coherent strain, it can conclude that $\varepsilon_{\parallel} = f$. Sign of $f$ depends on the lattice constant of the epitaxial layer respect to the substrate as shown in Figure 2.19 (b) and (c). In general, the elastic energy density ($w$) of such a solid strained material can be obtained by, eq. (25).

$$w = \frac{E}{V} = \frac{1}{2}\sum_{i=1}^{6}\sum_{k=1}^{6} C_{ik}\varepsilon_i\varepsilon_k \qquad (25).$$

In this equation, E and V are the elastic strain energy and material volume. For a cubic material, this equation including the three respective terms of hydrostatic, uniaxial, and shear strains can be written as follows:

$$w = \frac{E}{V} = \frac{1}{2}(C_{11}\left(\varepsilon_{xx}^2 + \varepsilon_{yy}^2 + \varepsilon_{zz}^2\right) + 2C_{12}\left(\varepsilon_{xx}\varepsilon_{yy} + \varepsilon_{xx}\varepsilon_{zz} + \varepsilon_{yy}\varepsilon_{zz}\right) +$$

$$2C_{44}\left(\varepsilon_{xy}^2 + \varepsilon_{xz}^2 + \varepsilon_{yz}^2\right)) \qquad (26).$$

In eq. (26), the $w$ increases quadratically with strain elements in the harmonic approximation of Hooke's law. If a cubic, biaxially strained layer is considered, which can elastically relax according Poisson's ratio, the $w$ can be obtained by eq. (27).

$$w = \frac{E}{At_L} = 2G{\varepsilon_{\parallel}}^2\frac{1+\nu}{1-\nu} \qquad (27).$$

In this equation, $V = At_L$ where $A$ , $t_L$ are the area and the strained layer thickness, respectively. It can conclude based on eq. (27) that the $E$ or $w$ has an inverse proportionality with $t_L$ and furthermore, it increases quadratically with $\varepsilon_{\parallel}$ which can include $f$. Thus, increasing the $t_L$ results in the increase of strain energy inside the epilayer (the epitaxial thin film). The thickness of the epitaxial layer is very critical in order to sustain such a coherent interface, which means beyond a critical layer thickness ($t_c$), this energy is too high and requires formation of structural defects such as threading dislocations through a plastic relaxation.

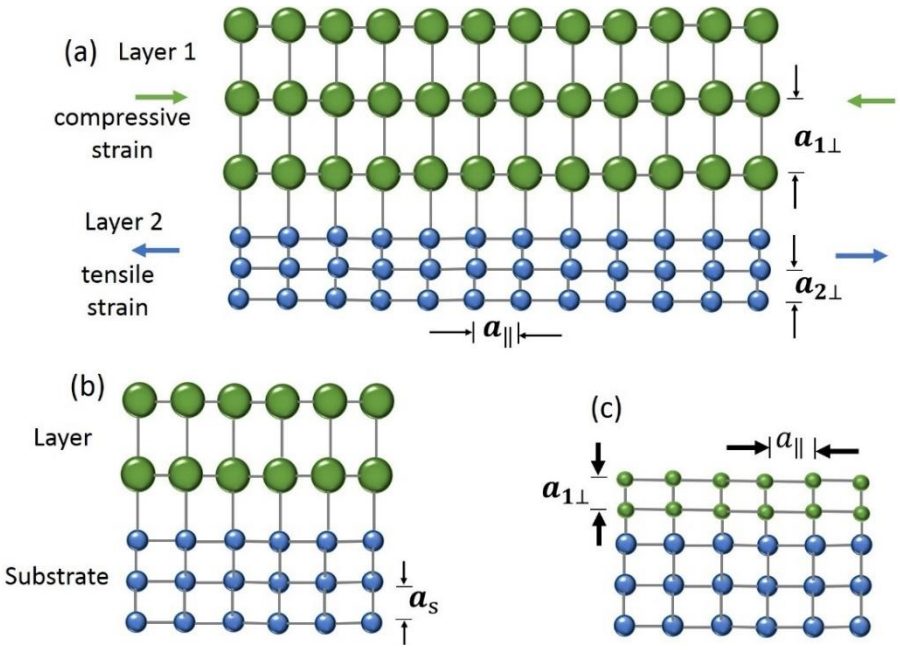


Figure 2.19 Effect of strain on lattice constants of epilayer heterostructures (a) Schematic of a heterostructure consisting of two layers with a common interface. $a_{\parallel}$ is the common in-plane lattice constant, $a_{1\perp}$ and $a_{2\perp}$ denote the out-of-plane lattice constants of the strained layers 1 and 2. In (b) and (c), biaxially strained layers (yellow atoms) on substrates (blue atoms) with another lattice constant $a_s$. In (b) the unstrained lattice constant of the layer $a_L$ is larger than $a_s$, and the layer is compressive strained in lateral direction ($f > 0$ or $a_L > a_s$); in (c) the layer is tensile strained ($f < 0$ or $a_L < a_s$) as defined by eq. (10).

Having described the strain in planar epitaxial thin film layers, the focus is on how strain deformation appears in core/shell nanowires with their non-planar interface. The distinct feature of nanowires in terms of strain is that strain relaxation in them is far more efficient than the corresponding epilayers, which is simply due to their lower volume or in another word their narrower lateral size. The small volume of nanowires makes them more flexible under the misfit strain and result in single crystals without dislocations such as threading dislocations [94].

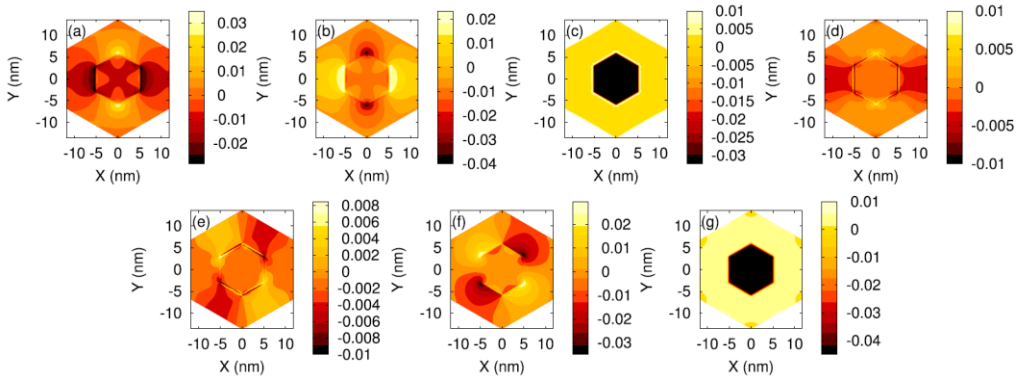


Figure 2.20 Strain maps for an infinite core/shell nanowire based on VFF model is shown. Plots from (a) to (g) belong to $\varepsilon_{xx}, \varepsilon_{yy}, \varepsilon_{zz}, \varepsilon_{yz}, \varepsilon_{xz}, \varepsilon_{xy}$, and $\varepsilon_h = \varepsilon_{xx} + \varepsilon_{yy} + \varepsilon_{zz}$, respectively. Reproduced from [171], with the permission of AIP Publishing.

J Grönqvist, N Søndergaard, F Boxberg et al gave a comprehensive discussion on the strain profile for semiconductor core/shell nanowires in ZB phase [171]. Their theoretical computations were based on both continuum elasticity theory using finite elements method (FEM) and an atomistic valence force-field (VFF) model while considering both finite and infinite wires. The few assumptions in VFF model makes the computation time faster than the continuum elasticity theory. The results of these two types of modeling have a good agreement in terms of generic properties of the strain distributions in core/shell nanowires, as J Grönqvist et al predicted [171]. They found that the strain distributions for infinite wires are excellent approximations to the strain distributions in finite wires, except in the regions close to the ends. Based on their 2D simulation results (see Figure 2.20), all individual strain components show a complex strain profile, except $\varepsilon_{zz}$ and the hydrostatic strain ($\varepsilon_h$) profile which have much simpler strain maps. Furthermore, all diagonal strain elements have very similar magnitude. The off-diagonal strain elements (meaning shear strain values) are small but non-vanishing. This points out that the material in such a core/shell geometry is not only under tensile or compressive strain but also is warped. Interestingly, theoretically it is proved that hydrostatic strain in the core is always dominated by the axial strain (out-of-plane strain), $\varepsilon_{zz}$, along the growth axis [111]-direction. However, the mean values of in-plane strain elements, $\varepsilon_{xx}$, $\varepsilon_{yy}$, of the core or shell in parallel to $[1\bar{1}0]$, X-axis, and $[11\bar{2}]$, Y-axis, have less than 20% of the $\varepsilon_{zz}$ on a given cross-section of the nanowires, like an example in Figure 2.21 (a) [171], [175]. The theoretical modeling from J Grönqvist et al has the possibility to be extend for core/multi-shell nanowires as well as WZ phase crystal structure [171].

Under a certain misfit, there is a critical core radius, below which the nanowire heterostructure will be coherent regardless of shell thickness. For core/shell heterostructure nanowire with a core radius larger than the critical core radius, there is a critical shell thickness, below that no dislocations appear. As an example, for a GaAs/$In_{0.20}Ga_{0.80}As$ core/shell nanowire with a core radius of 100 nm, the critical $In_{0.20}Ga_{0.80}As$ shell thickness is determined to be 37 nm, which is larger than that of $In_{0.20}Ga_{0.80}As$ film grown on planar GaAs substrate with about 14 nm predicted by the simulation shown in X Yan et al [62]. They used finite element method (FEM) to analyze the stress distribution and calculate the strain energy by dividing the whole system into small units and calculating the variables one by one [62]. The dependence of the critical shell thickness for $In_xGa_{1-x}As$ as a function of the core (GaAs) radius for different compositions is shown in Figure 2.21 (b). The blue dashed line in Figure 2.21 (b) is the thinnest possible GaAs core (10 nm in radius) which can be grown by MBE at HZDR. This thickness of the GaAs nanowire

for the core is still suitable since it is far away from the coherency limit as predicted by X Yan et al [62]. Critical dimensions for the core and shell are playing a significant role in controlling the strain distribution to avoid the formation of the dislocations. By staying in the range lower than the critical core radius as shown in Figure 2.21 (b), one can grow the infinite shell thickness without formation of dislocations based on this simulation result and in fact, this is highly intriguing feature of the core/shell nanowires with their 6-folded hexagonal facets as compare to epilayers. Relying on the numerical calculation (FEM) of coherency limit for a GaAs/$In_xGa_{1-x}As$ core/shell nanowires, the critical core dimension at x=0.30 is around 44 nm in diameter in order to achieve a dislocation-free system as shown in Figure 2.21 (b) [62].

In another example for epilayers, the $t_c$ in a single layer of $In_{0.20}Ga_{0.80}As$ on GaAs buffer layer was predicted using a different model (Matthews theory) to be around 7 nm by J Zou et al [176]. It should be noted that different models used by X Yan et al or J Zou et al regarding to the exact value of $t_c$ have a slight difference which might be attributed to different assumptions in both models. Nonetheless, because of the enhanced elastic relaxation, the $t_c$ is higher in nanowires as compare to epilayers. The critical dimensions of a core/shell structure are combinations of core and shell dimensions that will lead to coherently strained structures [94].

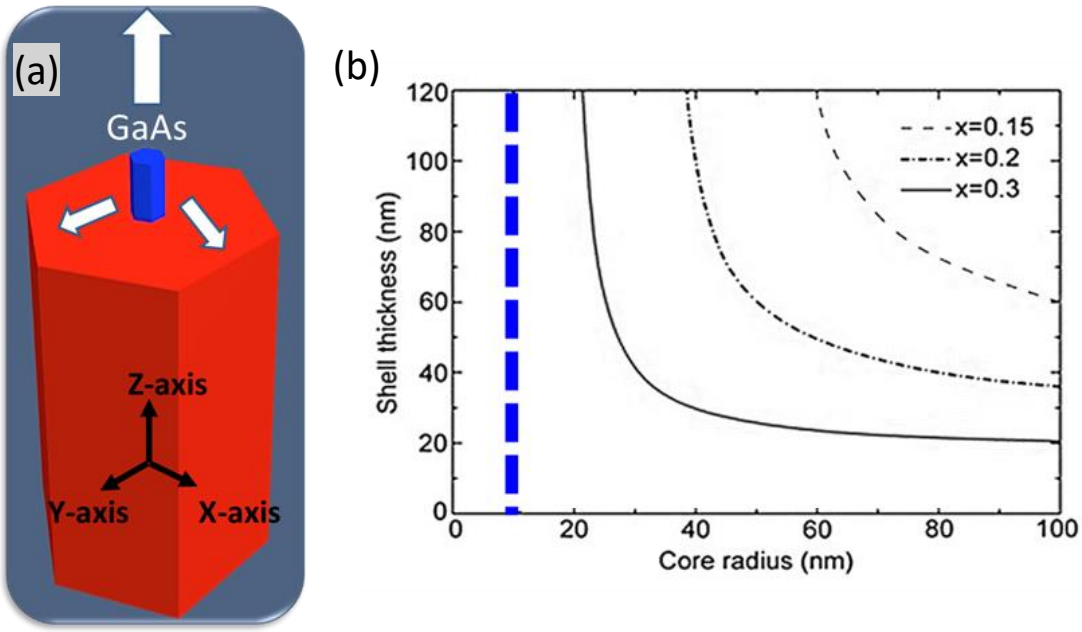


Figure 2.21 Distinct feature of nanowires such as their different strain symmetry (strain distribution) and their higher range of coherency limit as compared to epilayers. (a) The sketch of a GaAs (in blue)/$In_xGa_{1-x}As$ (in red) core/shell nanowire shows the majority of the strain is along the growth axis (Z-axis). (b) The simulation report for the coherency limit of GaAs/$In_xGa_{1-x}As$ core/shell nanowires which is adapted from [62]. Reprinted from [62], according to the License agreement of SpringerOpen. The blue dashed line in (b) is the current GaAs core radius that can be grown by MBE at HZDR. It should be noted that GaAs/$In_xGa_{1-x}As$ are the core/shell materials which have been investigated in this thesis.

While planar thin films for the $In_xGa_{1-x}As/GaAs$ systems suffer from a high density of dislocations due to the lattice-mismatched substrates, core/shell nanowires can efficiently pass the strain into the core and are thus promising for a coherent system. Theoretical simulations can be implemented for understanding strain distribution in nanowire geometry. Among other models for the strain distribution simulation, the continuum elasticity theory suffices to elucidate the strain in nanowires. Based on the theoretical reports in this direction, the results for strain distributions in infinite nanowires are excellent approximations to the strain distributions in finite nanowires, except of the both ends of the nanowires and their nearby [65], [171].

$$W = \int w dV \equiv \frac{1}{2}\int_0^L dz \int_0^R dr \int_0^{2\pi} \sigma_{ij}\varepsilon_{ij} r d\theta = \frac{1}{2}\int \sum_{ijkl} C_{ijkl}\varepsilon_{ij}\, dV \qquad (28)$$

$$w = \frac{1}{2}C_{11}\left(\varepsilon_{xx}^2 + \varepsilon_{yy}^2 + \varepsilon_{zz}^2\right) + C_{12}\left(\varepsilon_{xx}\varepsilon_{yy} + \varepsilon_{xx}\varepsilon_{zz} + \varepsilon_{yy}\varepsilon_{zz}\right) + 2C_{44}\left(\varepsilon_{xy}^2 + \varepsilon_{xz}^2 + \varepsilon_{yz}^2\right) \qquad (29)$$

The strain energy ($W$) can written as eq. (28), where $w$ stands for the strain energy density inside the defined volume ($V$) where L is the nanowire length and R is its total radius (assuming a circular cross section). Due to the cubic symmetry of the material, the elastic stiffness tensor can be simplified as , the $C_{11} = C_{iiii}$ $(i = x, y, z)$, $C_{12} = C_{iijj}$ $(i, j = x, y, z; i \neq j)$, and $C_{44} = C_{ijij} = C_{ijji}$ $(i, j = x, y, z; i \neq j)$. For this reason, eq. (29) has only three independent terms. This is also the condition in previous eq. (14), and eq. (26).

In this thesis, the focus is on strain engineered GaAs nanowires where the source of strain is from epitaxial overgrowth of the $In_xGa_{1-x}As$ and $In_xAl_{1-x}As$ shell. These two materials are lattice mismatched materials with GaAs and thereby the strain state, the type of strain as well as the symmetry of the strain in such core/shell nanowires are systematically studied. The GaAs core diameter is 20-25 nm which is a perfect diameter in terms of having enough distance from the predicted theoretical coherency limit.

### 2.5 Strain engineering in core/shell nanowires and its effect on band parameters

In this chapter, strain/bandgap engineering in core/shell nanowires and its effect on their opto-electrical properties are described. Engineering lattice strain through the overgrowth of

the shell offers a wealth of possibilities and novel functionalities. The key strength of nanowires with narrow lateral size is their high tolerance to misfit strain enables the growth of new heterostructures with a high crystal quality and thus the enhancement of device characteristics in electronics or photonics [63]. Eventually, strain/bandgap engineering allows manipulate the intrinsic properties of material and add more freedom in the design of heterostructures which is not possible in planar layers. There are different methods to probe the strain in a solid crystal such as XRD, Raman scattering spectroscopy and PL measurements which allow us to probe the lattice parameter of the material as well as the bandgap under strain or stress. The principles of the three mentioned techniques are briefly described in chapter 3.

Due to the band structure and atomic distance (lattice parameter) manipulations in solid crystals, unique changes and benefits such as i) tuning the bandgap and thus achieving to a desirable range of wavelength, ii) increasing (decreasing) the effective mass and thus increasing (decreasing) charge carrier mobility, iii) degeneracy lifting, iv) indirect-to-direct bandgap transition, v) piezoelectric field enhancement, vi) surface properties modifications occur, thereby paving the way for very interesting applications in photonics and electronics with only strain engineering [65], [177], [178], [179]. Various studies on strain-induced property changes in core/shell nanowires have been reported that some of these property changes are mentioned in the following section.

B Wei et al studied the size-dependent bandgap variation imposed by the tensile strain for ZnO nanowires with diameters ranging between 100 and 760 nm. They used a mechanical setup to apply uniaxial tensile stress on the nanowires and performed *in-situ* optical measurements showing the modulation tensile strain from 1.7% up to 7.8% by increasing the nanowire diameter. The change in the strength of tensile stress to maximum 13.2 GPa results in 110 meV shift in the bandgap [180]. J Treu et al showed up to $110$ times enhancements of the emission intensities from InAs nanowires by the overgrown InAsP shell. They varied the thickness and P composition inside the shell and could shift the bandgap energy via strain above 100 meV that exceed above 100 meV at comparatively low fractional P-contents [26]. M Hetzl et al demonstrated strain-Induced bandgap engineering in a SAG of GaN/(Al,Ga)N core/shell nanowires. PL spectroscopy performed at room temperature on the nanowires showed a large blue shift of the GaN band gap from 3.40 to 3.64 eV while reducing the core diameter. The reason for the increase of the GaN bandgap by decreasing the core diameter is the increase of the build-in compressive strain inside the GaN core which was proved by Raman scattering spectroscopy [181]. G Signorello et al utilized PL to investigate the electronic properties of GaAs/$Al_{0.3}Ga_{0.7}$As/GaAs core/shell/cap nanowires and the states of the applied uniaxial stress

by their mechanical setup. It is demonstrated that GaAs bandgap reduced remarkably up to 296 meV at 3.5% tensile strain. The nature of uniaxial stress as an anisotropic strain style caused the symmetry breaking of the crystal lattice and thus VB splitting. Their work opens up the path for the great potential of strain engineered nanowires in order to tune the wavelength to a broader range [178].

G Signorello et al demonstrated a direct-to-pseudodirect bandgap transition in WZ GaAs nanowires with uniaxial stress. They showed a remarkable shift of GaAs bandgap due to both tensile and compressive uniaxial strain (± 2%) by using a mechanical setup. They determined all band structure parameters of the WZ GaAs nanowire in unstrained conditions such as the crystal field and spin–orbit splitting, the bandgap and, most importantly, the splitting between the bright and the dark conduction bands by the Raman and PL experiments and k.p modeling [182]. L Zeng et al investigated on the intrinsic mechanical and electromechanical characteristics of individual InAs/$In_{0.6}Ga_{0.4}As$ core/shell nanowires as compared to the characteristics of bare InAs nanowires. Mechanical stress, lattice strain and electrical transport properties of InAs/$In_{0.6}Ga_{0.4}As$ core/shell nanowires were measured by an electromechanical *in-situ* TEM set up. They showed electromechanical properties such as piezoresistance coefficient, resistivity of the core/shell nanowire are different from the bare InAs nanowire due to the presence of the strain in the latter. They believe the reduced bandgap by strain engineering causes the increase of electron concentration inside the core and thus the change in resistivity. Their findings have the potential use for ultrasensitive nanoscale sensors [183]. M Hocevar et al reported a gradual red shift up to 14 meV of the band-edge of passivated GaAs/$Al_{0.35}Ga_{0.65}As$ core/shell nanowires by increasing shell thickness (up to 100 nm) which is due to the residual lattice mismatch between GaAs and AlGaAs that induced the small tensile strain into the GaAs core. The other reason for this shift can be due to axial piezoelectric fields which improve inside the nanowire core due to Al fluctuations [24].

To the best of our knowledge, the state-of-the-art with regards to an extreme material combination via epitaxial method belongs to L Balaghi et al. They fabricated GaAs/$In_xGa_{1-x}As$ core/shell nanowires with $0.10<x<0.56$ and GaAs/$In_xAl_{1-x}As$ core/shell nanowires with $0.38<x<0.55$ where the thin GaAs core undergoes to the heavily tensile strain up to ≈ 7% for the highest x. The magnitude of the strain can be tuned via the composition and the thickness of the shell. The resulted bandgap reduction renders GaAs nanowires suitable for photonic devices across the near-infrared range, including telecom photonics at 1.3 and potentially 1.55 µm, with the additional possibility of monolithic integration in Si-CMOS chips [65].

J Petykiewicz et al reported highly tensile (> 2.3%) strained Ge nanowires where the gain properties of material improved in order to realize high-Q optical nanocavity. They found the reduction of optical loss inside cavities provided by the tensile strain. Their high-strain nanocavities offer new possibilities for low-threshold Ge based lasers for on-chip optical interconnects [184]. S Bao et al demonstrated lasing from highly strained Ge nanowires with a robust mechanical, optical, and thermal properties enabling low-threshold lasing (3.0 kW $cm^{-2}$) at 83 K which is the one of the lowest reported value for IV group nanowires to date. They believe the room temperature lasing is possible by increasing the applied stress field inside the nanowires [185]. Y Zhang et al showed the highly compressive strained GaAsP/GaAs coaxial nanowire quantum wires nanowires without formation of dislocations. Their structure consists of three quantum wells with the lasing properties such as a low-threshold power and a narrow laser line [186].

Z Zhu et al showed the presence of compressive strain in GaSb core nanowires along [111] via epitaxially shell overgrowth of $GaAs_xSb_{1-x}$ and varied the core/shell dimensions and the shell composition to achieve the highest possible compressive strain in their system, which is -0.88% as the axial strain and -1.46% as the hydrostatic strain. VB splitting is reported in their structure where the LH band stays 33.4 meV above the HH band at Γ-point. Therefore, their strain-engineered GaSb nanowires with the more contribution of LH may provide an enhanced hole mobility by reducing both the interband scattering and the hole effective mass [187]. F Wen and E Tutuca reported the structural and electrical characterization of coherently strained $Si_{0.5}Ge_{0.5}$-Ge-Si core-double-shell nanowires by CVD growth. Both Ge and Si shell layers gained large hydrostatic compressive and tensile strain of up to -0.90% and +0.67%, respectively, which exploit carrier transport, and without observable dislocation defects. They showed *p*- and *n*-type MOSFETs based on these nanowires and observe a 500% (20%) increase of the average hole (electron) mobility compared to control devices based on Si nanowires, because of an increased hole (electron) mobility in the compressively strained Ge (tensile strained Si) shell [188].

P Alekseev et al showed the relative solar efficiency can be increased by 6.3% under −0.75% uniaxial compression imposed inside the GaAs nanowire solar cell [189]. H Li et al fabricated a novel type II InAs/AlSb core/shell nanowires (without dislocations) on Si(111) by MBE and demonstrated photodetectors based on these single lattice mismatched core/shell nanowires that the dark current significantly reduced and thus the negative photo-response improved as compare to bare InAs nanowire based devices. This report proves the great possibility of strain-engineered nanowires for fabrication of the next generation infrared photodetectors on Si

platform operating at room temperature [190]. K Chiba et al fabricated InGaAs nanowire array photodiodes on Si that operates at room temperature for two wavelengths of 635 nm and 1.55 µm. The overgrown InP shell around InGaAs nanowires imposed tensile stress into the core while passivating it. This thin shell growth improved the photocurrent density of the device at 1.55 µm. Their introduced photodiodes can be utilized as Si photonic optical device for telecommunication bands [191]. This report can be considered as the state-of-the-art for the monolithic integration III-Vs core/shell nanowires operating as a photodiodes [191].

In the following section, the theoretical background related to the effect of the strain on lattice parameter as well as band structure under the strain are described. To begin with, the effect of strain on phonons are discussed. The misfit strain causes noticeable changes in the bond length and angle of crystal structure and therefore it will affect the phonon vibrational frequencies of the solids.

Phonons are the collective vibrations of atoms or molecules in solid, which also designated as a quasi-particle. Therefore, they can be treated either by classical physics or quantum mechanics. Now a system with two different atoms (e.g. GaAs) with the distance as a diatomic chain (α) with their interatomic forces can be assumed [37], [163].

The four lattice vibrations of TA, LA, TO and LO are represented in Figure 2.22, where the transverse modes are always degenerate. The phonon frequency depends on the mass of the atoms and the interatomic forces as proved by the theory for an example in diatomic chain [37], [163]. After understanding conceptually about the lattice vibration modes, the phonon dispersion lines in BZ is shown for GaAs in Figure 2.23. The interatomic forces can be visualized by the stiffness of the string. Basically, the smaller the lattice constant, the stiffer the spring will be. This concept can be seen easily over a range of III-V semiconductors in the in Figure 2.24. The Raman shift (phonon wave number ($cm^{-1}$)) vs. lattice constant in different III-Vs has been depicted in this figure within medium infrared (MIR) and far infrared (FIR) spectral range. The lower Raman shift of both TO and LO phonon modes for the larger lattice constant implies to the stiffer spring and thus the weaker oscillation strength [163], [37], [165]. The principles of the Raman spectroscopy are described in methods chapter 3.3.

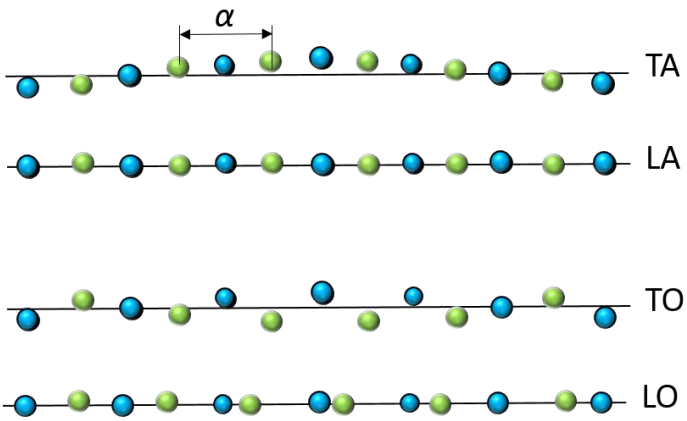


Figure 2.22 Sketch of acoustic (A) and optical (O) waves in a diatomic chain in longitudinal (L) or transverse (T) directions.

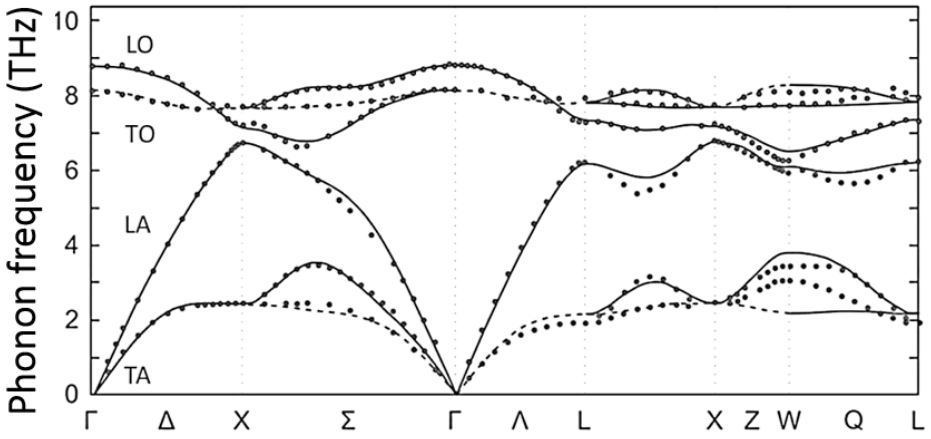


Figure 2.23 Phonon dispersion of GaAs in BZ with TO, LO and TA and LA where the experimental (dotted lines) and theoretical (solid lines) data are depicted. Reproduced from [163] with permission of Springer.

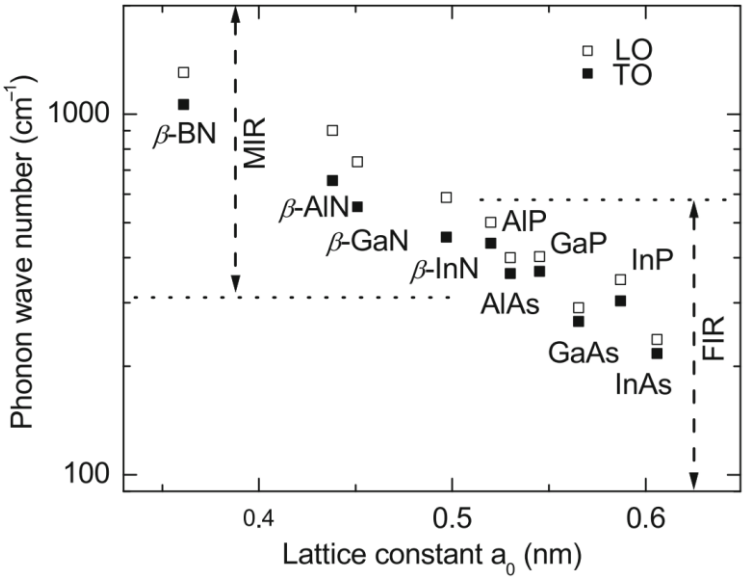


Figure 2.24 TO and LO phonons over a range of III-Vs between the MIR and FIR range. Reproduced from [163] with permission of Springer.

Raman and PL have been extensively used to understand physical properties of bulk semiconductors. From 1970, besides these techniques, high-pressure spectroscopy was applied on many diamond/ZB semiconductors to study their electronic and structural properties as a function of pressure. Applying a high pressure on the semiconductor affects the PL and Raman response meaning the change in band structure and shift of the bandgap and phonons, respectively [192].

I Zardo et al showed for the first time the dependence of the lattice parameter of GaAs nanowires on the applied pressure in comparison with the bulk GaAs [192]. Raman spectroscopy experiments as a function of pressure on GaAs nanowires were performed and thus the Raman shift of the optical mode as a function of $\frac{\Delta\alpha}{\alpha_0}$ (relative change in lattice parameter under the hydrostatic compression) was extracted. The fitting of the extracted plot (in [192]) gives the eq. (30) and (31) with a sublinear trend.

$$\omega_{TO} = (266.7 \pm 0.4) + (1.6 \pm 0.04) \times 10^3 \left(-\frac{\Delta\alpha}{\alpha_0}\right) - (1.3 \pm 0.9) \times 10^3 \left(-\frac{\Delta\alpha}{\alpha_0}\right)^2 \quad (30).$$

$$\omega_{LO} = (289.9 \pm 0.4) + (1.15 \pm 0.04) \times 10^3 \left(-\frac{\Delta\alpha}{\alpha_0}\right) - (3.2 \pm 0.9) \times 10^3 \left(-\frac{\Delta\alpha}{\alpha_0}\right)^2 \quad (31).$$

In eq. (30) and (31), $\omega_{TO}$ and $\omega_{LO}$ are the Raman shift frequencies with the unit of $cm^{-1}$ in which 266.6 and 289.9 $cm^{-1}$ are the corresponding Raman shift frequencies for the relaxed GaAs nanowire (the zero pressure) based on the measurement from I Zardo et al [192].

Th ZB GaAs crystal structure exhibit two peaks at Γ point which are TO and LO phonons (as shown in Figure 2.23). The bond-stretching or compressing or bending interactions, all can be shifted by the strain. In case of uniaxial strain, the splitting and shift of doubly-degenerate-TO phonon lines appear while LO phonon is still single but shifted. This shift due to hydrostatic strain yields a value for the mode-Grüneisen parameter ($\gamma$) which is an empirical parameter based on the hydrostatic pressure measurements [168], [169], [193].

$$\Delta\omega_h = \left(\frac{\sigma}{6\omega_0}\right)(p + 2q)(S_{11} + 2S_{12}) \quad (32).$$

$$\gamma = \frac{-(p + 2q)}{6\omega_0^2} \quad (33).$$

The spring constants in interatomic forces of the atoms can be described by $(p, q, r)$ as phenomenological parameters. The shift of optical phonons under hydrostatic strain ($\Delta\omega_h = (\omega - \omega_0)$) can be calculated by eq. (32) and $\omega_0$ is the strain-free frequency of phonon (TO or LO) at k=0 (Γ point). Considering the definition of Grüneisen parameter in eq. (33), the eq.(32) can be written as

$$\Delta\omega_h = -(\varepsilon_h)\,\gamma\,\omega_0 \quad (34),$$

where $\varepsilon_h$ is hydrostatic strain ($\varepsilon_h = \varepsilon_{xx} + \varepsilon_{yy} + \varepsilon_{zz}$) [65],[168],[169],[193],[194].

Recalling the Figure 2.24, it is shown that by increasing the lattice constant, the phonon energy reduces. In principle, applying the tensile or compressive stress on a certain lattice constant results in the shift of phonon energies to the lower or higher frequency values, respectively [163].

The other remarkable effect of strain is to lift the certain degeneracies in BZ, change the bandgap, band edges as well as the density of states. Effect of isotropic-hydrostatic strain on GaAs band structure in BZ has been plotted using 8x8 k.p method as shown in Figure 2.25 (a). It is shown that tensile (compressive) strain results in the decrease(increase) of GaAs band gap and due to the isotropic character of the strain, the symmetry of the crystal has been preserved. Therefore VB splitting did not occure in the examples of Figure 2.25 (a). The stronger effect of the strain on the reduction of CB edge compare to the VB has been observed because the modeling of the nextnano is based on I Vurgaftman et al [3]. The shift of the VB is in the order of $10^{-4}$ which is not visible in the plot.

Effect of strain anisotropy on band structure of GaAs has been presented in Figure 2.25 (b). Due to the beaking the crystal symmetry in the example of Figure 2.25 (b), VB splitting is observed in the nextnano simulations based on 8×8 k.p method with the assumption of equal in-plane strain ($\varepsilon_{xx} = \varepsilon_{yy}$).

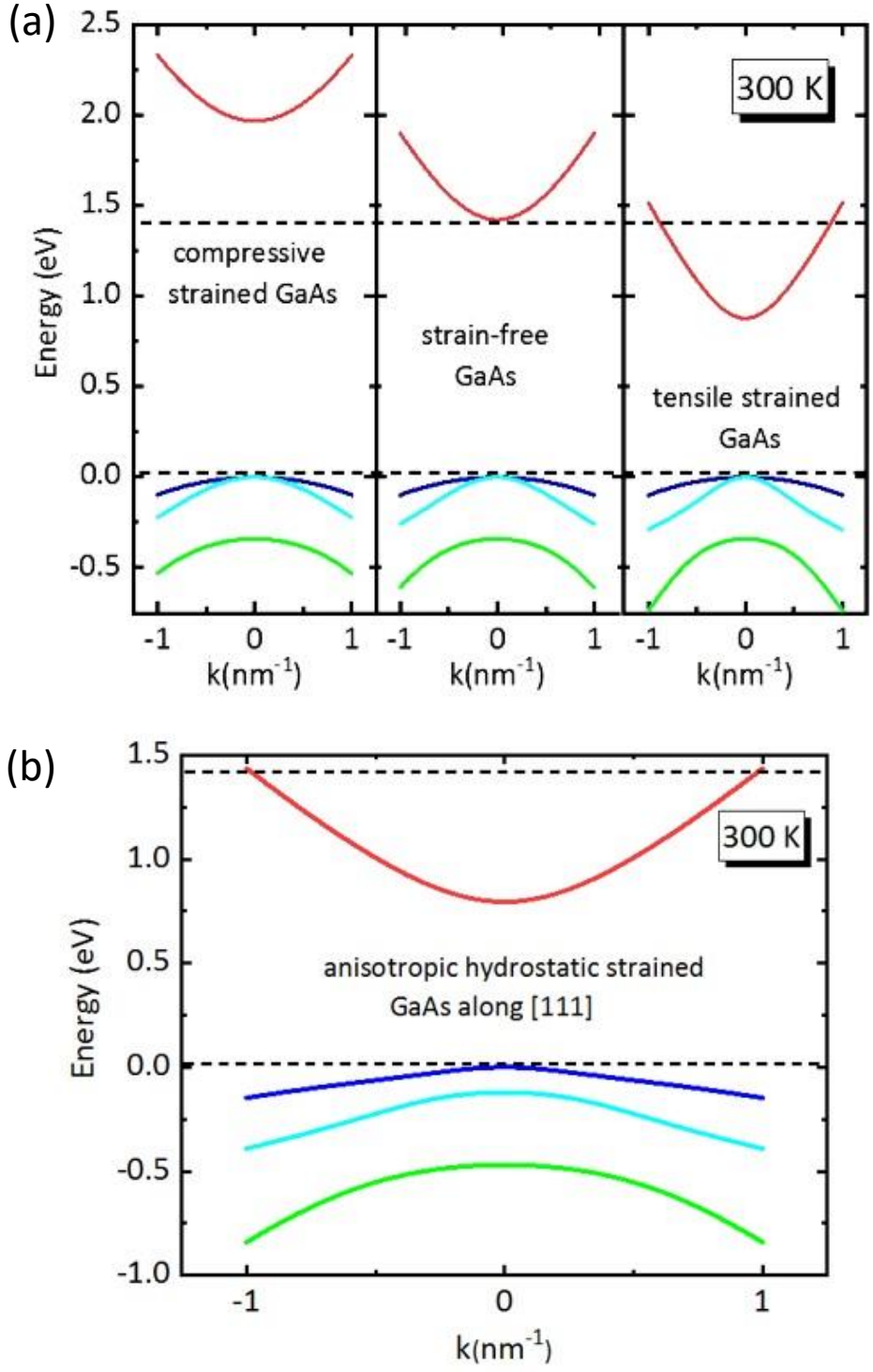


Figure 2.25 The effect of strain on band structures of GaAs (a) Band structures of GaAs at 300 K (by k.p 8x8) along [111] in strain-free state (center) where dashed line shows the minima of VB and CB of it and in compressive strain (left) and tensile strain (right) and both left and right panels with total isotropic-hydrostatic strain of 2.33%. The red, blue, cyan, and green lines are represented for CB, HH, LH, and SO bands, respectively. (b) Band structures of GaAs at 300 K (by k.p 8x8) under anisotropic strain ($\varepsilon_{xx} = \varepsilon_{yy} = 1.23\%$, and $\varepsilon_{zz} = 4.23\%$) where in-plane strain values are assumed to be equal. The red, blue, cyan, and green lines are represented for CB, HH, LH, and SO bands, respectively. Band structure in k-space is along [111].

A theoretical model of Van de Walle and Martin was predicted the band offsets at both lattice-matched and pseudomorphic strained-layer interfaces. Their theory is based on the local-density-functional pseudopotential formalism and the "model-solid approach" [195]. In bulk semiconductors, typically the relative shift of CB with respect to VB is considered which is expressed by the deformation potential. In ZB crystal structures with a direct band gap, the position of the CB and VB edges can be dictated by the hydrostatic component of the strain based on the eq. (34) [195].

$$E_c = E_c^0 + a_c.\varepsilon_h\,, \quad E_v = E_v^0 + a_v.\varepsilon_h \quad \rightarrow \quad E_g = E_g^0 + a.\varepsilon_h \quad (35).$$

In eq. (35), $E_c^0$ or $E_v^0$ are the CB edge or the VB edge of the strain-free material and $a_c$ and $a_v$ are the hydrostatic deformation potentials of CB and VB, respectively. $E_g^0$ is the strain-free bandgap energy of $E_g$. The bandgap deformation potential ($a$) is $a = a_c - a_v$ [3], [195], [196]. The corresponding values for $a_c$= -7.17 and $a_v$ =1.16 are reported by C G Van de Walle et al [195]. For bulk GaAs, $E_g^0$ = 1.52 eV and $a$ ≈ -8.5 eV are reported [3] . There is a difference between different reports concerning to the bandgap deformation potential ($a$). In this thesis, $a$ is based on the report of I Vurgaftman et al [3].

Anisotropic strain along [111] results to additional shift of the VB, which is different for HH and LH and thus lifts the degeneracy at k=0:

$$\Delta E_{v(hh)} = -\frac{1}{2}\delta E_{111} \quad (36),$$

$$\Delta E_{v(lh)} = -\frac{1}{2}\Delta_0 + \frac{1}{4}\delta E_{111} + \frac{1}{2}\left[\Delta_0^2 + \Delta_0\delta E_{111} + \frac{9}{4}(\delta E_{111})^2\right]^{1/2} \quad (37),$$

$$\delta E_{111} = 2\sqrt{3}d\,\frac{\varepsilon_{zz}-\varepsilon_{xx}}{3} \quad (38),$$

where $d$= 4.5 eV is the corresponding deformation potential and $\Delta_0$= 0.34 eV is the spin-orbit splitting energy of bulk GaAs [195].

In 1984, N E Christensen has reported a comprehensive study of the electronic structure of GaAs under hydrostatic and uniaxial strain. Considering the effect of hydrostatic pressure on GaAs, the corresponding effective mass of electrons can be described using the following equations at 300 K:

$$\frac{dE_g}{dP} = 12.02\,\frac{\text{eV}}{\text{Mb}} \quad (39),$$

$$\frac{1}{m_e^*}\frac{dm_e^*}{dP} = 6.8\ \mathrm{Mbar}^{-1} \quad (40),$$

where $dE_g$ is the change of the bandgap induced by a relative change of pressure $dP$ and $m_e^*$ in GaAs core is expected to decrease (increase) with increasing tensile (compressive) strain [197].

In this thesis, the symmetry and type of strain in the GaAs/$In_xGa_{1-x}As$ and GaAs/$In_xAl_{1-x}As$ core/shell nanowires are theoretically and experimentally studied and their effect on optical phonons, band structure, and electron effective mass is evaluated in a systematic way.

## 2.6 Modulation-doped III-V semiconductor heterostructures

$In_xGa_{1-x}As$ is an interesting alloy due to its tunable bandgap in NIR range or telecommunication wavelengths, where depending on its composition the different applications can be realized in photonics or high speed low noise electronics [18], [65]. Due to the high purity of the material grown by MBE, the highest record of mobility (≈ 3.5x10$^7$ cm$^2$/Vs) at ultra-low temperature (300 mK) belongs to the MBE systems for modulation-doped heterostructures of GaAs/AlGaAs including two dimensional electron gas (2DEG) at the interface. This technique allows spatial separation of 2DEG from their parent donor impurities, which results in the remarkable enhancement of the carrier mobility. One of the ways to have a good control of the intentional doping density is to use a delta-doping layer (δ). Si impurities generate n-type doping inside the AlGaAs under a certain growth condition [198], [199], [200].

CB profile and the schematic of 2DEG formation at the interface in the modulation-doped structure of GaAs/AlGaAs on GaAs substrate are illustrated in Figure 2.26 (a) and (b), respectively. The stacks of materials are defined by (1), (2), (3), and (4) as a thin GaAs capping layer to avoid Al oxidation, un-doped AlGaAs layer, a spacer layer of undoped AlGaAs, and GaAs substrate, respectively. The δ-Si inside AlGaAs is formed after a certain undoped layer so-called spacer. The spacer is responsible for the spatial separation of free electrons at 2D interface or 2DEG from the corresponding ions, that results in lowering the free electron scattering and consequently boosting the mobility [198], [199], [200].

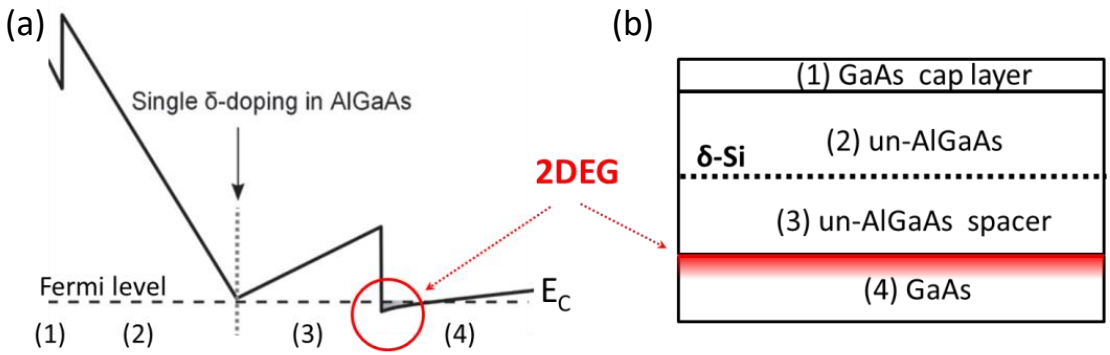


Figure 2.26 Introduction to 2DEG (a) Traditional GaAs/AlGaAs modulation-doped heterostructure including 2DEG at the interface. Reprinted with permission from [198]. Copyright 2013 Elsevier, and (b) the related CB diagram which is adapted from.

In fact, finding a good compromise between the four factors such as doping level, spacer, carrier concentration and mobility in order to obtain the high device performance is very crucial. Increasing the carrier concentration or doping level degrades the carrier mobility and decreasing the spacer thickness enhances the carrier scattering due to the higher interactions between 2DEG and the ions that resulting degradation of the carrier mobility as well [198], [199], [200].

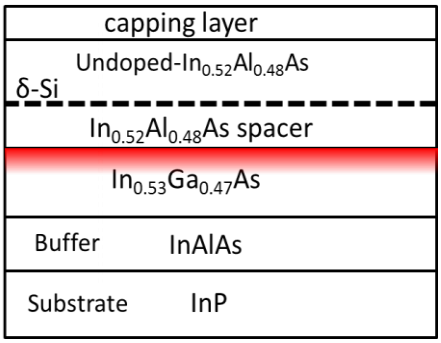


Figure 2.27 Traditional InGaAs-HEMT/InP. The red line shows the location of generated 2DEG at the interface between InGaAs and InAlAs (inside the InGaAs side).

After the discovery of quantum Hall effect, the observation of fractional quantum Hall effect based on 2DEG systems was recorded. The lattice-matched GaAs/AlGaAs heterostructure has perhaps the most perfect crystalline interface that has been grown so far. AlGaAs with its higher band gap energy enables the excellent surface passivation of GaAs. After the discovery of quantum Hall effect, the observation of fractional quantum Hall effect based on 2DEG systems was recorded, which opened a new unexpected field in quantum computing technology and devices. The first HEMT based on GaAs/AlGaAs in a commercial level originates from Fujitsu in 1983 operating at 20 GHz with low noise characteristics and later lots of progresses took place

for different applications like low noise transistors for communicational systems (e.g. WLAN). Alongside the rapid development of GaAs-HEMT technology, other material systems based on modulation-doping technique including 2D hole gas or electron gas or both have been introduced. Among those material combinations, InGaAs-based HEMTs on InP wafers showed a unique high mobility (≈ $10^4$ $cm^2$/Vs) at room temperature. One of the common structures for InGaAs-HEMTs is depicted in the Figure 2.27. InGaAs is one of the favorable materials for high speed n-type transistors due to its low electron effective mass compare to GaAs. The advantages of InGaAs based transistors such as its lower thermal budget process, high electron mobility, lower electron effective mass, impressive cut-off frequencies make this material attractive to be used as a channel in n-type transistors, especially for high frequency applications. Traditionally, to achieve HEMTs in planar systems, $In_xGa_{1-x}As$ is grown epitaxially on lattice-matched InP substrates with a high cost and the limited composition (x) in around 0.53. Undoubtedly, except of x≈ 0.53, there are large unavailable band gaps between two endpoints binaries, GaAs and InAs, due to the lack of lattice-matched substrates related to thin film growth arena [11], [12], [13], [121], [198], [199], [201] , [202], [203], [204], [205], [206].

The idea of 2DEG systems can be tested in core/shell nanowire structures. If nanowires are combined with modulation doping new perspectives in nanoelectronics seem to be achieved. D Lucot et al presented modulation doped GaAs/AlGaAs core/shell nanowires embedded in an insulating GaAs overlayer. They measured the conductance of nanowires showing a non-ohmic behavior as a function of temperature and the differential conductance dependence to volatge-bias. Their findings indicate the potential of nanowires for quasi 1D-transport systems [203]. S Funk et al demonstrated 1DEG and 2DEG in modulation doped core/multishell nanowires by spatially resolved resonant inelastic light scattering and PL measurements. They observed that the electronic properties are not uniform along the single nanowires and high mobility electron gases are only recorded in specific segments along the single nanowire axis . J Boland et al using THz spectroscopy proved the electron mobility of about 2200 $cm^2$/Vs (at 300 K) inside the modulation doped GaAs/AlGaAs core/shell nanowires with Si delta-doped layer The mobility value was almost the same as the undoped nanowire measurements. S Morkötter et al demonstrated the formation of 2DEG resulting the enhancemnets of the electron mobility in the Si delta-doped GaAs/AlGaAs core/shell nanowire based FETs. The report of Tomioka et al can be counted as the state-of-the-art related to the modulation doped InGaAs/InP/InAlAs/InGaAs core/multishell nanowires with the InGaAs as a channel. They fabricated for the first time the vertical transistors with the gate-all-around based on SAG

nanowires and proved high-electron-mobility transistor structure with increased the on-state current and transconductance while keeping good gate controllability.

In this thesis, a complex material combination based on GaAs/InGaAs/InAlAs/InGaAs core/multishell nanowires for the potential application of HEMTs is investigated by using nextnano software (see chapter 4.6).

# 3 Methods

This chapter is dedicated to the description of the instrumentations and methods used, of the measurements performed and the corresponding fundamentals.

## 3.1 Optical and electron microscopes

The bright-field mode of the light microscopy is the simplest microscopy. In this mode, the illumination light is transmitted through the material and the resulted contrast is due to the absorption of light in dense areas of the sample. The limitations of the bright-field optical microscopy are the low contrast for weakly absorbing samples and low resolution. In bright-field mode (as shown Figure 3.1 (a), left), majority of the light from the condenser lens go through the objective lens after interacting with the object to participate in a formation of an image. This mode generally results in an image with a bright background, so-called bright-field microscopy. The condensing system for the illumination of dark-field mode (as shown Figure 3.1 (a), right) utilizes a central circular disk to bock direct rays from entering the objective lens. Only those rays that have been suitably scattered by the object pass the objective lens to form the final image. Due to the weak and higher angular diffracted rays, the dark background is observed, so-called dark-field microscopy. The dark-field mode generates a higher contrast in imaging than the bright-field mode. Dark-field mode of the optical microscopy can be useful in understanding photonics and plasmonics in nanostructure e.g. nanowires. Therefore, exploiting the certain advantages of dark-field optical microscopy, the diameter determination along a single semiconductor nanowire and shape effects in plasmon resonances over single silver nanoparticles were reported by G Brönstrup et al [207] and J J Mock et al [208], respectively. The similar configuration exists in the transmission electron microscopy, in which the directly transmitted beam is omitted. Dark-field mode of transmission electron microscopy can be implemented in characterizing the size and morphology of the sample and the crystal lattice.

Negatively charged sub-atomic particles are called electrons with a wavelength, which is dictated by the de Broglie wavelength. Electron microscopy (EM) is a great system enabling us to image a sample in a higher resolution than a general light microscope and exploring the detailed morphology of the sample for an example. There are many advanced types of EMs but the two major types of EM are scanning-EM (SEM) and transmission-EM (TEM). Both types of these EMs have an electron gun containing an electron source (a filament that produces a cloud of electrons) with an anode (to accelerate the e (electron)-beam). Both SEM and TEM are consisted of electromagnetic lenses and apertures to control the focus of the e-beam and the coherence/convergence of it, respectively. Apertures affect the resolution and the amount of

contrast in the signal. In a SEM, e-beam is guided through different lenses and apertures (as shown in a simplified picture in Figure 3.1 (b)), and at the end reaches to the surface of the sample. An SEM image is formed from the signals originating from e-beam that gets scattered or reflected from the sample and later gets captured by the detectors. The interaction volume of e-beam with the sample is shown in Figure 3.2 (a) and its size depends on the applied high voltage. The SEM images are created based on the secondary electrons (SE) and back-scattered electrons (BSE). The detection of the other types of signals like X-ray and auger electrons and photons needs different detectors or additional systems. The resolution of the SEM image is determined by the spot size of the beam as it hits to the sample. Working distance (as shown in Figure 3.1 (b)) adjustments will be helpful to increase or decrease the spot size on the sample. Decreasing the working distance allow us to detect significantly SE or BSE signals, meaning enhancing the contrast quality of the image. Additionally, the angle of the specimen (in where the sample is mounted) plays an important role for the quality of the image of nanostructures. SE detector or In-lens detector can be used for the imaging, depending on the angle of the specimen. In case that e-beam is perpendicular to the sample meaning 0 angle of the specimen, In-lens detector results in a better-quality image compare to SE detector because it is located inside the same path for e-beam of the source. For the nanowire to have a good image, often the In-lens detector was employed with the lowest possible working distance. To suppress the charging effect of the very thin nanowires, a very small aperture size was selected to reduce the current.

TEM is a fantastic tool, as the name indicates; signals such as the transmitted electrons by passing through a thin sample (in the range of 70 nm) are collected onto a screen or camera/detector which will provide us information on the inner structure of the sample in an atomic scale (see Figure 3.2 (b)). The spatial resolution and accelerating voltage of TEM due to its complex system (e.g. a large amount of the lenses) is higher than SEM. Energy-dispersive X-ray spectroscopy (EDXS) allow us to explore the elemental/compositional mapping of the sample. Another new version of microscopy in the current technology is Helium ion microscope (HIM), in which instead of the e-beam, He ion replaced. He ion beam is much narrower compare to e-beam that results in a smaller volume interaction and consequently a better resolution compares to SEM. TEM or HR-TEM (high resolution-TEM), TEM/EDX measurements for the exploration of the crystal structure, compositional mapping, and crystal quality have been accomplished by Dr. R Hübner and the He-ion beam alignment of the HIM has been performed by Dr. G Hlawacek.

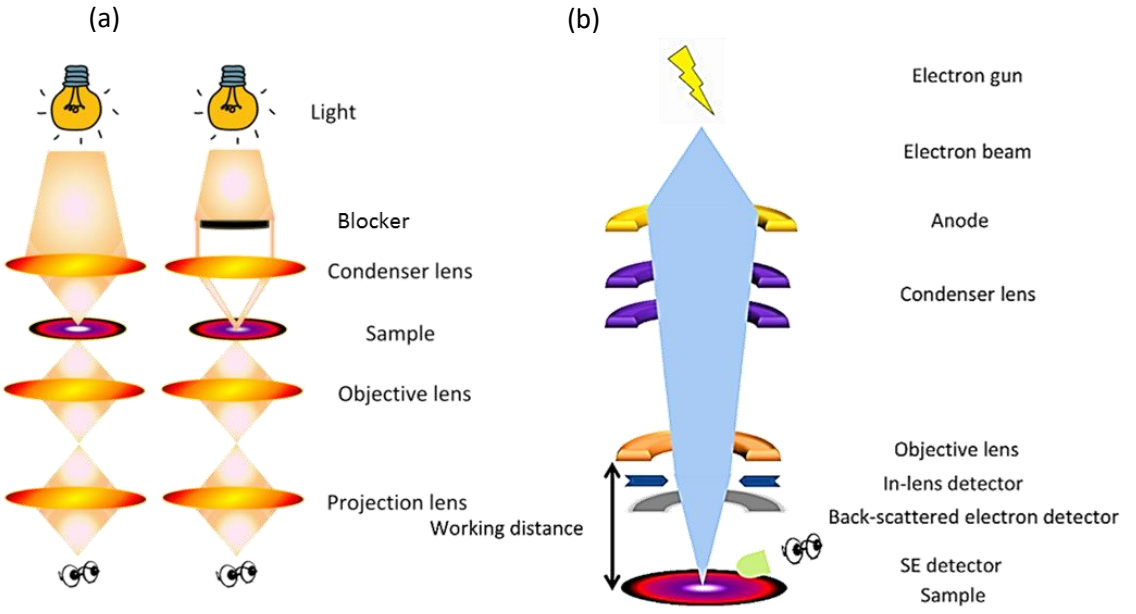


Figure 3.1 Light and electron microscopy (a) bright field (left) and dark (right) mode, (b) a simplified sketch of SEM system.

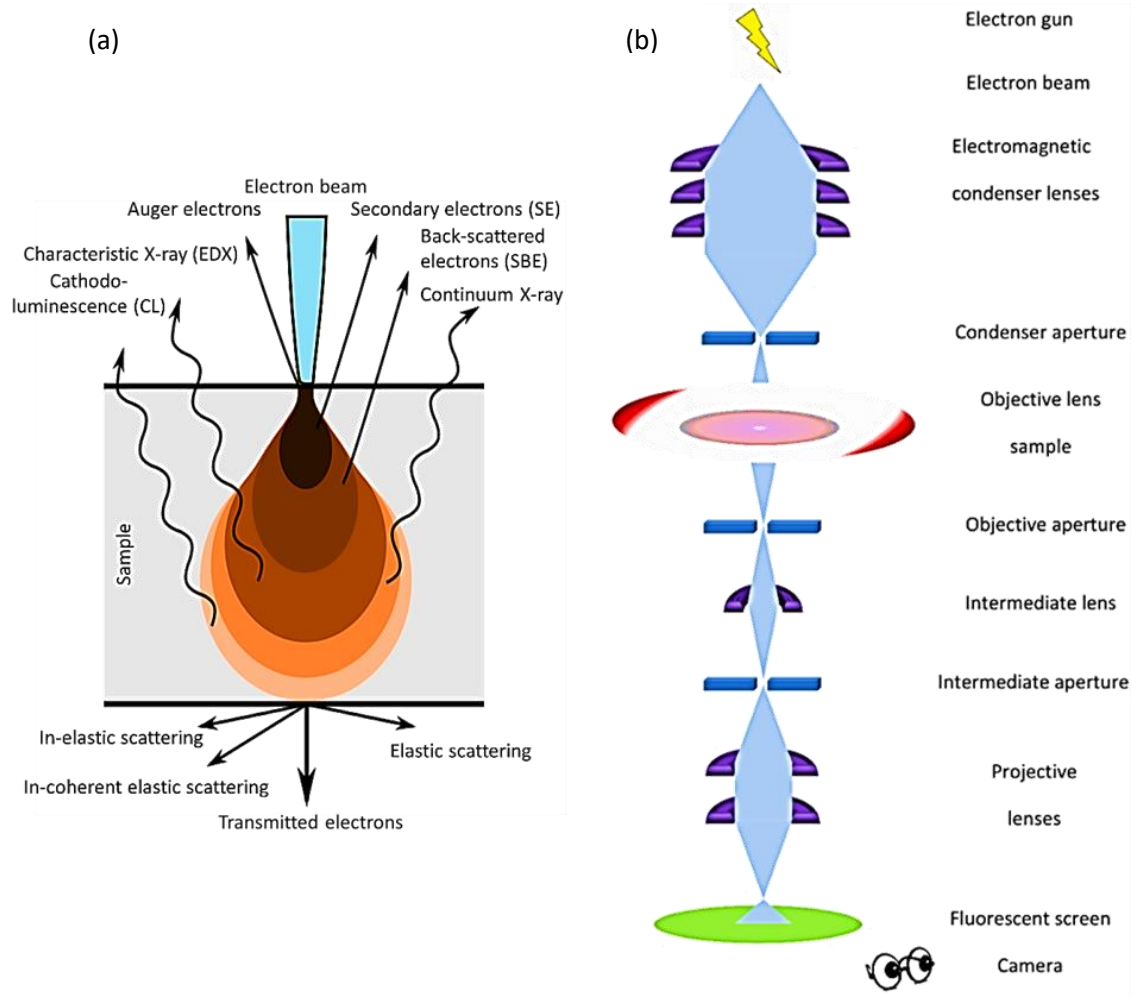


Figure 3.2 (a) Volume interactions of a sample with e-beam resulting different reflected or transmitted signals for variant purposes (www.AZO.com), (b) a simple sketch of TEM system.

## 3.2 X-ray diffraction

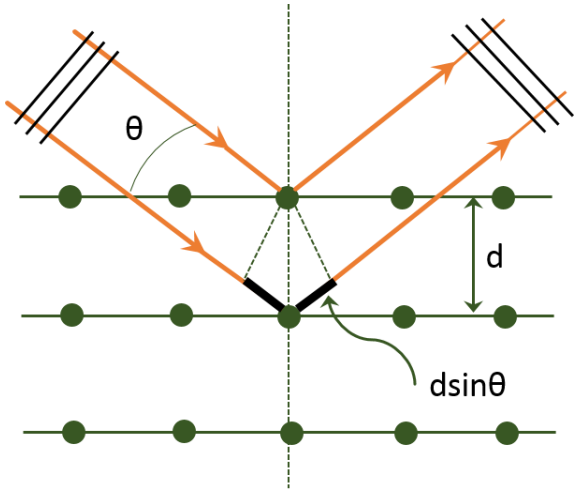


Figure 3.3 Schematic representation of Bragg diffractions

X-ray diffraction (XRD) is a powerful nondestructive technique utilized for identifying the atomic structures of a crystal in which the layers of the atoms generates the diffraction of the incident X-rays. By XRD, the average spacing between atomic layers can be measured. Various information e.g. the crystal structure, phase, lattice constant or parameter, shape, strain, crystallographic disorder etc. can be determined through the recorded diffraction pattern as a reciprocal space map. The Bragg's law, $n\lambda=2d\sin\theta$, reveals the average of atomic layer distances (d) depending on the miller indices. Basically, θ varies to satisfy the Bragg's law by the constructive interference as shown as a simple sketch in Figure 3.3. θ and n are the angle of X-ray incidence and integer, respectively [209]. The lattice-constant ($a_0$) is calculated by $a_0= d_{hkl}/(h^2+k^2+l^2)^{½}$. High resolution XRD (HR-XRD) is possible by so-called synchrotron light source. A synchrotron is a giant device for acceleration of a particle through bent magnets in a circular shape. The synchrotron light source is about $10^8$ times brighter than the normal XRD source. Tunable X-ray wavelength via synchrotron light source allows the right energies interact with atoms, resulting in higher quality mapping of the diffraction in the reciprocal space. GID or Grazing incidence diffraction through the synchrotron light source was been employed in this work. Incoming X-ray beam in GID has a very narrow angle which makes it suitable to explore the surfaces of the materials. For the nanowires, this technique makes the measurement of the in-plane lattice constants possible.

In this work, the normal XRD, HR-XRD and GID experiments have been performed by Dr. J Grenzer at HZDR (Germany) and Diamond Light Source in Didcot (UK), and Dr. G Bussone,

together with Dr. R Grifone at beamline P08, at the PETRA III synchrotron in Hamburg, DESY, (Germany), and at beamline I07, at the Diamond Light Source in Didcot (UK).

### 3.3 Raman scattering spectroscopy

Raman spectroscopy is a spectroscopic tool utilized to probe vibrational, rotational, and other states in a molecular system. Raman spectroscopy provides useful information on characteristic properties of thin crystalline films of compound semiconductors such as crystal orientation, carrier concentration, scattering times of charge carriers, composition of mixed crystals and depth profiles. There are two important features of Raman scattering spectroscopy which makes it a more powerful tool in the sample characterization (especially when other tools fail in terms of characterization): i) Lattice vibrational spectra of different layers are recorded as a superposition of the spectra of each layer. Thus, it is possible to analyze individual layers in a nondestructive way by using different lasers with different penetration depths. ii) Lattice vibrations are very sensitive to the nearest neighborhood and thus one can probe the crystal structure and quality on an extremely small scale, a scale which is of the order of the lattice spacing [210], [211].

In 1905, Albert Einstein (1879–1955) presented his revolutionary hypothesis of light quanta, which in succeeding years was addressed by physicists with a high skepticism. Max Planck (1858–1947) said ‘‘a speculation that missed the target’’ and Robert A. Millikan (1868–1953) said ‘‘it was a bold, not to say reckless hypothesis.’’ It was getting accepted only after 1923, when Arthur Holly Compton (1892–1962) discovered the Compton effect, the change in wavelength of an X-ray quantum when striking a free electron in a substance such as carbon in a billiard-ball collision process. After Compton’s discovery, the Indian physicist Chandrasekhara Venkata Raman (1888–1970) and his student Kariamanikam Srinivasa Krishnan (1898–1961) discovered a novel effect that involves a change in wavelength of scattered monochromatic visible light. The American physicist Robert Williams Wood (1868–1955), who was very well-known for his work in experimental optics, acknowledged the discovery of Raman effect with the words: ‘‘It appears to me that this very beautiful discovery, which resulted from Raman’s long and patient study of phenomena of light scattering, is one of the most convincing proofs of the quantum theory of light which we have at the present time.’’ Because at the time of discovery of Raman and even three decades afterwards, lasers were not available, Raman and Krishnan used a mercury lamp and photographic plates to record spectra. Those early spectra had a long measurement time of hours and even days in order to obtain a very weak Raman scattering from most of materials due to very low sensitivity of the detector as well as weak light sources. Later, modern Raman spectroscopy involves the use of lasers as an exciting light

source and powerful detectors such as charge-coupled devices (CCDs) with photodiode arrays, and photomultiplier tubes [212], [213], [214].

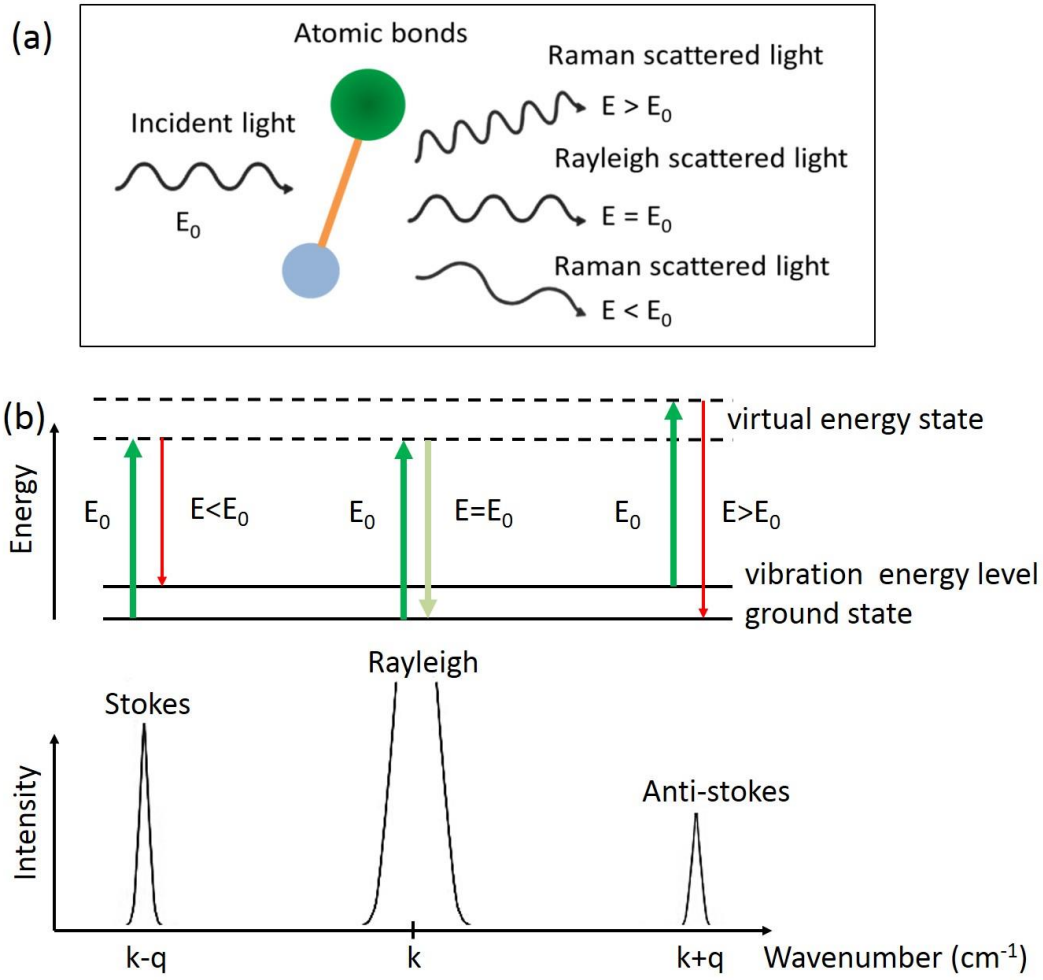


Figure 3.4 Raman scattering (a) A simple sketch for different inelastic Raman scattering signals and elastic scattering signals after excitation of an atomic bond, Rayleigh scattering (no exchange of energy: incident and scattered photons have the same energy), Stokes Raman scattering (atomic bonds absorb energy: scattered photons have less energy than incident photons) and anti-Stokes Raman scattering (atomic bonds lose energy: scattered photons have more energy than incident photons), (b) Energy states in Raman spectroscopy in upper plot, the corresponding Raman spectrum in the lower plot involving two arbitrary examples for the stokes , anti-stoke signals that placed in left and right hand side of the laser line. Typically, laser line is called zero line (k=0 $cm^{-1}$) and the stokes and anti-stokes are shown with negative and positive sign of wavenumbers, respectively.

After illumination of the laser light to a material, the light is scattered by the atoms or molecules of the material. The significant amount of the scattered frequencies has the same frequencies of the incident laser beam (Rayleigh scattered light) but only the small fraction of light has different frequencies (inelastic scattering) which are called Raman scattering. In

principle, these different frequencies originate from the interaction of the laser light and the polarization with the molecular or atomic bonds vibrations (see Figure 3.4 (a)). Such a frequency modulation is specific to molecular vibrations or phonons in crystals allowing study of the composition or lattice constant analyses [215]. Raman scattering involves a virtual electronic energy level which is corresponding to the energy of the laser excitation. Absorption of a photon ($E_0$) excites the atomic bonds to the imaginary state and re-emission leads to Raman or Rayleigh scattering. In all these three types, the final state has the same electronic energy as the starting state but is higher in vibrational energy in the case of Stokes Raman scattering, lower in the case of anti-Stokes Raman scattering or the same in the case of Rayleigh scattering (see Figure 3.4 (b)) [214], [215]. During the light scattering event, a quasi-particle like for example a phonon, plasmon, or magnon is created or annihilated, respectively. In a quantum mechanical perspective, Raman scattering is explained as: (i) a photon impinging on a semiconductor crystal generates an electron-hole pair, (ii) the electron is scattered by one phonon and loses fraction of its energy to the phonon, and (iii) the electron recombines and a Raman scattered photon is emitted [216], [217]

In this scattering process, the energy and the momentum are conserved:

$$\omega_s = \omega_i \pm \omega_p \quad , \quad \vec{k}_s = \vec{k}_i \pm \vec{q}_p \qquad (41).$$

Here, $\omega_{s,i}$ , and $\vec{k}_{s,i}$ are the frequencies and wave vectors of the scattered and incident light, and $\omega_p$ and $\vec{q}_p$ are the frequency and wave vector of so-called quasi-particles. When the momentum of light in the visible range is relatively small with respect to the size of the BZ, scattering mainly happens close to the center of the BZ, and the phonons participating in the scattering process are long wavelength phonons with $q \approx 0$. Raman scattering originates due to the change of the polarizability of a molecular vibration resulting in a dipole emission of light with a frequency different from the frequency of the incident light [216].

The short-range interaction between optical phonons and electronic states is due to the deformation which accompanies the phonons. The deformation potential causes the dipole-allowed Raman scattering by optical phonons which follows the usual Raman tensor selection rules. In addition to the deformation, $q \approx 0$ the LO-phonon is accompanied by a macroscopic electric field which yields the Fröhlich interaction in Raman scattering. There is a short-range part of the Fröhlich interaction which contributes to the dipole-allowed Raman scattering by LO-phonons. The long-range q-dependent contribution of the Fröhlich interaction accounts for the dipole-forbidden Raman scattering by LO phonons, which is seen close to the resonance for polarizations of the incident and scattered light parallel to each other. It is worth to mention

that the resonant Raman scattering is observed when the energy of the incident light lies in the vicinity of an interband critical point in the joint density of states of the semiconductor [217], [218].

The intensity of the Raman scattered radiation is proportional with the polarization induced by a phonon in the crystal [219], [217]. The Raman scattered intensity can be related to

$$I_s \propto |\hat{e}_i . R . \hat{e}_s|^2 \qquad (42).$$

In the relation (42), $\hat{e}_{i,s}$ are the polarization direction of the incident ($i$) and scattered ($s$) light, respectively. For ZB GaAs, the Raman tensors are introduced by

$$R(X) = \begin{pmatrix} 0 & 0 & 0 \\ 0 & 0 & d_1 \\ 0 & d_1 & 0 \end{pmatrix} , R(Y) = \begin{pmatrix} 0 & 0 & d_1 \\ 0 & 0 & 0 \\ d_1 & 0 & 0 \end{pmatrix} , R(Z) = \begin{pmatrix} 0 & d_1 & 0 \\ d_1 & 0 & 0 \\ 0 & 0 & 0 \end{pmatrix} \quad (43).$$

The coordinates of crystals X, Y, and Z are shown by [100],[010], and [001], respectively [217], [218]. These Raman tensors are related to the deformation potential scattering and the allowed Fröhlich scattering. In the case of the forbidden Fröhlich interaction, the Raman scattering follows new selection rules according to the diagonal Raman tensor as shown below

$$R_{Forbidden-Fröhlich} = \begin{pmatrix} d_2 & 0 & 0 \\ 0 & d_2 & 0 \\ 0 & 0 & d_2 \end{pmatrix} \qquad (44),$$

in which, the scattering is only possible when it is polarized parallel to the incident light meaning $\hat{e}_i \parallel \hat{e}_s$ [217], [218]. The Raman tensor of the WZ phase can be found in these references [219],[220], [221].

Table 2: Allowed Raman modes in ZB and WZ phases of GaAs nanowires

| structure | configuration | allowed modes |
|---|---|---|
| ZB | $\mathrm{x}(-,-)\bar{\mathrm{x}}$ | TO |
| WZ | $\mathrm{x}(\mathrm{y},\mathrm{y})\bar{\mathrm{x}}$ | $\mathrm{E}_2^{\mathrm{h}}, \mathrm{A}_1$ (TO) |
| | $\mathrm{x}(\mathrm{y},\mathrm{z})\bar{\mathrm{x}}$ | $\mathrm{E}_1$ (TO) |
| | $\mathrm{x}(\mathrm{z},\mathrm{z})\bar{\mathrm{x}}$ | $\mathrm{A}_1$ (TO) |

The backscattering configuration from ZB nanowires is shown in Figure 3.5. In case of WZ, the [111] orientation of the crystal lattice along Z axis should be replace by [0001] in the configuration of this figure. The allowed modes for this kind of configuration are brought in Table 2. The porto notation $\hat{k}_i(\hat{e}_i, \hat{e}_s)\hat{k}_s$ is applied in this configuration, where $\hat{k}_{i,s}$ are the directions of the incident and scattered photons. and $\hat{e}_{i,s}$ are the polarizations of the incident and scattered photons. In ZB phase of a GaAs nanowire, the backscattered photon from the $\{110\}$ facet is only allowed for TO phonons. While in the similar situation for WZ phase, the $\mathrm{E}_2^{\mathrm{h}}, \mathrm{A}_1\ (\mathrm{TO})$, and $\mathrm{E}_1\ (\mathrm{TO})$ modes are allowed [216],[217],[219],[221].

A simplified sketch of commercial LabRAM Raman setup is shown in Figure 3.5. The Raman system is a fully integrated confocal Raman microscope instrument which is very useful for nanoscale analyses. The optical path commutations can be motorized and controlled by computer (lasers, multichannel detectors, gratings etc.). Such systems with many options and accessories are available to permit different micro and macro measurements, mapping, and temperature dependent measurements and analyses. The system can be used as a powerful characterization tool in the range from visible (400 nm) to near infrared (2200 nm). The Figure 3.5 shows the optical path of the laser and different optical components and the scattered Raman signal from a sample (the red line). The laser is mounted on the back of the instrument and it is a vertical polarized excitation of 532 nm. The laser light (the green line) is directed by extra mirrors (not shown in the sketch) in order to go through the laser absorption filters so-called 6- or 9- (neutral density) filter wheel driven by the Raman software. This filter wheel reduces the intensity of the laser light with different optical densities (100%, 50%, 25%, 10%, 5%, 3%, 1%, 0.1%, 0.01%). Then the laser is focused by lens 1 on the mirror 1. The lens and mirror are guided the laser beam into a pinhole which suppresses the extra intensity scattering of laser and makes the beam narrower. Later, beam passes through a notch filter (edge filter) with a specific angle in order to completely reflected toward the sample by passing the lens 2. This filter is utilized to purify the plasma lines of the laser and is necessary and different for every laser excitation. The lens 2 provides a parallel beam that is focused onto the sample by the infinite-optics microscope objectives. The camera can be coupled in this optical path where one can see the backscattered laser beam as well as the sample with different resolution of the microscope objectives. The Raman beam reflects toward the notch or edge filter (the back-scattering configuration). The Raman signal after hitting the mirror 3, can be analyzed by an optical tool so-called analyzer in order to study the polarization of the Raman signal. Afterwards, Raman signal through different optics Lens 3 and 4 is collected and guided into the entrance slit of the spectrograph. The optical path inside the spectrograph is very simplified in this sketch.

Mirror 4 for an example reflects the Raman signal toward the grating and CCD detector. The type of the grating and detector depends on the range of the extracted Raman frequency.

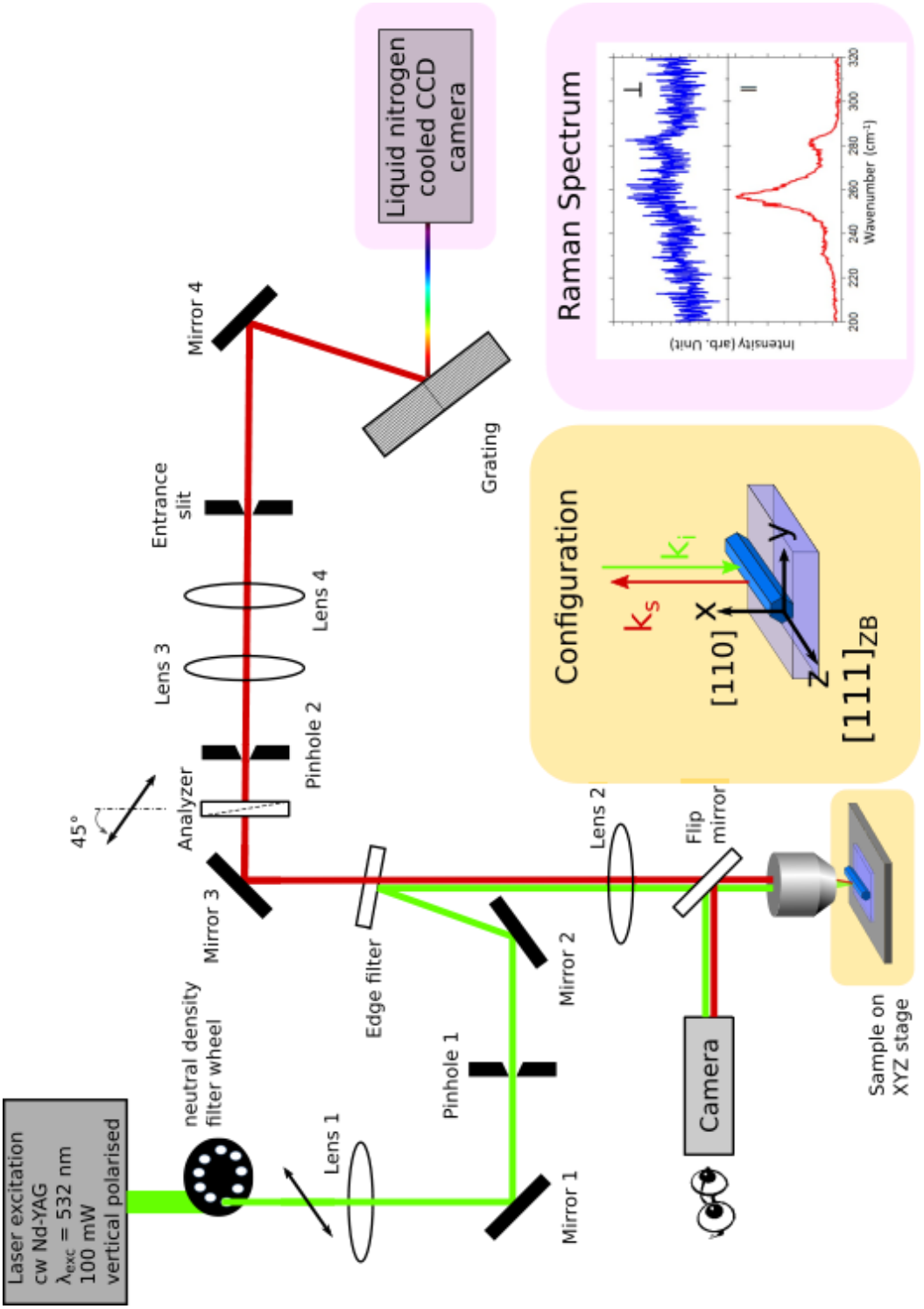


Figure 3.5 A simple sketch for Raman spectroscopy setup.

Two Raman spectra of a single GaAs/$In_{0.20}Ga_{0.80}As$ core/shell nanowire with 25 nm core diameter and 40 nm shell thickness are displayed in the Figure 3.5. The intensity enhancement

of Raman signal when the incident laser light is polarized to nanowire axis, is well-known for optical antenna effect [219], [222]. This effect is more visible in the example of the Raman spectrum shown in Figure 3.5 where the upper (lower) panel corresponds to scattered Raman signal for the laser polarization perpendicular (parallel) to nanowire growth axis. G. Chen et al reported for GaP nanowires that, for the small diameters below 65 nm, nanowires act nearly like a perfect dipole antenna where the bulk selection rules dictates the polarized scattering intensity of nanowires [222].

In Raman scattering spectroscopy, the tensile(compressive) strain is characterized by a shift toward lower(higher) wavenumbers since the strain affects the lattice parameter and consequently the lattice vibrations [65], [219]. In this thesis, to measure the strain in core/shell nanowires, extensive micro-Raman measurements in back-scattering configuration of $\bar{\mathrm{x}}\,(\mathrm{z},-)\mathrm{x}$ have been carried out, where the nanowires were previously transferred on an Au-coated Si substrate. All the Raman experiments have been conducted at room temperature, by a LabRAM spectrometer (already described as a simple sketch in Figure 3.5) equipped with a holographic 1800 lines $mm^{-1}$ grating and liquid nitrogen cooled CCD detector. The laser power was set to around 0.08 mW with 100X objective (0.9 NA) and the laser spot size was about 800 nm. To avoid any background Raman signal from the substrate, nanowires were transferred (by mechanical rubbing) on wafers coated with 150 nm of Au. These wafers can also reduce the heating of nanowires during laser excitation by an efficient heat dissipation through Au. Both the laser power and the integration time have been selected in a way to prevent any downshift of the phonon modes due to the laser heating.

Figure 3.6 shows representative Raman spectra from a single GaAs/$In_xGa_{1-x}As$ (x=0.45 and shell thickness ($L_S$)= 40 nm) core/shell nanowire for four different polarization configurations (based on the defined configuration shown in Figure 3.5). Due to the selection rules for ZB GaAs in the specific measurement configuration as shown in Figure 3.5, the TO phonon modes related to GaAs are stronger for $x(z,z)\bar{x}$ and much weaker or even vanished for the rest of configurations. Furthermore, the $E_2^H$ mode related to WZ GaAs is not observed [193].

In Figure 3.7, the upper panel shows the Raman spectrum for an unstrained GaAs nanowire (with a diameter of ≈22 nm) with its corresponding TO and very weak LO phonon modes at 268.6 $cm^{-1}$ and 283 $cm^{-1}$ (± 1.5 $cm^{-1}$), respectively. The difference of LO phonon of GaAs nanowires (at 283 $cm^{-1}$) and GaAs bulk (at 291 $cm^{-1}$) can be due to the thin width of the core diameter where the surface oxidation of nanowires becomes more critical. Quantum confinement effect can cause the shift of the phonons to the lower wavenumbers. The surface oxide for the case of thin

nanowires can affect the Raman peaks due to its roughness which causes a shift by breaking the selection rules. Another reason for the shift of Raman peaks toward lower energies is the laser heating which is avoided in the measurements of this study [223].

The Raman spectrum in the lower panel of Figure 3.7 was acquired from a GaAs/$In_{0.20}Ga_{0.80}As$ core/shell nanowire with 40 nm shell thickness. The raw data of Raman spectrum for the single GaAs/$In_{0.20}Ga_{0.80}As$ nanowire is plotted with the black color. Using Lorentzian curves for the fitting of the line shape, three scattering contributions were identified: scattering in the core from GaAs TO phonons and scattering in the shell from GaAs-like and InAs-like TO phonons. The accumulative fitting curve is shown with green color. Compared to strain-free bare GaAs nanowires, the GaAs TO phonon energy of the core (blue curve) in the GaAs/$In_{0.20}Ga_{0.80}As$ core/shell nanowire shows a clear shift toward lower wavenumbers (≈ 10 $cm^{-1}$) manifesting a highly tensile strained core. The remaining peaks (red curves) correspond to scattering in the shell with GaAs-like TO, InAs-like TO and GaAs-like LO phonons, which are located at 264.5 $cm^{-1}$, 233 $cm^{-1}$, and 280.5 $cm^{-1}$ (± 1.5 $cm^{-1}$), respectively. The comparison of the GaAs-like TO with its corresponding relaxed value (vertical red dashed line at 263 $cm^{-1}$ [168]) exhibits a small shift to higher wavenumbers due to the small compressive strain in the $In_{0.20}Ga_{0.80}As$ shell. The relaxed peak positions of $In_xGa_{1-x}As$ can be extracted from the Figure 3.8 based on the report of J Groenen et al [168].

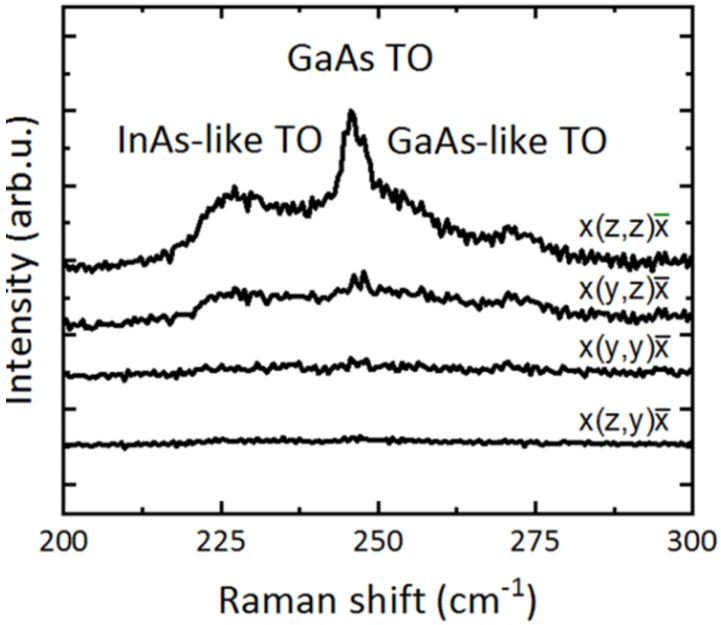


Figure 3.6 Raman spectra from a GaAs/$In_xGa_{1-x}As$ nanowire (with x=0.45 and $L_s$=40 nm) for the 4 main polarization configurations at 300 K. The Raman spectra have been shifted vertically for the sake of clarity.

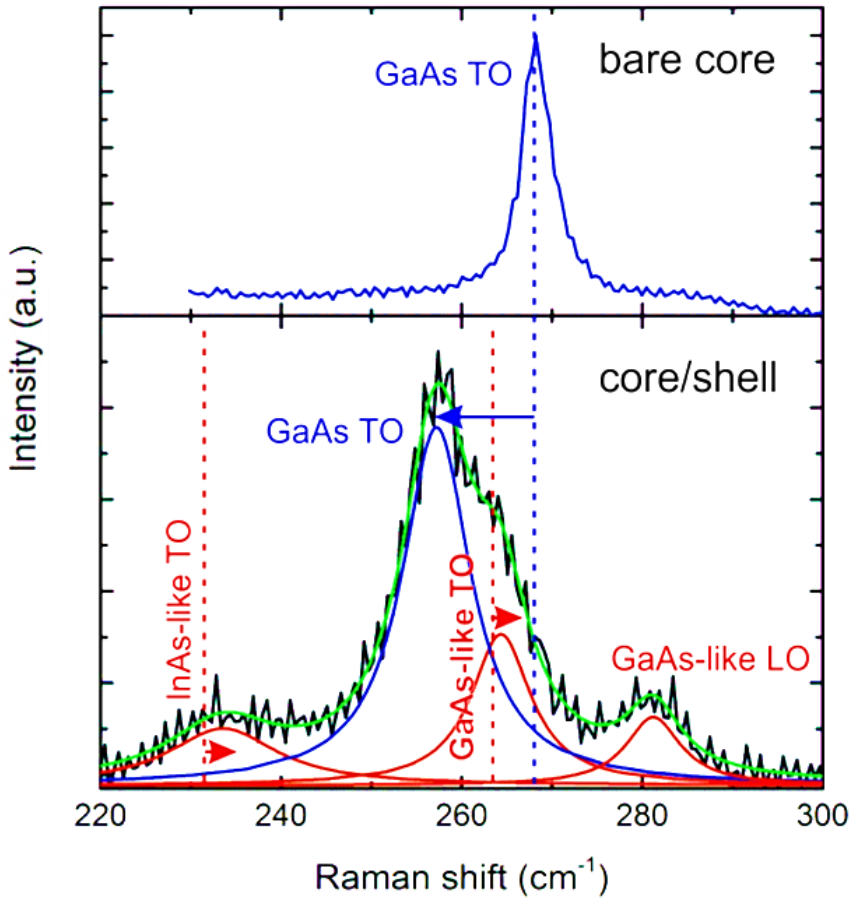


Figure 3.7 An example of Raman spectrum of bare GaAs nanowire (in the upper panel) together with a single GaAs/$In_{0.20}Ga_{0.80}As$ core/shell nanowire (core diameter of 22 nm and $L_s$= 40 nm) are displayed.

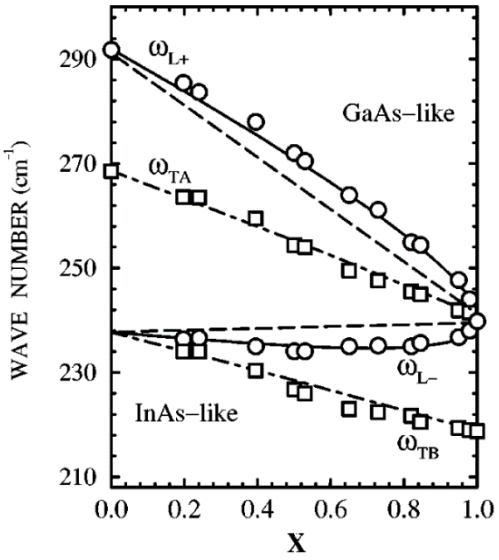


Figure 3.8 Dependencies of LO (circles) and TO (squares) frequencies on the In-content (X) for strain-free InGaAs. The solid lines are calculated LO values: $\omega_{L,+}$ and $\omega_{L,-}$ are extracted from the equation shown in the reference [168]. The dot-dashed lines are the calculated TO values: $\omega_{T,A}$ and $\omega_{T,B}$ are extracted from the linear interpolation between x=0 and 1. For more detailed understanding of this figure please refer to the corresponding reference [168]. Reprinted with permission from [168]. Copyright 1998 by the American Physical Society.

To confirm that the removal of nanowires from the as-grown substrate does not affect the strain state of the nanowires, Raman measurements were performed (see Figure 3.9), in two different configurations: (a) on transferred nanowires, and (b) on as-grown nanowires from the $(1\bar{1}0)$ side. For this purpose, GaAs/$In_{0.20}Ga_{0.80}As$ core/shell nanowires with $L_S$= 40 nm and core diameter of 22 nm were measured. The corresponding optical microscopy images and Raman spectra are shown in Figure 3.9 (a), (b). Comparison of Raman spectra in (a) and (b) does not show any significant difference in the peak positions. Thus, it is shown that the transfer of the nanowires from their original substrate does not affect their strain state.

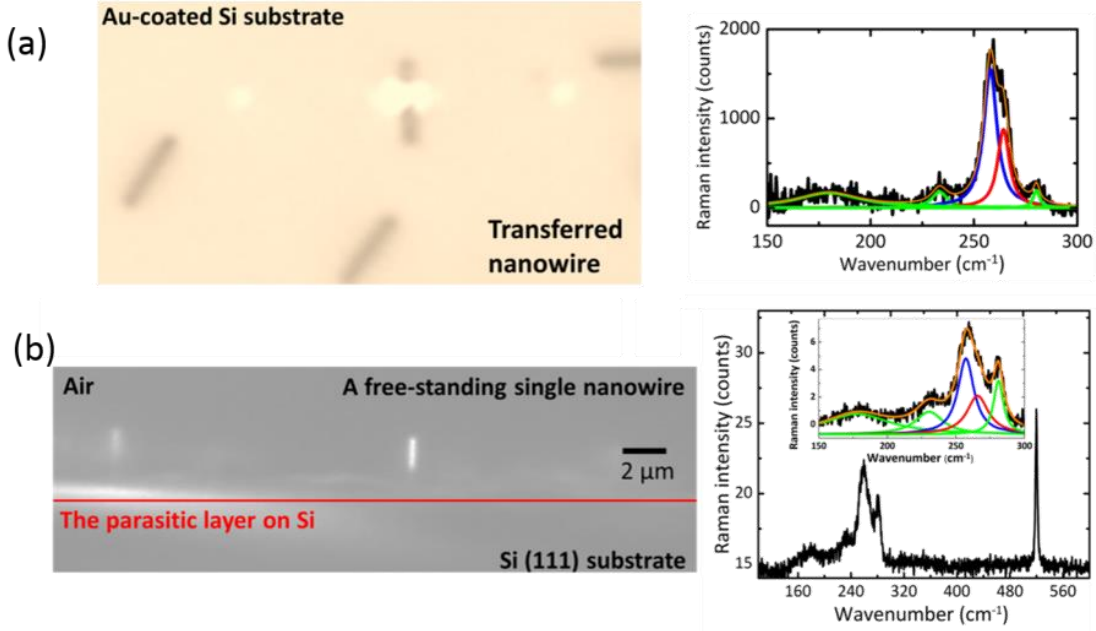


Figure 3.9 Two different Raman configuration measurements at 300 K : optical microscopy images (exciatation normal to the image plane) and corresponding Raman spectra from the nanowires in (a) transferred nanowires on Au coated Si, and (b) as-grown nanowires with excitation from the side $(1\bar{1}0)$ planes. The black spectrum in (a) and (b) are the experimental raw data. In (b) the spectrum shows the Si peak position of the original substrate at 520 $cm^{-1}$. The Lorentzian fitting profile is used for spectra of (a) and the inset of (b). The blue, red, three green curves are assigned for GaAs TO phonon of the core, the GaAs-like TO phonon of the shell and InAs-like TO, LO phonons (below 240 $cm^{-1}$) and the GaAs-like LO of the shell (at around 280 $cm^{-1}$), respectively.

The one-dimensional structure and 6-folded facets of the nanowires can result in a different light-matter interaction as compare to planar thin films with a simpler geometry [224]. For an example, due to the one dimensionality of nanowires and the dielectric mismatch with the surrounding medium, the bulk Raman selection rules can be modified, resulting in a strong dependence of the polarization angle between the incident light and the nanowire axis. This effect is also known as antenna effect (see also the spectrum of Figure 3.5). There are further

effects in this light, such as a strong enhancement of the spontaneous Raman scattering from a single nanowire, which depends on its diameter and the excitation wavelength as well as the incident light polarization [224]. Thus, the electromagnetic field distribution inside the nanowires can be very complicated which requires additional theoretical simulations for the peak assignment and understanding the Raman spectra, rather than the simpler depth profile calculation as often performed in planar thin films [224]. Upon the mentioned effects, F Amaduzzi et al demonstrated the enhancement of the forbidden LO modes on $\{110\}$ surface excitations which was achieved by suspending nanowires over a trench. Their results paved the way for the use of Raman spectroscopy to investigate the free-carriers or plasmons with optical phonons detection [225]. In the Raman experiment on the free-standing single nanowire as shown in Figure 3.9 (b), the enhancement of the LO phonon has been recorded as well even though the wire was excited on $\{110\}$ surfaces.

### 3.4 Photoluminescence spectroscopy

When light with $\hbar\boldsymbol{\omega} > \boldsymbol{E_g}$ (bandgap energy) is shone on the semiconductors, it excites many electrons from VB to CB everywhere and generates holes in VB. It is then viable for an electron in CB to recombine with a hole in VB. If the momentum of the electron while falling to the VB doesn't change, this electron-hole (e-h) recombination is radiative recombination which is well-known as photoluminescence (PL), as shown in Figure 3.10 (a). Following the excitation, different types of relaxation processes for the electron or hole (e-h) occur after which radiative or non-radiative emission generates (e.g. Coulomb scattering or interaction with phonons). In semiconductors with a direct band gap, energy excitation of the material above its band gap results in the formation of e-h bound pairs, so-called excitons, which the momentum of the e stays unchanged while recombining with the h. The relaxation of the e from the higher energy states in CB to the band gap minimum can have several non-radiative processes which results in the thermal emission. In Figure 3.10 (a), the yellow and blue color curves are dedicated to the DOS (density of state) in CB and CB, respectively. For an example, if the excitation energy is far from the minimum of the conduction band, heating up the material will take place due to the high amount of the thermal emission. For most of semiconductors, the exciton binding energy is small and in the range of ~ 25 meV. A simple picture of the PL setup for low temperature experiments is also depicted in Figure 3.10 (b). A non-equilibrium distribution of e-h pairs generate after pumping above bandgap. Consequently, these charge carries interact with each other (carrier-carrier scattering) and also, they interact with LO phonons and then thermalize and relax and reach to the band minima's VB and CB meaning top of the VB and bottom of the

CB. The e-h recombination can happen in different ways. Two types of the most common e-h recombination have been shown in Figure 3.11. In this figure, (a) band-to-band transition, (b) defect-mediated or band-to-defect transition are schematically depicted. In this figure (b) the energy of PL is dissimilar with bandgap energy of the material meaning it has lower energy compare to the energy of PL of (a). One of the ways to distinguish the type of e-h recombination is implementation of temperature dependent PL experiments [163].

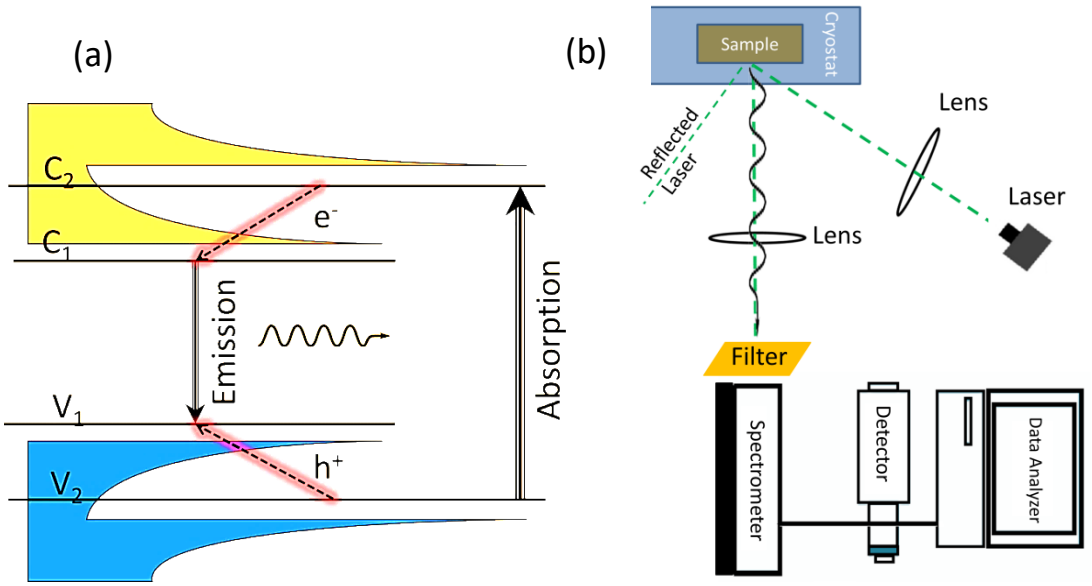


Figure 3.10 (a) Generation of the photons in radiative recombination of e-h in PL spectroscopy. $C_1$, $C_2$, $V_1$, and $V_2$ are first and second excited states of conduction band or ground states of the valence band, respectively. The typical DOS is drawn inside CB and VB by yellow and blue curves (b) a simplified and generalized sketch for the Macro-PL setup.

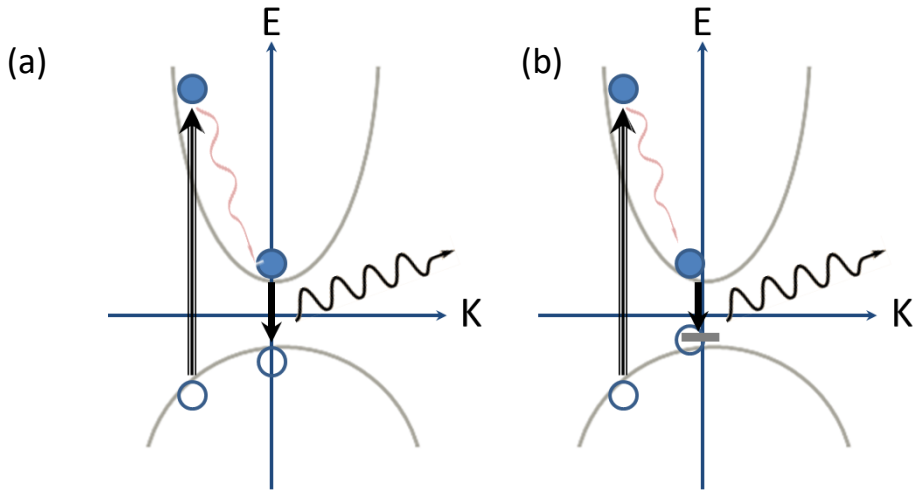


Figure 3.11 Generation of the photons in radiative recombination of e-h in PL spectroscopy. (a) band-to-band transition, (b) defect-mediated or band-to-defect transition.

### 3.5 Optical-pump terahertz-probe spectroscopy and photoconductivity in semiconductors

Terahertz (THz) spectroscopy offers probing the electronic properties of the material with an invasive contact-free way. Dynamics of minority and majority carriers can be understood by time-resolved THz spectroscopy. This method and set up used for the electron transport properties of the nanowires will be briefly introduced.

The THz field can be produced by a non-linear optical crystal or a photoconductive antenna (PCA). In this study, a PCA has been utilized based on GaAs with Cr/Au microstructure contacts (a home-built structure at HZDR in Germany). These microstructure contacts were deposited on GaAs film which was grown by MBE at low temperature≈ 200˚C and followed by post-growth rapid thermal annealing to gain intentional point defect density> $10^{18}$ $cm^3$. The carrier lifetime for this material is in range of few sub-picoseconds e.g. 0.2 ps and the effective mobility of it is in the range of 200 $cm^2$/Vs. Due to the very low mobility of the holes, like one order of magnitude less, compare to the electrons, charge carrier transport properties in THz spectroscopy is dominated by electrons [226].

Once the optical femtosecond pulse laser hits to PCA, the free carriers above the bandgap of mentioned grown GaAs are excited. Later, these excited carries are accelerated by the applied static DC bias voltage and simultaneously, the recombination of these carriers via point defects takes place which results in the charge density reduction. The whole procedure from the charge acceleration by the static bias field to the recombination of part of those carriers via traps is the origin of the sub-picosecond pulses of THz radiation. In another word, the generated impulse current produces THz field emission [226].

The Hertzian dipole antenna is a common way to model the THz radiation from the small slit (as shown in Figure 3.12) which its size is similar to the spot size of the beam∼ 10 µm. This spot size is much smaller than the wavelength of THz radiation ∼ 300 µm. Therefore, the approximation of such a dipole antenna for THz field is correct [226].

The aforementioned THz dipole radiation field after solving the continuity equation is proportional to the 1st time derivate of photocurrent ($I_{PCA}$) inside the photoconductive gap of the antenna, as written in the following eq. (45) [226].

$$E_{THz}(t) \propto \frac{dI_{PCA}(t)}{dt} \qquad (45)$$

The use of off-axis parabolic mirrors (usually coated by Al or Au) is very common to focus or collimate THz probe beams with 99% reflectivity and without chromatic aberration. After THz beam passes through the sample, it is detected by THz detector compartment. The THz field

pulses were detected by electro-optic (EO) sampling in a nonlinear optical medium (ZnTe crystal). Both ZnTe and PCA in the Figure 3.12 can be used for THz generation and THz detection or vice versa. When THz field interacts with ZnTe depends on the angle between the THz field and sampling beam, there will be different generated field after passing ZnTe. The nature of the phenomena is related to the birefringence character of the medium as well as second-order nonlinear polarizations. The EO sampling can be described by the Pockels effect in EO crystals e.g. ZnTe. The Pockels effect (in a nonlinear crystal with electric susceptibility of $\chi^2$) is very similar to optical rectifications. The field-induced birefringence reaches its maximum state when the THz electric field and the optical sampling beam are polarized linearly parallel to $\langle 110 \rangle$ axis of ZnTe; therefore the sampling beam in the setup is perpendicular to the ZnTe and in parallel to THz field polarization. In fact, THz field is in picosecond regime while optical beam is in few femtoseconds regime ~ 60 fs. Due to the birefringence medium, THz phase velocity matches with the optical group velocity (with 800 nm wavelength). The principle of EO sampling compartments is depicted in Figure 3.13 [226].

$$I_s = I_y - I_x = I_0 \Delta\phi = \frac{I_0 \omega L}{c} n_O^3 r_{41} E_{THz} \propto E_{THz} \qquad (46).$$

Nevertheless, the slightly elliptical polarization of the probe pulse induced by EO crystal with the presence of THz field is unavoidable. After passing the λ/4 plate, with presence of THz field, the probe pulse will be almost circular. A Wollaston prism divides the probe pulse into two orthogonal intensities, which are guided into a balanced photodetector. This detector measures the intensity difference between the two orthogonal intensities of the probe beam as the x- and y-polarizations. $I_s$ (the corresponding intensity difference of them) is then proportional to the THz field amplitude which was required to be detected. $\Delta\phi$ (phase change) inside the Figure 3.13 is due to the imperfect circular polarization. The origin of $\Delta\phi$ is due to the nonlinear medium specifications such as the propagation distance ($L$), refractive index ($n_O$) at the optical frequency and EO coefficient ($r_{41}$). Finally, the output signal of balanced photodetector is proportional to the target THz field amplitude as written in eq. (46), where $I_0$ is the incident probe intensity without the effect of differential phase retardation [226].

A simplified scheme of the corresponding THz spectroscopy setup has been drawn in Figure 3.14. Ti: Sapphire femtosecond laser with 800 nm wavelength as the excitation source for the optical beam has been utilized. By a 50/50 beam splitter, the laser beam is divided into 2 paths with two different directions. In one path, laser passes through the pump delay stage and acts as the optical pump beam for the excitation of the sample. In another path, the laser beam hits

to another 50/50 beam splitter where it re-splits in two different paths as one travels into sampling delay stage and acts as sampling beam and the other one is the path for the optical beam used for the THz beam generation and hits through the PCA. The DC bias of the experimental setup in PCA compartment was replaced by a square wave with a modulation frequency of $f_1$=63 kHz and peak to peak voltage of 10 V. Note that $f_1 >> f_2$ meaning that THz probe stays in a longer period than the pump beam in one cycle on the sample. The pump and probe temporal and spatial overlap on the sample are obtained through the adjustment of the pump delay stage. We take the time related to the temporal overlap of the pump and probe equal to zero delay in the measurement analysis; meaning that the time that THz transmitted signal reaches to maximum value.

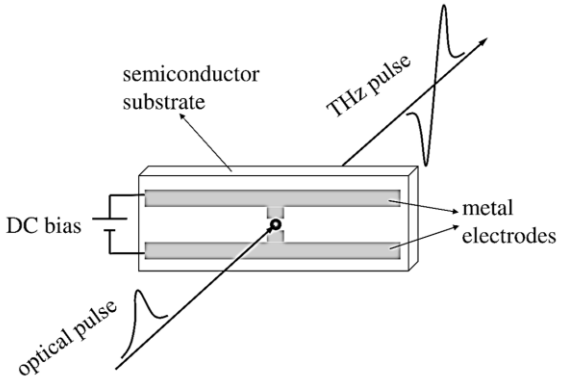


Figure 3.12 THz pulse emission via PCA excited by optical pulse laser (femtosecond laser). This PCA structure can be used for both generation and detection of THz field. Reproduced from [226] with permission of Springer.

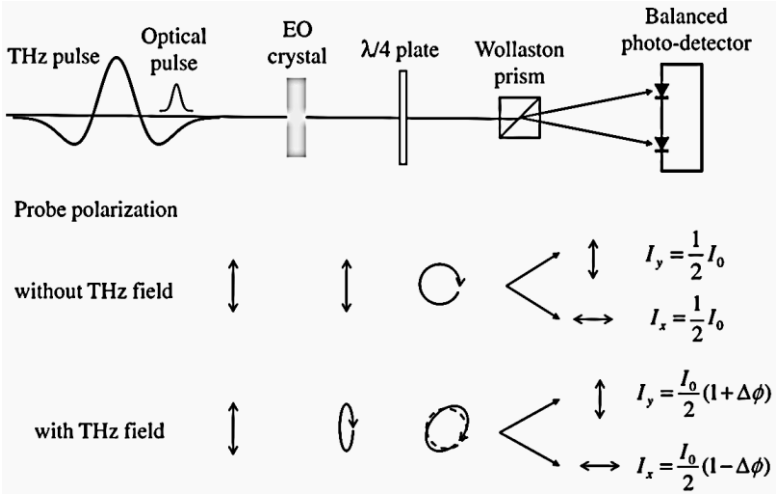


Figure 3.13 Simplified scheme for EO sampling setup including THz detection systems. Probe polarizations with and without the THz field are shown before and after the λ/4 plate. Reproduced from [226] with permission of Springer.

After the EO sampling in THz detection compartment, $I_s$ enters two lock-in amplifiers: L1 and L2. Basically, L1 demodulates this THz intensity signal ($I_s$) at $f_1$. This demodulated signal after passing through L1 inputs to L2 in order to be demodulated at $f_2$. Finally, the output signal after these two series of lock-in amplifiers is the differential OPTP signal ($\Delta E$). I Fotev, S Shan, J Schmidt, F Moebus, Dr. A Pashkin, and Dr. H Schneider at HZDR have collaborated in THz spectroscopy.

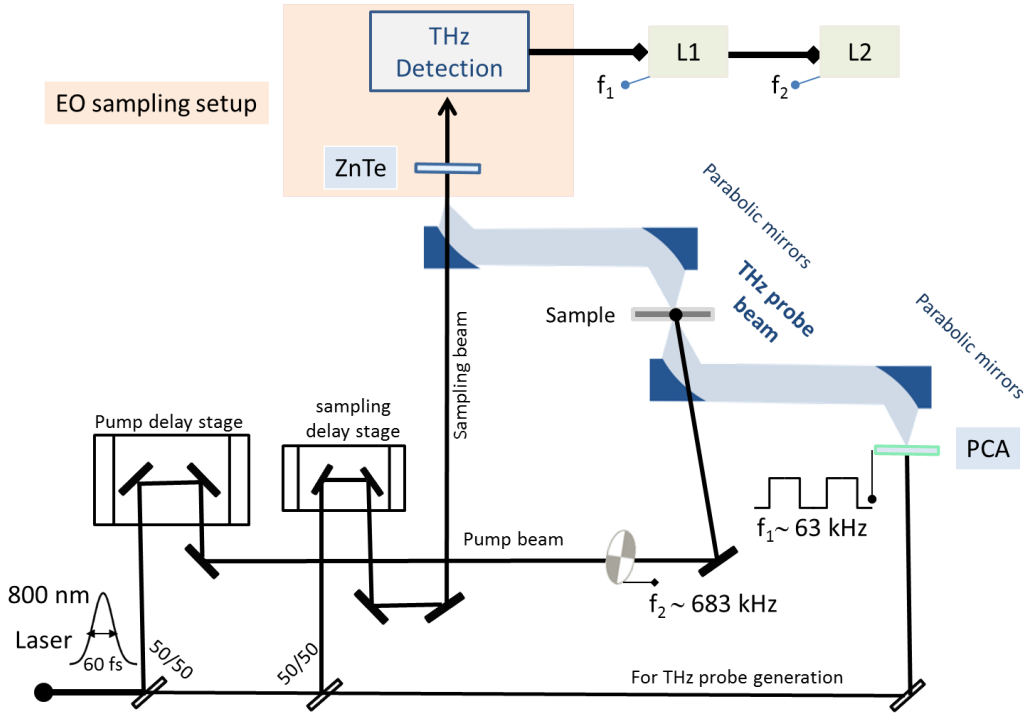


Figure 3.14 Simplified scheme for the experimental setup used in the THz spectroscopy

Applying an electric field to the material causes accelerating of electrons and consequently formation of the current density as written:

$$J(\omega) = \sigma(\omega)E(\omega) \quad (47).$$

The conductivity ($\sigma(\omega)$) of a material is complex and frequency-dependent, consisting of a real part and imaginary part. The complex nature of $\sigma(\omega) = \sigma_{Re}(\omega) + i\sigma_{Im}(\omega)$ can be explained simply by resistance and reactance of the material. The dielectric function of the material is also complex ($\epsilon(\omega) = \epsilon_1(\omega) + i\epsilon_2(\omega)$) [163],[226].

The $\epsilon(\omega)$ is related to the $\sigma(\omega)$ as following:

$$\epsilon(\omega) = \epsilon_{background}(\omega) + i\frac{\sigma(\omega)}{\omega\epsilon_0} \quad (48).$$

In eq. (48), $\epsilon_0$ is the dielectric permittivity of free space and $\epsilon_{background}(\omega)$ is the dielectric function related to the lattice contribution [163],[226].

$$\epsilon_{background}(\omega) = \epsilon_{\infty}(\omega) + (\epsilon_{static} - \epsilon_{\infty})\frac{\omega_{TO}^2}{\omega_{TO}^2 - \omega^2 - i\omega\gamma_{TO}} \quad (49).$$

At THz regime: $\epsilon_{background}(\omega) = \epsilon_{\infty}(\omega)$ (50).

In semiconductors with TO and LO phonons, it is given by eq. (49), where $\epsilon_{\infty}(\omega)$ is the high frequency dielectric constant of the material and $\epsilon_{static}$ is the low frequency (static) dielectric constant. At mid-infrared or terahertz range of frequencies, the $\epsilon_{background}(\omega)$ can be assumed to be equal to $\epsilon_{\infty}(\omega)$ [163],[226].

Recalling the relation of complex refractive index $n'(\omega)$ and the dielectric function of material $\epsilon(\omega)$, the real and imaginary part of the $n'(\omega)$ can be written as following [163],[226]

$$n'(\omega) = n(\omega) + ik(\omega) = \sqrt{\epsilon(\omega)\tilde{\mu}} \quad (51).$$

Conceptually, $n(\omega)$ is the refractive index of material related to the phase delay of a wave passing through the material and $k(\omega)$ is the imaginary part related to the absorption and $\tilde{\mu}$ is the permeability of the material describing the magnetic behavior of the material and for the non-magnetic material, it will be as $\tilde{\mu} = 1$ [163],[226].

$$\Delta\sigma(\omega) = i\omega\epsilon_0\big(\epsilon(\omega) - \epsilon^*(\omega)\big) = i\omega\epsilon_0(n'(\omega)^2 - n'^*(\omega)^2) \quad (52)$$

During the photoexcitation of the materials e.g. namely semiconductors in this discussion, the $\sigma(\omega)$ can be changed. The change of conductivity induced by the photoexcitation is called photoconductivity ($\Delta\sigma(\omega)$) and defined as eq. (52), where the terms with superscript * is associated for the value after the photoexcitation [49], [156], [56], [147], [163],[226].

A technique that allows us to measure $\Delta\sigma(\omega)$ is optical-pump terahertz-probe spectroscopy (OPTPS). This method provides a wealth of information related to the charge transport properties of the material, such as momentum of charge carrier scattering ($\gamma_c$), mobility (μ) and carrier density ($N$). The Drude model is one of the classical models, used to fit the spectra of $\Delta\sigma(\omega)$ that extracted out of the experimental measurements in OPTPS. This model is associated to the motions of the charge carriers (electrons or holes) under the influence of the external pulsed electric field ($E(\omega)$). Under $E(\omega)$, the carriers are scattered, and their momentum will randomize. According to the Drude model, the conductivity is defined as following [49], [156], [56], [147], [163].

$$\sigma(\omega) = \frac{Ne^2}{m^*}\frac{i}{\omega + i\gamma_c} \quad (53),$$

$$\mu = \frac{e}{m^* \gamma_c} \qquad (54).$$

In this model, $e$ is the electronic charge and $N$ is the charge carrier density and $m^*$ is the effective mass of the charge carriers. The fitted Drude model allows us to calculate the μ as given by eq. (54) [49], [156], [56], [147], [163].

In nano-scale regime (e.g. semiconductor nanowires), the $\Delta\sigma(\omega)$ spectra do not reproduce the typical shape of spectra as bulk. For the case of nanowires, the high back scattering of electrons from the surface of nanowires, surface depletion and field screening at the boundaries of the nanowires and depolarization field can be the reasons for their deviation from the standard Drude response. In order to accurately model the conductivity for the case of the nanowires, a modified Drude response, so-called localized surface plasmon model which fits to Lorentzian profile, has been introduced as following [49], [227], [156], [56], [147], [163]

$$\sigma(\omega) = \frac{Ne^2}{m^*} \frac{i\omega}{\omega^2 - \omega_{0p}^2 + i\omega\gamma_c} \qquad (55).$$

In eq. (55), $\omega_{0p}$ is the resonant plasma frequency which can be defined as

$$\omega_{0p} = \sqrt{g \frac{Ne^2}{\epsilon_0 m^*}} \qquad (56),$$

where $g$ is called geometrical parameter which is proportional to the nanowire dimensions or aspect ratios as well as the dielectric constants of them and their surrounding medium and can vary between 0 and 1, [49], [156], [56], [147], [163].

### 3.6 Device processing

In this work, the *ex-situ* fabrication of the metal contacts has been implemented on both ends of the nanowires in order to investigate the electrical characterization of the nanowires. There are the major challenges in obtaining the low contact resistivity such as; highly doping which is required in order to decrease the depletion region in the semiconductors; surface preparation which is very crucial and has a significant effect on the resistivity, therefore the surface oxides removal is mandatory; type of the metal contact as refractory metals (like W, Mo, or Ir) are preferable to obtain thermal stability while high current passing through the contacts although in the investigations, this goal may remain for developments of future devices based on nanowires. Furthermore, an accurate calculation of the contact resistivity is also challenging [228], [229],[230],[231],[232],[233],[234].

In the following, the flow of fabrication process to apply metal contacts on both ends of nanowires is written. To begin with, finding the proper way of nanowires transfer was required for the single nanowire metallization. Based on the literatures, considering to surface preparation such as removal of native oxide and avoiding the sources from any contamination namely carbon in order to obtain low resistivity are highly pivotal [228], [229],[230],[231],[232],[233],[234]. Due to the significance of keeping the surface of the semiconductor as clean as possible, the mechanical rubbing way is recommended for the nanowire transfer from the as-grown wafer. Other ways like the use of ultra-sonication is also common for this purpose but there is a high chance that some unintentional contamination sources affect the quality of surface cleaning according to the experiences of this work.

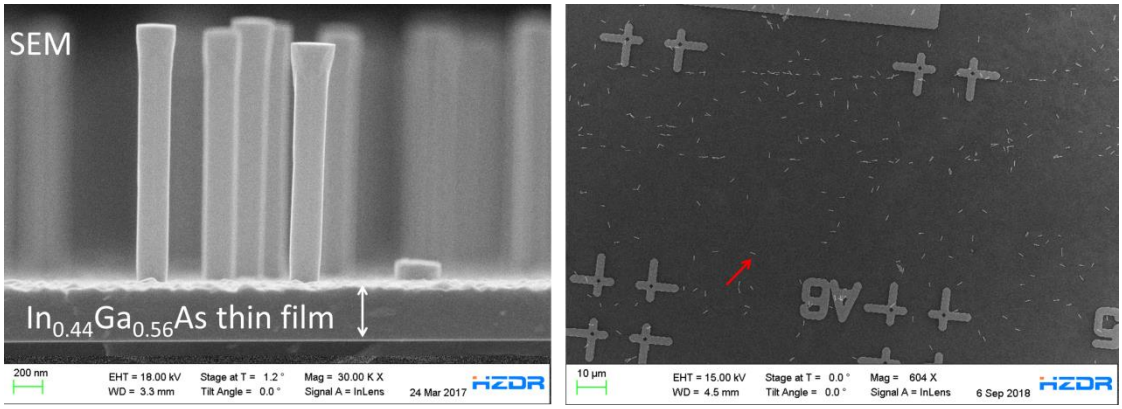


Figure 3.15 (a) SEM image of as-grown GaAs/$In_{0.44}Ga_{0.56}As$ core/shell nanowires with a homogeneous Si doping concentration~ $9\times10^{18}$ $cm^3$ inside the shell; (b) SEM image of the transferred nanowires from as-grown substrate to another substrate (including the special metal markers on $SiO_2$/Si substrate) via mechanical rubbing method. The red arrow inside the right image points out the position of the single nanowire that placed flat on the receiver substrate after harvesting of the nanowires.

The SEM image of as-grown nanowires with the heavily doped shell (Si doping concentration~ $9\times10^{18}$ $cm^3$) is shown in Figure 3.15 (a). The parasitic $In_{0.44}Ga_{0.56}As$ thin film growth during the shell growth by MBE is also shown in this picture. One way to get rid of this parasitic thin film is to harvest the nanowires and transfer them to another substrate so-called receiver substrate. The receiver substrate is an undoped Si substrate with a thick $SiO_2 \approx 200$ nm including the micro markers as shown in Figure 3.15 (b). After the successful transfer of nanowires, the saving the positions of the target single nanowires inside the e-beam lithography (EBL) is needed. Therefore, the small markers will help us to save and measure the precise positions of the selected single isolated nanowires through the EBL software. Next step is to remove the native oxide which is optional at this phase. Here, 37% HCl have been diluted down to 3.7% by DI water. The receiver substrate including nanowires is immersed into the mentioned

diluted-HCl for about 30 seconds and later the substrate is dried by $N_2$ gun inside the fume hood of the clean room. The mentioned HCl step for the removal of the oxide is not highly necessary at this phase. The spin-coating of the photoresist (PR) with the speed rate of 3000 rpm is the next step. Based on the observations of this work, the nanowires can be slightly shifted to another position either due to the spin coating or the earlier HCl step. Therefore, the saving of the nanowires position is done very carefully after the removal of the oxide by wet chemical etching step or PR spin coating step. Passing the steps of saving of the spatially distribution of nanowires on receiver substrate, it is the time to develop the PR inside the EBL chamber. Here it is the time to adjust the exposure parameters of EBL to develop the pattern. At this step, those small markers nearby the selected nanowires are visible and extremely helpful to have a precise alignment of the future metal contacts.

Afterwards, IPA mixed with DI water is used to open the mask. After opening the masks, the simple but very important step comes up which is removal of the native oxide by mentioned diluted HCl. Since it is highly significant to keep the surface of the nanowires very clean, DI water cleaning in every step where a chemical solution involved (e.g. HCl or IPA) is necessary. Drying the DI water by $N_2$ gun from the surface of the receiver substrate is always necessary. It is worth to mention that a try and error test followed by very high magnification SEM imaging has been done initially with different HCl percentages in DI water to avoid any damage of the erosive HCl on the surface of the nanowires. It is very important that the surface of the nanowires stays as smooth as possible without being affected by the higher etching rate of HCl step. Passing the step for the removal of the oxide, the immediate transfer of the sample into metal evaporation chamber is expected in order to avoid further oxidation of the nanowires surface. Nevertheless, in case of a manual transfer and loading of the sample into metal evaporation chamber, the sample will be remained in air. Hence, 100% preventing the native oxide formation in the current *ex-situ* procedure is not possible. The next step is deposition of metal stacks (Ti Pd/Au). Finally, after metallization, lift-off is done by splashing the samples with acetone, followed by rinsing with IPA and DI water, and then blown dry using a $N_2$ gun. In Figure 3.16 (a), the picture of the EBL system is shown. T Schönherr, C Neisser for e-beam BL, and B Scheumann for metals depositions are collaborated in this project related to the device processing [228], [229],[230],[231],[232],[233],[234].

To reduce the Schottky barrier height, RTA is utilized in several steps. First, the RTA temperature is calibrated and then the temperature of the RTA has been increased in multi-steps which were followed by IV measurement in each of those steps. The recipe of the RTA

process can be summarized as following. 1) Evacuate the chamber for several times and fill with $N_2$ for several times. 2) Ramp up to 100 ˚C. 3) Ramp up to the target temperature starting with e.g. 350˚C. 4) a short annealing time. 5) Ramp down to room temperature. At the end $N_2$ gas was kept still constant in the rest of the process to ensure a clean environment. In every RTA step with a gradual increase of the temperature, the IV measurement by the probe station equipped with micro-manipulators (as shown in Figure 3.16 (c)) has been performed on both end of the nanowires to check the quality of the resistivity [228], [229],[230],[231],[232],[233],[234].

## 3.7 Semiconductor nanodevice software "nextnano"

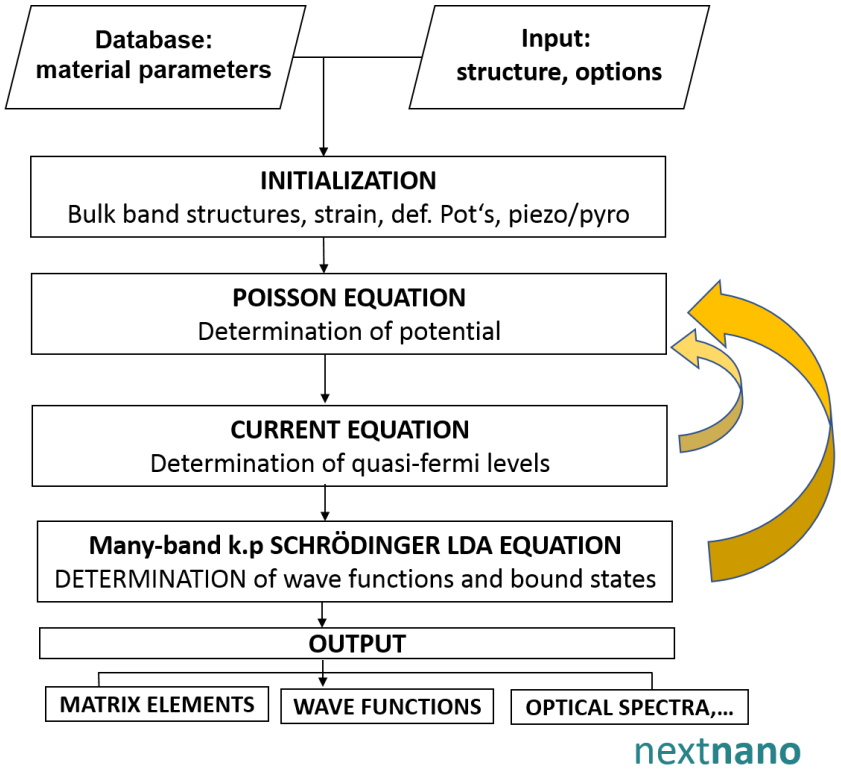


Figure 3.17 Program flow for a typical nextnano simulation. Adapted from [236], [237].

Nextnano software can be used as a predictive tool for the design of semiconductor based heterostructures in the mesoscopic physics for 1D, 2D, and 3D nanostructures. The founder of this software is Dr. S Birner from Walter Schottky Institute at TU-München. The nextnano provides an effective and quick insight into physical properties of mesoscopic semiconductor structures including calculation of the electronic band structures via TB modeling or 8x8 k.p Schrödinger and Poisson equations or strain minimization theory through continuum elasticity model and the effect of piezoelectric charges and many other examples.

In this work, the focus is on effect of the strain on the properties of materials. Thus, continuum elasticity modeling of nextnano is exploited frequently. Semiconductor heterostructures with different lattice constants are under elastic deformations. Such deformations can be investigated within a continuum mechanical model based on classical elasticity ( see chapter 2.4) [235]. The nextnano simulations are via the numerical principles and techniques e.g. iterative solutions (4000 times) for Schrödinger-Poissons equations. This software is quite useful in the field of nano-devices based on different compound semiconductors and the alloy [236], [237]. The nextnano program flow is shown in Figure 3.17.

### 3.8 MBE for crystal growth and core/shell nanowire growth

Molecular beam epitaxy (MBE) is an excellent material growth technique that can be simply described as a very high pure form of vacuum evaporation with an exquisite control over the material growth, interface formation, alloy compositions, and doping concentrations. The main reason for these qualities is a super high clean ultrahigh-vacuum (UHV) environment in the epitaxial growth of materials. UHV conditions typically feature very low pressures ($<10^{-14}$ Torr e.g. in our case$\approx 10^{-11}$ Torr) leading to extremely low background impurity levels in the target grown materials. In MBE, non-interacting molecular beams of material elements are evaporated or sublimed and later having chemical interactions on a heated substrate. Due to the UHV conditions, the beams do not have any interaction with each other in the gas phase owing mean free paths beyond typical 20–30 cm in the distance from source to substrate. Using pure solid-source material (e.g., highly purified gallium) enables to have not only an excellent quality of epitaxial growth but also much simplified chemistry in the interaction between source materials with the substrate. One of the great advantages of MBE grown heterostructures over other growth techniques is very sharp interfaces. The effusion cells of MBE produce the molecular/atomic beams of source materials. These effusion cells are typically paired with a mechanical shutter allowing very fast start or stop of the beams in much shorter time than it takes to grow an atomic layer of material. The temperature of the effusion cells is typically stable, enabling the control of the flux generated from those cells. Therefore, the generation of specific fluxes of material elements can be simple in controlling the accurate alloy compositions and doping concentrations, as well. Owing the UHV environment, different *in-situ* monitoring techniques can be utilized during the growth such as reflection high-energy electron diffraction (RHEED). To achieve high-purity epitaxial layers, it is pivotal that the target materials that loaded inside MBE chamber to be very pure because of the UHV condition. Growth rates are usually in

the range of a few Å $s^{-1}$. Therefore, the molecular beams can be shuttered in a fraction of a second, allowing that exquisite control of the composition, doping level, and thicknesses of the growing layers in the atomic or molecular levels [238]. A simple picture of the MBE device has been depicted in Figure 3.18. Dr E Dimakis has performed the MBE experiments at HZDR.

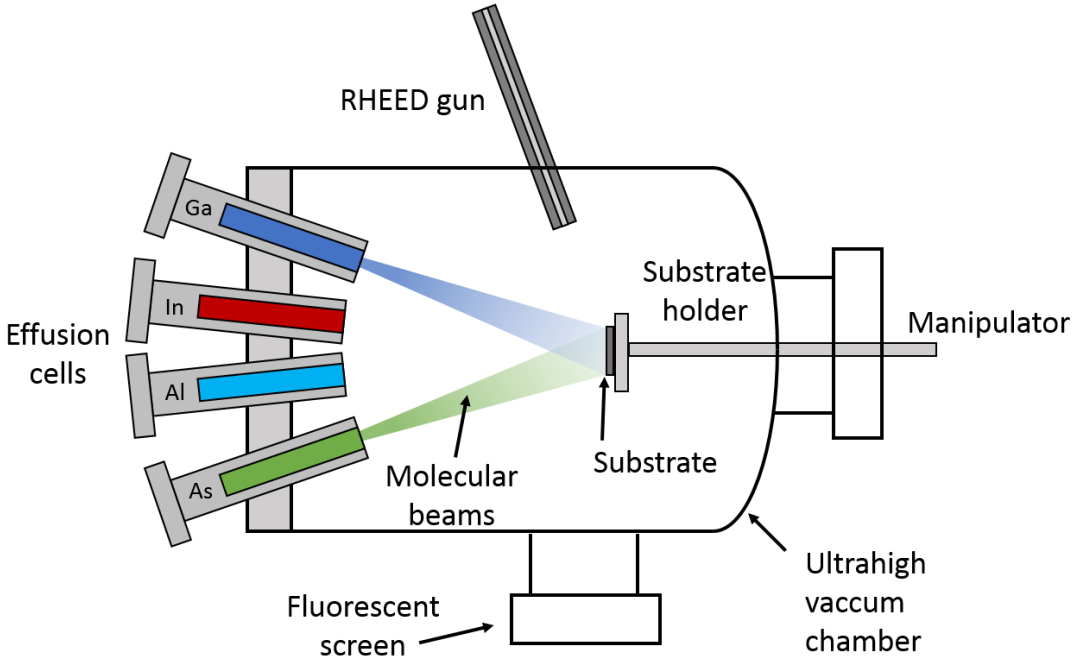


Figure 3.18 A generalized picture of MBE. Molecular beams originate from effusion cells. The substrate is heated up to the certain temperature and, while continuously rotated, if it is required in order to improve the growth homogeneity. A RHEED gun is implemented for *in-situ* monitoring during the growth.

In this thesis, free-standing GaAs/$In_xGa_{1-x}As$ and GaAs/$In_xAl_{1-x}As$ core/shell nanowires were grown on Si(111) substrates by MBE. It is very common to grow nanowires by Au-catalyst; however, using Au may cause Au contamination inside nanowires and the Si substrate degrading their electrical and optical properties [105], [99], [100]. Therefore, the Ga-assisted or self-catalyzed growth mode was employed [14], [15] (see Figure 3.19). A thin native oxide on Si substrate is an important layer for the core growth procedure. After an *in-situ* pre-treatment of the native oxide ($SiO_x$) layer with Ga droplets, nano-sized holes form inside the very thin native $SiO_x$ layer, exposing the underlying Si(111) surface. Then continuous Ga and $As_4$ beam fluxes are supplied simultaneously and subsequently, the GaAs nanowires nucleate inside the nano-holes in vapor liquid solid (VLS) growth mode. The nanowires grow perpendicular to Si substrate along [111]B with six $\{1\bar{1}0\}$ crystallographically oriented facets. The GaAs core nanowires were grown for 10 min at a substrate temperature of 615 °C with V/III≈ 16 resulting in nanowires with a diameter of 20-25 nm and a length of ≈ 2 µm (see Figure 3.19 (a)). The core growth was

interrupted by closing the Ga shutter and the substrate temperature was reduced up to 370 °C in an As-rich environment. Due to the continuous exposure to $As_4$, the Ga droplets at the tip of the nanowire were converted into the solid GaAs. The In-content x can be adjusted by the flux ratio of In flux/(Ga (Al) flux + In flux). The shell growth was performed at 370 °C using In and Ga or Al and $As_4$ or $As_2$ beams and its growth rate was 0.7 monolayer/s (see Figure 3.19 (b)).

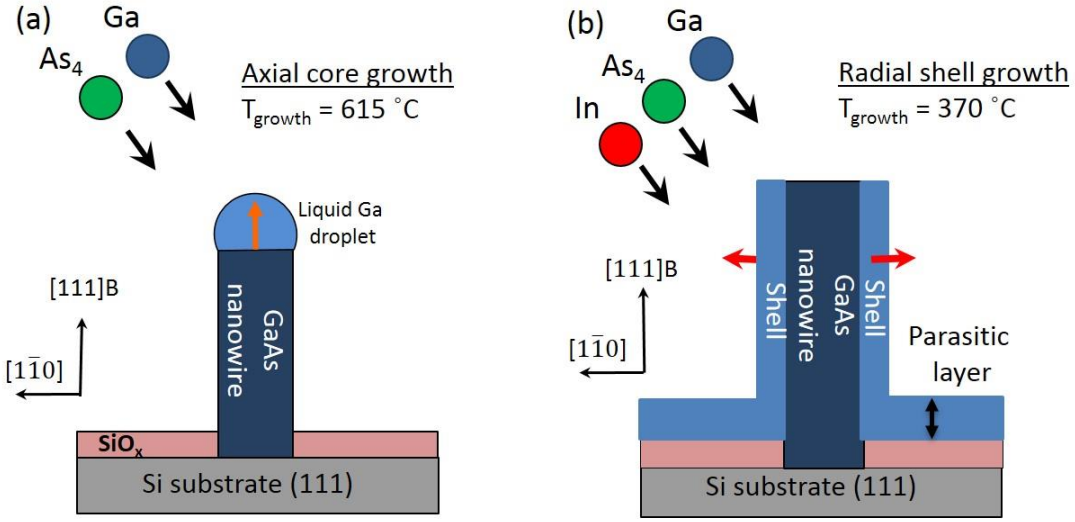


Figure 3.19 Schematic description of the MBE growth of (a) the core GaAs nanowire in VLS mode and (b) $In_xGa_{1-x}As$ or $In_xAl_{1-x}As$ shell growth in VS mode (b). The growth direction is indicated with the red arrows in (a) and (b).

Controlling the shape of the nanowire during the growth of lattice-mismatched core/shell nanowires can be very challenging. Often several growth procedures are necessary to suppress the growth kinetics which causes nanowire bending. In the following, some reports in this regard are pointed out

Y Greenberg et al reported strain-mediated bending in InP/InAs core/shell nanowires. They showed that the reduction of the nanowire diameter increases the bending angle of their core/shell nanowires. Their simulations which is in a good agreement with their experiments prove the interplay between shell composition and thickness as well as tapering which all these factors affect the bending of the core/shell nanowires [239]. Strain-induced bending morphology has also studied in WZ GaP/$In_xGa_{1-x}P$ core/shell nanowires where TEM and XRD spectroscopy proved the geometric and compositional inhomogeneity with respect to the growth axis. Their findings for the origin of the bending are valid for any type of lattice-mismatched core/shell nanowires. They also offer the strategy for curing the bending of these nanowires by the growth of a graded buffer shell, where a gradual elastic strain relaxation

occurs during the shell growth [28]. Better detailed description for the kinetics of the bending is reported by R W Day et al in 2016. They demonstrated Plateau–Rayleigh (P-R) crystal growth that occurs during the lattice mismatched shell growth around the 1D nanowire core. P-R crystal growth means the development of the periodic shell growth along a nanowire core to shape diameter-modulated nanowire homostructures with tunable morphologies. They extended P-R crystal growth for heterostructure nanowires such as Ge(Si) core/shell nanowires. Growth of Ge around Si cores results in a single set of periodic shells, and in different growth conditions yields multi-modulated 1D nanowires with two distinct sets of shell periodicities. Based on their growth study, P-R crystal growth on a thin nanowire core formed 2D loop structures, in which Ge (Si) shells were prone to grow primarily on the outside (inside) of a highly bent Si (Ge) core [240].

R B Lewis et al fabricated arrays of extremely bent nanowires due to asymmetric misfit strain in their core/shell heterostructure nanowires. The generated strain was enough to bend the nanowires backward to touch the neighboring nanowire or the substrate. Their highly ensemble bent nanowires may open the way for the design of nanowire networks and interconnects [241]. Considering the different reports for the epitaxial grown bent nanowires via MBE, the state-of-the-art in this regard may belong to R B Lewis et al [241].

*Richard P. Feynman*

*"I... a universe of atoms, an atom in the universe."*

# 4 Results and discussions

In this chapter, the results and findings of this work for GaAs/$In_xGa_{1-x}As$ ($In_xAl_{1-x}As$) core/shell nanowires are presented. The first part of the results is dedicated for structural and compositional analyses of these nanowires and their limits for the coherency limit, and the bent nanowires. The second part shows the major finding of this work where the strain simulations and the measurements as a function of the nanowire dimension are shown. In the third part, the effect of the strain on the bandgap and effective mass and later in the fourth part, the effect of the strain on the electron mobility are demonstrated. Finally, in the last part of this chapter, the simulations for modulation doped core/multishell nanowires and the preliminary current-voltage (IV) characterization are introduced.

## 4.1 Structural, compositional analyses of straight nanowires and coherent growth limit

The In-content x in the shell was adjusted by the ratio of In and Ga or Al fluxes (see methods), whereas the shell thickness was determined by the shell growth duration. The $In_xAl_{1-x}As$ shells were capped with a 5 nm thick $In_xGa_{1-x}As$ shell to avoid Al oxidation in air. The shell thickness ($L_S$) and In-content x were varied independently from each other in this study. As an example, Figure 4.1 (a) and 4.1 (b) show SEM images of bare GaAs core and GaAs/$In_{0.20}Ga_{0.80}As$ core/shell nanowires ($L_S$= 40 nm), respectively. During the shell growth, an $In_xGa_{1-x}As$ planar layer with polycrystalline structure (parasitic thin film) with similar x also grew on Si. This parasitic layer is very defective because it grows directly on the amorphous native oxide layer. Figure 4.1 (c) and 4.1 (d-f) show elemental maps along and perpendicular to the nanowire axis, respectively, as measured by EDXS in TEM. It can be seen that In distribution inside the shell is quite homogeneous within the resolution of the measurement, except for the nanowire corners, where the incorporation of In was reduced, giving rise to six $< 11\bar{2} >$ lines of lower x. The same occurs in $In_xAl_{1-x}As$ shells with Al rich lines. Similar types of phenomena have been reported for core/shell GaAs/$Al_xGa_{1-x}As$, GaAs/$In_xAl_{1-x}P$, and $GaAs_xP_{1-x}$/$Ga_yAs_{1-y}P$ nanowires [67], [242], [243]. According to recent findings, competing capillary fluxes of adatoms, originating from the higher diffusivity of In adatoms than Ga or Al adatoms, account for the formation of the Ga(Al)-rich lines [243], [150]. Similar growth results for higher x in $In_xGa_{1-x}As$ or $In_xAl_{1-x}As$ shells have been obtained. For an example, cross-sectional EDXS elemental maps for $In_xGa_{1-x}As$ and $In_xAl_{1-x}As$ shells with x=0.45 and x=0.44 ($L_S$= 80 nm) are shown in Figure 4.1 (e) and 4.1 (f), respectively.

The crystal structure of the nanowires was studied carefully by HR-TEM. The crystal structure of the core is ZB as shown by the selective area electron diffraction (SAED) pattern in

Figure 4.2 (a) middle. Only the bottom of nanowires contains a high number of rotational twins, defects, which is attributed to flux transients during the nucleation stage of the core. Due to flux transients at the end of the core growth, only a few rotational twin defects are also present at the tip of the nanowires. The shell adopts the crystal structure of the core illustrating by SAED over A, B, C segments (as shown in Figure 4.2 (b)) thus both core and shell grow in the ZB structure including a few twins, mostly at the bottom of the nanowires.

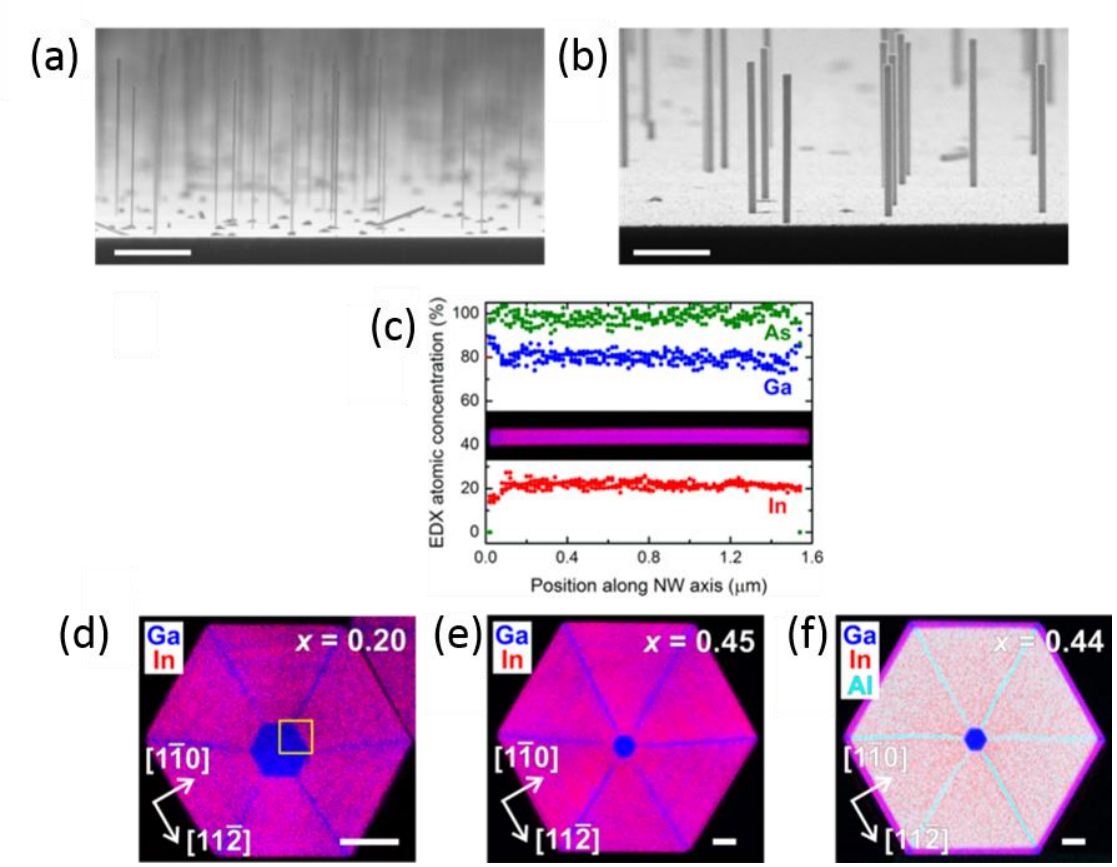


Figure 4.1 Morphological, and compositional analysis of GaAs/$In_xGa_{1-x}As$ and GaAs/$In_xAl_{1-x}As$ core/shell nanowires grown on Si(111) substrates. (a) Side-view SEM image of as-grown GaAs core nanowires and (b) GaAs/$In_xGa_{1-x}As$ core/shell nanowires (x=0.20, $L_S$=40 nm). (c) EDXS compositional analysis along the axis of one nanowire from the sample shown in (b). The inset depicts the corresponding compositional map. (d) EDXS compositional map perpendicular to the axis of one nanowire from the sample shown in (b). (e) EDX compositional map perpendicular to the axis of a GaAs/$In_xGa_{1-x}As$ core/shell nanowire with x=0.45, and $L_S$=80 nm. f) EDXS compositional map perpendicular to the axis of a GaAs/$In_xAl_{1-x}As$ core/shell nanowire with x=0.44, and $L_S$=80 nm. The scale bars correspond to 1 μm in (a) and (b), 30 nm in (d), (e), and (f). High resolution TEM image inside the yellow square in (d) is shown in Figure 4.2 (c).

Finally, the coherent growth along the $[11\bar{2}]$ crystallographic direction of the core/shell interface is proved by the absence of misfit dislocations as shown in Figure 4.2 (c). The high quality of interface has been proved by the high resolution TEM in this figure and the corresponding SAED patterns. The absence of misfit dislocations at the core/shell interface

across the whole nanowire length was confirmed with TEM weak-beam dark-field measurements using the 220 reflection and the so-called (g, 3 g) condition. The example of a GaAs/$In_{0.49}Al_{0.51}As$ nanowire, of the same type as the one in Figure 4.1 (f), is shown in Figure 4.2 (d). Coherent growth without dislocations was obtained for x up to 0.55 ($L_S$= 80 nm). The next higher In-content that was tried, was for x=0.70 (as shown in HIM image of Figure 4.3 (a)) for which misfit dislocations at the core/shell interface (as shown in HR-TEM image of Figure 4.3 (b)) are found. Therefore, the highest possible x for dislocation-free nanowires with $L_S$= 80 nm resides between 0.55 and 0.70. Even though, these misfit dislocations at the interface for $In_{0.70}Ga_{0.30}As$ shell are found, still these nanowires have smooth facets (as shown in Helium ion microscope (HIM) image of Figure 4.3 (a)). R B Lewis et al showed the surface roughness e.g. mounds or island-like features for GaAs/$In_xGa_{1-x}As$ core/shell nanowires with $0.40<x<0.60$ for a very thick core size of 140 nm, and $L_S$=18 nm [20]. The thin core diameter of 22 nm in the nanowires of this work is the main reason for the absence of surface roughness and thus it was possible to grow such highly mismatched core/shell nanowires in the current study.

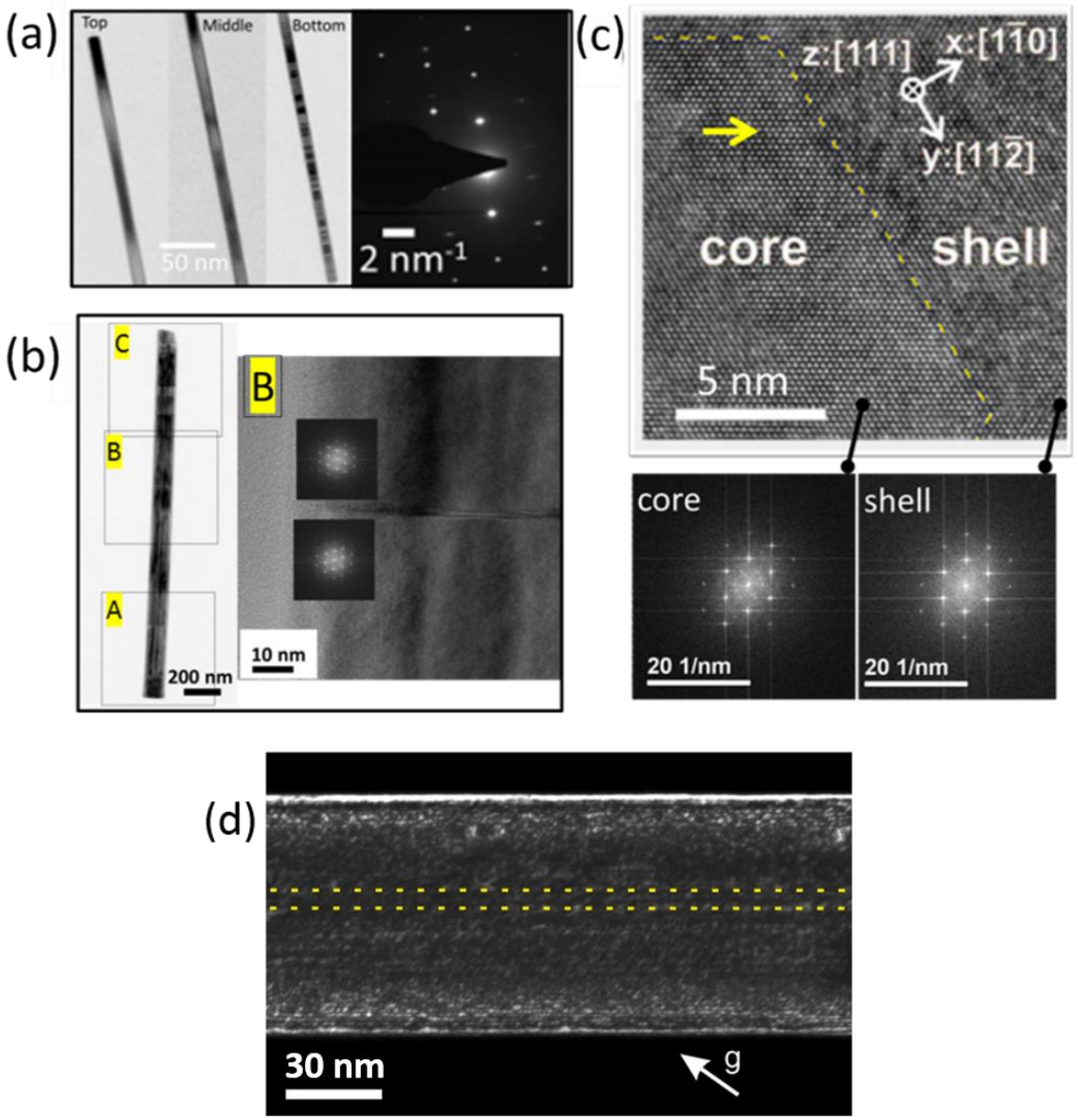


Figure 4.2 Structural analysis of nanowires (a) TEM images from 3 segments (top, middle, bottom) of a single GaAs core nanowire, and SAED pattern of pure ZB of middle segments and (b) TEM image of a GaAs/$In_{0.20}Ga_{0.80}As$ core/shell nanowire ($L_S$=40 nm) in 3 segments (A: tip, B: middle, C: bottom) in left and SAED pattern of pure ZB for segment B, in right from segment B. (c) High resolution TEM micrograph (in the area shown with a yellow box in Figure 4.1 (d)) is displayed. The $[1\bar{1}0]$, $[11\bar{2}]$, and $[111]$ crystallographic directions are indicated as x-, y- and z-axes, respectively. (d) The corresponding SAED pattern of ZB for the core and shell regions is pointed out. (d) (220) weak-beam dark-field TEM image of a GaAs/$In_xAl_{1-x}As$ nanowire as in Figure 4.1 (f) that shows no misfit dislocations in the region of the core (between the yellow dotted lines).

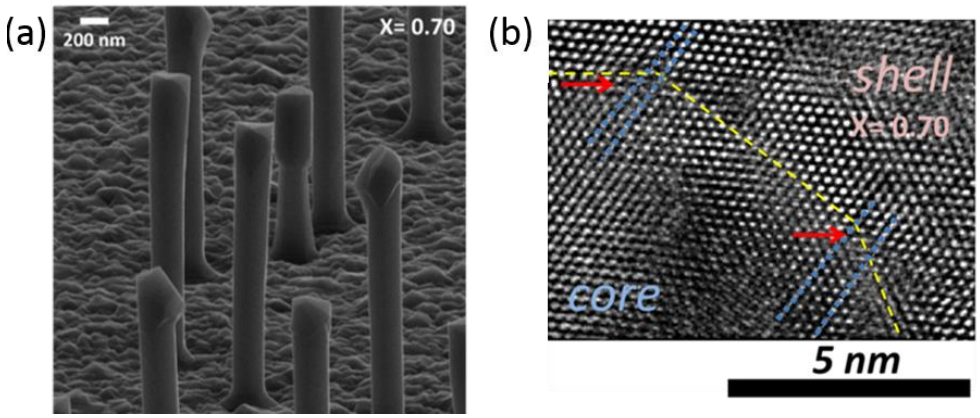


Figure 4.3 GaAs/$In_{0.70}Ga_{0.30}As$ core/shell nanowires with $L_S$=80 nm, (a) Titled-view HIM image of as-grown nanowires on Si, where nanowires are vertical freestanding respect to substrate. (b) High resolution of TEM at the interface of the core and shell of the related nanowires.

### 4.2 Bent nanowires

The growth conditions for the shell (relatively low growth temperature and high growth rate) were chosen in order to achieve conformal growth around the core and straight nanowires. In contrast, strong bending of the nanowires was observed at higher growth temperatures and lower growth rates (see Figure 4.4 (a), (b)).

To clarify the reasons of bending, TEM/EDXS and scanning TEM-Tomography (STEM-TOMO) have been performed on the highly bent nanowires with the same thin core≈ 25 nm and $In_{0.37}Ga_{0.63}As$ shell thickness of ≈ 25 nm. According to the results shown in Figure 4.5, the two evident reasons for bending of nanowires are the larger shell thickness and higher In-content on one side of the nanowire, which both induce an asymmetric stress on the core. Therefore, the nanowires bent toward the thinner shell side with the lower x. The observations by 3D imaging of STEM-TOMO show the bending orientations of the nanowires are random, toward either the $< 11\bar{2} >$ or $< 1\bar{1}0 >$. The preferential incorporation of In adatoms on one side of the nanowires is attributed to the large lattice mismatch and the tendency of the system to minimize the total elastic energy, as already suggested by Day et al [65], [240] (see methods chapter 3.8). However, the surface diffusion of In adatoms is drastically limited at low growth temperatures and high growth rates and, thus homogeneous growth of the shell around the core can be obtained. This is the reason why straight nanowires despite of the large lattice mismatch were achieved in this work.

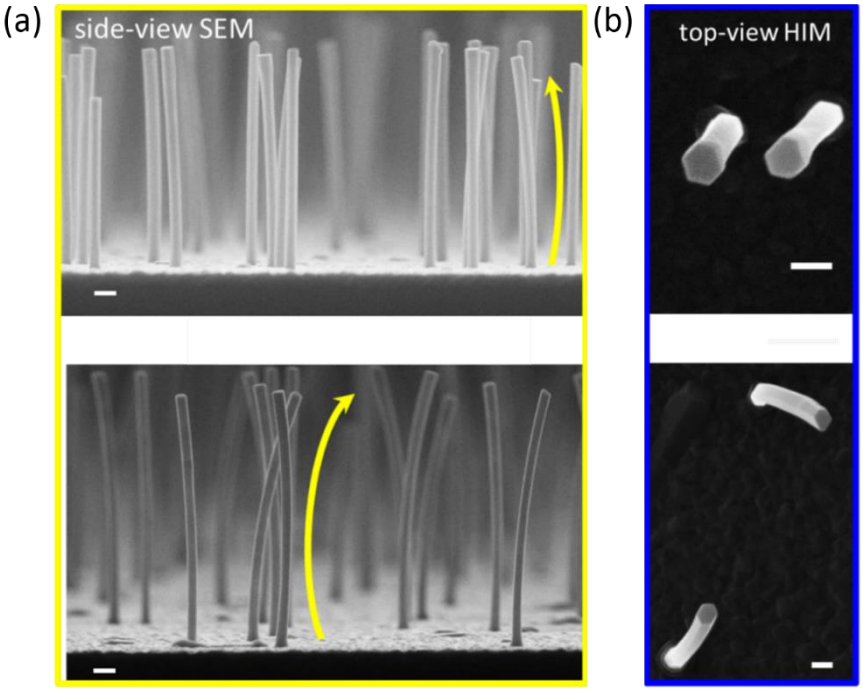


Figure 4.4 Side-view SEM and top-view HIM of bent GaAs/$In_xGa_{1-x}As$ core/shell nanowires are displayed in (a) x=0.20, growth temperature= 420°C, and growth rate= 0.096 ML/s and (b) x=0.40, growth temperature= 420°C, and growth rate= 0.122 ML/s respectively. All of scale bars are 100 nm.

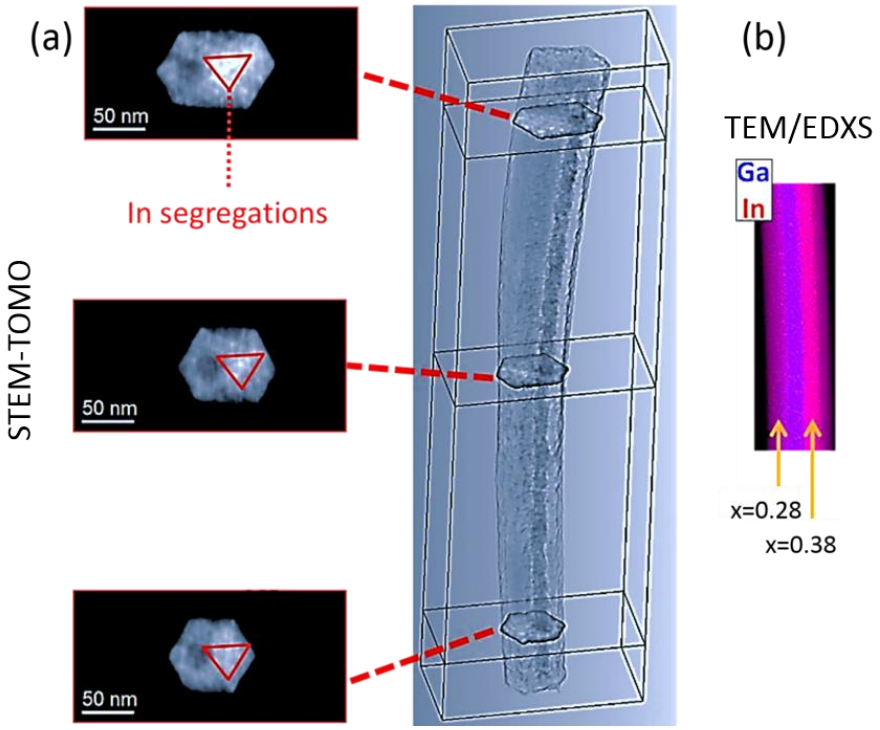


Figure 4.5 Reasons of bending (a) STEM-TOMO of bent GaAs/$In_{0.37}Ga_{0.63}As$ nanowires. (b) EDX-TEM result belongs to the bent GaAs/$In_{0.37}Ga_{0.63}As$ nanowires from a middle segment of the nanowire.

## 4.3 Strain analyses in core/shell nanowires

In this chapter, strain simulations and measurements on GaAs/$In_xGa_{1-x}As$ core/shell nanowires as a function of the shell thickness, the core diameter, and the shell composition are described. At the end, the strain measurements on GaAs/$In_xAl_{1-x}As$ core/shell nanowires as a function of the shell composition are presented.

### 4.3.1 Dependence of strain on shell thickness

To elucidate the strain evolution inside the GaAs core and $In_xGa_{1-x}As$ shell with increasing the shell thickness, strain simulations using nextnano modeling were performed as shown in Figure 4.6. In the sketch of the inset in Figure 4.6, the orientation of the extracted strain profile has been shown which is along $[1\bar{1}0]$ (perpendicular to nanowire facets). In the simulations, the core diameter of 20 nm, the In-content x=0.20, and the $L_S$= 5-80 nm are assumed. The simulation results are based on continuum-elasticity theory using nextnano (see chapter 3.7 and 2.4). Since InGaAs has larger lattice constant compared to GaAs, to accommodate the strain, GaAs will be tensile-strained while InGaAs will be compressively strained. For the thinnest shell of 5 nm, the compressive strain value in the shell reached to 1% which is similar in absolute value to the tensile strain inside the core. As expected, the simulations show that the larger the shell thickness, the higher the strain inside the core and the smaller the compressive strain inside the shell will be. For the shells thicker than approximately 40 nm, the tensile strain inside the core saturates, whereas the strain in the shell becomes almost zero.

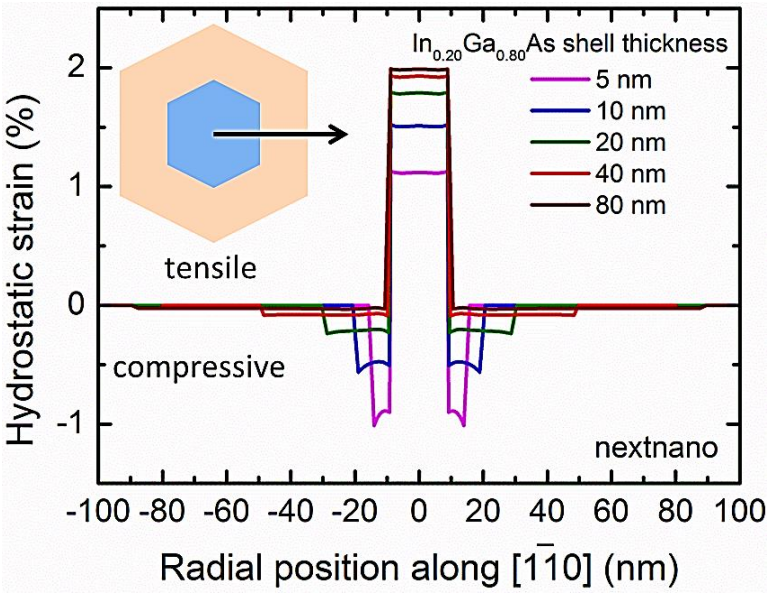


Figure 4.6 Strain profile along $[1\bar{1}0]$ as a function of the shell thickness for GaAs/$In_{0.20}Ga_{0.80}As$ core/shell nanowires.

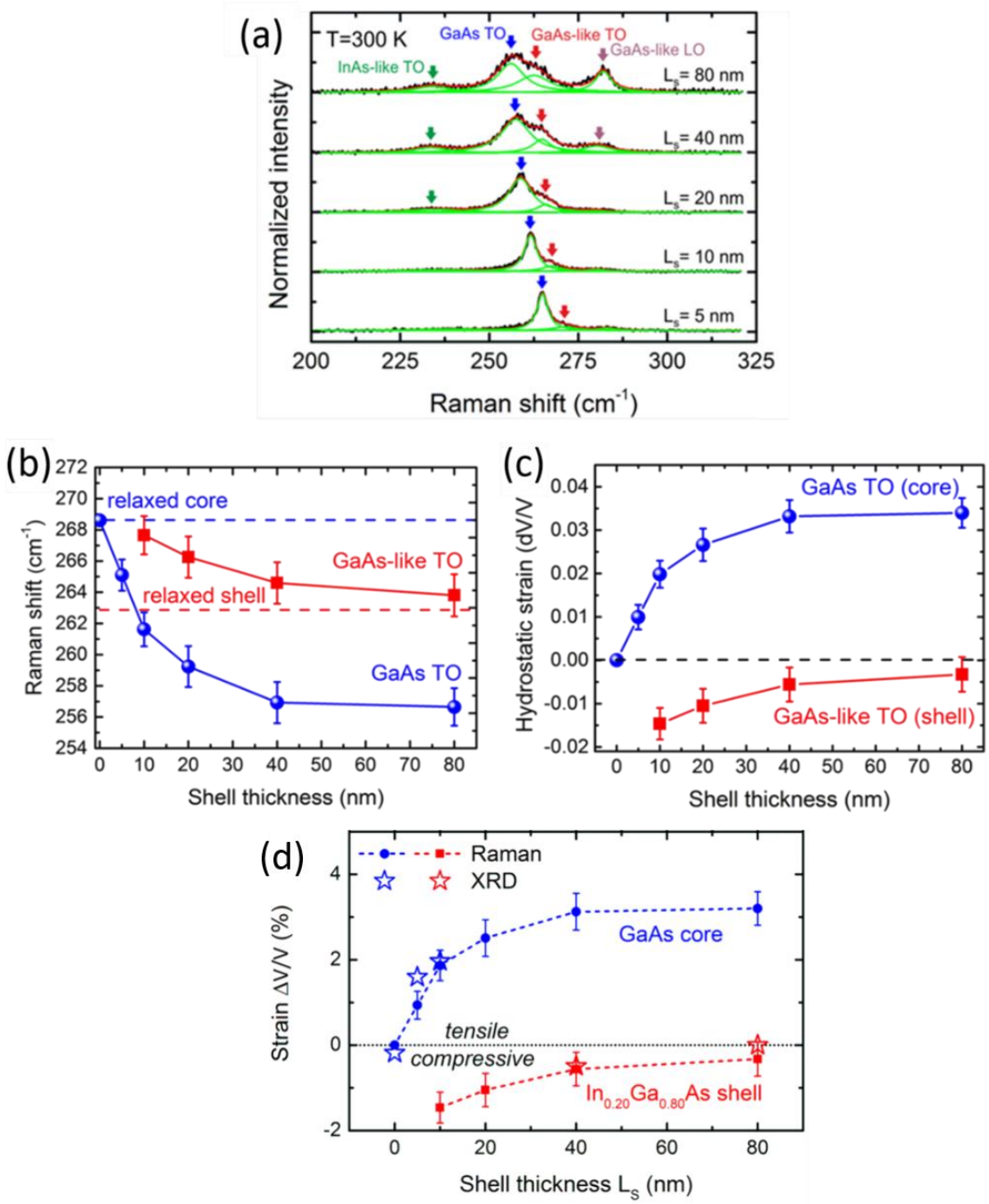


Figure 4.7 Analyses of samples with different shell thicknesses (a) Fitted Raman spectra for GaAs/$In_xGa_{1-x}As$ core/shell nanowires at 300 K with a fixed core size of 22 nm and x=0.20 as a function of $L_S$. In these spectra, the green, red, black colored curves are associated to the individual decomposed curves using the Lorentzian fitting profile, the cumulative fitting profile, and the raw data, respectively. The arrows indicate the peak positions of the corresponding phonon scattering signals. (b-c) Raman shifts and calculated strain values for the GaAs/$In_{0.20}Ga_{0.80}As$ core/shell nanowires as a function of $L_S$ at 300 K, respectively. The data points in blue correspond to the core, whereas the ones in red to the shell. Raman shifts in (b) and calculated strain values in (c) for the GaAs/$In_{0.20}Ga_{0.80}As$ nanowires as a function of $L_S$. The dashed lines in (b) indicate the strain-free phonon positions for the core and the shell. The dashed line in (c) indicate the zero-strain state. (d) XRD (star symbols) and Raman (filled circles) results comparison for GaAs/$In_{0.20}Ga_{0.80}As$ core/shell nanowires at 300 K.

In Figure 4.8, the diagonal elements of the strain tensor (which are simulated via finite-element method for 2D continuum-elasticity modeling) are presented for two different shell thicknesses ($L_s$=10 and 80 nm). According to these simulation results, the in-plane strain ($\varepsilon_{xx}, \varepsilon_{yy}$) distribution is very complex, in contrast to the axial strain ($\varepsilon_{zz}$) and hydrostatic strain ($\varepsilon_h$) which have far simpler structure. This complicates the strain measurements by XRD as it will be shown in Figure 4.9 (b-c). The strain color outside of the hexagonal shell denotes to zero strain.

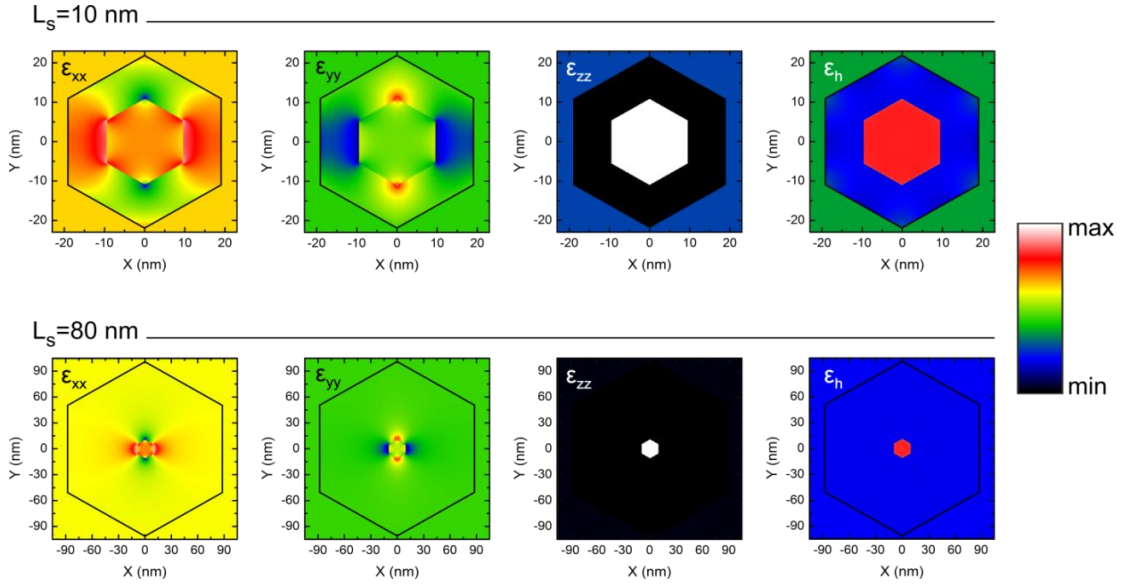


Figure 4.8 2D strain simulations as a function of the shell thickness for GaAs/$In_{0.20}Ga_{0.80}As$ core/shell nanowires with an infinite length. For $L_S$=10 nm, the color scale bar values are as following: (min: -2.16%, max: +1.25%) for $\varepsilon_{xx}$, (min: -1.43%, max: +1.90%) for $\varepsilon_{yy}$, (min: -0.38%, max: +1.05%) for $\varepsilon_{zz}$, and (min: -1.10%, max: +1.96%) for $\varepsilon_h$. For $L_S$=80 nm, the color scale corresponds to values as following: (min: -1.55 %, max: +1.05 %) for $\varepsilon_{xx}$, (min: -1.11%, max:+1.40%) for $\varepsilon_{yy}$, (min: -0.02%, max: +1.42%) for $\varepsilon_{zz}$, and (min: -0.59%, max: +2.44%) for $\varepsilon_h$.

Raman spectra from single GaAs/$In_xGa_{1-x}As$ nanowires at 300 K with x=0.20 and various shell thicknesses $L_S$ are presented in Figure 4.7 (a). The measured raw data (black curves) were fitted using Lorentzian profiles (green curves for the individual decomposed peaks and red curves for the cumulative curves). Scattering from different types of phonons are pointed out by arrows with different colors. As explained in Methods (see chapter 3.3), GaAs TO phonons are associated with the GaAs core, while GaAs-like and InAs-like phonons with the InGaAs shell. Figure 4.7 (b), and (c) show the corresponding Raman shifts of the GaAs and GaAs-like TO phonon peaks and the corresponding strain in the core and the shell. With increasing $L_S$, the compressive strain in the shell decreases, whereas the tensile strain in the core increases in the qualitive agreement with the simulations in Figure 4.6. In other words, the compressive misfit

strain that exists in thin shells is elastically relaxed with increasing $L_S$ by stretching the core (later it will be shown that this is not the only mechanism of the strain relaxation in the shell). Eventually, for $L_S \geq 40$ nm the shell becomes almost strain-free and the strain in core saturates at 3.2%. Strain values were calculated from phonon shifts using eq. (34), where the Grüneisen parameter ($\gamma$) of bulk GaAs was used for the core and that of bulk $In_{0.20}Ga_{0.80}As$ for the shell. The $\gamma$ of the bulk $In_xGa_{1-x}As$ is calculated by the linear interpolation of GaAs and InAs based on the report of K Aoki et al [244]. These results already show that thin enough nanowires can be used as flexible substrates for overgrowth with lattice-mismatched shells, going far beyond what is possible in equivalent thin-film heterostructures.

The strain state of the GaAs core and the $In_{0.20}Ga_{0.80}As$ shell were verified using high-resolution X-ray diffraction (XRD) at synchrotron light sources. The lattice parameters of the core and the shell were measured along the three orthogonal crystallographic directions x, y, z defined in Figure 4.2 (c), (z-axis is parallel to the nanowire axis, whereas x- and y- axes are perpendicular to it). For this purpose, three-dimensional reciprocal space maps were recorded for nanowire ensembles around the $[20\bar{2}]$, $[22\bar{4}]$, and $[\bar{1}\bar{1}\bar{1}]$ Bragg reflections, respectively [65].

Two examples of the reciprocal space map for out-of-plane and in-plane-reflections are shown in Figure 4.9 (a), (b), respectively. In the out-of-plane reflections, the reflection of the Si crystal substrate as a single dot shape has been recorded which it is the reference for all the experimental measurements. The narrow-elongated signal (the red horizontal stripe) as a strong reflection along $[\bar{1}\bar{1}\bar{1}]$ has been pointed out in Figure 4.9 (a) which it originates from GaAs/$In_{0.20}Ga_{0.80}As$ core/shell nanowires with $L_S$= 40 nm. To prove the validity of the reflections of nanowires, they have been removed from the original substrate by ultra-sonication method, whereas the parasitic layer on as-grown samples is remained on the substrate. Therefore, by having an as-grown sample without nanowires, the strong red horizontal stripe was disappeared. The reflection of parasitic layer features a powder-like signal which is an indication for a polycrystalline layer.

In the other example, the reciprocal space map around the $[22\bar{4}]$ reflection, projected on the $(Q_{[11\bar{2}]}, Q_{[1\bar{1}0]})$ plane, for nanowires with $L_S$ = 10 nm is depicted in Figure 4.9 (b). The contributions from the core and the shell are indicated with dashed rectangles. The corresponding 1D plot along $Q_{[11\bar{2}]}$, after integration of the intensity along $Q_{[1\bar{1}0]}$, is also shown in Figure 4.9 (c). The comparison of the 1D plot (continuous curve) with simulations (dashed curve) based on elasticity theory using nextnano (see Figure 4.8) shows a reasonable agreement.

Measurements and simulations were also performed on nanowires with $L_S$ = 0, 5, 40, and 80 nm. The diffraction signal from the core was strong enough and, thus, could be unambiguously identified only for $L_S$ = 0, 5, and 10 nm. On the other hand, the complexity of the radial strain profile in thin shells (see Figure 4.8) allowed for extracting single lattice parameters for the shell along x or y direction only for $L_S$ = 40 and 80 nm. The extracted average lattice parameters of the core ($a_x^c, a_y^c, a_z^c$) and the shell ($a_x^s, a_y^s, a_z^s$) are plotted in Figure 4.9 (d) as a function of $L_S$.

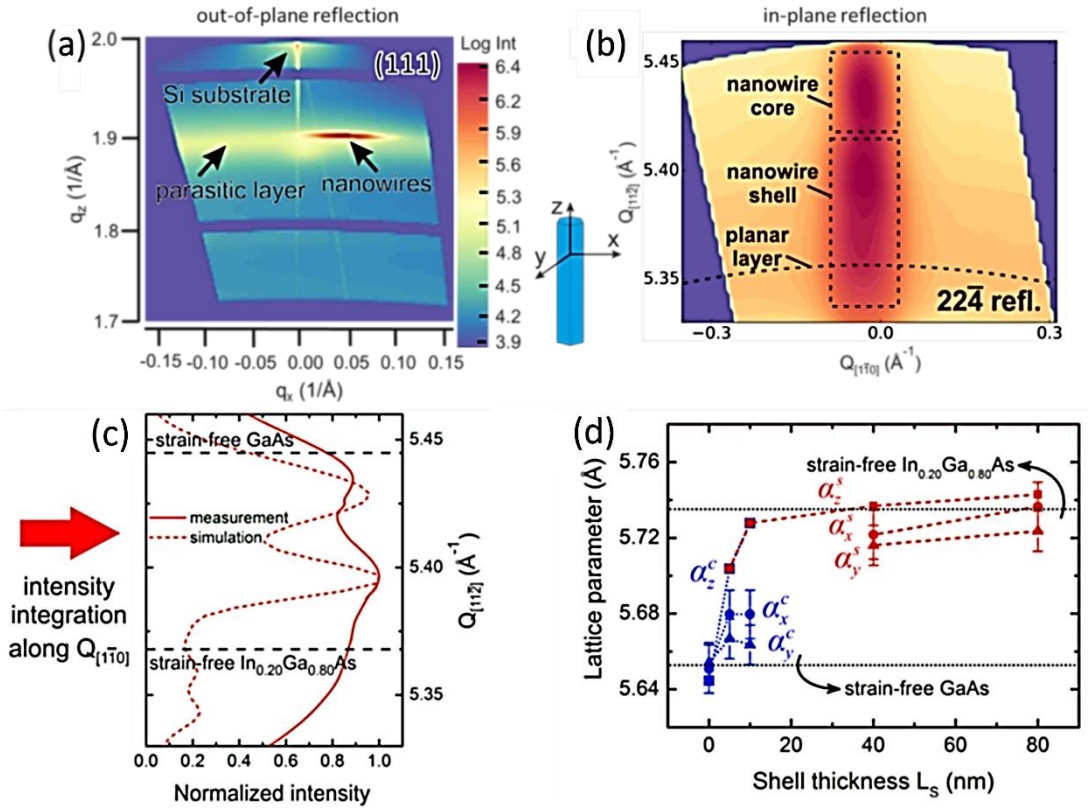


Figure 4.9 Two examples of 2D reciprocal space map in out-of-plane reflection (in (a)) and in-plane-reflection (in (b)) on esemble as-grown GaAs/$In_{0.20}Ga_{0.80}As$ core/shell nanowires (core diameter of 22 nm) with $L_S$= 40 nm (in (a)) and $L_S$ =10 nm (in (b)), are shown, respectively, where the crystallographic orientations in a cartesian system are $z$:(111), $x$:(202), $y$: (224) in an sketch between (a) and (b).(c) 1D plot for in-plane reflections extracted from Grazing incidence X-ray diffraction measurements and the simulation result are displayed. The identification of the core and shell contributions in the 2D reciprocal space map of (b) was based on the comparison of the measurement (continuous curve in (c)) with the theoretical simulation (dashed curve in (c)). (d) XRD-measured average lattice parameters of the core (blue data points) and the shell (red data points) as a function of $L_S$. $a_z$ is the lattice parameter parallel to the nanowire axis, extracted from the $\bar{1}\bar{1}\bar{1}$ reflection. $a_x$ and $a_y$ are two orthogonal lattice parameters perpendicular to the nanowire axis, extracted from the $20\bar{2}$ and the $22\bar{4}$ reflections, respectively. The dashed lines are guides to the eye, whereas the horizontal dotted lines show the strain-free lattice parameters for GaAs and $In_{0.20}Ga_{0.80}As$. The error bars are extracted from the fitting error of the corresponding 1D XRD spectra.

The fact that all three lattice parameters of the core increased with $L_S$ is a manifestation of the hydrostatic character of strain in the core. $a_z^c$, which was found equal to $a_z^s$, increased gradually with $L_S$ from the value of strain-free GaAs to that of strain-free $In_{0.20}Ga_{0.80}As$. This means that for thick enough shells, the misfit along the nanowire axis was elastically accommodated exclusively by stretching the core. The situation is not the same in the x–y plane. $a_x^c$ and $a_y^c$ also increased with $L_S$, but they showed a tendency to saturate well below the value of strain-free $In_{0.20}Ga_{0.80}As$. Nevertheless, $a_x^s$ and $a_y^s$ reached almost strain-free values, which suggests that the misfit perpendicular to the nanowire axis was only partly accommodated by stretching the core. We speculate that the reason for that is the continuously increasing width of the nanowire sidewalls during shell growth, which also enables the elastic accommodation of misfit. The strain components along ($\varepsilon_{zz}$) and perpendicular ($\varepsilon_{xx}$, $\varepsilon_{yy}$) to the nanowire axis were calculated for the GaAs core as $\varepsilon_n=(a_n^c-a_0)/a_0$ (where $n = xx, yy, zz$, and $a_0$ = 5.6533 Å is the lattice parameter of strain-free GaAs), whereas the corresponding hydrostatic strain was calculated as $\Delta V/V=\varepsilon_{xx}+\varepsilon_{yy}+\varepsilon_{zz}$. As shown in Figure 4.7 (d), the results for $\Delta V/V$ (star symbols) are in good agreement with the strain measured by Raman scattering. Thus, it is two independent experimental techniques that verify the unusually large strain in the GaAs core.

### 4.3.2 Dependence of strain on the shell chemical composition

To study the dependence of strain on the shell composition, GaAs/$In_xGa_{1-x}As$ and GaAs/$In_xAl_{1-x}As$ core/shell nanowires with different x ($L_S$=40-80 nm) were grown. $In_xAl_{1-x}As$ has a larger bandgap than $In_xGa_{1-x}As$ and the strained GaAs core (this will be shown in chapter 4.4) and as a result, it can serve as a quantum barrier for electrons and holes. Their lattice constants are the same (see Figure 2.10), therefore the strain state inside the core is expected to be the same. The corresponding Raman spectra are plotted in Figure 4.10 (a), and (b). The experimental raw data (black curves) were fitted using Lorentzian profiles (green curves for the individual decomposed peaks and red curves for the cumulative curves). Different types of phonons are pointed out by arrows with different colors. It is clear that the phonon peaks shift toward lower wavenumbers by increasing the x for both $In_xGa_{1-x}As$ and $In_xAl_{1-x}As$ shell. The Raman shift of the GaAs and GaAs-like phonons as a function of x are plotted in Figure 4.10 (c). Raman shift for the GaAs TO of the core (blue data points) increases linearly with x, while GaAs-like TO of the shell (red data points) follows the expected strain-free shell values (the red dotted line). The strain values of the core and shell have been calculated for every x as shown in Figure 4.10 (c) in the lower panel. Extremely high strain values up to 7% have been achieved inside the core for

x=0.55. In fact, the linear dependence of the strain in the core on x is suggestive of an elastically strained system, where no plastic relaxation has taken place. From linear fit of the strain in the GaAs core for both $In_xGa_{1-x}As$ and $In_xAl_{1-x}As$ shells, the following equation is obtained:

$$\frac{\Delta V}{V} = 1.8\, f \quad (57).$$

Assuming that $\varepsilon_{zz} = f$ (as found by XRD and as predicted by continuum elasticity theory) in chapter 4.3.1, it was found from eq. (57) that $\varepsilon_{xx}\left(= \varepsilon_{yy}\right) = 0.40\ \varepsilon_{zz}$. This is by a factor of 2 higher than the values from elasticity theory. The reason of this contrast is not understood and can be the subject for the future work.

Furthermore, the effect of the capping layer on the Raman and PL spectroscopy is needed to be clarified. All the aforementioned GaAs/$In_xAl_{1-x}As$ core/shell nanowires consisted of a very thin capping layer (≈ 5 nm) of $In_xGa_{1-x}As$, as it was shown already in Figure 4.1 (f), to avoid any possible Al oxidation. For simplicity, it was mentioned frequently GaAs/$In_xAl_{1-x}As$ core/shell nanowires than GaAs/$In_xAl_{1-x}As$/$In_{x+0.01}Ga_{1-x+0.01}As$ core/shell/capping layer nanowires. In Figure 4.11, the black- and orange-colored spectra are dedicated for the GaAs/$In_{0.44}Al_{0.56}As$/ $In_{0.45}Ga_{0.55}As$ nanowire sample and GaAs/$In_{0.44}Al_{0.56}As$ nanowire sample, respectively. As shown in this figure, it was confirmed that the capping layer has no effect on the Raman shift. Later, the similar measurements have been conducted on the same nanowire samples for PL spectroscopy to check the influence of the capping layer in PL spectra. As it is shown in Figure 4.12, it was confirmed that the capping layer has no effect on the shift of the PL peaks, only with a very small ignorable shift of about 10 meV.

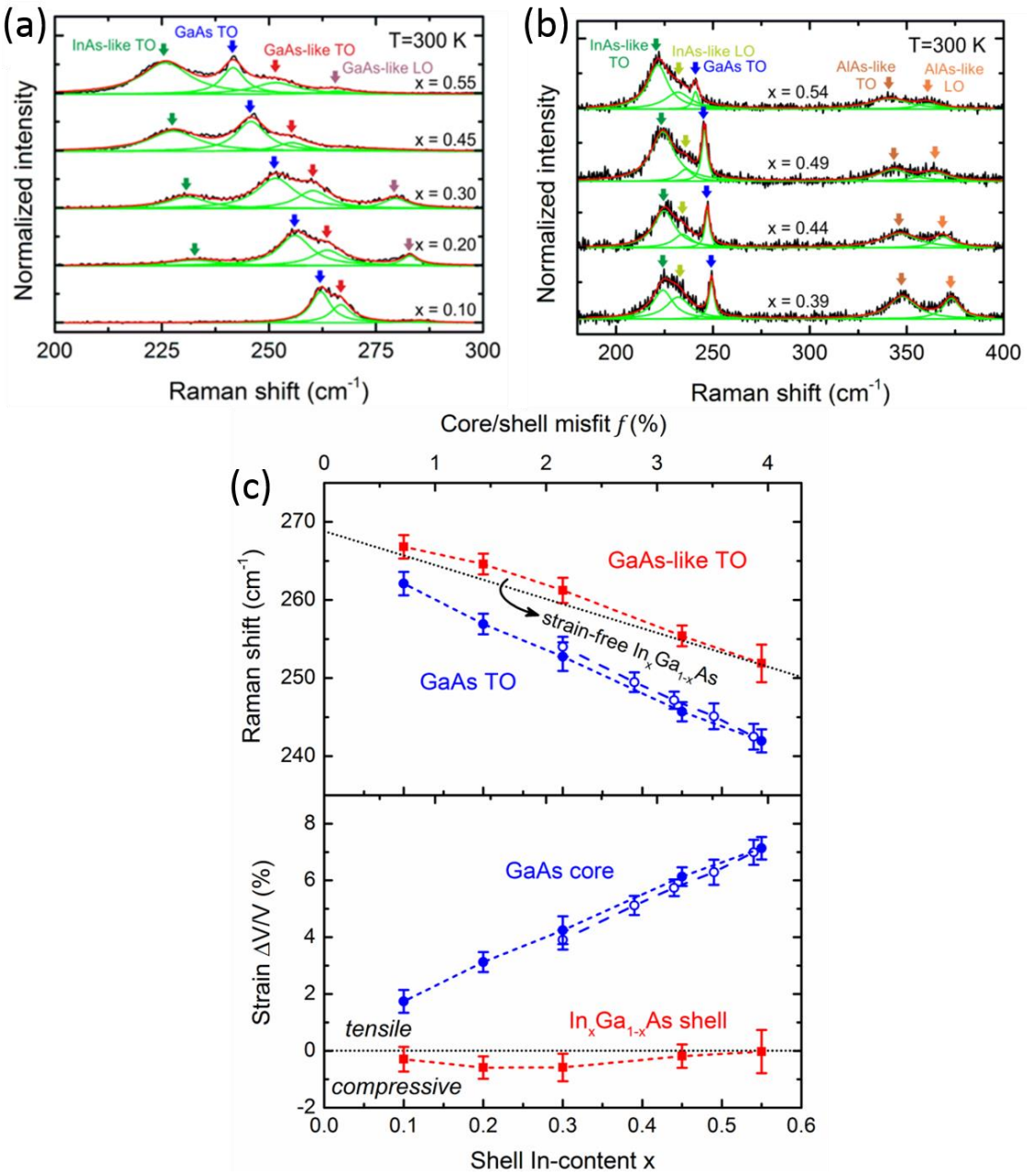


Figure 4.10 Deconvolution of Raman signal curves for GaAs/$In_xGa_{1-x}As$ core/shell nanowires in (a) and GaAs/$In_xAl_{1-x}As$ core/shell nanowires in (b) at 300 K with a fixed core size of 22 nm and thick enough shell ($L_S$= 40-80 nm) as a function of x. In these spectra, the green, red, black colored curves are associated to the individual decomposed curves using the Lorentzian fitting profile, the cumulative fitting profile, the raw data before the fitting, respectively. The arrows are pointed toward the peak positions of the corresponding phonon scattering signals. (c) Strain analyses of single GaAs/$In_xGa_{1-x}As$ ($L_S$= 40 – 80 nm; closed symbols) and GaAs/$In_xAl_{1-x}As$ ($L_S$= 80 nm; open symbols) core/shell nanowires vs x in the shell (bottom x-axis) and the corresponding core/shell misfit $f$ (top x-axis) at 300 K. Upper plot: Raman peak positions of the GaAs-TO inside the core and the GaAs-like TO phonons inside the shell vs x and $f$. The plot in lower panel depicts the calculated strain for various $x$ and $f$.

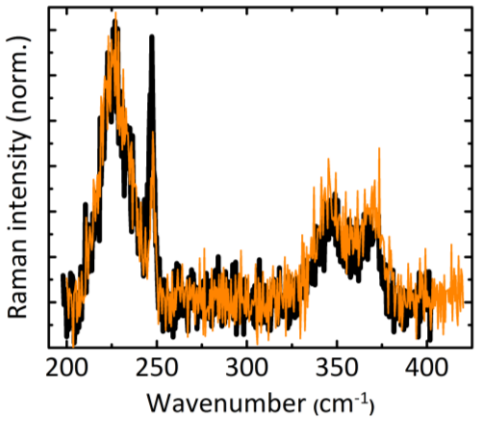


FIGURE 4.11 Effect of $In_{0.45}Ga_{0.55}As$ capping layer in Raman spectra for single $GaAs/In_{0.44}Al_{0.56}As$ core/shell nanowires, at 300 K (532 nm excitation). Black and orange curves belong to the nanowires with and without capping layer, respectively.

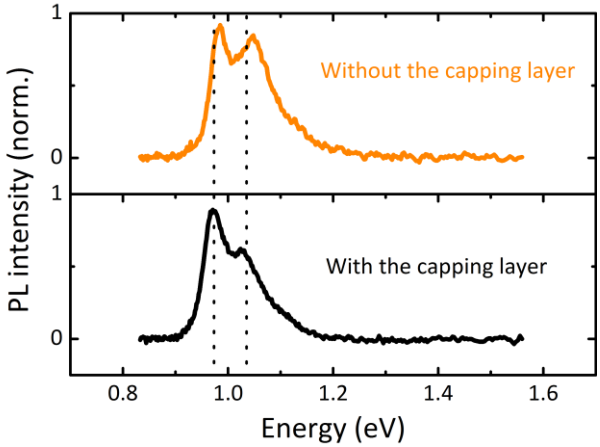


FIGURE 4.12 Effect of the $In_{0.45}Ga_{0.55}As$ capping layer in PL spectra for $GaAs/In_{0.44}Al_{0.56}As$ core/shell nanowires at 300 K with the same excitation power of 90 mW and CW 532 nm on an ensemble of nanowires.

### 4.3.3 Dependence of strain on the core diameter

To identify the role of the core diameter in strain, three samples of $GaAs/In_{0.20}Ga_{0.80}As$ core/shell nanowires ($L_S$= 20 nm) have been studied with different core diameters (25, 55, and 100 nm) by Raman spectroscopy. In Figure 4.13, the Raman spectroscopy analyses of these 3 types of nanowires with different core diameters are displayed. As shown in Figure 4.13 (a) and (b), all phonon peaks shift to lower wavenumbers as the core diameter decreases. This means that the tensile strain in the core increases at smaller diameters, whereas the compressive strain in the shell decreases as shown in Figure 4.13 (c). This is again in the qualitative agreement with the elasticity theory simulations as also shown in Figure 4.13 (c).

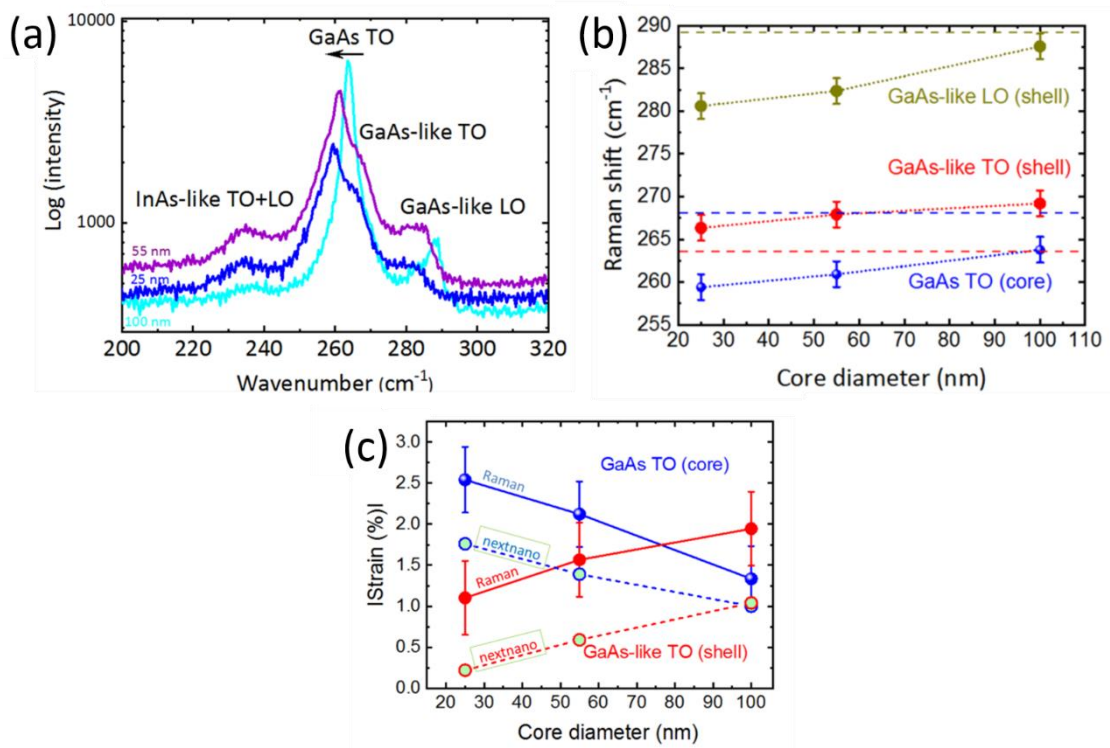


Figure 4.13 Dependence of strain on the core diameter of GaAs/$In_{0.20}Ga_{0.80}As$ core/shell nanowires ($L_S$= 20 nm) (a) Raman spectra are shown for 25, 55, 100 nm core diameter in blue, violet, and cyan, respectively. (b) Raman shift as a function of the core. (c) Absolute values of the measured and calculated strain as a function of the core diameter.

### 4.4 Strain-induced modification of electronic properties

In chapter 4.3, it has been demonstrated that the tensile strain inside the GaAs core with the thick enough $In_xGa_{1-x}As$ or $In_xAl_{1-x}As$ shells can be as high as 7%. Based on the expectations from theory, the hydrostatic tensile strain should affect the electronic properties of the core. Here, the effect on the bandgap and the effective mass and mobilities of electrons are studied.

Macro-PL measurements have been carried out from 12 to 300 K with the laser excitation of 532 nm on ensembles of GaAs/$In_xAl_{1-x}As$ core/shell nanowires ($L_S$=80 nm). The nanowires were transferred from the original substrates onto amorphized Ge substrates by implantation of Ge ions, which do not exhibit any PL signal in the range of interest. The peak fitting was done with Voigt profiles, as shown in Figure 4.14 (a), where the half of full-width half-maximum (FWHM/2) is used as error bars in Figure 4.14 (b). In Figure 4.14, the PL spectra as a function of x at 12 K and 300 K are shown. The PL signal detected in the range from 0.80 to 1.20 eV is attributed to radiative recombination of e-h pairs inside the heavily strained GaAs core. The strain-engineered GaAs core shows a sizeable shift from its strain-free bandgap of 1.42 (1.52) eV at 300 (12) K,

respectively. The PL peaks exhibit a gradual shift to lower energies with increasing x, which is a clear effect of the increasing tensile strain in the GaAs core. At 12 K, the spectra can be fitted with a single peak named as $E_1$, whereas two peaks are detected named as $E_1$ and $E_2$ at 300 K. At 12 K, the high energy shoulder is neglected because it cannot be resolved well due to its low intensity. To identify the origin of $E_1$ as a function of x and the corresponding tensile strain in the core, its peak energy at 12 K has been plotted in Figure 4.14 (b). The linear fit shown with blue dashed line (see Figure 4.14 (b)), agrees well with the hydrostatic deformation potential (DP) theory for the bandgap of GaAs.

$$E_1 = E^o + a \cdot \frac{\Delta V}{V} \qquad (58).$$

In eq. (58), $E^o$ is the strain-free bandgap energy at low temperature and $a$ is the corresponding hydrostatic deformation potential coefficient. The fitted values $E^o$=1.55±0.03 eV and $a$= -9±0.5 eV are almost equal to the strain-free bandgap energy of 1.52 eV and the hydrostatic deformation potential of -8.5 eV, respectively, of bulk GaAs at low temperature (see chapter 2.5) [3], [195], [196]. The anisotropic strain on the bandgap energy of GaAs was calculated with equations similar to eq. (58). Based on the theory and the simulations (nextnano), the anisotropic strain causes VB splitting due to breaking the symmetry of the crystal. Here, the VB splitting has been considered in the calculations. Therefore, the additional shift of the bandgap ($\Delta E_v$) due to strain an-isotropy was extracted via the following equations (36-38), in which $\Delta_0$ = 0.34 eV is the spin-orbit coupling effect at the VB maxima of bulk GaAs and $d$ = -4.5 eV stands for the deformation potential of GaAs [3], [195], [196]. The results of these calculations were depicted as a black short-dashed line in Figure 4.14 (b). The theoretical bandgap in Figure 4.14 (b) is calculated based on the energy difference between the electron CB minima and the HH of VB maxima at the Γ-point [3], [195], [196].

The results are compared in Figure 4.14 (b) with the bandgap of strained GaAs calculated either from first-principles (a combination of density-functional theory, DFT, with GW approximation; black dash-dotted line) or with the band-edge deformation potential (DP) theory (black short-dashed line) [65],[195],[245]. The GW approximation is an approximation made to calculate the self-energy of a many-body system of electrons [65],[246]. The theoretical bandgap here is defined as the energy difference between the electron CB minimum and the HH of VB maximum at the Γ-point of the BZ (the HH/LH degeneracy of the VB is lifted owing to the strain anisotropy).

Thus, the nice agreement of the theoretical results with the experimental PL results show that the lower energy peak in the PL spectra originates from strained GaAs cores. Therefore, $E_1$ can be confidently associated to band-edge transition in tensile-strained core.

An empirical relation that describes the change of GaAs bandgap ($\Delta E_g$) at 12 K as a function of x is extracted from the linear dependence of $E_1$ on x in Figure 4.14 (b):

$$\Delta E_g = (-1.124 \pm 0.008)\, x \text{ eV} \quad (59).$$

The small deviation of this black short-dashed line (≈ 40 meV) with blue PL data points can be due to the presence of small quantization energy inside the thin GaAs core or radial confinement of photoexcited charge carriers.

However, still there is not a clear explanation for the $E_2$ peak ~40–50 meV higher in energy compared to $E_1$. Its origin is ambiguous but could be associated either with the complex radial profile of strain inside the core, which leads to complex localization patterns of carriers [247], or with unintentional composition/strain inhomogeneity. It is noted that $E_2$ appears even at 12 K if optical excitation power is high enough.

Further examinations for the nature of the radiative e-h recombination at $E_1$ were performed using the polarization-resolved PL spectroscopy as well as temperature dependent PL spectroscopy. In order to prove the HH character of this PL emission due to VB splitting, the polarization-resolved PL experiment on GaAs/$In_{0.39}Al_{0.61}As$ core/shell nanowires were performed. The transfer of nanowires from the original substrate onto Ge was done in a way that the nanowires remained reasonably-well oriented. The bulk selection rules dictate that HH emission is perpendicular to nanowire axis in ZB structures [245]. For the measurement, a λ/2 plate and a polarizer (specifically for the range of the green laser) were located in the light path before and after the nanowire sample, respectively. As shown in the polar plot of Figure 4.15 where the integrated intensity of $E_1$ is plotted as function of the polarization angle, $E_1$ is polarized perpendicular to the nanowire axis. This evidences that $E_1$ is indeed associated with recombination of electrons with HH [245].

Temperature dependent PL experiments were also performed, and the results are shown in Figure 4.16. The shift of the peak energy was successfully fitted (black line in Figure 4.16) with empirical Varshni equation [3]:

$$E_1(T) = E_1(T=0) - \frac{\mathrm{A}T^2}{T+B} \quad (60).$$

The two reasonable fitting parameters were found equal to A= $2.78\times10^{-4}$ eV/K and B=240.9 K. The agreement with Bulk GaAs values (A= $5.405\times10^{-4}$ eV/K and B= 204 K [3]) is in line with the interpretation that $E_1$ emission originates from the strained GaAs core in the nanowires.

It should be emphasized that the bandgap of GaAs at 12 K was reduced from the strain-free value of 1.52 eV to 0.91 eV for the highest strain (obtained for *x* = 0.54), i.e. a striking reduction by 40%. The same behavior was observed at 300 K, where the bandgap energy of strained GaAs (indicated with blue arrows in Figure 4.14 (a)) was reduced to 0.87 eV with increasing x to 0.54. This is particularly important for applications in optical fiber telecommunications because the emission from strained GaAs nanowires can now cover the 1.3 µm (O-band) and potentially the 1.55 µm (C-band) of telecommunication wavelengths. This is better illustrated in Figure 4.17 (the upper panel), where these results (blue data points) are also compared to the bandgap of strain-free ternary alloys (continuous curves). Although these experiments and discussion are focusing on the narrowest achievable bandgap for GaAs, all intermediate values should also be feasible by using shells with lower $L_S$ and/or lower x.

The tensile-strained GaAs core is expected to be accompanied by the shrinkage of the electron effective mass based on the theory. Assuming isotropic hydrostatic character of the strain, the related $m_e^*$ can be approximated using the pressure ($P$) dependent eq. (39) and eq. (40) [197], in which $dE_g$ is the change of the bandgap energy of $E_1$ imposed by a relative pressure $dP$. Based on the theory, it is expected that $m_e^*$ in GaAs core to be reduced with increasing x, reaching a value of $m_e^*$= 0.0448 $m_0$ at 300 K for the highest x with the assumption of isotropic hydrostatic strain. The shrinkage of bandgap up to 40% , as shown Figure 4.17 (the upper panel), in concert with the reduction of electron effective mass up to 30% for GaAs , as shown Figure 4.17 (the lower panel), are the novel findings in this work [65]. Indeed, the lowest achieved value of $m_e^*$ is in a close proximity to bulk $In_{0.53}Ga_{0.47}As$ which is traditionally used in HEMTs on lattice matched InP substrates (as shown in Figure 4.17 the lower panel).

Eventually, strained GaAs nanowires on Si substrates are very promising for HEMTs on Si substrate. Therefore, high-frequency photonics as well as high-mobility transistors could now be possible with strained GaAs nanowires and without the need for lattice-matched substrates.

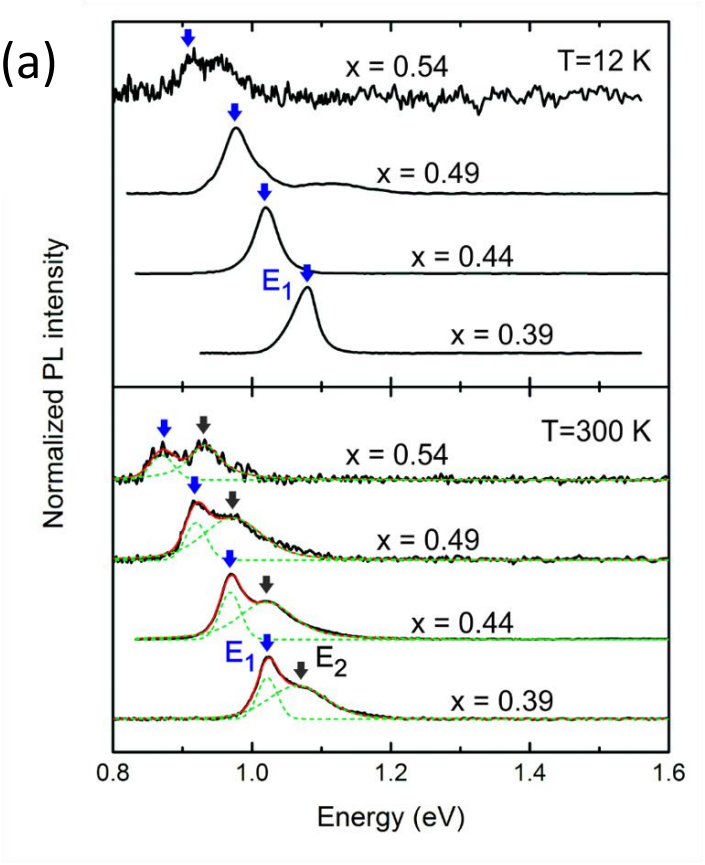


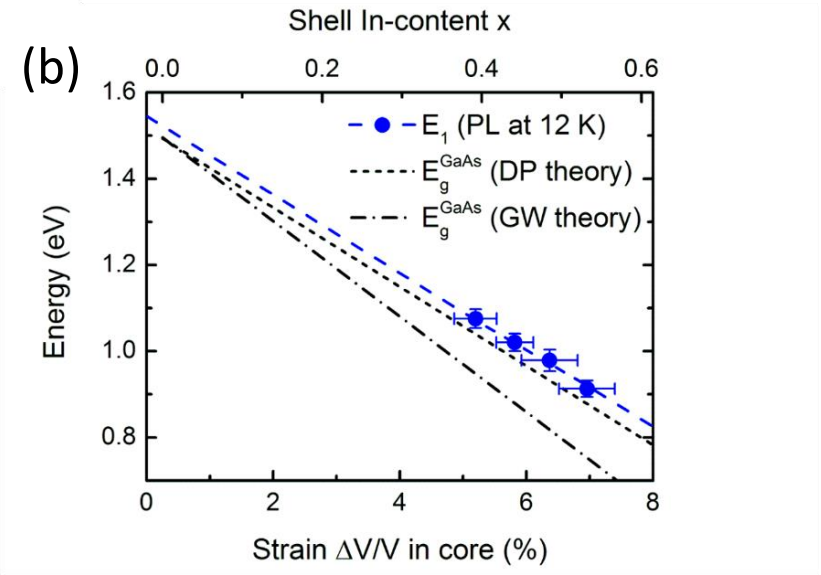


Figure 4.14 Large shrinkage of GaAs bandgap induced by tensile strain. (a) PL spectra at 12 K in upper panel and 300 K in lower panel for GaAs/$In_xAl_{1-x}As$ core/shell nanowires on ensemble of nanowires transferred onto the mentioned Ge substrate. (b) Theoretical calculations of bandgap based on the deformation potential (DP) theory as shown with the short-dashed line and its comparison with the PL experiment data points ($E_1$ peaks in blue) , the linear fit (in blue dashed line) of these blue data points and first-principles (GW; dash-dotted line) at low temperature.

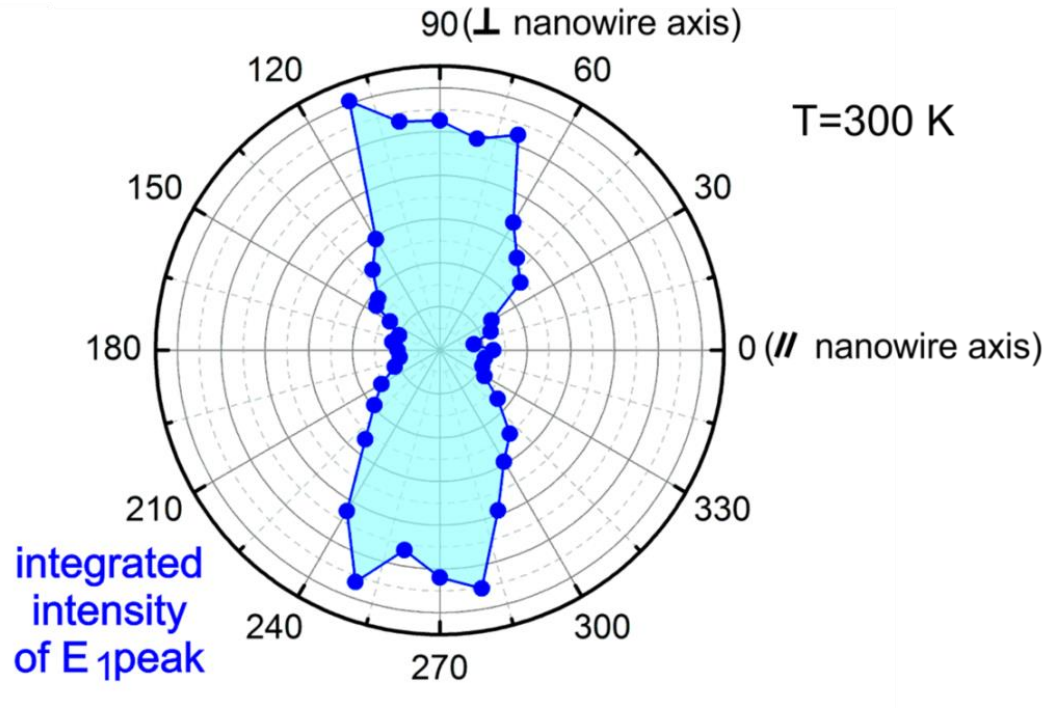


Figure 4.15 The polar plot extracted from polarization-resolved PL spectroscopy on GaAs/$In_{0.39}Al_{0.61}As$ core/shell nanowires at 300 K

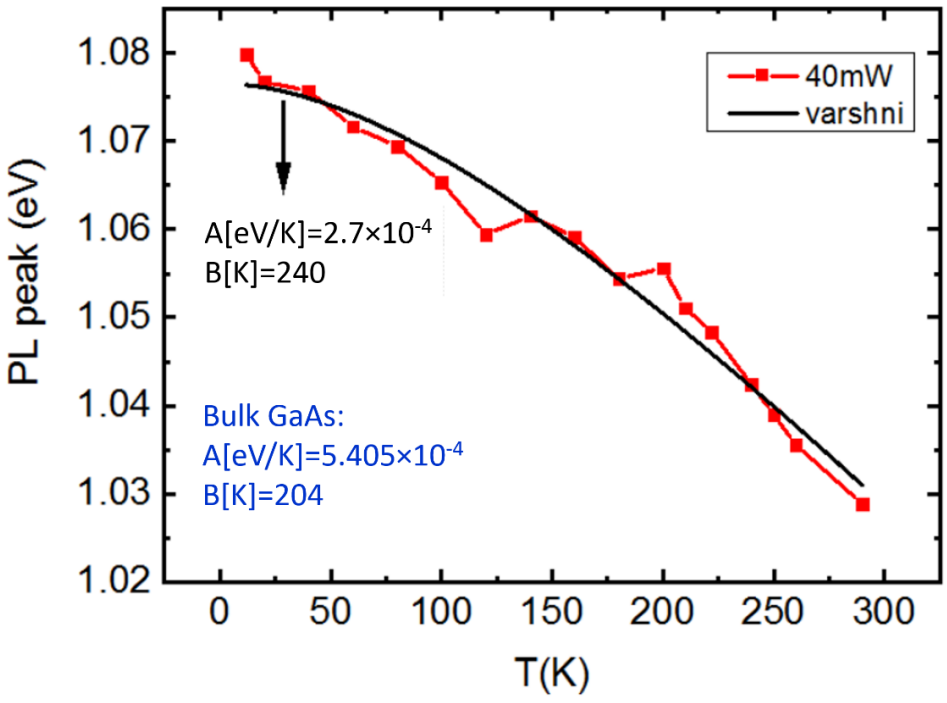


Figure 4.16 Temperature dependent PL spectroscopy on GaAs/$In_{0.39}Al_{0.61}As$ core/shell nanowires shows that, the $E_1$ peaks of PL originate from GaAs core because of the similarities between experimental data points (red colors) and the Varshni fitting (black colored curve) parameters (A and B in black) of GaAs. A and B parameters in blue color are the reported values for GaAs [3].

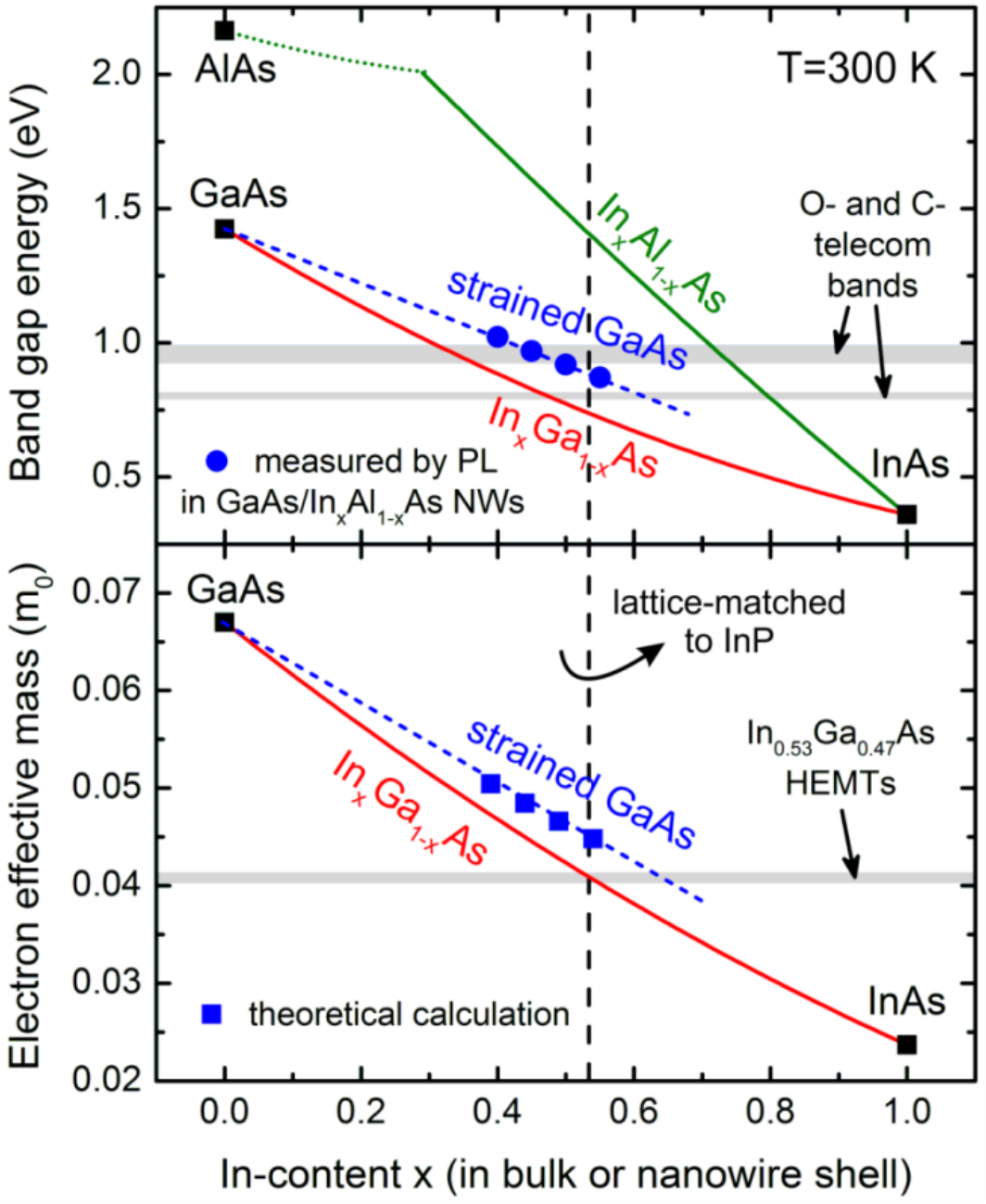


Figure 4.17 Summary of the findings: effect of strain on band gap and effective mass of electrons. The upper panel shows the bandgap energies ($E_1$) of strained GaAs in blue data points. The lower panel shows the corresponding electron effective mass at 300 K in blue data points with the assumption of isotropic- hydrostatic strain. The grey shadow belongs to the energy range proportional to low loss wavelengths of fiber optical systems in upper panel. The other grey shadow in the lower panel relates to the range for the effective mass of typical HEMTs on InP substrates.

### 4.5 Strain-enhanced electron mobility of GaAs nanowires higher than the bulk limit

Strain engineering (as a focus in this study) allows us to change the intrinsic properties of material (optical and electrical properties) and achieve novel functionalities, especially in nano scale regimes [248], [249], and [250]. In chapter 4.4, the changes of optical properties were demonstrated [65] and in this chapter the electron transport properties of nanowires, as studied by OPTPS, will be presented.

In principle, the growth of lattice-mismatched heterostructures is difficult, since strain can generate easily misfit-dislocations and other types of defects in an inappropriate growth design, which can degrade easily device performance like charge carrier mobility [251], [252]. Nevertheless, in coherently strained heterostructures, it has been already proven that the device performance can be substantially enhanced [253],[254],[255],[256].

Traditionally, to achieve HEMTs in planar systems, $In_xGa_{1-x}As$ is grown epitaxially on the available lattice-matched InP substrates, limiting the composition to around x=0.52. However, in the case of nanowires, owing to their high tolerance to strain, HEMTs with high crystal quality $In_xGa_{1-x}As$ material on Si substrates should be feasible with more freedom in the composition. It has been shown in chapter 4.4 that the very thin GaAs core (= 20-25 nm in diameter) in GaAs/$In_xGa_{1-x}As$ and GaAs/$In_xAl_{1-x}As$ core/shell nanowires on Si undergoes a very high hydrostatic tensile strain, even up to 7%. The built-in strain in the core results in a large reduction of GaAs bandgap up to 40%, which should be accompanied by a reduction of electron effective mass. That means that the strained GaAs as a binary material can have similar characteristics to $In_xGa_{1-x}As$, but without limiting factors that typically exist in ternary alloys, such as alloy scattering, surface segregation, and phase separation [65], [204], and [257].

Using OPTPS, the transport properties of photo-excited electrons have been investigated in the core of highly mismatched GaAs/$In_xAl_{1-x}As$ core/shell nanowires (which are undoped in this study) with a core diameter of around 20 nm.

After MBE growth, the nanowires were transferred from the Si substrates to z-cut quartz substrates (with zero photoconductivity in the range of 0-3.8 THz [49]). The nanowires distribution on the quartz substrate have been examined by dark-field optical microscopy [15]. As it is shown in Figure 4.18 (a), most of the nanowires are oriented in the same direction. In OPTPS, the transmitted THz-probe field and its change with and without optical-pump excitation were analyzed as a function of the pump-probe delay time. Here, nanowires were photo-excited with an optical laser pulse at 810 nm (1.53 eV) with 60 fs duration. The sensitivity of THz field

detector is at 0.2-2.7 THz. Details of the experimental setup have been described in chapter 3.5. The polarization of the optical pump has been kept parallel to the majority of nanowires axes while THz probe has been examined in both parallel and perpendicular to the nanowires axes as it is shown in the sketch of Figure 4.18 (b). It has been already documented that GaAs nanowires exhibit localized surface plasmon modes within the THz range[49], [227].

Since the electrons in the conduction band are faster than the holes in the valence band, the electrons have the major contribution to Drude or any Drude-like photoconductivity models [258] , [227]. The complex photo-induced conductivity ($\Delta\sigma(\omega)$) for generated free-carriers in the nanowires is given by

$$\Delta\sigma(\omega) = \frac{iN_e e^2 \omega}{m^*_{e-[111]}(\omega^2 - \omega_{0p}^2 + i\omega\gamma_e)} \qquad (61),$$

where $N_e$ is electron density, $\omega_{0p}$ is the resonant plasma frequency, and $\gamma_e$ is the momentum scattering frequency of the carriers [258], [227]. $\gamma_e$ is a crucial parameter for the calculation of the mobility, showing the randomization in the momentum of charge carriers due to any scattering source inside the crystal structure.

In $\Delta\sigma(\omega)$ spectra, like those shown in Figure 4.18 (c), the plasmon resonance frequency (indicated by the arrows) is related to $N_e$ by

$$\omega_{0p}(N_e) = \sqrt{\frac{gN_e e^2}{m^*_{e-[111]}\varepsilon_r \varepsilon_0}} \qquad (62),$$

where $g$ is a geometrical factor [227], $\varepsilon_r$ is the electric permittivity of the material in the THz range, $\varepsilon_0$ is the permittivity of free space, and $e$ is the electronic charge [259].

As it is shown in Figure 4.18 (a), most of the nanowires are oriented in the same direction. In Figure 4.18 (c), the fitted spectra to eq. (60) are illustrated and normalized $\Delta\sigma(\omega)$ in two different THz polarizations, parallel (the left column) and perpendicular (the right column) to nanowires axes, as well as the extracted real parts and imaginary parts of $\Delta\sigma(\omega)$ have been plotted for two delay times (0, and 100 ps). At the same pump-probe delay time, the amplitude of $\Delta\sigma(\omega)$ for the parallel-probed type is about one order of magnitude higher than the perpendicular one. Thus, the plasmon response depends on to the THz probe polarization and the depicted arrows in Figure 4.18 (c), show the position of $\omega_{0p}$. The presence of the longitudinal plasmon mode has been confirmed in this work, which agrees well with the other studies [49] and [260].

In Figure 4.18 (c), the shift of the $\omega_{0p}$ in these two delay times (while assuming a constant effective mass of electrons and geometrical factor) is a distinct feature of localized surface

plasmon model and a proof that carrier concentration is dropping to a lower potential (the strained GaAs core in this current work) by the increase of the delay time [261]. Other reasons for the down shift of $\omega_{0p}$ toward lower frequencies can be the reduction of the nanowire diameter or expansion of their length. Both of the mentioned reasons fail due to the uniform geometry of these nanowires [227].

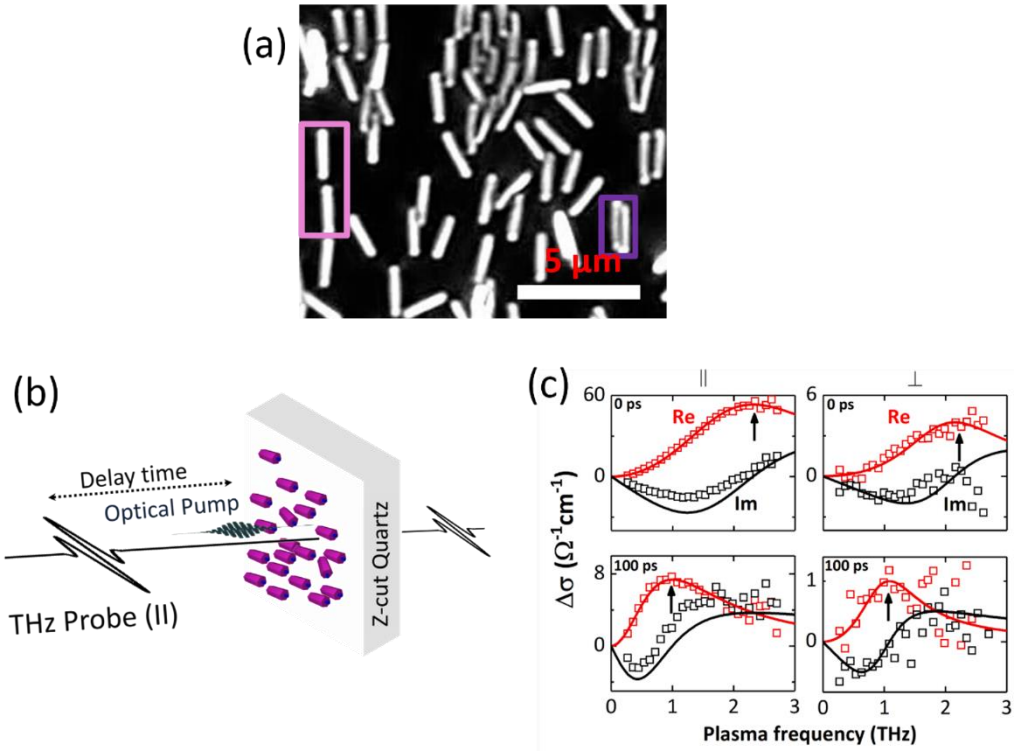


Figure 4.18 Measurement configuration for GaAs/$In_xAl_{1-x}As$/$In_{x+0.01}Ga_{1-x+0.01}As$ core/shell/capping layer nanowires (x=0.39-0.49, core diameter≈ 20 nm, $L_S$=80 nm, and capping layer = 5 nm). (a) Dark-field-optical micrograph of GaAs/$In_{0.49}Al_{0.51}As$/$In_{0.50}Ga_{0.50}As$ core/shell/capping layer nanowires placed flat on a quartz substrate (100× objective). Note: nanowires look thicker than the usual thickness due to the diffraction. (b) Simplified scheme of the experiment where the polarization of optical pump and THz probe are along the axes of nanowires. (c) Real part and imaginary part of photoconductivity in two types of a THz polarization (parallel and perpendicular polarized probe to the nanowire growth axes, in the left and right column, respectively). These experiments confirm longitudinal plasmon mode in the nanowires. The spectra belong to GaAs/$In_{0.49}Al_{0.51}As$/$In_{0.50}Ga_{0.50}As$ core/shell/capping layer nanowires.

The electron mobility ($\mu_{e-[111]}$) can be calculated by

$$\mu_{e-[111]} = \frac{e}{m^*_{e-[111]}\gamma_e} \qquad (63).$$

The experimental $\Delta\sigma(\omega)$ was fitted by a Lorentzian function in which the fitting parameters are $\omega_0$ and $\gamma_e$ in eq. (61). To calculate $N_e$, the $g$ (as a geometrical factor) is required which is

proportional to the aspect ratio of the nanowires. By the definition, $g$ relates to the geometry of nanowires and dielectric constant of nanowires and their surrounding medium. In these core/shell/cap nanowires, carriers were excited above the band gap of the core and capping layer in nanowires with x=0.39-0.49. However, the excitation energy of the pump is only above the shell band gap for nanowires with x=0.49 (Figure 4.19 (a)). Therefore, it is not so straight forward to predict the $g$ for the whole range of the pump-probe delay time (ps) due to the excitation of the core, shell, and capping layer for the corresponding samples. This parameter, $g$, is a time-transient parameter because of the temporal carrier dynamics varying immediately after optical pumping. Nevertheless, at the end, $g$ stabilizes until the carriers accumulate inside the GaAs core passing the initial transient phase due to the capping layer excitation or shell excitation, and surface of the core. To simplify this calculation for $N_e$ and $\mu_{e-[111]}$ inside the core, the transient phase has been neglected (this means that only delay times in which $\omega_{0p}$ reaches the least fluctuating state have been considered). Here, $g$= 0.01 is assumed, which is correlated to the effective filling factor (FF) as well as the equal aspect ratio of the nanowires with x=0.39-0.49 [227], [21], [262], and [263].

$$\frac{\partial ln\epsilon}{\partial P} = -17.3 \pm 0.3\ (10^{-3}\ GPa^{-1}) \quad (64).$$

G A Samara et al reported the effect of the hydrostatic pressure on the dielectric constant of GaAs at 300 K. Therefore, the $\varepsilon_r$ by assuming the hydrostatic tensile strain can be calculated. The amount of the corresponding hydrostatic pressure based on the bandgap energy of these nanowires can be extracted from the eq. (39) as N E Christensen et al reported [264]. Afterwards, the related $\varepsilon_r$ (see Figure 4.19) using the following equation by G A Samara et al can be obtained [259]. In eq. (62), $\varepsilon_r$ of the tensile-strained core was calculated using eq. (64). The calculated $\varepsilon_r$ values are approximate values.

The band alignment of GaAs/$In_xAl_{1-x}As$ core/shell nanowires (x=0.39-0.49) along $[1\bar{1}0]$ (radial direction; zero position at the center of the nanowire core) has been simulated using nextnano and the results are shown in Figure 4.20 (a). The three sets of curves correspond to x= 0.39, 0.44, and 0.49. The GaAs core can be distinguished from the lower band gap compared to the relaxed $In_xAl_{1-x}As$ shell, in which the bold square-like symbol (as an end of the red line) represents the energy level of optical pump laser. Only for the nanowires with x=0.49, both core and shell are under the pump excitation. For the nanowires with x=0.39 and x= 0.44, the shell excitation by optically pumping is not expected. The two vertical black arrows show the direction of energy change in both VBM and CBM due to the increasing tensile strain.

The corresponding band structure of the strained core (x=0.49) along the [111] direction has been simulated using nextnano (8 x 8 k.p model) at 12 K in Figure 4.20 (b). The comparison with strain-free GaAs (dashed line) shows the expected lift of the degeneracy at the VBM due to anisotropic character of strain (symmetry-breaking). The validity of these calculations is confirmed by the very good agreement between the theoretical calculation of band gap (black filled circles) which was shown in Figure 4.20 (c). and experimental PL bandgap energies of reported in chapter 8 (the grey cross symbols) at 12 K [65]. The effective mass of the electrons (at 300 K) at k = 0 have been calculated along [111] direction ($m^*_{e\_[111]}$) and plotted in Figure 4.20 (c). It should be reminded that the previous calculations of the electron effective mass in chapter 4.4 were upon the assumption of the isotropic hydrostatic strain. In this chapter the electron effective mass calculations are according to the experimental strain values with the anisotropic character. These new obtained $m^*_{e\_[111]}$ shows 39% reduction of the electron effective mass in strained GaAs as compared to the value of strain-free GaAs (0.0635 $m_0$).

By varying the time delay in OPTPS, the temporal evolution of $\omega_{0p}$ (thus, $N_e$) and $\gamma$ (thus, $\mu_e$) as shown in Figure 4.20 for GaAs/$In_{0.39}Al_{0.61}As$ nanowires ($L_S$ = 80 nm) can be probed. Here, carriers are excited only in the core and the capping layer. The comparison of the results for samples with and without the $In_{0.40}Ga_{0.60}As$ capping layer in Figure 4.21 (a) proves that the capping layer causes a fast decay of $N_e$ (regime highlighted in grey). This effect of the capping layer has been already reported by H. J. Joyce et al for GaAs/AlGaAs core/shell nanowires and has been attributed to carrier recombination at surface states of the capping layer [50]. In these nanowires, electrons in the capping layer recombine within the first ~ 20 ps with the characteristic lifetime of ~ 3 ps (from biexponential fit), whereas those in the core live much longer. The lifetime of electrons in the core is more reliably extracted from the mono-exponential fit of the nanowires without the capping layer (132 ps). The corresponding $\gamma$ and $\mu_e$ are shown in Figure 4.21 (b). After the capping layer-related transient, $\gamma_e$ and $\mu_e$ stabilize at ~ 1.1 THz and 6150 $cm^2$/Vs, respectively.

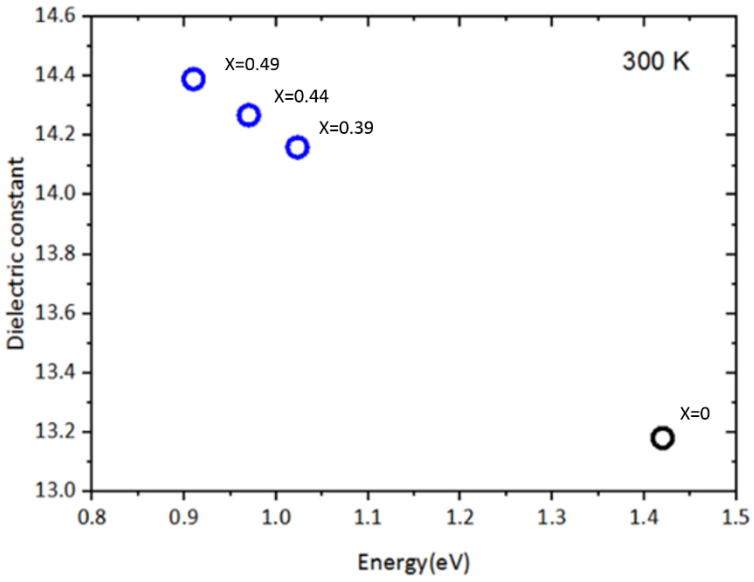


Figure 4.19 Dielectric constant ($\varepsilon_r$) of the tensile strained GaAs. The black data point belongs to strain-free GaAs and the blue ones to the corresponding tensile-strained GaAs. The x-axis is displayed the bandgap values for each nanowire sample with x=0.39-0.49.

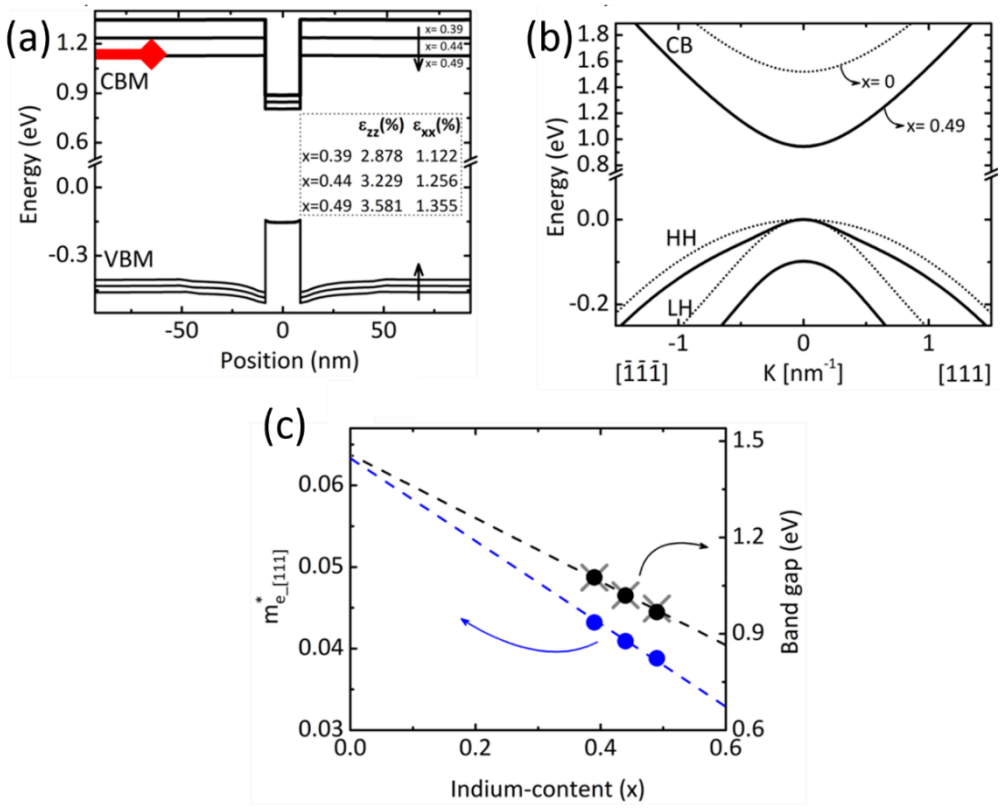


Figure 4.20 Band parameters of the strained GaAs. (a) Real space band alignment of the strained core and relaxed shell for x= 0.39, 0.44, and 0.49 at 300 K with the table of experimental strain values of each x. (b) Band structure (in K space) of the strained core (x=0.49) and strain-free GaAs at 12 K. (c) The $m^*_{e-[111]}$ (blue filled circles) along [111] at 300 K and band gap calculations (black filled circles) at 12 K are shown and the grey cross symbols are representative band gap energies from experimental PL at 12 K.

The measurements on nanowires of the same type at different pump fluences, as well as on the nanowires with x= 0.44 and x= 0.49 are continued. As shown in Figure 4.22, the corresponding $\mu_e$ vs. $N_e$ data exhibit significant scattering in the range of 4000 to 6000 cm$^2$/Vs without any obvious dependence on x. For comparison, results from unstrained GaAs/AlGaAs nanowires with a core diameter of 20 nm are also shown.

The scattering of the measurements is attributed to proximity effects in the dense nanowire ensembles. We have observed that larger $\gamma_e$ (lower $\mu_e$) are measured for denser nanowire ensembles, where the nanowires can be in close proximity or even in contact with each other. Two examples are shown in Figure 4.23 (a) and (b), where the nanowire density is indicated by the filling factor (FF). To understand the effect of nanowire proximity on $\gamma_e$ (width of $\Delta\sigma(\omega)$ resonance) COMSOL simulations for two types of nanowire alignments, either in series or in parallel have been performed. As shown in in Figure 4.23 (c), nanowires in series shift the resonance to lower frequencies, whereas nanowires in parallel shift the resonance to higher frequencies. Consequently, a random combination of nanowire alignments would result in a broadening of the spectrum, which is measurable as an increased $\gamma_e$ (decreased $\mu_e$). Compared to the literature, these mobility values are the highest reported values for GaAs nanowires, exceeding even the value for strain-free bulk GaAs (2000-4500 cm$^2$/Vs,[50], [265]). The second highest value (3000 cm$^2$/Vs) has been reported for lattice matched GaAs/AlGaAs core/shell nanowires with a core diameter of 50 nm [37]. After all, strained GaAs/InAlAs nanowires appear to be promising candidates for the realization of HEMTS.

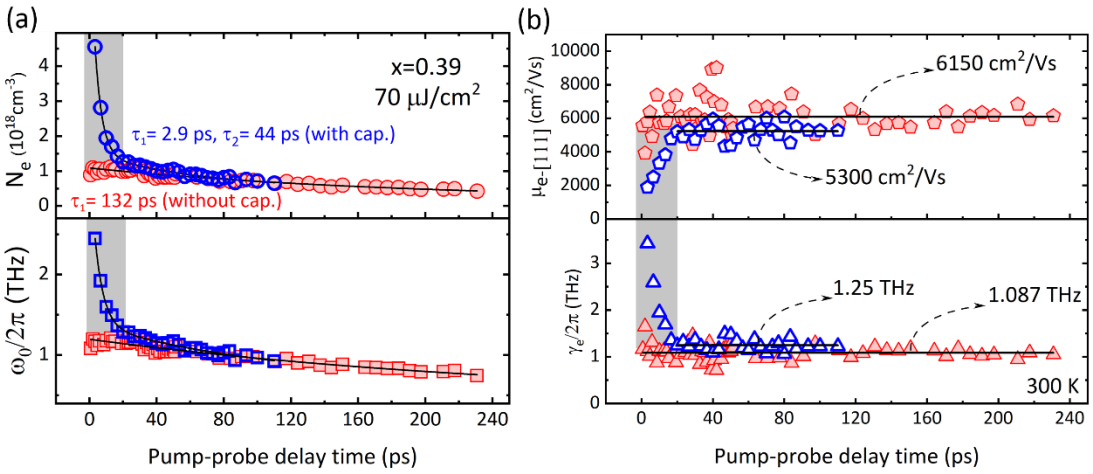


Figure 4.21 Electron transport properties of GaAs/$In_{0.39}Al_{0.61}As$ core/shell nanowires with/without capping layer (blue/red colored data points, respectively). (a) $N_e$ (in the upper panel with the error bar of ~ $3\times10^{16}$ $cm^{-3}$) and plasma frequency (in the lower panel with the error bar of ~ 0.3 THz) vs. delay time and extracted carrier relaxation life times by a mono-exponential fitting profile are shown (for 70 μJ/$cm^2$). (b) $\mu_e$ and scattering frequency of charge carriers for 70 μJ/$cm^2$ are also plotted (with the error bar of ~ 900 $cm^2$/Vs and ~ 0.5 THz, respectively). The average mobility and scattering frequency values for both samples with/without capping layer are pointed by the curved arrows (in (b)) within the delay time range inside the stable phase meaning after passing the transient phase originating from the capping layer (shown by a grey colored highlight in panels of (a) and (b)).

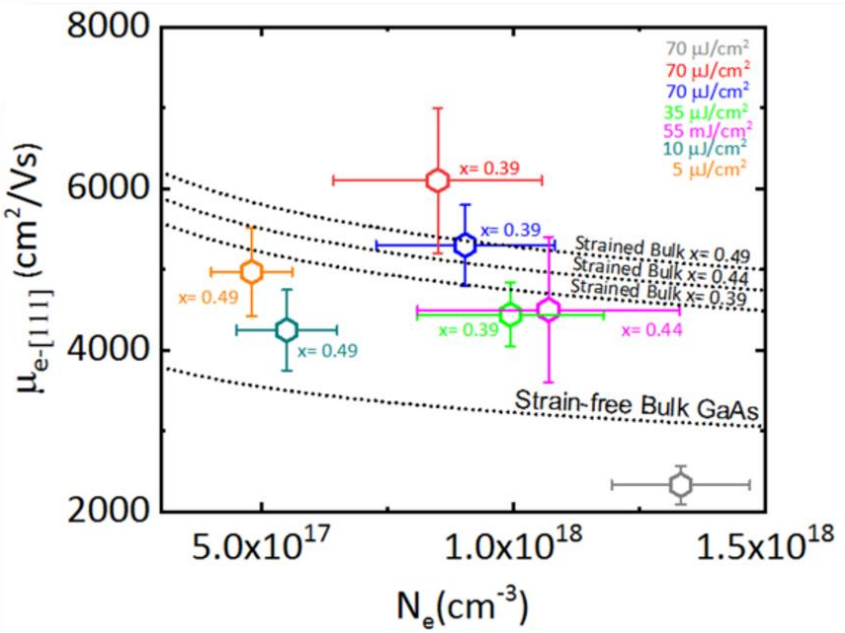


Figure 4.22 Electron mobility of strained GaAs above strain-free bulk GaAs at 300 K. Comparison of average electron mobility for every nanowire sample (x=0.39-0.49) where the average mobilities are above predicted strain-free bulk GaAs (dotted line). For nanowires with x=0.39, the average mobility values exceed the expected values of strained bulk GaAs (dotted lines). The red and magenta data points belong to the nanowires without capping layer. The grey data point belongs to GaAs/$Al_{0.30}Ga_{0.70}As$ core (22nm)/shell ($L_S$=80nm) nanowires. Note: the error bars relate to the fluctuations of the real data points.

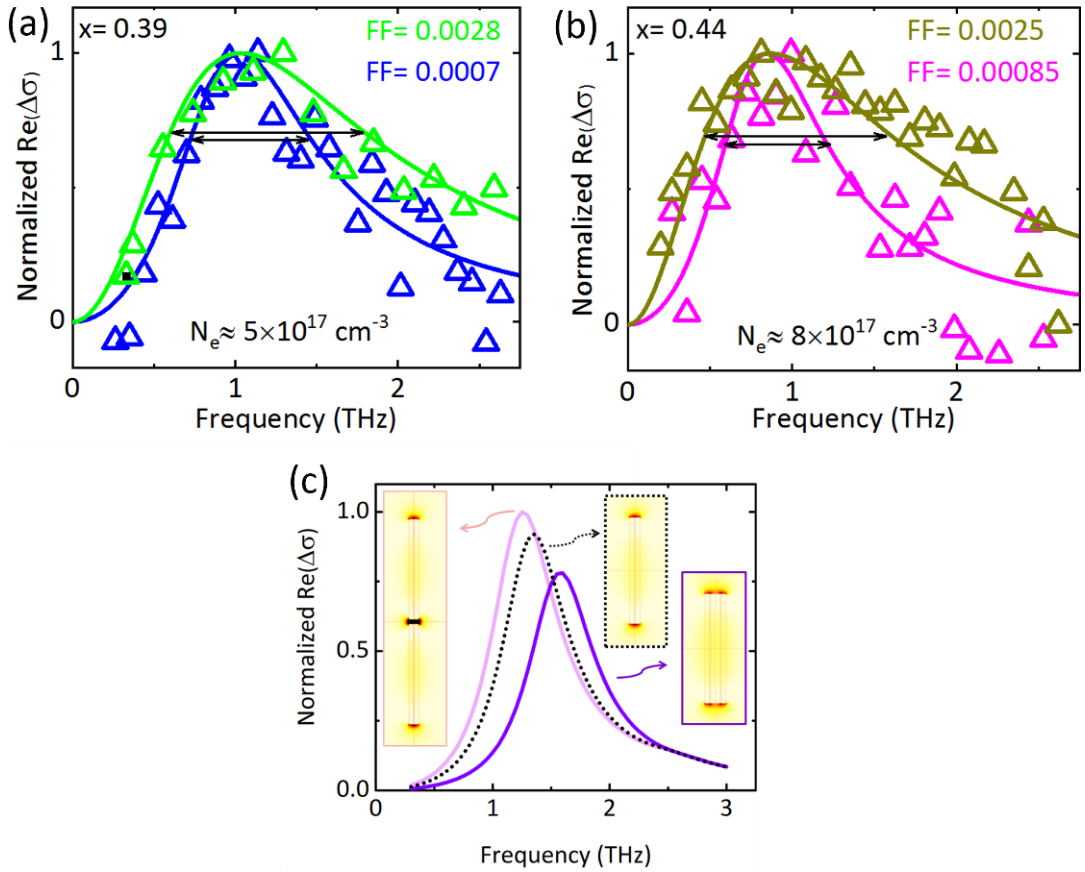


Figure 4.23 Close proximity effect of nanowires causing broadening of plasmon and consequently its effect on $\mu_e$. (a), (b) Re(Δσ) in a dense (FF=0.003, 0.0025) and dilute area (FF=0.0005, 0.0005) of the sample with x=0.44, and x= 0.39, respectively. (c) Numerical simulation of Re(Δσ) on a single nanowire shows the shift of the plasmon resonance depending on the alignment of two nanowires (in series or parallel). This COMSOL simulation has been carried out by Ivan Fotev.

### 4.6 Towards high electron mobility transistors

The core/shell nanowires which have been studied in the previous chapters could be potentially employed in modulation-doped heterostructures, for the realization of FET for future electronic applications. To that end, two designs of modulation-doped heterostructures have been modeled using nextnano (Self-consistent solver of Schrödinger and Poisson equations). The first one is schematically depicted in Figure 4.24 (a) and consists of 1) the GaAs core (20 nm in diameter), 2) a 40 nm thick $In_{0.45}Ga_{0.55}As$ shell to serve as an electron conduction channel, 3) a 40 nm thick $In_{0.44}Al_{0.56}As$ shell, which is delta-doped with Si (doping concentration of $4.5\times10^{12}$ $cm^{-2}$) at a distance of 10 nm (so-called spacer) from $In_{0.45}Ga_{0.55}As$ channel, and 4) a 5 nm thick $In_{0.45}Ga_{0.55}As$ to serve as a capping layer to prevent oxidation of the Al-containing shell. Figure 4.24 (b) and (c) show the simulation results in the (111) plane (nanowire cross-section) and along [11-2], respectively. A confinement of the electrons takes place in $In_{0.45}Ga_{0.55}As$ shell, next to the interface with $In_{0.44}Al_{0.56}As$ shell. A higher concentration of electrons is formed at the six corners. Such a higher electron confinement at the corners have been observed for the conventional GaAs/AlGaAs core/shell nanowires. These charge densities are due to the occupation of an increasing number of energy subbands. While the doping level is rising, these subbands fall more and more below the Fermi level.

A Bertoni et al showed that the spatial distribution of electron and hole gases inside the core of GaAs/AlGaAs core/shell nanowires can be tuned as a function of the doping density [266]. They simulated that at lower doping levels, electrons are localized deep into the core rather than corners. As they reported, by increasing the doping level, a depletion of carriers emerges at the center of the core, and the carriers move closer to the interface with the shell forming a six-fold symmetry and for the large doping levels, the charges are strongly localized at the six corners of the core. This is the situation that it was also observed in the simulations of this work for $GaAs/In_{0.45}Ga_{0.55}As/In_{0.44}Al_{0.56}As/In_{0.45}Ga_{0.55}As$ nanowires. The new feature in the 2DEG distribution as shown in Figure 4.24 (b) is the three-fold symmetry instead of six-fold symmetry which is the typical case for 2DEG systems in GaAs/AlGaAs core/shell nanowires. The origin of this feature is from the enhancement of piezoelectric field induced by strain [267]. After all, such a higher electron confinement at the corners opens up the possibility for new studies on 1D electron channels related to quantum transport, and quantum information investigations [203] and [268].

The equivalent band diagram along the x axis in Figure 4.24 (b) (from the center of one facet, through the center of the core, to the center of the opposite facet) is plotted in Figure 4.24 (c). The formation of the triangular well in CB (red curve) close to the $In_{0.45}Ga_{0.55}As/In_{0.44}Al_{0.56}As$

interface results in the formation of a 2DEG (or a quasi-1DEG, if the limited lateral dimension of the nanowire facets) inside the $In_{0.45}Ga_{0.55}As$ channel is considered. The corresponding electron concentration is also plotted (black curve) showing the peak of electron distribution at the interface inside the generated quantum well. Other properties that one can see in this band diagram, is the VB splitting especially inside the GaAs core which was expected due to the presence of strain anisotropy as described in chapter 4.4. Furthermore, the inversion between HH/LH inside the $In_{0.45}Ga_{0.55}As$ channel close to the interface with the core, which can be attributed to the existence of the compressive strain inside shell. A similar effect in the band diagram has been reported for compressively strained GaSb nanowires [187]. The band inversion as a result of strain engineering in the nanowires of this study introduces the possibility of using LH instead of HH [269].

In chapter 4.4, it has been shown that electronic properties of strained GaAs are very similar to $In_xGa_{1-x}As$, thus this stimulates the idea of having strained GaAs as the 2DEG channel as an alternative to $In_xGa_{1-x}As$. In the second design, the InGaAs shell is omitted as shown in Figure 4.25 (a). The corresponding band diagram of this new material structure is shown in Figure 4.25 (b). The electron concentration in CB peaks at the center of the strained core, which represents the formation a quasi-1DEG. The inversion of VBM between HH and LH next to the GaAs/InAlAs interface is, most likely, an artifact due to the low resolution of the meshing in the simulation.

After all, the aforementioned results appear to be very promising for the fabrication of nanowire HEMTs. Furthermore, the confined electron gas inside such 1D-like structures is anticipated to extend mesoscopic studies of conductance quantization, e.g. by quantum point contacts, as well as magneto transport investigations [30], [203], [270], [271].

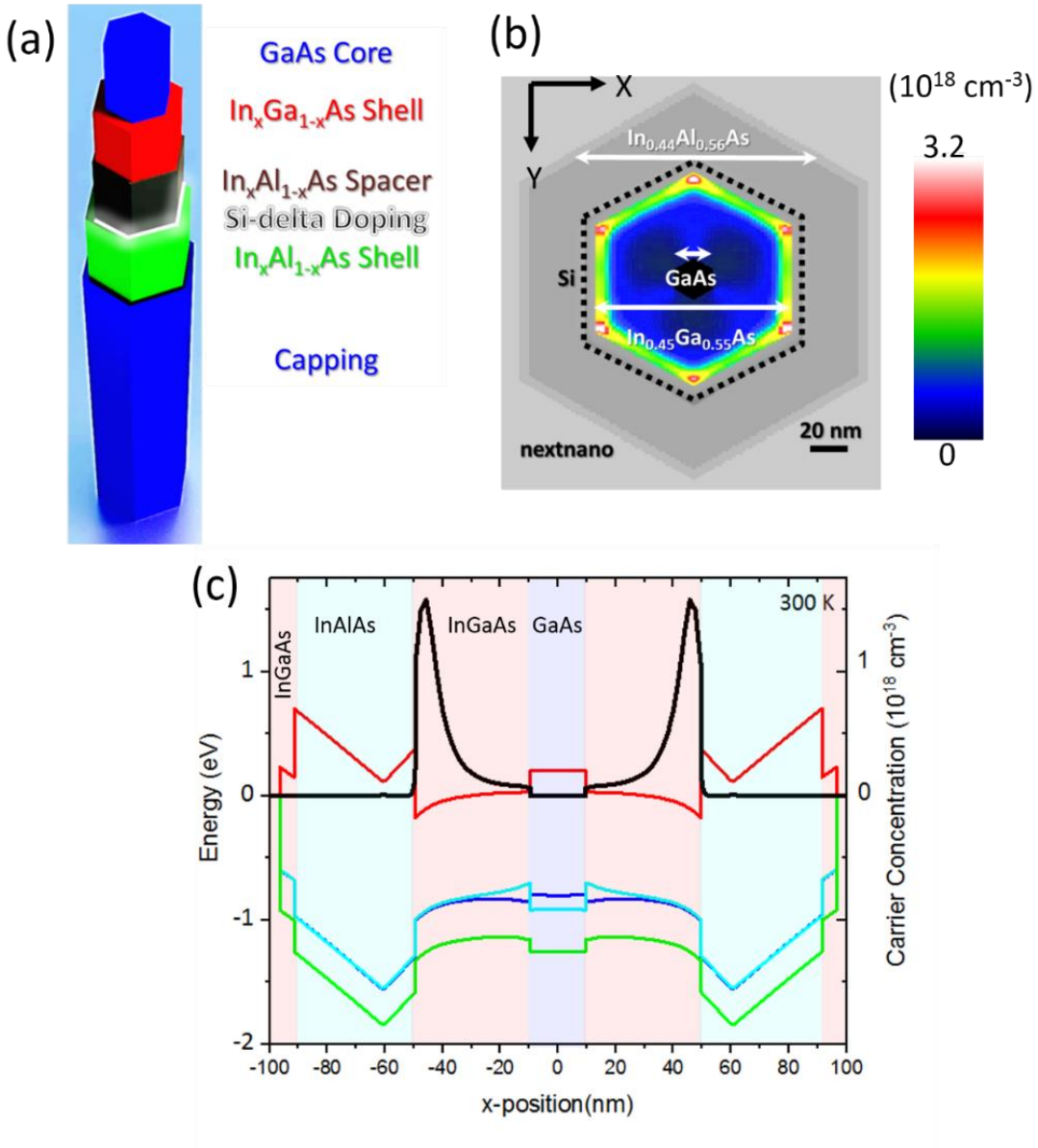


Figure 4.24 (a) Schematic representation of a modulation-doped nanowire heterostructure with InGaAs channel. (b) Simulated 2D spatial distribution of electrons. The color scale and the corresponding electron density are also shown. (c) Simulated band alignment and electron concentration along the x-axis (through the center of the core at x=0). VBM for LH, HH, and SO are shown in cyan, blue, and green curves, respectively. The red and black curves correspond to the CBM and the electron concentration, respectively. All simulations were performed with nextnano.

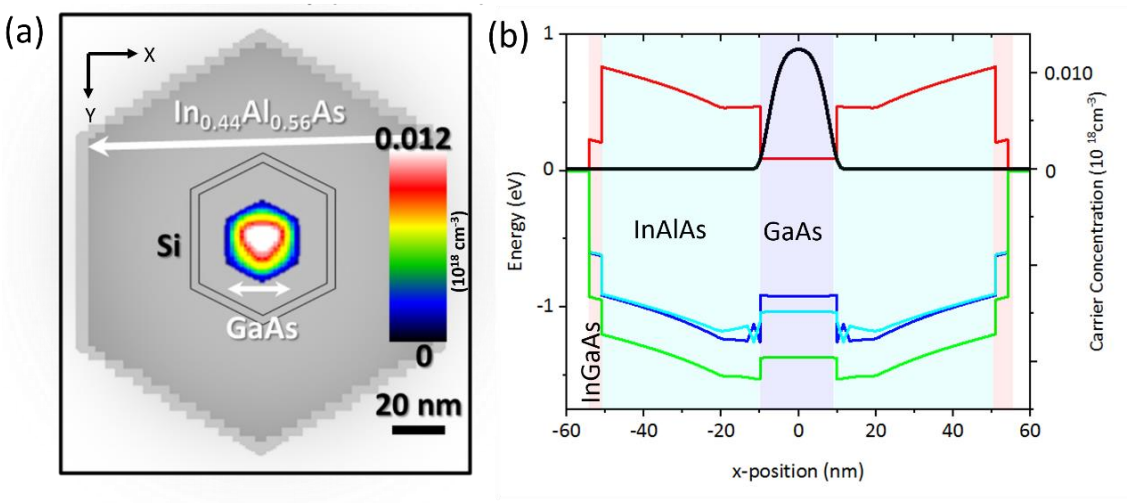


Figure 4.25 Simulation results for a modulation-doped nanowire heterostructure with strained GaAs channel. (a) Simulated 2D spatial distribution of electrons. The color scale and the corresponding electron density are also shown. (b) Simulated band alignment and electron concentration along the x-axis (through the center of the core at x=0). VBM for LH, HH, and SO are shown in cyan, blue, and green curves, respectively. The red and black curves correspond to the CBM and the electron concentration, respectively. All simulations were performed with nextnano.

Due to the limited time of the PhD, it was not possible to develop the processing methods which are necessary for the fabrication of FETs. Only the fabrication of ohmic contacts was initiated and the perliminary results are shown here. Instead of the modulation doped nanowires, a simpler structure of GaAs/$In_{0.45}Ga_{0.55}As$ core/shell nanowires with a homogeneously doped shell with Si was used. The process was as follows:

1. Mechanical transfer of nanowires onto a $SiO_2$(300 nm)/Si substrate
2. Identification of the position of selected nanowires using substrate markers
3. Spin coating of the photoresist
4. EBL
5. Development by IPA
6. Oxide etching (15s with 1:10 HCl: DI-water, 30s DI-water, drying with $N_2$)
7. Immediate transfer to the metal evaporator
8. Deposition of Ti/Pd/Au (18 nm/36nm/180nm)
9. Lift-off by acetone

Ti/Pd/Au metal contacts for n-type InGaAs have been commonly reported to exhibit very low resistance [228], [272], [273]. Therefore, the same metalization scheme was used on single nanowires for this project . An example of a contacted nanowire is shown in the SEM image of Figure 4.26 (a). After the contact fabrication, RTA steps were performed at various temperatures in $N_2$ atmosphere, followed by IV measurements. The effect of the annealing

temperature on the IV characteristics, is shown in Figure 4.26 (b). The total resistance decreased with increasing the temperature up to 340˚C, without any obvious degradation of the nanowires. The ohmic behaviour also improved with temperature. Further work is required on the characterization of the ohmic contacts, such as temperature dependent IV or transmission line model measurements [228], [274]. HR-TEM and EDX analyses would be helpful to investigate the metal diffusion into the nanowires and the metal-semiconductor contact quality [275].

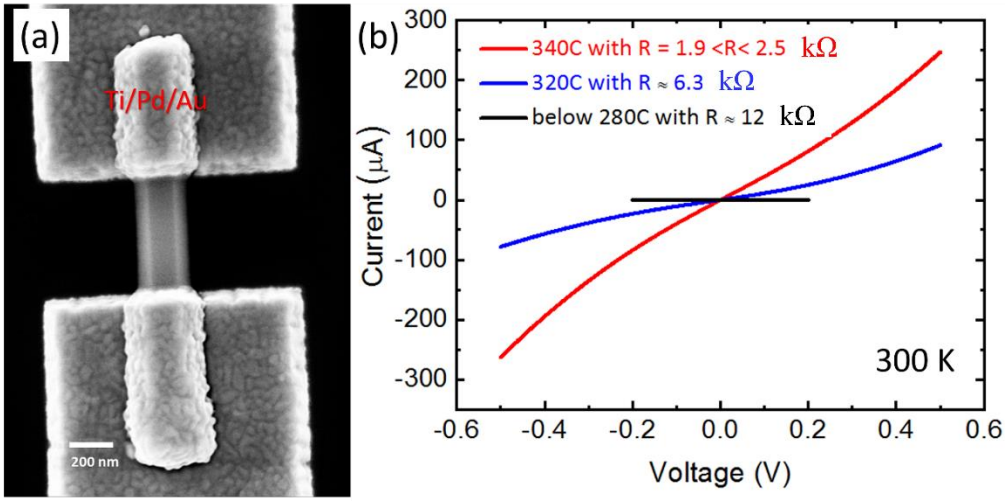


Figure 4.26 (a) Ti/Pd/Au metal contacts on both ends of GaAs/$In_{0.4}$ $Ga_{0.55}$As core/shell nanowires (20 nm core size and $L_S$= 80 nm with a homogeneous Si-doped shell : $9\times10^{18}$ $cm^{-3}$). (b) I-V plot at 300 K showing the improvement of the conductivity by increasing the RTA.

## 5 Conclusion and outlook

Strain engineering in core/shell nanowires can be an alternative route to tailor the properties of III-V semiconductors without changing their chemical composition. In particular, it is demonstrated that the GaAs core in GaAs/$In_xGa_{1-x}As$ or GaAs/$In_xAl_{1-x}As$ core/shell nanowires can sustain unusually large misfit strains (as shown in chapter 4.3) that would have been impossible in equivalent thin-film heterostructures, and results in a significant modification of its electronic properties (as shown in chapter 4.4 and 4.5).

Self-catalyzed GaAs/$In_xGa_{1-x}As$ and GaAs/$In_xAl_{1-x}As$ core/shell nanowires were grown on $SiO_x$/Si(111) by MBE (as shown in chapter 3.8). The growth conditions were optimized in order to minimize the bending of the nanowires, a phenomenon that originates from the large misfit between the core and the shell (as shown in chapter 4.2). Synchrotron XRD and Raman scattering measurements showed that for a given core diameter, the magnitude and the spatial distribution of the built-in misfit strain can be regulated via the composition and the thickness of the shell (as shown in chapter 4.3). Beyond a critical shell thickness, a heavily tensile-strained core and a strain-free shell (as shown in chapter 4.3) are obtained. The tensile strain of the core exhibits an anisotropic-hydrostatic character (as shown in chapter 4.4) and causes the reduction of the GaAs band gap energy (as proved by PL experiments) in accordance with the theoretical predictions reaching, the remarkable value of 40 % (0.87 eV at 300 K) for 7 % of strain in nanowires with x=0.54 (as shown in chapters 4.3 and 4.4). Signatures of valence-band splitting were also identified in polarization-resolved PL measurements, as a result of the strain anisotropy in GaAs (as shown in chapter 4.4). The achieved bandgap reduction makes GaAs nanowires suitable for photonic devices across the NIR range, including telecommunication photonics at 1.3 and potentially 1.55 µm, with the extra possibility of monolithic integration in Si CMOS (as shown in chapter 4.4).

The tensile strain induced shrinkage of the electron effective mass in the GaAs core, the value of which was extracted by band structure simulations (as shown in chapter 10). The electron transport properties were assessed by OPTPS. The unprecedented range of very high electron mobility values of 6150 $cm^2/Vs$ for an electron concentration $9 \times 10^{17}$ $cm^{-3}$ in the strained core, higher than the bulk GaAs, at 300 K was achieved (as shown in chapter 4.5). The high electron mobility in strained GaAs nanowires/Si opens new possibilities for HEMT designs that could replace the planar $In_{0.44}Al_{0.56}As/In_{0.52}Ga_{0.48}As$/InP devices. To that end, new designs of modulation doped GaAs/$In_{0.45}Ga_{0.55}As/In_{0.44}Al_{0.56}As$ core/multi-shell nanowires were modeled and different electron distribution schemes were suggested (as shown in chapter 4.6).

The results presented here could be extended with further optical and electrical characterization of the core/shell nanowires. Temperature-dependent PL experiments on single GaAs/InGaAs (InAlAs) core/shell nanowires can be continued to understand the origin of the secondary PL peaks observed in the present study. Lasing in NIR regime could be an intriguing possibility [205], which could be pursued by PL experiments on single nanowires. The electron transport properties of homogeneously Si-doped shells in the core/shell nanowires can be also probed in a systematic study including Raman spectroscopy in combination with OPTPS [276]. The temperature dependent Raman and THz spectroscopy on these nanowires may allow us to understand the scattering mechanism of the electrons and the electron dynamics in both the relaxed shell and the strained core [31]. In THz spectroscopy, broadening of plasmon due to close proximity effect of nanowires can be studied in more detail, to elucidate the plasmonic interactions in nanowire behaviors.

The investigation of transport properties in modulation doped nanowires could be performed optically could be (by OPTPS) or electrically [30], [45]. For the fabrication of ohmic contacts, the work initiated in this thesis should be completed with more RTA experiments on nanowires with different doping levels and schemes. Performing Hall Effect measurements on a single nanowire including a 2DEG at very low temperature, e.g. in the mK or μK regime would allow investigations on 1-D transport that could be potently employed in quantum information technology [270],[277],[278],[268]. It will be also intriguing to compare the transport properties (e.g. electron mobility) of these nanowires obtained by using the Hall Effect measurements with those found by OPTPS. Of course, the ultimate goal is the fabrication and characterization of FETs.

**Bibliography**

[1] D. A. B. Miller, “Optical interconnects to electronic chips,” *Appl. Opt.*, vol. 49, no. 25, p. F59, Sep. 2010, doi: 10.1364/AO.49.000F59.

[2] H. Kim, A. C. Farrell, P. Senanayake, W.-J. Lee, and D. L. Huffaker, “Monolithically Integrated InGaAs Nanowires on 3D Structured Silicon-on-Insulator as a New Platform for Full Optical Links,” *Nano Lett.*, vol. 16, no. 3, pp. 1833–1839, Mar. 2016, doi: 10.1021/acs.nanolett.5b04883.

[3] I. Vurgaftman, J. R. Meyer, and L. R. Ram-Mohan, “Band parameters for III–V compound semiconductors and their alloys,” *J. Appl. Phys.*, vol. 89, no. 11, p. 5815, 2001, doi: 10.1063/1.1368156.

[4] P. C. Eng, S. Song, and B. Ping, “State-of-the-art photodetectors for optoelectronic integration at telecommunication wavelength,” *Nanophotonics*, vol. 4, no. 3, Jan. 2015, doi: 10.1515/nanoph-2015-0012.

[5] V. Palankovski and R. Quay, *Analysis and Simulation of Heterostructure Devices*. Vienna: Springer Vienna, 2004.

[6] M. A. Green, Y. Hishikawa, E. D. Dunlop, D. H. Levi, J. Hohl-Ebinger, and A. W. Y. Ho-Baillie, “Solar cell efficiency tables (version 52),” *Prog. Photovoltaics Res. Appl.*, vol. 26, no. 7, pp. 427–436, Jul. 2018, doi: 10.1002/pip.3040.

[7] C.-Z. Ning, L. Dou, and P. Yang, “Bandgap engineering in semiconductor alloy nanomaterials with widely tunable compositions,” *Nat. Rev. Mater.*, vol. 2, no. 12, p. 17070, Dec. 2017, doi: 10.1038/natrevmats.2017.70.

[8] F. Glas, C. Gors, and P. Hénoc, “Diffuse scattering, size effect and alloy disorder in ternary and quaternary III–V compounds,” *Philos. Mag. B*, vol. 62, no. 4, pp. 373–394, Oct. 1990, doi: 10.1080/13642819008215242.

[9] A. Dimoulas, A. Derekis, G. Kyriakidis, and A. Christou, “Alloy disorder effects in III–V ternaries studied by modulation spectroscopy,” *Appl. Surf. Sci.*, vol. 50, no. 1–4, pp. 353–358, Jun. 1991, doi: 10.1016/0169-4332(91)90197-R.

[10] R. Alcotte *et al.*, “Epitaxial growth of antiphase boundary free GaAs layer on 300 mm Si(001) substrate by metalorganic chemical vapour deposition with high mobility,” *APL Mater.*, vol. 4, no. 4, p. 046101, Apr. 2016, doi: 10.1063/1.4945586.

[11] V. Deshpande *et al.*, “Three-dimensional monolithic integration of III–V and Si(Ge) FETs for hybrid CMOS and beyond,” *Jpn. J. Appl. Phys.*, vol. 56, no. 4S, p. 04CA05, Apr. 2017, doi: 10.7567/JJAP.56.04CA05.

[12] E. A. Fitzgerald *et al.*, “Monolithic III-V/Si integration,” in *2008 9th International Conference on Solid-State and Integrated-Circuit Technology*, Oct. 2008, pp. 1421–1424, doi: 10.1109/ICSICT.2008.4734819.

[13] D.-M. Geum *et al.*, “Ultra-high-throughput Production of III-V/Si Wafer for Electronic and Photonic Applications,” *Sci. Rep.*, vol. 6, no. 1, p. 20610, Feb. 2016, doi: 10.1038/srep20610.

[14] L. Balaghi *et al.*, “Droplet-confined alternate pulsed epitaxy of GaAs nanowires on Si substrates down to CMOS-compatible temperatures,” *Nano Lett.*, vol. 16, no. 7, pp. 4032–4039, 2016, doi: 10.1021/acs.nanolett.6b00527.

[15] T. Tauchnitz *et al.*, “Decoupling the Two Roles of Ga Droplets in the Self-Catalyzed Growth of GaAs Nanowires on SiO x /Si(111) Substrates,” *Cryst. Growth Des.*, vol. 17, no.

10, pp. 5276–5282, Oct. 2017, doi: 10.1021/acs.cgd.7b00797.

[16] J. Treu *et al.*, "Widely tunable alloy composition and crystal structure in catalyst-free InGaAs nanowire arrays grown by selective area molecular beam epitaxy," *Appl. Phys. Lett.*, vol. 108, no. 5, 2016, doi: 10.1063/1.4941407.

[17] M. Heiss, B. Ketterer, E. Uccelli, J. R. Morante, J. Arbiol, and A. Fontcuberta i Morral, "In(Ga)As quantum dot formation on group-III assisted catalyst-free InGaAs nanowires.," *Nanotechnology*, vol. 22, no. 19, p. 195601, 2011, doi: 10.1088/0957-4484/22/19/195601.

[18] E. Dimakis *et al.*, "Coaxial multishell (In,Ga)As/GaAs nanowires for near-infrared emission on Si substrates," *Nano Lett.*, vol. 14, no. 5, pp. 2604–2609, 2014, doi: 10.1021/nl500428v.

[19] B. Mayer *et al.*, "Lasing from individual GaAs-AlGaAs core-shell nanowires up to room temperature," *Nat. Commun.*, vol. 4, no. 1, p. 2931, Dec. 2013, doi: 10.1038/ncomms3931.

[20] R. B. Lewis, L. Nicolai, H. Küpers, M. Ramsteiner, A. Trampert, and L. Geelhaar, "Anomalous strain relaxation in core-shell nanowire heterostructures via simultaneous coherent and incoherent growth," *Nano Lett.*, vol. 17, pp. 136–142, 2017, doi: 10.1021/acs.nanolett.6b03681.

[21] J. L. Boland *et al.*, "Modulation Doping of GaAs/AlGaAs Core-Shell Nanowires With Effective Defect Passivation and High Electron Mobility.," *Nano Lett.*, vol. 15, no. 2, p. 1336−1342, Jan. 2015, doi: 10.1021/nl504566t.

[22] P. Krogstrup *et al.*, "Single-nanowire solar cells beyond the Shockley–Queisser limit," *Nat. Photonics*, vol. 7, no. 4, pp. 306–310, Apr. 2013, doi: 10.1038/nphoton.2013.32.

[23] M. Montazeri *et al.*, "Direct Measure of Strain and Electronic Structure in GaAs / GaP Core - Shell Nanowires," *Nano Lett.*, vol. 10, pp. 880–886, 2010, doi: 10.1021/nl903547r.

[24] M. Hocevar *et al.*, "Residual strain and piezoelectric effects in passivated GaAs/AlGaAs core-shell nanowires," *Appl. Phys. Lett.*, vol. 102, no. 19, p. 191103, May 2013, doi: 10.1063/1.4803685.

[25] M. Hetzl *et al.*, "Strain-Induced Band Gap Engineering in Selectively Grown GaN-(Al,Ga)N Core-Shell Nanowire Heterostructures," *Nano Lett.*, vol. 16, no. 11, pp. 7098–7106, 2016, doi: 10.1021/acs.nanolett.6b03354.

[26] J. Treu *et al.*, "Enhanced Luminescence Properties of InAs–InAsP Core–Shell Nanowires," *Nano Lett.*, vol. 13, no. 12, pp. 6070–6077, Dec. 2013, doi: 10.1021/nl403341x.

[27] N. Sköld *et al.*, "Growth and Optical Properties of Strained GaAs−Ga x In 1 - x P Core−Shell Nanowires," *Nano Lett.*, vol. 5, no. 10, pp. 1943–1947, Oct. 2005, doi: 10.1021/nl051304s.

[28] L. Gagliano, M. Albani, M. A. Verheijen, E. P. A. M. Bakkers, and L. Miglio, "Twofold origin of strain-induced bending in core–shell nanowires: the GaP/InGaP case," *Nanotechnology*, vol. 29, no. 31, p. 315703, Aug. 2018, doi: 10.1088/1361-6528/aac417.

[29] K. Tomioka, M. Yoshimura, and T. Fukui, "A III–V nanowire channel on silicon for high-performance vertical transistors," *Nature*, vol. 488, no. 7410, pp. 189–192, Aug. 2012, doi: 10.1038/nature11293.

[30] S. Morkötter *et al.*, "Demonstration of confined electron gas and steep-slope behavior in

delta-doped GaAs-AlGaAs core-shell nanowire transistors," *Nano Lett.*, vol. 15, no. 5, pp. 3295–3302, 2015, doi: 10.1021/acs.nanolett.5b00518.

[31] J. L. Boland *et al.*, "Towards higher electron mobility in modulation doped GaAs/AlGaAs core shell nanowires," *Nanoscale*, vol. 9, no. 23, pp. 7839–7846, 2017, doi: 10.1039/c7nr00680b.

[32] P. Bhattacharya, R. Fornari, and H. Kamimura, *Comprehensive Semiconductor Science and Technology*. Elsevier Science, 2011.

[33] J. Mishra, Umesh, Singh, *Semiconductor Device Physics and Design*. 2008.

[34] M. K. Hudait and R. Chau, "Integrating III-V on Silicon for Future Nanoelectronics," in *2008 IEEE Compound Semiconductor Integrated Circuits Symposium*, Oct. 2008, pp. 1–2, doi: 10.1109/CSICS.2008.8.

[35] Y. Kamata, "High-k/Ge MOSFETs for future nanoelectronics," *Mater. Today*, vol. 11, no. 1–2, pp. 30–38, Jan. 2008, doi: 10.1016/S1369-7021(07)70350-4.

[36] D.-H. Kim and J. A. del Alamo, "Logic Performance of 40 nm InAs HEMTs," in *2007 IEEE International Electron Devices Meeting*, 2007, pp. 629–632, doi: 10.1109/IEDM.2007.4419018.

[37] S. H. Simon, "The Oxford Solid State Basics," *J. Chem. Inf. Model.*, vol. 53, no. 9, pp. 1689–1699, 2013, doi: 10.1017/CBO9781107415324.004.

[38] S. Adachi, *GaAs and Related Materials*. WORLD SCIENTIFIC, 1994.

[39] B. Raton, L. New, and F. Group, *Holgate - 2010 - Understanding solid state physics*. .

[40] M. S. Leite, R. L. Woo, W. D. Hong, D. C. Law, and H. A. Atwater, "InAlAs epitaxial growth for wide band gap solar cells," in *2011 37th IEEE Photovoltaic Specialists Conference*, Jun. 2011, pp. 000780–000783, doi: 10.1109/PVSC.2011.6186070.

[41] A. S. Huntington, M. A. Compton, and G. M. Williams, "Improved breakdown model for estimating dark count rate in avalanche photodiodes with InP and InAlAs multiplication layers," May 2006, p. 62140R, doi: 10.1117/12.668659.

[42] C. J. K. Richardson and M. L. Lee, "Metamorphic epitaxial materials," *MRS Bull.*, vol. 41, no. 3, pp. 193–198, Mar. 2016, doi: 10.1557/mrs.2016.7.

[43] S. Adachi, *Properties of Semiconductor Alloys: Group-IV, III-V and II-VI Semiconductors*. 2009.

[44] S. Adachi, "III-V Ternary and Quaternary Compounds," in *Springer Handbook of Electronic and Photonic Materials*, Cham: Springer International Publishing, 2017, pp. 1–1.

[45] J. L. Boland *et al.*, "Modulation doping of GaAs/AlGaAs core-shell nanowires with effective defect passivation and high electron mobility," *Nano Lett.*, vol. 15, no. 2, pp. 1336–1342, 2015, doi: 10.1021/nl504566t.

[46] S. Adachi, *Physical Properties of III-V Semiconductor Compounds*. Wiley, 1992.

[47] J. A. del Alamo, "Nanometre-scale electronics with III–V compound semiconductors," *Nature*, vol. 479, no. 7373, pp. 317–323, Nov. 2011, doi: 10.1038/nature10677.

[48] N. Waldron, "III-V Devices and Technology for CMOS," in *High Mobility Materials for CMOS Applications*, Elsevier, 2018, pp. 231–280.

[49] H. J. Joyce *et al.*, "The influence of surfaces on the transient terahertz conductivity and electron mobility of GaAs nanowires," *J. Phys. D. Appl. Phys.*, vol. 50, no. 22, 2017, doi: 10.1088/1361-6463/aa6a8f.

[50] H. J. Joyce *et al.*, “Electron mobilities approaching bulk limits in ‘surface-free’ GaAs nanowires,” *Nano Lett.*, vol. 14, no. 10, pp. 5989–5994, 2014, doi: 10.1021/nl503043p.

[51] X. Dai, A. Olivier, C. Wilhelm, S. A. Dayeh, and C. Soci, “Advanced III–V nanowire growth toward large-scale integration,” in *Semiconductor Nanowires*, Elsevier, 2015, pp. 71–124.

[52] T. Dursap *et al.*, “Crystal phase engineering of self-catalyzed GaAs nanowires using a RHEED diagram,” *Nanoscale Adv.*, vol. 2, no. 5, pp. 2127–2134, 2020, doi: 10.1039/D0NA00273A.

[53] E. Dimakis *et al.*, “In situ doping of catalyst-free InAs nanowires with Si: Growth, polytypism, and local vibrational modes of Si,” *Appl. Phys. Lett.*, vol. 103, no. 14, p. 143121, Sep. 2013, doi: 10.1063/1.4824344.

[54] J. Johansson, J. Bolinsson, M. Ek, P. Caroff, and K. A. Dick, “Combinatorial Approaches to Understanding Polytypism in III–V Nanowires,” *ACS Nano*, vol. 6, no. 7, pp. 6142–6149, Jul. 2012, doi: 10.1021/nn301477x.

[55] X. Qian, M. Kawai, H. Goto, and J. Li, “Effect of twin boundaries and structural polytypes on electron transport in GaAs,” *Comput. Mater. Sci.*, vol. 108, pp. 258–263, Oct. 2015, doi: 10.1016/j.commatsci.2015.06.011.

[56] J. L. Boland *et al.*, “Towards higher electron mobility in modulation doped GaAs/AlGaAs core shell nanowires,” *Nanoscale*, vol. 9, no. 23, pp. 7839–7846, 2017, doi: 10.1039/c7nr00680b.

[57] K. Shinohara *et al.*, “Ultrahigh-speed pseudomorphic InGaAs/InAlAs HEMTs with 400-GHz cutoff frequency,” *IEEE Electron Device Lett.*, vol. 22, no. 11, pp. 507–509, Nov. 2001, doi: 10.1109/55.962645.

[58] T. Akazaki, T. Enoki, K. Arai, and Y. Ishii, “Improving the characteristics of an inverted HEMT by inserting an InAs layer into the InGaAs channel,” *Solid. State. Electron.*, vol. 38, no. 5, pp. 997–1000, May 1995, doi: 10.1016/0038-1101(95)98667-R.

[59] S. R. Bank, M. A. Wistey, L. L. Goddard, H. B. Yuen, V. Lordi, and J. S. Harris, “Low-threshold continuous-wave 1.5-/spl mu/m GaInNAsSb lasers grown on GaAs,” *IEEE J. Quantum Electron.*, vol. 40, no. 6, pp. 656–664, Jun. 2004, doi: 10.1109/JQE.2004.828249.

[60] G. Belenky, L. Shterengas, D. Wang, G. Kipshidze, and L. Vorobjev, “Continuous wave operated 3.2 µm type-I quantum-well diode lasers with the quinary waveguide layer,” *Semicond. Sci. Technol.*, vol. 24, no. 11, p. 115013, Nov. 2009, doi: 10.1088/0268-1242/24/11/115013.

[61] N. Tansu and L. J. Mawst, “High-performance strain-compensated InGaAs-GaAsP-GaAs (/spl lambda/=1.17 µm) quantum well diode lasers,” *IEEE Photonics Technol. Lett.*, vol. 13, no. 3, pp. 179–181, 2001, doi: 10.1109/68.914313.

[62] X. Yan, S. Fan, X. Zhang, and X. Ren, “Analysis of Critical Dimensions for Nanowire Core-Multishell Heterostructures,” *Nanoscale Res. Lett.*, vol. 10, no. 1, 2015, doi: 10.1186/s11671-015-1097-7.

[63] C. Z. N. Peidong Yang, L. Dou, and P. Yang, “Bandgap engineering in semiconductor alloy nanomaterials with widely tunable compositions,” *Nat. Rev. Mater.*, vol. 2, 2017, doi: 10.1038/natrevmats.2017.70.

[64] J. Johansson and K. A. Dick, “Recent advances in semiconductor nanowire heterostructures,” *CrystEngComm*, vol. 13, no. 24, p. 7175, 2011, doi:

10.1039/c1ce05821e.

[65] L. Balaghi *et al.*, “Widely tunable GaAs bandgap via strain engineering in core/shell nanowires with large lattice mismatch,” *Nat. Commun.*, vol. 10, no. 1, 2019, doi: 10.1038/s41467-019-10654-7.

[66] E. Barrigón, M. Heurlin, Z. Bi, B. Monemar, and L. Samuelson, “Synthesis and Applications of III–V Nanowires,” *Chem. Rev.*, vol. 119, no. 15, pp. 9170–9220, Aug. 2019, doi: 10.1021/acs.chemrev.9b00075.

[67] M. Royo, M. De Luca, R. Rurali, and I. Zardo, “A review on III–V core–multishell nanowires: growth, properties, and applications,” *J. Phys. D. Appl. Phys.*, vol. 50, no. 14, p. 143001, Apr. 2017, doi: 10.1088/1361-6463/aa5d8e.

[68] S. Barth, F. Hernandez-Ramirez, J. D. Holmes, and A. Romano-Rodriguez, “Synthesis and applications of one-dimensional semiconductors,” *Prog. Mater. Sci.*, vol. 55, no. 6, pp. 563–627, Aug. 2010, doi: 10.1016/j.pmatsci.2010.02.001.

[69] R. G. Hobbs, N. Petkov, and J. D. Holmes, “Semiconductor Nanowire Fabrication by Bottom-Up and Top-Down Paradigms,” *Chem. Mater.*, vol. 24, no. 11, pp. 1975–1991, Jun. 2012, doi: 10.1021/cm300570n.

[70] M. Lee, K. Y. Baik, M. Noah, Y.-K. Kwon, J.-O. Lee, and S. Hong, “Nanowire and nanotube transistors for lab-on-a-chip applications,” *Lab Chip*, vol. 9, no. 16, p. 2267, 2009, doi: 10.1039/b905185f.

[71] P. Yang, R. Yan, and M. Fardy, “Semiconductor Nanowire: What’s Next?,” *Nano Lett.*, vol. 10, no. 5, pp. 1529–1536, May 2010, doi: 10.1021/nl100665r.

[72] C. M. Lieber and Z. L. Wang, “Functional Nanowires,” *MRS Bull.*, vol. 32, no. 2, pp. 99–108, Feb. 2007, doi: 10.1557/mrs2007.41.

[73] A. Heinzig, S. Slesazeck, F. Kreupl, T. Mikolajick, and W. M. Weber, “Reconfigurable Silicon Nanowire Transistors,” *Nano Lett.*, vol. 12, no. 1, pp. 119–124, Jan. 2012, doi: 10.1021/nl203094h.

[74] O. Hayden, R. Agarwal, and C. M. Lieber, “Nanoscale avalanche photodiodes for highly sensitive and spatially resolved photon detection,” *Nat. Mater.*, vol. 5, no. 5, pp. 352–356, May 2006, doi: 10.1038/nmat1635.

[75] Z. Fan, J. C. Ho, Z. A. Jacobson, H. Razavi, and A. Javey, “Large-scale, heterogeneous integration of nanowire arrays for image sensor circuitry,” *Proc. Natl. Acad. Sci.*, vol. 105, no. 32, pp. 11066–11070, Aug. 2008, doi: 10.1073/pnas.0801994105.

[76] C. Soci, A. Zhang, X.-Y. Bao, H. Kim, Y. Lo, and D. Wang, “Nanowire Photodetectors,” *J. Nanosci. Nanotechnol.*, vol. 10, no. 3, pp. 1430–1449, Mar. 2010, doi: 10.1166/jnn.2010.2157.

[77] K. E. Fischer *et al.*, “Biomimetic Nanowire Coatings for Next Generation Adhesive Drug Delivery Systems,” *Nano Lett.*, vol. 9, no. 2, pp. 716–720, Feb. 2009, doi: 10.1021/nl803219f.

[78] C. K. Chan *et al.*, “High-performance lithium battery anodes using silicon nanowires,” *Nat. Nanotechnol.*, vol. 3, no. 1, pp. 31–35, Jan. 2008, doi: 10.1038/nnano.2007.411.

[79] E.-S. Liu, J. Nah, K. M. Varahramyan, and E. Tutuc, “Lateral Spin Injection in Germanium Nanowires,” *Nano Lett.*, vol. 10, no. 9, pp. 3297–3301, Sep. 2010, doi: 10.1021/nl1008663.

[80] C. Rehnstedt, T. Martensson, C. Thelander, L. Samuelson, and L.-E. Wernersson, “Vertical

InAs Nanowire Wrap Gate Transistors on Si Substrates," *IEEE Trans. Electron Devices*, vol. 55, no. 11, pp. 3037–3041, Nov. 2008, doi: 10.1109/TED.2008.2005179.

[81] K. Kneipp, H. Kneipp, and J. Kneipp, "Surface-Enhanced Raman Scattering in Local Optical Fields of Silver and Gold NanoaggregatesFrom Single-Molecule Raman Spectroscopy to Ultrasensitive Probing in Live Cells," *Acc. Chem. Res.*, vol. 39, no. 7, pp. 443–450, Jul. 2006, doi: 10.1021/ar050107x.

[82] M. T. Björk *et al.*, "Si–InAs heterojunction Esaki tunnel diodes with high current densities," *Appl. Phys. Lett.*, vol. 97, no. 16, p. 163501, Oct. 2010, doi: 10.1063/1.3499365.

[83] K. Tomioka and T. Fukui, "Tunnel field-effect transistor using InAs nanowire/Si heterojunction," *Appl. Phys. Lett.*, vol. 98, no. 8, p. 083114, Feb. 2011, doi: 10.1063/1.3558729.

[84] S. Mauthe *et al.*, "Monolithic Integration of III -V on silicon for photonic and electronic applications," in *2018 76th Device Research Conference (DRC)*, Jun. 2018, pp. 1–2, doi: 10.1109/DRC.2018.8442241.

[85] Y. Cui *et al.*, "Boosting Solar Cell Photovoltage via Nanophotonic Engineering," *Nano Lett.*, vol. 16, no. 10, pp. 6467–6471, Oct. 2016, doi: 10.1021/acs.nanolett.6b02971.

[86] D. van Dam *et al.*, "High-Efficiency Nanowire Solar Cells with Omnidirectionally Enhanced Absorption Due to Self-Aligned Indium–Tin–Oxide Mie Scatterers," *ACS Nano*, vol. 10, no. 12, pp. 11414–11419, Dec. 2016, doi: 10.1021/acsnano.6b06874.

[87] N. Waldron *et al.*, "InGaAs Gate-All-Around Nanowire Devices on 300mm Si Substrates," *IEEE Electron Device Lett.*, vol. 35, no. 11, pp. 1097–1099, Nov. 2014, doi: 10.1109/LED.2014.2359579.

[88] J. Zhang *et al.*, "Multi-spectral optical absorption in substrate-free nanowire arrays," *Appl. Phys. Lett.*, vol. 105, no. 12, p. 123113, Sep. 2014, doi: 10.1063/1.4896772.

[89] J. J. Gu, Y. Q. Liu, Y. Q. Wu, R. Colby, R. G. Gordon, and P. D. Ye, "First experimental demonstration of gate-all-around III–V MOSFETs by top-down approach," in *2011 International Electron Devices Meeting*, Dec. 2011, pp. 33.2.1-33.2.4, doi: 10.1109/IEDM.2011.6131662.

[90] X. Zhao, A. Vardi, and J. A. del Alamo, "Sub-Thermal Subthreshold Characteristics in Top–Down InGaAs/InAs Heterojunction Vertical Nanowire Tunnel FETs," *IEEE Electron Device Lett.*, vol. 38, no. 7, pp. 855–858, Jul. 2017, doi: 10.1109/LED.2017.2702612.

[91] S. Ramesh *et al.*, "Top-down InGaAs nanowire and fin vertical FETs with record performance," in *2016 IEEE Symposium on VLSI Technology*, Jun. 2016, pp. 1–2, doi: 10.1109/VLSIT.2016.7573419.

[92] N. P. Dasgupta *et al.*, "25th Anniversary Article: Semiconductor Nanowires - Synthesis, Characterization, and Applications," *Adv. Mater.*, vol. 26, no. 14, pp. 2137–2184, Apr. 2014, doi: 10.1002/adma.201305929.

[93] C. García Núñez, F. Liu, W. T. Navaraj, A. Christou, D. Shakthivel, and R. Dahiya, "Heterogeneous integration of contact-printed semiconductor nanowires for high-performance devices on large areas," *Microsystems Nanoeng.*, vol. 4, no. 1, p. 22, Dec. 2018, doi: 10.1038/s41378-018-0021-6.

[94] Anna Fontcuberta i Morral Shadi Dayeh Chennupati Jagadish, *Semiconductor Nanowires I: Growth and Theory, Volume 93, 1st Edition*. 2015.

[95] J. Vukajlovic-Plestina *et al.*, “Fundamental aspects to localize self-catalyzed III-V nanowires on silicon,” *Nat. Commun.*, vol. 10, no. 1, p. 869, Dec. 2019, doi: 10.1038/s41467-019-08807-9.

[96] R. S. Wagner and W. C. Ellis, “VAPOR-LIQUID-SOLID MECHANISM OF SINGLE CRYSTAL GROWTH,” *Appl. Phys. Lett.*, vol. 4, no. 5, pp. 89–90, Mar. 1964, doi: 10.1063/1.1753975.

[97] K. Haraguchi, T. Katsuyama, K. Hiruma, and K. Ogawa, “GaAs p - n junction formed in quantum wire crystals,” *Appl. Phys. Lett.*, vol. 60, no. 6, pp. 745–747, Feb. 1992, doi: 10.1063/1.106556.

[98] X. Duan and C. M. Lieber, “General Synthesis of Compound Semiconductor Nanowires,” *Adv. Mater.*, vol. 12, no. 4, pp. 298–302, Feb. 2000, doi: 10.1002/(SICI)1521-4095(200002)12:4<298::AID-ADMA298>3.0.CO;2-Y.

[99] M. R. Ramdani, J. C. Harmand, F. Glas, G. Patriarche, and L. Travers, “Arsenic Pathways in Self-Catalyzed Growth of GaAs Nanowires,” *Cryst. Growth Des.*, vol. 13, no. 1, pp. 91–96, Jan. 2013, doi: 10.1021/cg301167g.

[100] G. Bemski, “Recombination Properties of Gold in Silicon,” *Phys. Rev.*, vol. 111, no. 6, pp. 1515–1518, Sep. 1958, doi: 10.1103/PhysRev.111.1515.

[101] J. B. Hannon, S. Kodambaka, F. M. Ross, and R. M. Tromp, “The influence of the surface migration of gold on the growth of silicon nanowires,” *Nature*, vol. 440, no. 7080, pp. 69–71, Mar. 2006, doi: 10.1038/nature04574.

[102] S. Kodambaka, J. B. Hannon, R. M. Tromp, and F. M. Ross, “Control of Si Nanowire Growth by Oxygen,” *Nano Lett.*, vol. 6, no. 6, pp. 1292–1296, Jun. 2006, doi: 10.1021/nl060059p.

[103] J. E. Allen *et al.*, “High-resolution detection of Au catalyst atoms in Si nanowires,” *Nat. Nanotechnol.*, vol. 3, no. 3, pp. 168–173, Mar. 2008, doi: 10.1038/nnano.2008.5.

[104] O. Moutanabbir, D. Isheim, H. Blumtritt, S. Senz, E. Pippel, and D. N. Seidman, “Colossal injection of catalyst atoms into silicon nanowires,” *Nature*, vol. 496, no. 7443, pp. 78–82, Apr. 2013, doi: 10.1038/nature11999.

[105] M. Bar-Sadan, J. Barthel, H. Shtrikman, and L. Houben, “Direct Imaging of Single Au Atoms Within GaAs Nanowires,” *Nano Lett.*, vol. 12, no. 5, pp. 2352–2356, May 2012, doi: 10.1021/nl300314k.

[106] E. Dimakis, M. Ramsteiner, A. Tahraoui, H. Riechert, and L. Geelhaar, “Shell-doping of GaAs nanowires with Si for n-type conductivity,” *Nano Res.*, vol. 5, no. 11, pp. 796–804, 2012, doi: 10.1007/s12274-012-0263-9.

[107] S. Plissard, G. Larrieu, X. Wallart, and P. Caroff, “High yield of self-catalyzed GaAs nanowire arrays grown on silicon via gallium droplet positioning,” *Nanotechnology*, vol. 22, no. 27, p. 275602, Jul. 2011, doi: 10.1088/0957-4484/22/27/275602.

[108] M. Heilmann *et al.*, “Vertically Oriented Growth of GaN Nanorods on Si Using Graphene as an Atomically Thin Buffer Layer,” *Nano Lett.*, vol. 16, no. 6, pp. 3524–3532, Jun. 2016, doi: 10.1021/acs.nanolett.6b00484.

[109] C. Colombo, D. Spirkoska, M. Frimmer, G. Abstreiter, and A. Fontcuberta i Morral, “Ga-assisted catalyst-free growth mechanism of GaAs nanowires by molecular beam epitaxy,” *Phys. Rev. B*, vol. 77, no. 15, p. 155326, Apr. 2008, doi: 10.1103/PhysRevB.77.155326.

[110] G. Zhang, K. Tateno, M. D. Birowosuto, M. Notomi, T. Sogawa, and H. Gotoh, “Controlled 1.1–1.6 μ m luminescence in gold-free multi-stacked InAs/InP heterostructure nanowires,” *Nanotechnology*, vol. 26, no. 11, p. 115704, Mar. 2015, doi: 10.1088/0957-

4484/26/11/115704.

[111] T. Tauchnitz, Y. Berdnikov, V. G. Dubrovskii, H. Schneider, M. Helm, and E. Dimakis, “A simple route to synchronized nucleation of self-catalyzed GaAs nanowires on silicon for sub-Poissonian length distributions,” *Nanotechnology*, vol. 29, no. 50, p. 504004, Dec. 2018, doi: 10.1088/1361-6528/aae361.

[112] D. W. Shaw, “Selective Epitaxial Deposition of Gallium Arsenide in Holes,” *J. Electrochem. Soc.*, vol. 113, no. 9, p. 904, 1966, doi: 10.1149/1.2424153.

[113] D. A. Andrews, M. A. Z. Rejman-Greene, B. Wakefield, and G. J. Davies, “Selective area growth of InP/InGaAs multiple quantum well laser structures by metalorganic molecular beam epitaxy,” *Appl. Phys. Lett.*, vol. 53, no. 2, pp. 97–98, Jul. 1988, doi: 10.1063/1.100360.

[114] H. J. Yoo, J. R. Hayes, C. Caneau, R. Bhat, and M. Koza, “Fabrication of lateral planar InP/GaInAsP heterojunction bipolar transistor by selective area epitaxial growth,” *Electron. Lett.*, vol. 25, no. 3, p. 191, 1989, doi: 10.1049/el:19890138.

[115] T. Hamano, H. Hirayama, and Y. Aoyagi, “New Technique for Fabrication of Two-Dimensional Photonic Bandgap Crystals by Selective Epitaxy,” *Jpn. J. Appl. Phys.*, vol. 36, no. Part 2, No. 3A, pp. L286–L288, Mar. 1997, doi: 10.1143/JJAP.36.L286.

[116] K. Ikejiri *et al.*, “Growth characteristics of GaAs nanowires obtained by selective area metal–organic vapour-phase epitaxy,” *Nanotechnology*, vol. 19, no. 26, p. 265604, Jul. 2008, doi: 10.1088/0957-4484/19/26/265604.

[117] K. Tomioka, P. Mohan, J. Noborisaka, S. Hara, J. Motohisa, and T. Fukui, “Growth of highly uniform InAs nanowire arrays by selective-area MOVPE,” *J. Cryst. Growth*, vol. 298, pp. 644–647, Jan. 2007, doi: 10.1016/j.jcrysgro.2006.10.183.

[118] M. Inari, J. Takeda, J. Motohisa, and T. Fukui, “Selective area MOVPE growth of InP and InGaAs pillar structures for InP-based two-dimensional photonic crystals,” *Phys. E Low-dimensional Syst. Nanostructures*, vol. 21, no. 2–4, pp. 620–624, Mar. 2004, doi: 10.1016/j.physe.2003.11.091.

[119] J. Motohisa, J. Noborisaka, J. Takeda, M. Inari, and T. Fukui, “Catalyst-free selective-area MOVPE of semiconductor nanowires on (111)B oriented substrates,” *J. Cryst. Growth*, vol. 272, no. 1–4, pp. 180–185, Dec. 2004, doi: 10.1016/j.jcrysgro.2004.08.118.

[120] F. Ishizaka, Y. Hiraya, K. Tomioka, and T. Fukui, “Growth of wurtzite GaP in InP/GaP core–shell nanowires by selective-area MOVPE,” *J. Cryst. Growth*, vol. 411, pp. 71–75, Feb. 2015, doi: 10.1016/j.jcrysgro.2014.10.024.

[121] J. Treu *et al.*, “Lattice-Matched InGaAs-InAlAs core-shell nanowires with improved luminescence and photoresponse properties,” *Nano Lett.*, vol. 15, no. 5, pp. 3533–3540, 2015, doi: 10.1021/acs.nanolett.5b00979.

[122] G. Koblmüller and G. Abstreiter, “Growth and properties of InGaAs nanowires on silicon,” *Phys. status solidi - Rapid Res. Lett.*, vol. 8, no. 1, pp. 11–30, Jan. 2014, doi: 10.1002/pssr.201308207.

[123] O. Arif *et al.*, “Growth and Strain Relaxation Mechanisms of InAs/InP/GaAsSb Core-Dual-Shell Nanowires,” *Cryst. Growth Des.*, vol. 20, no. 2, pp. 1088–1096, Feb. 2020, doi: 10.1021/acs.cgd.9b01421.

[124] A. W. Dey, J. Svensson, M. Ek, E. Lind, C. Thelander, and L.-E. Wernersson, “Combining Axial and Radial Nanowire Heterostructures: Radial Esaki Diodes and Tunnel Field-Effect

Transistors," *Nano Lett.*, vol. 13, no. 12, pp. 5919–5924, Dec. 2013, doi: 10.1021/nl4029494.

[125] E. M. T. Fadaly *et al.*, "Direct-bandgap emission from hexagonal Ge and SiGe alloys," *Nature*, vol. 580, no. 7802, pp. 205–209, Apr. 2020, doi: 10.1038/s41586-020-2150-y.

[126] Y.-H. Ra and C.-R. Lee, "Core–Shell Tunnel Junction Nanowire White-Light-Emitting Diode," *Nano Lett.*, p. acs.nanolett.0c00420, May 2020, doi: 10.1021/acs.nanolett.0c00420.

[127] A. Manolescu, A. Sitek, J. Osca, L. Serra, V. Gudmundsson, and T. D. Stanescu, "Majorana states in prismatic core-shell nanowires," *Phys. Rev. B*, vol. 96, no. 12, p. 125435, Sep. 2017, doi: 10.1103/PhysRevB.96.125435.

[128] J. Ridderbos *et al.*, "Hard Superconducting Gap and Diffusion-Induced Superconductors in Ge–Si Nanowires," *Nano Lett.*, vol. 20, no. 1, pp. 122–130, Jan. 2020, doi: 10.1021/acs.nanolett.9b03438.

[129] P. Zellekens *et al.*, "Phase coherent transport and spin-orbit interaction in GaAs/InSb core/shell nanowires," *Semicond. Sci. Technol.*, Mar. 2020, doi: 10.1088/1361-6641/ab8396.

[130] "The rise of integrated quantum photonics," *Nat. Photonics*, vol. 14, no. 5, pp. 265–265, May 2020, doi: 10.1038/s41566-020-0634-9.

[131] H. Arab, S. MohammadNejad, A. KhodadadKashi, and S. Ahadzadeh, "Recent advances in nanowire quantum dot (NWQD) single-photon emitters," *Quantum Inf. Process.*, vol. 19, no. 2, p. 44, Feb. 2020, doi: 10.1007/s11128-019-2542-9.

[132] S. Fust *et al.*, "Quantum-Confinement-Enhanced Thermoelectric Properties in Modulation-Doped GaAs–AlGaAs Core–Shell Nanowires," *Adv. Mater.*, vol. 32, no. 4, p. 1905458, Jan. 2020, doi: 10.1002/adma.201905458.

[133] L. J. Lauhon, M. S. Gudiksen, D. Wang, and C. M. Lieber, "Epitaxial core–shell and core–multishell nanowire heterostructures," *Nature*, vol. 420, no. 6911, pp. 57–61, Nov. 2002, doi: 10.1038/nature01141.

[134] M. Ben-Ishai and F. Patolsky, "A Route to High-Quality Crystalline Coaxial Core/Multishell Ge@Si(GeSi) n and Si@(GeSi) n Nanowire Heterostructures," *Adv. Mater.*, vol. 22, no. 8, pp. 902–906, Feb. 2010, doi: 10.1002/adma.200902815.

[135] F. Qian, Y. Li, S. Gradečak, D. Wang, C. J. Barrelet, and C. M. Lieber, "Gallium Nitride-Based Nanowire Radial Heterostructures for Nanophotonics," *Nano Lett.*, vol. 4, no. 10, pp. 1975–1979, Oct. 2004, doi: 10.1021/nl0487774.

[136] F. Qian, S. Gradečak, Y. Li, C.-Y. Wen, and C. M. Lieber, "Core/Multishell Nanowire Heterostructures as Multicolor, High-Efficiency Light-Emitting Diodes," *Nano Lett.*, vol. 5, no. 11, pp. 2287–2291, Nov. 2005, doi: 10.1021/nl051689e.

[137] P. Mohan, J. Motohisa, and T. Fukui, "Fabrication of InP/InAs/InP core-multishell heterostructure nanowires by selective area metalorganic vapor phase epitaxy," *Appl. Phys. Lett.*, vol. 88, no. 13, p. 133105, Mar. 2006, doi: 10.1063/1.2189203.

[138] P. K. Mohseni, C. Maunders, G. A. Botton, and R. R. LaPierre, "GaP/GaAsP/GaP core–multishell nanowire heterostructures on (111) silicon," *Nanotechnology*, vol. 18, no. 44, p. 445304, Nov. 2007, doi: 10.1088/0957-4484/18/44/445304.

[139] J. C. Tracy, W. Wiegman, R. A. Logan, and F. K. Reinhart, "Three-dimensional light guides in single-crystal GaAs–Al x Ga 1 − x As," *Appl. Phys. Lett.*, vol. 22, no. 10, pp. 511–512, May 1973, doi: 10.1063/1.1654488.

[140] A. Fontcuberta i Morral, D. Spirkoska, J. Arbiol, M. Heigoldt, J. R. Morante, and G. Abstreiter, “Prismatic Quantum Heterostructures Synthesized on Molecular-Beam Epitaxy GaAs Nanowires,” *Small*, vol. 4, no. 7, pp. 899–903, Jul. 2008, doi: 10.1002/smll.200701091.

[141] M. Heigoldt *et al.*, “Long range epitaxial growth of prismatic heterostructures on the facets of catalyst-free GaAs nanowires,” *J. Mater. Chem.*, vol. 19, no. 7, p. 840, 2009, doi: 10.1039/b816585h.

[142] L. Mancini *et al.*, “Three-dimensional nanoscale study of Al segregation and quantum dot formation in GaAs/AlGaAs core-shell nanowires,” *Appl. Phys. Lett.*, vol. 105, no. 24, p. 243106, Dec. 2014, doi: 10.1063/1.4904952.

[143] C. Zhou *et al.*, “Epitaxial GaAs/AlGaAs core–multishell nanowires with enhanced photoluminescence lifetime,” *Nanoscale*, vol. 11, no. 14, pp. 6859–6865, 2019, doi: 10.1039/C9NR01715A.

[144] M. S. Sydney G. Davison, *Basic Theory of Surface States*. Sydney G. Davison is at University of Waterloo, Ontario. Maria Steslicka is at University of Wroclaw, Cybulskiego.: Clarendon Press, 1996.

[145] R. S. Lee *et al.*, “Electrical Properties of Surface-Passivated GaAs Nanowires,” *Appl. Sci. Converg. Technol.*, vol. 27, no. 6, pp. 166–168, Nov. 2018, doi: 10.5757/ASCT.2018.27.6.166.

[146] P. A. Alekseev *et al.*, “Nitride Surface Passivation of GaAs Nanowires: Impact on Surface State Density,” *Nano Lett.*, vol. 15, no. 1, pp. 63–68, Jan. 2015, doi: 10.1021/nl502909k.

[147] J. L. Boland *et al.*, “Increased Photoconductivity Lifetime in GaAs Nanowires by Controlled n-Type and p-Type Doping,” *ACS Nano*, vol. 10, no. 4, pp. 4219–4227, 2016, doi: 10.1021/acsnano.5b07579.

[148] N. Jiang *et al.*, “Enhanced minority carrier lifetimes in GaAs/AlGaAs core-shell nanowires through shell growth optimization,” *Nano Lett.*, vol. 13, no. 11, pp. 5135–5140, 2013, doi: 10.1021/nl4023385.

[149] D. Rudolph *et al.*, “Spontaneous Alloy Composition Ordering in GaAs-AlGaAs Core–Shell Nanowires,” *Nano Lett.*, vol. 13, no. 4, pp. 1522–1527, Apr. 2013, doi: 10.1021/nl3046816.

[150] Y. Zhang *et al.*, “Polarity-driven quasi-3-fold composition symmetry of self-catalyzed III-V-V ternary core-shell nanowires,” *Nano Lett.*, vol. 15, no. 5, pp. 3128–3133, 2015, doi: 10.1021/acs.nanolett.5b00188.

[151] S. Assali *et al.*, “Kinetic Control of Morphology and Composition in Ge/GeSn Core/Shell Nanowires,” *ACS Nano*, vol. 14, no. 2, pp. 2445–2455, Feb. 2020, doi: 10.1021/acsnano.9b09929.

[152] R. Bergamaschini, F. Montalenti, and L. Miglio, “Sunburst pattern by kinetic segregation in core-shell nanowires: A phase-field study,” *Appl. Surf. Sci.*, vol. 517, p. 146056, Jul. 2020, doi: 10.1016/j.apsusc.2020.146056.

[153] M. Heiss *et al.*, “Self-assembled quantum dots in a nanowire system for quantum photonics,” *Nat. Mater.*, vol. 12, no. 5, pp. 439–444, May 2013, doi: 10.1038/nmat3557.

[154] N. Jeon *et al.*, “Alloy Fluctuations Act as Quantum Dot-like Emitters in GaAs-AlGaAs Core–Shell Nanowires,” *ACS Nano*, vol. 9, no. 8, pp. 8335–8343, Aug. 2015, doi: 10.1021/acsnano.5b04070.

[155] H. A. Fonseka *et al.*, “Self-Formed Quantum Wires and Dots in GaAsP–GaAsP Core–Shell Nanowires,” *Nano Lett.*, vol. 19, no. 6, pp. 4158–4165, Jun. 2019, doi: 10.1021/acs.nanolett.9b01673.

[156] H. J. Joyce, J. L. Boland, C. L. Davies, S. A. Baig, and M. B. Johnston, “A review of the electrical properties of semiconductor nanowires: Insights gained from terahertz conductivity spectroscopy,” *Semicond. Sci. Technol.*, vol. 31, no. 10, 2016, doi: 10.1088/0268-1242/31/10/103003.

[157] A. Fontcuberta i Morral, “Nanostructured alloys light the way to silicon-based photonics,” *Nature*, vol. 580, no. 7802, pp. 188–189, Apr. 2020, doi: 10.1038/d41586-020-00976-8.

[158] T. Vasen *et al.*, “Vertical Gate-All-Around Nanowire GaSb-InAs Core-Shell n-Type Tunnel FETs,” *Sci. Rep.*, vol. 9, no. 1, p. 202, Dec. 2019, doi: 10.1038/s41598-018-36549-z.

[159] G. Koblmüller, B. Mayer, T. Stettner, G. Abstreiter, and J. J. Finley, “GaAs–AlGaAs core–shell nanowire lasers on silicon: invited review,” *Semicond. Sci. Technol.*, vol. 32, no. 5, p. 053001, May 2017, doi: 10.1088/1361-6641/aa5e45.

[160] S. Conesa-Boj *et al.*, “Boosting Hole Mobility in Coherently Strained [110]-Oriented Ge-Si Core-Shell Nanowires,” *Nano Lett.*, vol. 17, no. 4, pp. 2259–2264, 2017, doi: 10.1021/acs.nanolett.6b04891.

[161] S. Takagi, J. Koga, and a. Toriumi, “Subband structure engineering for performance enhancement of Si\nMOSFETs,” *Int. Electron Devices Meet. IEDM Tech. Dig.*, vol. 410, pp. 219–222, 1997, doi: 10.1109/IEDM.1997.650345.

[162] J. P. de S. D. K. Sadana, S. W. Bedell, A. Reznicek and and K. F. H. Chen, “Strain Engineering for Si CMOS Technology,” *207th ECS Meet. Abstr. #719, Copyr. ECS, T.J. Watson Res. Cent. IBM, Yorkt. Height. NY 10598*, 2005.

[163] M. Grundmann, *The Physics of Semiconductors*. Cham: Springer International Publishing, 2016.

[164] S. A. Holgate, *Understanding Solid State Physics*. 2013.

[165] J. H. Davies, *THE PHYSICS OF LOW-DIMENSIONAL SEMICONDUCTORS*. CAMBRIDGE UNIVERSITY PRESS, 2005.

[166] C. Kittel, *Introduction to Solid State Physics, 8th Edition*. Wiley, 2004.

[167] J. Singh, “Physics of semiconductors,” *Springer Ser. Mater. Sci.*, 2014, doi: 10.1007/978-3-319-09985-9_6.

[168] J. Groenen, R. Carles, G. Landa, C. Guerret-Piécourt, and C. Fontaine, “Optical-phonon behavior in The role of microscopic strains and ionic plasmon coupling,” *Phys. Rev. B - Condens. Matter Mater. Phys.*, vol. 58, no. 16, pp. 10452–10462, 1998, doi: 10.1103/PhysRevB.58.10452.

[169] R. Eryiğit and I. P. Herman, “Lattice properties of strained GaAs, Si, and Ge using a modified bond-charge model,” *Phys. Rev. B - Condens. Matter Mater. Phys.*, vol. 53, no. 12, pp. 7775–7784, 1996, doi: 10.1103/PhysRevB.53.7775.

[170] A. H. W. N. R.E. Smallman, *Modern Physical Metallurgy (Eighth Edition)*. Chapter 10, 2014.

[171] J. Grönqvist, N. Søndergaard, F. Boxberg, T. Guhr, S. Åberg, and H. Q. Xu, “Strain in semiconductor core-shell nanowires,” *J. Appl. Phys.*, vol. 106, 2009, doi: 10.1063/1.3207838.

[172] M. Ohring, “Epitaxy,” in *Materials Science of Thin Films*, Elsevier, 2002, pp. 417–494.

[173] Q. Li and K. M. Lau, “Epitaxial growth of highly mismatched III-V materials on (001) silicon for electronics and optoelectronics,” *Prog. Cryst. Growth Charact. Mater.*, vol. 63, no. 4, pp. 105–120, Dec. 2017, doi: 10.1016/j.pcrysgrow.2017.10.001.

[174] U. W. Pohl, *Epitaxy of Semiconductors*. Berlin, Heidelberg: Springer Berlin Heidelberg, 2013.

[175] F. Boxberg, N. Søndergaard, and H. Q. Xu, “Photovoltaics with piezoelectric core-shell nanowires.,” *Nano Lett.*, vol. 10, no. 4, pp. 1108–12, Apr. 2010, doi: 10.1021/nl9040934.

[176] J. Zou, D. J. H. Cockayne, and B. F. Usher, “Misfit dislocations and critical thickness in InGaAs/GaAs heterostructure systems,” *J. Appl. Phys.*, vol. 73, no. 2, pp. 619–626, Jan. 1993, doi: 10.1063/1.353372.

[177] G. Signorello *et al.*, “Manipulating Surface States of III-V Nanowires with Uniaxial Stress,” *Nano Lett.*, vol. 17, no. 5, pp. 2816–2824, 2017, doi: 10.1021/acs.nanolett.6b05098.

[178] G. Signorello, S. Karg, M. T. Björk, B. Gotsmann, and H. Riel, “Tuning the light emission from GaAs nanowires over 290 meV with uniaxial strain,” *Nano Lett.*, vol. 13, no. 3, pp. 917–924, 2013, doi: 10.1021/nl303694c.

[179] P. Ghosh and M. Huang, “Effects of strain on various properties and applications on one-dimensional nano-/microstructures,” *J. Mater. Sci.*, vol. 55, no. 17, pp. 7208–7225, Jun. 2020, doi: 10.1007/s10853-020-04500-1.

[180] B. Wei, K. Zheng, Y. Ji, Y. Zhang, Z. Zhang, and X. Han, “Size-Dependent Bandgap Modulation of ZnO Nanowires by Tensile Strain,” *Nano Lett.*, vol. 12, no. 9, pp. 4595–4599, Sep. 2012, doi: 10.1021/nl301897q.

[181] M. Hetzl *et al.*, “Strain-Induced Band Gap Engineering in Selectively Grown GaN–(Al,Ga)N Core–Shell Nanowire Heterostructures,” *Nano Lett.*, vol. 16, no. 11, pp. 7098–7106, Nov. 2016, doi: 10.1021/acs.nanolett.6b03354.

[182] G. Signorello *et al.*, “Inducing a direct-to-pseudodirect bandgap transition in wurtzite GaAs nanowires with uniaxial stress,” *Nat. Commun.*, vol. 5, no. 7491, 2014, doi: 10.1038/ncomms4655.

[183] L. Zeng *et al.*, “Correlation between Electrical Transport and Nanoscale Strain in InAs/In 0.6 Ga 0.4 As Core–Shell Nanowires,” *Nano Lett.*, vol. 18, no. 8, pp. 4949–4956, Aug. 2018, doi: 10.1021/acs.nanolett.8b01782.

[184] J. Petykiewicz *et al.*, “Direct Bandgap Light Emission from Strained Germanium Nanowires Coupled with High-Q Nanophotonic Cavities,” *Nano Lett.*, vol. 16, no. 4, pp. 2168–2173, Apr. 2016, doi: 10.1021/acs.nanolett.5b03976.

[185] S. Bao *et al.*, “Low-threshold optically pumped lasing in highly strained germanium nanowires,” *Nat. Commun.*, vol. 8, no. 1, p. 1845, Dec. 2017, doi: 10.1038/s41467-017-02026-w.

[186] Y. Zhang *et al.*, “Highly Strained III–V–V Coaxial Nanowire Quantum Wells with Strong Carrier Confinement,” *ACS Nano*, vol. 13, no. 5, pp. 5931–5938, May 2019, doi: 10.1021/acsnano.9b01775.

[187] Z. Zhu, J. Svensson, A. R. Persson, R. Wallenberg, A. V. Gromov, and L.-E. Wernersson, “Compressively-strained GaSb nanowires with core-shell heterostructures,” *Nano Res.*, Jun. 2020, doi: 10.1007/s12274-020-2889-3.

[188] F. Wen and E. Tutuc, “Strained Si x Ge 1−x -Ge-Si core-double-shell nanowire heterostructures for simultaneous hole and electron mobility enhancement,” *Appl. Phys. Lett.*, vol. 113, no. 11, p. 113102, Sep. 2018, doi: 10.1063/1.5047212.

[189] P. A. Alekseev, V. A. Sharov, B. R. Borodin, M. S. Dunaevskiy, R. R. Reznik, and G. E. Cirlin, “Effect of the Uniaxial Compression on the GaAs Nanowire Solar Cell,” *Micromachines*, vol. 11, no. 6, p. 581, Jun. 2020, doi: 10.3390/mi11060581.

[190] H. Li *et al.*, “Novel Type-II InAs/AlSb Core-Shell Nanowires and Their Enhanced Negative Photocurrent for Efficient Photodetection,” *Adv. Funct. Mater.*, vol. 28, no. 8, p. 1705382, Feb. 2018, doi: 10.1002/adfm.201705382.

[191] K. Chiba, A. Yoshida, K. Tomioka, and J. Motohisa, “Vertical InGaAs Nanowire Array Photodiodes on Si,” *ACS Photonics*, vol. 6, no. 2, pp. 260–264, Feb. 2019, doi: 10.1021/acsphotonics.8b01089.

[192] I. Zardo *et al.*, “Pressure-Tuning of the Optical Properties of GaAs Nanowires,” *ACS Nano*, vol. 6, no. 4, pp. 3284–3291, 2012, doi: 10.1021/nn300228u.

[193] I. Zardo *et al.*, “Raman spectroscopy of wurtzite and zinc-blende GaAs nanowires: Polarization dependence, selection rules, and strain effects,” *Phys. Rev. B*, vol. 80, no. 24, p. 245324, Dec. 2009, doi: 10.1103/PhysRevB.80.245324.

[194] F. Cerdeira, C. J. Buchenauer, F. H. Pollak, and M. Cardona, “Stress-induced shifts of first-order Raman frequencies of diamond- and zinc-blende-type semiconductors,” *Phys. Rev. B*, vol. 5, no. 2, pp. 580–593, 1972, doi: 10.1103/PhysRevB.5.580.

[195] C. G. Van de Walle, “Band lineups and deformation potentials in the model-solid theory,” *Phys. Rev. B*, vol. 39, no. 3, pp. 1871–1883, Jan. 1989, doi: 10.1103/PhysRevB.39.1871.

[196] S.-H. Wei and A. Zunger, “Predicted band-gap pressure coefficients of all diamond and zinc-blende semiconductors: Chemical trends,” *Phys. Rev. B*, vol. 60, no. 8, pp. 5404–5411, Aug. 1999, doi: 10.1103/PhysRevB.60.5404.

[197] N. E. Christensen, “Electronic structure of GaAs under strain,” *Phys. Rev. B*, vol. 30, no. 10, pp. 5753–5765, Nov. 1984, doi: 10.1103/PhysRevB.30.5753.

[198] V. Umansky and M. Heiblum, “MBE growth of high-mobility 2DEG,” in *Molecular Beam Epitaxy*, Elsevier, 2013, pp. 121–137.

[199] V. Umansky, R. de-Picciotto, and M. Heiblum, “Extremely high-mobility two dimensional electron gas: evaluation of scattering mechanisms,” *Appl. Phys. Lett.*, vol. 71, no. 5, pp. 683–685, 1997, doi: 10.1063/1.119829.

[200] M. Zervos, “Delta(δ)-doping of semiconductor nanowires,” *Phys. Status Solidi - Rapid Res. Lett.*, vol. 7, no. 9, pp. 651–654, 2013, doi: 10.1002/pssr.201307219.

[201] H. L. Störmer, R. Dingle, A. C. Gossard, W. Wiegmann, and M. D. Sturge, “Two-dimensional electron gas at a semiconductor-semiconductor interface,” *Solid State Commun.*, vol. 29, no. 10, pp. 705–709, Mar. 1979, doi: 10.1016/0038-1098(79)91010-X.

[202] R. Dingle, H. L. Störmer, A. C. Gossard, and W. Wiegmann, “Electron mobilities in modulation-doped semiconductor heterojunction superlattices,” *Appl. Phys. Lett.*, vol. 33, no. 7, pp. 665–667, 1978, doi: 10.1063/1.90457.

[203] D. Lucot *et al.*, “Quasi one-dimensional transport in single GaAs/AlGaAs core-shell nanowires,” *Appl. Phys. Lett.*, vol. 98, no. 14, 2011, doi: 10.1063/1.3574026.

[204] K. Tomioka, M. Yoshimura, and T. Fukui, “A III-V nanowire channel on silicon for high-performance vertical transistors,” *Nature*, vol. 488, no. 7410, pp. 189–192, 2012, doi:

10.1038/nature11293.

[205] H. Kim, W. J. Lee, A. C. Farrell, A. Balgarkashi, and D. L. Huffaker, “Telecom-Wavelength Bottom-up Nanobeam Lasers on Silicon-on-Insulator,” *Nano Lett.*, vol. 17, no. 9, pp. 5244–5250, 2017, doi: 10.1021/acs.nanolett.7b01360.

[206] T. Chammah and T. Giuma, “Integrated Circuits 3D Silicon Integration,” in *2009 Fourth International Conference on Systems*, 2009, pp. 204–209, doi: 10.1109/ICONS.2009.13.

[207] G. Brönstrup *et al.*, “A precise optical determination of nanoscale diameters of semiconductor nanowires,” *Nanotechnology*, vol. 22, no. 38, p. 385201, Sep. 2011, doi: 10.1088/0957-4484/22/38/385201.

[208] J. J. Mock, D. R. Smith, and S. Schultz, “Local Refractive Index Dependence of Plasmon Resonance Spectra from Individual Nanoparticles,” *Nano Lett.*, vol. 3, no. 4, pp. 485–491, Apr. 2003, doi: 10.1021/nl0340475.

[209] Wikimedia Commons contributors, “Wikipedia.” https://commons.wikimedia.org/w/index.php?title=File:Bragg_XRD.svg&oldid=219002920 (accessed Apr. 18, 2020).

[210] G. Abstreiter, E. Bauser, A. Fischer, and K. Ploog, “Raman spectroscopy—A versatile tool for characterization of thin films and heterostructures of GaAs and AlxGa1−xAs,” *Appl. Phys.*, vol. 16, no. 4, pp. 345–352, Aug. 1978, doi: 10.1007/BF00885858.

[211] B. Ketterer, E. Uccelli, and A. Fontcuberta i Morral, “Mobility and carrier density in p-type GaAs nanowires measured by transmission Raman spectroscopy,” *Nanoscale*, vol. 4, no. 5, p. 1789, 2012, doi: 10.1039/c2nr11910b.

[212] “Chandrasekhara Venkata Raman, 1888-1970,” *Biogr. Mem. Fellows R. Soc.*, vol. 17, pp. 564–592, Nov. 1971, doi: 10.1098/rsbm.1971.0022.

[213] K. G. E, “Der Smekal-Raman-Effekt,” *Nature*, vol. 128, no. 3242, pp. 1026–1026, Dec. 1931, doi: 10.1038/1281026c0.

[214] R. Singh, “C. V. Raman and the Discovery of the Raman Effect,” *Phys. Perspect.*, vol. 4, no. 4, pp. 399–420, Dec. 2002, doi: 10.1007/s000160200002.

[215] D. A. Long, *The Raman Effect*. Chichester, UK: John Wiley & Sons, Ltd, 2002.

[216] R. Loudon, “The Raman effect in crystals,” *Adv. Phys.*, vol. 13, no. 52, pp. 423–482, Oct. 1964, doi: 10.1080/00018736400101051.

[217] W. Kauschke and M. Cardona, “Resonant Raman Scattering in Semiconductors,” *Phys. Scr.*, vol. T25, pp. 201–205, Jan. 1989, doi: 10.1088/0031-8949/1989/T25/036.

[218] R. Trommer and M. Cardona, “Resonant Raman scattering in GaAs,” *Phys. Rev. B*, vol. 17, no. 4, pp. 1865–1876, Feb. 1978, doi: 10.1103/PhysRevB.17.1865.

[219] I. Zardo *et al.*, “Raman spectroscopy of wurtzite and zinc-blende GaAs nanowires: Polarization dependence, selection rules, and strain effects,” *Phys. Rev. B*, vol. 80, no. 24, pp. 1–11, 2009, doi: 10.1103/PhysRevB.80.245324.

[220] C. A. Arguello, D. L. Rousseau, and S. P. S. Porto, “First-Order Raman Effect in Wurtzite-Type Crystals,” *Phys. Rev.*, vol. 181, no. 3, pp. 1351–1363, May 1969, doi: 10.1103/PhysRev.181.1351.

[221] S. Crankshaw, M. Moewe, L. C. Chuang, R. Chen, and C. Chang-Hasnain, “Polarized Raman Modes of a Single Wurtzite GaAs Needle,” in *Conference on Lasers and Electro-*

*Optics/International Quantum Electronics Conference*, 2009, p. CThCC7, doi: 10.1364/CLEO.2009.CThCC7.

[222] G. Chen *et al.*, "Optical Antenna Effect in Semiconducting Nanowires," *Nano Lett.*, vol. 8, no. 5, pp. 1341–1346, May 2008, doi: 10.1021/nl080007v.

[223] C. García Núñez *et al.*, "Surface optical phonons in GaAs nanowires grown by Ga-assisted chemical beam epitaxy," *J. Appl. Phys.*, vol. 115, no. 3, p. 034307, Jan. 2014, doi: 10.1063/1.4862742.

[224] F. Amaduzzi *et al.*, "Probing inhomogeneous composition in core/shell nanowires by Raman spectroscopy," *J. Appl. Phys.*, vol. 116, no. 18, p. 184303, 2014, doi: 10.1063/1.4901504.

[225] F. Amaduzzi *et al.*, "Tuning the response of non-allowed Raman modes in GaAs nanowires," *J. Phys. D. Appl. Phys.*, vol. 49, no. 9, p. 095103, Mar. 2016, doi: 10.1088/0022-3727/49/9/095103.

[226] Yun-Shik Lee, *Principles of Terahertz Science and Technology*. Boston, MA: Springer US, 2009.

[227] I. Fotev *et al.*, "Electron dynamics in In<inf>x</inf>Ga<inf>1-x</inf>As shells around GaAs nanowires probed by terahertz spectroscopy," *Nanotechnology*, vol. 30, no. 24, 2019, doi: 10.1088/1361-6528/ab0913.

[228] A. M. Crook *et al.*, "Low resistance, nonalloyed Ohmic contacts to InGaAs," *Appl. Phys. Lett.*, vol. 91, no. 19, p. 192114, Nov. 2007, doi: 10.1063/1.2806235.

[229] E. F. Chor, W. K. Chong, and C. H. Heng, "Alternative (Pd,Ti,Au) contacts to (Pt,Ti,Au) contacts for In0.53Ga0.47As," *J. Appl. Phys.*, vol. 84, no. 5, pp. 2977–2979, Sep. 1998, doi: 10.1063/1.368449.

[230] E. F. Chor, R. J. Malik, R. A. Hamm, and R. Ryan, "Metallurgical stability of ohmic contacts on thin base InP/InGaAs/InP HBT's," *IEEE Electron Device Lett.*, vol. 17, no. 2, pp. 62–64, Feb. 1996, doi: 10.1109/55.484124.

[231] Y. K. Fukai, K. Kurishima, N. Kashio, M. Ida, S. Yamahata, and T. Enoki, "Emitter-metal-related degradation in InP-based HBTs operating at high current density and its suppression by refractory metal," *Microelectron. Reliab.*, vol. 49, no. 4, pp. 357–364, Apr. 2009, doi: 10.1016/j.microrel.2009.01.005.

[232] A. . Baca, F. Ren, J. . Zolper, R. . Briggs, and S. . Pearton, "A survey of ohmic contacts to III-V compound semiconductors," *Thin Solid Films*, vol. 308–309, pp. 599–606, Oct. 1997, doi: 10.1016/S0040-6090(97)00439-2.

[233] V. Jain *et al.*, "Effect of surface preparations on contact resistivity of TiW to highly doped n-InGaAs," in *2009 IEEE International Conference on Indium Phosphide & Related Materials*, May 2009, pp. 358–361, doi: 10.1109/ICIPRM.2009.5012438.

[234] G. Stareev, H. Künzel, and G. Dortmann, "A controllable mechanism of forming extremely low-resistance nonalloyed ohmic contacts to group III-V compound semiconductors," *J. Appl. Phys.*, vol. 74, no. 12, pp. 7344–7356, Dec. 1993, doi: 10.1063/1.355002.

[235] S. Birner, *Modeling of semiconductor nanostructures and semiconductor – electrolyte interfaces ISBN 978-3-941650-35-0 Modeling of semiconductor nanostructures and semiconductor – electrolyte interfaces Stefan Birner*, vol. 135. 2011.

[236] W. S. Institut, T. U. München, C. T. Andlauer, P. Greck, T. Kubis, and P. Vogl, "next nano Nextnano : a predictive tool for mesoscopic semiconductor structures."

[237] S. Birner, “nextnano.” https://www.nextnano.de/.

[238] A. J. Ptak, “Principles of Molecular Beam Epitaxy,” in *Handbook of Crystal Growth*, Elsevier, 2015, pp. 161–192.

[239] Y. Greenberg, A. Kelrich, S. Cohen, S. Kar-Narayan, D. Ritter, and Y. Calahorra, “Strain-Mediated Bending of InP Nanowires through the Growth of an Asymmetric InAs Shell,” *Nanomaterials*, vol. 9, no. 9, p. 1327, Sep. 2019, doi: 10.3390/nano9091327.

[240] R. W. Day, M. N. Mankin, and C. M. Lieber, “Plateau-Rayleigh Crystal Growth of Nanowire Heterostructures: Strain-Modified Surface Chemistry and Morphological Control in One, Two, and Three Dimensions,” *Nano Lett.*, vol. 16, no. 4, pp. 2830–2836, 2016, doi: 10.1021/acs.nanolett.6b00629.

[241] R. B. Lewis, P. Corfdir, H. Küpers, T. Flissikowski, O. Brandt, and L. Geelhaar, “Nanowires Bending over Backward from Strain Partitioning in Asymmetric Core–Shell Heterostructures,” *Nano Lett.*, vol. 18, no. 4, pp. 2343–2350, Apr. 2018, doi: 10.1021/acs.nanolett.7b05221.

[242] N. Sköld *et al.*, “Phase segregation in AlInP shells on GaAs nanowires.,” *Nano Lett.*, vol. 6, no. 12, pp. 2743–2747, 2006, doi: 10.1021/nl061692d.

[243] Y. Y.-N. Guo, T. Burgess, Q. Gao, H. H. Tan, C. Jagadish, and J. Zou, “Polarity-driven Non-uniform Composition in InGaAs Nanowires.,” *Nano Lett.*, vol. 13, no. 11, pp. 5085–5089, 2013, doi: 10.1021/nl402244p.

[244] K. Aoki, E. Anastassakis, and M. Cardona, “Dependence of Raman frequencies and scattering intensities on pressure in GaSb, InAs, and InSb semiconductors,” *Phys. Rev. B*, vol. 30, no. 2, pp. 681–687, Jul. 1984, doi: 10.1103/PhysRevB.30.681.

[245] F. H. Pollak and M. Cardona, “Piezo-Electroreflectance in Ge, GaAs, and Si,” *Phys. Rev.*, vol. 172, no. 3, pp. 816–837, Aug. 1968, doi: 10.1103/PhysRev.172.816.

[246] W. G. Aulbur, L. Jönsson, and J. W. Wilkins, “Quasiparticle Calculations in Solids,” 2000, pp. 1–218.

[247] A. Sitek, M. Urbaneja Torres, K. Torfason, V. Gudmundsson, A. Bertoni, and A. Manolescu, “Excitons in Core–Shell Nanowires with Polygonal Cross Sections,” *Nano Lett.*, vol. 18, no. 4, pp. 2581–2589, Apr. 2018, doi: 10.1021/acs.nanolett.8b00309.

[248] M. Chu, Y. Sun, U. Aghoram, and S. E. Thompson, “Strain: A Solution for Higher Carrier Mobility in Nanoscale MOSFETs,” *Annu. Rev. Mater. Res.*, vol. 39, no. 1, pp. 203–229, Aug. 2009, doi: 10.1146/annurev-matsci-082908-145312.

[249] X. Li, K. Maute, M. L. Dunn, and R. Yang, “Strain effects on the thermal conductivity of nanostructures,” *Phys. Rev. B*, vol. 81, no. 24, p. 245318, Jun. 2010, doi: 10.1103/PhysRevB.81.245318.

[250] J. Cao and J. Wu, “Strain effects in low-dimensional transition metal oxides,” *Mater. Sci. Eng. R Reports*, vol. 71, no. 2–4, pp. 35–52, Jan. 2011, doi: 10.1016/j.mser.2010.08.001.

[251] P. J. Goodhew, “Dislocation behaviour at heterointerfaces in III–V semiconductors,” *J. Phys. Chem. Solids*, vol. 55, no. 10, pp. 1107–1114, Oct. 1994, doi: 10.1016/0022-3697(94)90128-7.

[252] A. Atkinson, S. C. Jain, and A. H. Harker, “Strain, dislocations, and critical dimensions of laterally small lattice-mismatched semiconductor layers,” *J. Appl. Phys.*, vol. 77, no. 5, pp. 1907–1913, Mar. 1995, doi: 10.1063/1.358822.

[253] F. Karimi, M. Fathipour, H. Ghanatian, and V. Fathipour, “Improvement of short channel effects in cylindrical strained silicon nanowire transistor,” *World Acad. Sci. Eng. Technol.*, vol. 70, pp. 467–470, 2010.

[254] F. Wen and E. Tutuc, “Enhanced Electron Mobility in Nonplanar Tensile Strained Si Epitaxially Grown on Si x Ge 1– x Nanowires,” *Nano Lett.*, vol. 18, no. 1, pp. 94–100, Jan. 2018, doi: 10.1021/acs.nanolett.7b03450.

[255] S. Conesa-Boj *et al.*, “Boosting Hole Mobility in Coherently Strained [110]-Oriented Ge-Si Core-Shell Nanowires,” *Nano Lett.*, vol. 17, no. 4, 2017, doi: 10.1021/acs.nanolett.6b04891.

[256] C.-H. Ge *et al.*, “Process-strained Si (PSS) CMOS technology featuring 3D strain engineering,” in *IEEE International Electron Devices Meeting 2003*, pp. 3.7.1-3.7.4, doi: 10.1109/IEDM.2003.1269169.

[257] J. a. del Alamo, “Nanometre-scale electronics with III–V compound semiconductors,” *Nature*, vol. 479, no. 7373, pp. 317–323, 2011, doi: 10.1038/nature10677.

[258] H. J. Joyce, J. L. Boland, C. L. Davies, S. A. Baig, and M. B. Johnston, “A review of the electrical properties of semiconductor nanowires: insights gained from terahertz conductivity spectroscopy,” *Semicond. Sci. Technol.*, vol. 31, no. 10, p. 103003, Oct. 2016, doi: 10.1088/0268-1242/31/10/103003.

[259] G. A. Samara, “Temperature and pressure dependences of the dielectric constants of semiconductors,” *Phys. Rev. B*, vol. 27, no. 6, pp. 3494–3505, 1983, doi: 10.1103/PhysRevB.27.3494.

[260] J. H. Strait, P. A. George, M. Levendorf, M. Blood-Forsythe, F. Rana, and J. Park, “Measurements of the Carrier Dynamics and Terahertz Response of Oriented Germanium Nanowires using Optical-Pump Terahertz-Probe Spectroscopy,” *Nano Lett.*, vol. 9, no. 8, pp. 2967–2972, Aug. 2009, doi: 10.1021/nl901373j.

[261] H. J. Joyce *et al.*, “Electronic properties of GaAs, InAs and InP nanowires studied by terahertz spectroscopy,” *Nanotechnology*, vol. 24, no. 21, p. 214006, 2013, doi: 10.1088/0957-4484/24/21/214006.

[262] P. Parkinson *et al.*, “Transient terahertz conductivity of GaAs nanowires,” *Nano Lett.*, vol. 7, no. 7, pp. 2162–2165, 2007, doi: 10.1021/nl071162x.

[263] J. M. Pitarke, J. B. Pendry, and P. M. Echenique, “Electron energy loss in composite systems,” *Phys. Rev. B*, vol. 55, no. 15, pp. 9550–9557, 1997, doi: 10.1103/PhysRevB.55.9550.

[264] N. E. Christensen, “Electronic structure of GaAs under strain,” *Phys. Rev. B*, vol. 30, no. 10, pp. 5753–5765, Nov. 1984, doi: 10.1103/PhysRevB.30.5753.

[265] C. M. Maziar and M. S. Lundstrom, “Caughey-Thomas parameters for electron mobility calculations in GaAs,” *Electron. Lett.*, vol. 22, no. 11, pp. 565–566, May 1986, doi: 10.1049/el:19860384.

[266] A. Bertoni, M. Royo, F. Mahawish, and G. Goldoni, “Electron and hole gas in modulation-doped GaAs/Al1−xGaxAs radial heterojunctions,” *Phys. Rev. B*, vol. 84, no. 20, p. 205323, Nov. 2011, doi: 10.1103/PhysRevB.84.205323.

[267] H. Y. S. Al-Zahrani, J. Pal, M. A. Migliorato, G. Tse, and D. Yu, “Piezoelectric field enhancement in III–V core–shell nanowires,” *Nano Energy*, vol. 14, pp. 382–391, May 2015, doi: 10.1016/j.nanoen.2014.11.046.

[268] M. Friedl *et al.*, “Template-Assisted Scalable Nanowire Networks,” *Nano Lett.*, vol. 18,

no. 4, pp. 2666–2671, Apr. 2018, doi: 10.1021/acs.nanolett.8b00554.

[269] Y. H. Huo *et al.*, "A light-hole exciton in a quantum dot," *Nat. Phys.*, vol. 10, no. 1, pp. 46–51, 2013, doi: 10.1038/nphys2799.

[270] C. B. Zota, D. Lindgren, L.-E. Wernersson, and E. Lind, "Quantized Conduction and High Mobility in Selectively Grown In x Ga 1– x As Nanowires," *ACS Nano*, vol. 9, no. 10, pp. 9892–9897, Oct. 2015, doi: 10.1021/acsnano.5b03318.

[271] J. Gooth *et al.*, "Ballistic one-dimensional transport in InAs nanowires monolithically integrated on silicon," *Appl. Phys. Lett.*, vol. 110, no. 8, 2017, doi: 10.1063/1.4977031.

[272] E. F. Chor, D. Zhang, H. Gong, W. K. Chong, and S. Y. Ong, "Electrical characterization, metallurgical investigation, and thermal stability studies of (Pd, Ti, Au)-based ohmic contacts," *J. Appl. Phys.*, vol. 87, no. 5, pp. 2437–2444, Mar. 2000, doi: 10.1063/1.372198.

[273] J. C. Lin, S. Y. Yu, and S. E. Mohney, "Characterization of low-resistance ohmic contacts to n - and p -type InGaAs," *J. Appl. Phys.*, vol. 114, no. 4, p. 044504, Jul. 2013, doi: 10.1063/1.4816097.

[274] S. Wirths *et al.*, "Preparation of Ohmic contacts to GaAs/AlGaAs-core/shell-nanowires," *Appl. Phys. Lett.*, vol. 100, no. 4, 2012, doi: 10.1063/1.3678639.

[275] R. Chen, K. L. Jungjohann, W. M. Mook, J. Nogan, and S. A. Dayeh, "Atomic Scale Dynamics of Contact Formation in the Cross-Section of InGaAs Nanowire Channels," *Nano Lett.*, vol. 17, no. 4, pp. 2189–2196, Apr. 2017, doi: 10.1021/acs.nanolett.6b04713.

[276] J. L. Boland *et al.*, "High Electron Mobility and Insights into Temperature-Dependent Scattering Mechanisms in InAsSb Nanowires," *Nano Lett.*, 2018, doi: 10.1021/acs.nanolett.8b00842.

[277] A. C. Clark, K. K. Schwarzwälder, T. Bandi, D. Maradan, and D. M. Zumbühl, "Method for cooling nanostructures to microkelvin temperatures," *Rev. Sci. Instrum.*, vol. 81, no. 10, p. 103904, Oct. 2010, doi: 10.1063/1.3489892.

[278] J. B. Miller *et al.*, "Fractional quantum Hall effect in a quantum point contact at filling fraction 5/2," *Nat. Phys.*, vol. 3, no. 8, pp. 561–565, Aug. 2007, doi: 10.1038/nphys658.

**List of abbreviations**

| | |
|---|---|
| HEMT | high electron mobility transistors |
| 2DEG | two-dimensional electron gas |
| nanowire-FETs | nanowires based field effect transistors |
| Si-CMOS | Si based complementary metal oxide semiconductor |
| OPTPS | optical-pump terahertz-probe spectroscopy |
| ZB | zincblende |
| WZ | wurtzite |
| fcc | face-centered cubic |
| BZ | Brillouin zone |
| CB | conduction band |
| HH | heavy holes |
| LH | light holes |
| SO | split-off |
| TB | tight-binding |
| H | Hamiltonian matrix |
| A | acoustic |
| O | optical |
| L | longitudinal |
| *eq.* | equation |
| MIR | medium infrared |
| FIR | far infrared |
| MBE | molecular beam epitaxy |
| VLS | vapor-liquid-solid |
| CVD | chemical vapor deposition |
| UHV | ultrahigh vacuum |
| RHEED | Reflection high-energy electron diffraction |

| | |
|---|---|
| $SiO_x$ | native oxide |
| $L_S$ | Shell thickness |
| x | composition |
| SAED | selective area electron diffraction |
| STEM-TOMO | scanning TEM-Tomography |
| BSE | back-scattered electrons |
| EDX(S) | energy-dispersive X-ray (spectroscopy) |
| HIM | Helium ion microscope |
| e-beam | Electron beam |
| XRD | X-ray diffraction |
| GID | Grazing incidence diffraction |
| HR-XRD | High resolution-XRD |
| PL | photoluminescence |
| DOS | density of state |
| THz | terahertz |
| PCA | photoconductive antenna |
| EO sampling | electro-optic sampling |
| L1 or L2 | lock-in amplifiers 1 or 2 |
| EBL | e-beam lithography |
| PR | photoresist |
| RTA | rapid thermal annealing |
| IV measurement | current voltage measurement |
| 1D or 2D or 3D | one or two or three dimension |
| FF | Filling factor |
| CBM | conduction band minimum |
| VBM | valence band minimum |

| | |
|---|---|
| TR-PL | Time-resolved photoluminescence |
| IBEP | Inhomogeneous broadening effect of plasmon |
| DI | deionized water |
| IPA | Isopropyl alcohol |

**List of Symbols**

| | |
|---|---|
| $S_{ij}$ | elastic compliance tensor |
| $\varepsilon_h$ | hydrostatic strain |
| $\perp$ | dislocation |
| $E_c^0$ or $E_v^0$ | CB or VB edge of strain-free material |
| $a_c$ or $a_v$ | hydrostatic deformation potential of CB or VB |
| $\varepsilon_{xx\ or\ yy\ or\ zz}$ | strain element along the x or y or z direction |
| $\Upsilon$ | (mode-)Grüneisen parameter |
| $\Upsilon_e$ | scattering rate of electrons |
| $p, q, r$ | phenomenological parameters |
| $\Delta\omega_h$ | shift of phonon based on hydrostatic strain |
| $\varepsilon_h$ | hydrostatic strain |
| $\omega_0$ | strain-free phonon frequency |
| $J(\omega)$ | current density |
| $\sigma(\omega)$ | complex conductivity |
| $\sigma_{Re}(\omega)$ or $\sigma_{Im}(\omega)$ | real or imaginary part of conductivity |
| $\epsilon(\omega)$ | complex dielectric function |
| $\epsilon_1(\omega)$ or $\epsilon_2(\omega)$ | real or imaginary part of conductivity |
| $\epsilon_0$ | dielectric permittivity of free space |
| $\epsilon_{background}(\omega)$ | dielectric function related to lattice contribution |
| $\epsilon_\infty(\omega)$ | high frequency dielectric constant |
| $\epsilon_{static}$ | low frequency (static) dielectric constant |
| $n'(\omega)$ | complex refractive index |

| | |
|---|---|
| $n(\omega)$ | refractive index of material |
| $k(\omega)$ | imaginary part related to the absorption |
| $\Delta\sigma(\omega)$ | photo-conductivity |
| $N$ | carrier density |
| μ | mobility |
| $m^*$ | effective mass of charge carriers |
| δ | delta-doping layer |
| $\varepsilon_{zz}$ | axial strain |
| $W$ | strain energy |
| $V$ | volume |
| d | average of atomic layer distances |
| $a_0$ | lattice-constant |
| λ | wavelength |
| 1/λ | wavenumber |
| $I_{PCA}$ | photocurrent |
| λ/4 plate | quarter-wave plate |
| $\Delta\phi$ | Phase change |
| $L$ | propagation distance |
| $r_{41}$ | EO coefficient |
| $I_s$ | THz intensity signal |
| $f_{1 \text{ or } 2}$ | demodulated frequency |
| $\Delta E$ | differential OPTP signal |
| $f$ | misfit |
| $\Delta V/V$ | relative change in a crystal volume |
| $E^o$ | strain-free bandgap |
| $a$ | hydrostatic deformation potential coefficient |

| | |
|---|---|
| $E_1$ | band-edge transitions |
| $\Delta E_v$ | shift of the bandgap in VB |
| $\Delta_0$ | SO coupling effect at the VB maxima |
| A and B | Varshni fitting parameters |
| $T$ | temperature |
| $P$ | pressure |
| $N_e$ | electron density |
| $\omega_{0p}$ | resonant plasma frequency |
| $e$ | electronic charge |
| $\varepsilon_0$ | permittivity of free space |
| $\varepsilon_r$ | electric permittivity of the material |
| $g$ | geometrical factor |
| $\mu_{e-[111]}$ | electron mobility along [111] |
| $m^*_{e-[111]}$ | electron effective mass along [111] |

**List of publications**

| Authors | Title | Journal | DOI |
|---|---|---|---|
| **L. Balaghi**, S. Shan, I. Fotev, F. Moebus, R. Rana, T. Venanzi, R. Hübner, H. Schneider, M. Helm, A. Pashkin, E. Dimakis | Strain-induced enhancement of electron mobility in GaAs nanowires | Submitted | |
| **L. Balaghi**, G. Bussone, R. Grifone, R. Hübner, J. Grenzer, M. Ghorbani-Asl, A. Krasheninnikov, H. Schneider, M. Helm, E. Dimakis | Widely tunable GaAs bandgap via strain engineering in core/shell nanowires with large lattice mismatch | Nature Communication (2019) 10, 2793 | https://doi.org/10.1038/s41467-019-10654-7 |
| **L. Balaghi**, T. Tauchnitz, R. Hübner, L. Bischoff, H. Schneider, M. Helm, E. Dimakis | Droplet-confined alternate pulsed epitaxy of GaAs nanowires on Si substrates down to CMOS-compatible temperatures | Nano Letters (2016) 16, 4032 | https://doi.org/10.1021/acs.nanolett.6b00527 |
| R. Rana, **L. Balaghi**, I. Fotev, H. Schneider, M. Helm, E. Dimakis, A. Pashkin | Nonlinear Charge Transport in InGaAs Nanowires at Terahertz Frequencies | Nano Letters (2020) 20, 3225 | https://doi.org/10.1021/acs.nanolett.9b05328 |
| I. Fortev, **L. Balaghi**, J. Schmidt, H. Schneider, M. Helm, E. Dimakis, A. Pashkin | Electron dynamics in $In_xGa_{1-x}As$ shells around GaAs nanowires probed by terahertz spectroscopy | Nanotechnology (2019) 30, 244004 | https://doi.org/10.1088/1361-6528/ab0913 |
| D. Lang, **L. Balaghi**, S. Winnerl, H. Schneider, R. Hübner, S. C. Kehr, L. M. Eng, M. Helm, E. Dimakis, A. Pashkin | Nonlinear plasmonic response of doped nanowires observed by infrared nanospectroscopy | Nanotechnology (2018) 30, 084003 | https://doi.org/10.1088/1361-6528/aaf5a7 |

**List of conference contributions**

| Authors | Title | Conference |
|---|---|---|
| **L. Balaghi**, S. Shan, I. Fotev, R. Hübner, G. Bussone, R. Grifone, G. Hlawacek, J. Grenzer, H. Schneider, M. Helm, A. Pashkin, E. Dimakis | Strain engineering in lattice-mismatched core/shell nanowires: extending the properties of GaAs | Nanowire Week 2018, 11.06.2018 - Hamilton, Ontario, Canada: |
| **L. Balaghi**, R. Hübner, G. Bussone, R. Grifone, G. Hlawacek, J. Grenzer, H. Schneider, M. Helm, E. Dimakis | Strain distribution in GaAs/InxGa1-xAs core/shell nanowires grown by molecular beam epitaxy on Si(111) substrates | Surface and Interface Diffraction in Condensed Matter Physics and Chemistry (CMPC), 10.03.2017 - DESY, Hamburg, Germany |
| **L. Balaghi**, R. Hübner, G. Bussone, R. Grifone, G. Hlawacek, D. Wolf, J. Grenzer, H. Schneider, M. Helm, E. Dimakis | Strain distribution in highly mismatched GaAs/(In,Ga)As core/shell nanowires | DPG Frühjahrstreffen, 24.03.2017 - Dresden, Germany |
| **L. Balaghi**, R. Hübner, G. Bussone, R. Grifone, G. Hlawacek, D. Wolf, J. Grenzer, H. Schneider, M. Helm, E. Dimakis | Extremely lattice mismatched GaAs/$In_xGa_{1-x}As$ core/shell nanowires: coherent growth and strain distribution | Nanowire Week 2017, 29.05.2017 - Lund, Sweden |

**Acknowledgements**

I would like to thank my direct supervisor Dr. E Dimakis as the project leader during my PhD for his great help, support, and guidance through each stage of my PhD research project and leaving his enough time for any additional scientific and non-scientific discussions. Next, I would like to thank Dr. A Pashkin (the leader of THz spectroscopy during my PhD) who trained me in understanding the OPTPS and his help over different technical issues in Lab. I would like to thank Dr. G Bussone, Dr. R Grifone, and Dr. J Grenzer for the great collaboration and excellent effort concerning to XRD experiments. I would like to acknowledge Prof. Dr. M Helm and Dr. PD. H Schneider jobs for inspiring my interest in developing new ideas either theoretically or experimentally within my PhD and their financial supports. I would like to thank Prof. Dr. T Mikolajick for accepting me as his PhD student at NaMLab- a TU Dresden company, for nanoelectronics and advising me during my PhD presentations. I would like to thank Dr. S Winnerl for his kind help and advice in solving issues in the labs. I would like to thank Dr. R Hübner for his great job in electron microscopy lab and providing me relaxed time to work in the corresponding lab and giving me ideas how to proceed in structural and compositional analyses related to the nanowires and I am grateful to Dr D Wolf for performing STEM Tomography on the nanowires. I would like to thank U Luccesi and Dr. M Krause for their technical assistance in Raman lab. I would like to thank I Fotev, S Shan, Dr. J Schmidt, and F Moebus for their excellent jobs and help in THz spectroscopy during my PhD. I would like to thank Dr M Ghorbani and Dr. A Krasheninnikov for their fruitful collaboration in DFT calculations. I would like to thank T Venanzi for TRPL measurements in the last phase of my PhD before ending my contract. I would like to thank the device processing group, especially T Schönherr, C Neisser for EBL, and B Scheumann for their help in fabrication metal contacts. I would like to thank Dr. L Bischoff and A Kunz for their kind help in SEM, and FIB lab and giving me enough time slots in the lab. I would like to thank Dr. G Hlawacek for training me in HIM and giving me ideas about TEM sample preparation and mutual scientific discussions related to the electron microscopy. I would like to thank Dr. S Prucnal and Dr. Y Berencen for their assistance with PL spectroscopy. I would like to thank J Wagner for developing the work related to preparation of nanowire cross section by ultramicrotomy. At the end I would like to thank all members of FWIH, namely Dr. J M Braun, Dr. J König Otto in helping me in ELBE and acknowledge the great team-work at HZDR inside ion beam center as well as ELBE for their assist and kind collaborations within my PhD time. I would like to thank especially Dr. T Tauchnitz as my friend and colleague for her kind help and sympathy in motivating me in my difficult time.